Nonlinear frequency conversion under general phase mismatched conditions: the role of phase locking and random nonlinear domains

---

A thesis submitted for the degree of
Doctor of Philosophy in Physical Science of

Vito Roppo

Directors

Dr. Crina Maria Cojocaru

Dr. Jose Francisco Trull

and

Dr. Ramon Vilaseca i Alavedra

Departament de Física i Enginyeria Nuclear

Terrassa, June 2011

UNIVERSITAT POLITÈCNICA
DE CATALUNYA
BARCELONATECH

a Ilaria, Giorgia, Serena e Ester.

Trattenete piu a lungo che potete la vostra curiositá.

Preface

You see things that are and say "why?"
But I dream of things that never were, and say "why not?"
George Bernard Shaw

The key to reading this thesis work is from the point of view of *fundamental research*. Here the main goal is to try to understand the physics and the general behavior that lie beneath a particular phenomenon. While the starting point may be fixed, we are dealing with a moving target that is pushed forward every time a new knowledge is acquired and a missing piece of the puzzle added to the scheme. On the other hand there is the *applied research* whose objectives may be fixed by device specifications, and the work consists of gathering relevant knowledge to reach the goal. These definitions are not completely static, as new knowledge causes also advances technology. For example, fundamental research is always the

breeding ground where seeds may be sown and eventually see the light of important applications. *The personal computer* may be the most significant example. It may also happen that researchers working on a particular device find important clues to a new fundament theory. For example, two engineers (now Nobel Prizes) of Bell Lab working on a communication microwave antenna were the first to record the distant, faint echo of what started it all: The Big Bang.

This distinction was not at all clear to me when first I approached the world of physics. I took my first tentative steps in the group of Dr. Michael Scalora at Charles M. Bowden Research Facility, RDECOM, Alabama, and then in the group of Prof. Ramon Vilaseca, Prof. Crina Cojocaru and Prof. Jose Trull, in the Physics and Nonlinear Engineering Department at Polytechnic University of Catalonia. At a time when both groups were facing two *fundamental* problems concerning what appeared to be small details in nonlinear optics. My role was to help the team to answer questions like: Why does this happen? How does it work? And, my favorite, what happens if…?

Fortunately, these small details turned out to be not small after all, and wielded the power to open the doors to fertile research grounds. This thesis is a semi-chronological review of the main results we obtained during the last three years. The scheme is essentially serial since each result was first forecast using the previous results and then verified, mostly experimentally. This body of work is more or less complete thanks to the influence of the method of work, the tools, and the analytical and experimental results we developed during our research. For the sake of overall simplicity and self-consistency, we did not include all our results in this thesis work. Suffice it to say that, thankfully, this work is never done. As Phil Russell, of the Max Plank Institute, once put it: Open a book, any book, to a page, any page, and you will find that there is work to be done.

For more than forty years, scientists working in the field of nonlinear optics have focused their attention mainly on improving the conversion efficiency of harmonics generation, particularly of the second harmonic. This is achievable thanks to the fulfillment of very special working conditions.

The result is that while our understanding of this particular phenomenon has much improved over time, at the same time one may freely state that this knowledge is quite narrow. As soon as one looks in another direction one may easily ascertain that the amount of work done so far in this field is not enough to systematically cover all possible working conditions where frequency conversion phenomenon can take place. The object of this thesis work is thus to shed light on the general situation of large phase mismatched harmonic generation. Even if conversion efficiency may at first sight be relatively small compared to phase matched situations, we will show that two important features (random quasi phase matching and phase locking mechanism) arise, concerning respectively each of the two portion of the generated electromagnetic field. This is the first time that these two aspects have been investigated so extensively and we believe that our results represent a significant step forward in understanding these particular aspects of the nonlinear interactions.

Going now into the details, this thesis is organized as follow. In Chapter 1 we will briefly define the field of *nonlinear optics*. Linear optics deals with the study of the interaction of electromagnetic fields with matter with the assumption that their intensities are low *enough* to treat the relation between the impinging field and the induced polarization as *linear*. In all the other cases where electromagnetic forces start to be comparable with atomic forces acting on the electrons of the material, a series of *nonlinear* effects occur. Among these, harmonic generation (second and third in particular) is one of the most manifest and well-studied. Then we will describe the features of a *two dimensional nonlinear photonic crystal* and it's naturally occurrence in nature: the ferroelectric crystals. In this section we will also describe the set of equations and the numerical model that we have developed and continuously improved to be used throughout all the particular situations studied in this work.

Part I is dedicated to the study of harmonic generation in random nonlinear photonic crystals. Starting from the description of the crystal and of the first set of experiments we will illustrate the characteristics of second harmonic emission in such structures. The emerging need was to have a

clearer view of the real nonlinear optical properties possessed by these crystals. For different reasons traditional imaging techniques were partially unsuccessful, so that one has to rely on numerical calculations aimed at material characterization (Chapter 2). The wide transparency window of real crystals (example SBN and $NiLiO_3$) gives us the opportunity to also study the behavior of cascaded third harmonic emission thanks to the quadratic nonlinearity of the material (Chapter 3). Finally, we gathered and applied all the information to study the behavior in the pulsed regime. We propose a new technique of electromagnetic pulse characterization that complement the actual existing techniques and show several important advantages in the case of ultrashort pulse characterization. (Chapter 4).

Part II concerns the *phase locking mechanism*. In a nonlinear interaction, besides the usual generated component, the second harmonic has also a particular component that travels with the same k-vector of the fundamental beam. This led us to ponder about a general *theorem*: this particular second harmonic component *always* experiences the same complex index of refraction of the fundament beam. In Chapter 5 we lay the basis of this theory, with an extension to third harmonic generation. In Chapter 6 we use this theory to inhibit material absorption at the harmonic wavelengths. Following analytical studies of field dynamics in a free standing cavity environment we proceeded with an experimental test using a simple, single mirror cavity, followed by an efficient high-Q cavity that allowed us to reach more impressive results (Chapter 7). Finally we pushed our findings in the direction of the harmonics generation in *spectral regions* where materials display metallic behavior, i.e. where in principle no light propagation should be observed (Chapter 8). These last steps have great importance, because they show that it possible to actually do nonlinear optics in materials like GaAs, GaP, and Si, to name a few, in the UV part of the spectrum. At UV wavelengths semiconductors like those described above are remarkably dull because they are most notable for reflecting light. However, the insights developed in this thesis may help to pave the way to the realization of devices that efficiently generate light in the deep UV and soft X-ray range using ordinary materials and equally ordinary laser sources.

Taken as a whole, the work presents a balanced composition of the three main ingredients: theoretical study, numerical calculation and experimental verification. This mosaic is well distributed among the different groups which each time, depending on the actual needs and possibilities, gave the best synergistic effort. Great part of my personal work dwelt on the field of numerical calculations, which have a crucial role in everything that follows. The approach that has been followed was based on the development of new numerical algorithms to solve the Maxwell's set of equations based on spectral Fast Fourier Transform (FFT) method. This has multi-faceted importance: First, the direct manipulation of the equations of motion helps the individual to "get inside" the problem to actually understand it. Second, FFT methods require much deeper manipulations that ordinary ones. Third, the method is far from being a block-box approach, as commercial software tends to be, which can solve a problem in an almost effortless manner but cannot help develop any insight into any particular aspect of the problem. Fortunately this high-risk approach has thus produced a high-pay off in the form of wide research activity. Nevertheless I never forgot to theoretically verify the results obtained and to put my hands on the experiments.

An important feature of this thesis is the strong *team collaboration*. Research is teamwork. None of research results presented in this thesis can be claimed as solely my own, but all projects reported on benefited from the ideas and suggestions of my supervisors and colleagues. The base was the Physics and Nuclear Engineering Department of the Polytechnic University of Catalunya, Spain. The first topic (Part I) was developed in collaboration with Dr. Wieslaw Krolikowski of the Australian National University, Australia, where I personally spent six month. The second topic (Part II) was developed in collaboration with Dr. Michael Scalora at the C.M. Bowden Research Facility, Redstone Arsenal, USA, where I personally spent one year in total. Moreover, we actively collaborated with the group of Dr. Rama Raj and Dr. Fabrice Raineri at Laboratoire de Photonique et de Nanostructures, CNRS, France, for samples fabrication and experimental verification.

Contents

Part I

Part II

Part I

Chapter 1

Introduction

1.1. Nonlinear Maxwell's equations

Maxwell's 1873 results constitute a fascinating and complete synthesis of the entire theory of classical electromagnetism. Still today, the deep comprehension of Maxwell's four equations is the key behind one of the greatest and most exciting challenges in physics: manipulating light.

The introduction of the laser in the early ´60s gave a strong impetus to the study of electromagnetic phenomena in the infrared and visible ranges for high intensity light beams giving rise to a new branch of physics: the nonlinear optics. The emergence of modulated structures and metamaterials last decade, has led to remarkable achievements in this field. Since the ´70 a lot of effort has been dedicated to the study and the experimental improvement of the efficiency of the different nonlinear effects. Nonlinear optical interactions have been incredibly enhanced by means of photonic band gap photonic crystals and metamaterials have revealed novel kind of nonlinearities. Recently, nonlinear optics have also been showed to be

suitable to mimick exotic linear effects, like for example perfect lensing [Pen08].

This introductory chapter is intended to review the basics of linear and nonlinear light propagation in both homogeneous and structured crystals paying particular attention to the second and third-harmonic generation process. We also describe in some detail the numerical method that we have used to study the particular nonlinear effects that constitutes the object of this work. In each of these sections, we will focus particularly on the studies that are mostly related to our purposes and will voluntarily omit certain aspects. These expanding fields have however the advantage of being presented by a consequent number of reviews and textbooks, which the reader can refer to [Boy08], [Yar67], [Joa08], [Sha07], [Woo07].

Nonlinear Optics

Nonlinear electromagnetic phenomena occur when the response of a material system is no longer proportional to the amplitudes of applied electric and magnetic fields. Typically, these phenomena are only observable by means of laser light, which is sufficiently intense to modify the optical properties of matter and hence generate detectable nonlinear effects. The nonlinear optics begins with the discovery of the Second Harmonic (SH) generation process by Franken *et al.* in 1961 [Fra61], shortly after the realization of the first working laser by Maiman [Mai60]. Lasers have particular characteristics of monochromaticity and coherence and their light can be concentrated in very small areas, of order of some hundreds square microns. This makes possible to obtain very intense electric fields associated to the propagating wave comparable to those existing inside atoms and consequently to induce local modifications in the material composition, which cause the nonlinear responses.

In order to describe more precisely the meaning of an optical nonlinearity, let us see how the polarization P of a material system depends upon the strength of the electric field E. We assume that the interaction time between the electrical oscillations and the bound electrons in the atoms is extremely short, so that the medium response can be regarded as

instantaneous. Then, in conventional optics (i.e., linear optics), the induced polarization is proportional to the amplitude of the applied electric field:

$$P = \varepsilon_0 \chi E \,, \tag{1.1}$$

where ε_0 is the permittivity of free space and χ is the electric susceptibility of the medium. In nonlinear optics, the relation between P and E is no more linear. In this case, the optical response can be described as a generalization of Eq.(1.1) (for non resonant process) by expressing the polarization P as a power series in the field strength E as:.

$$P = \varepsilon_0 \chi E + \varepsilon_0 \chi^{(2)} E^2 + \varepsilon_0 \chi^{(3)} E^3 + \ldots, \tag{1.2}$$

where the quantities $\chi^{(2)}$ and $\chi^{(3)}$ are known as the second- and third-order nonlinear optical susceptibilities, respectively. Typical values can range from 1 to 100 pm/V for $\chi^{(2)}$ and from 10^{-24} and 10^{-19} m^2/V^2 for $\chi^{(3)}$. Under this more general view, the linear polarization (1.1) turns out to be the linearization of (1.2) in the neighborhood of E=0, as illustrated in Fig.1.1. In writing Eqs.(1.1) and (1.2) we have taken, for simplicity, the fields P and E to be scalar quantities.

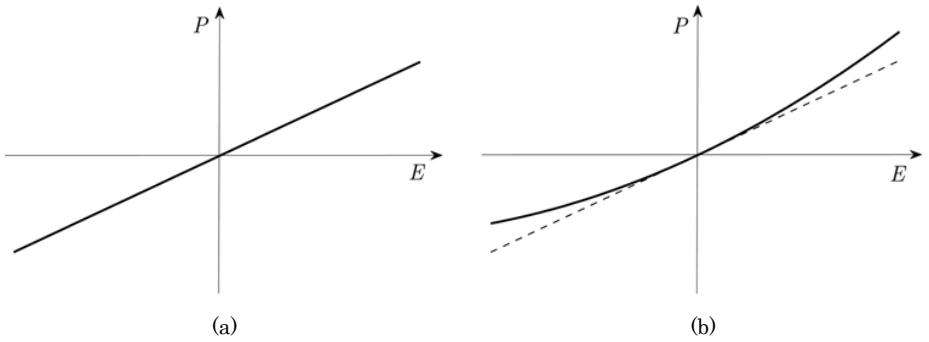

Figure 1.1. The polarization P as a function of the strength of the electric field. In linear optics (a) P is directly proportional to the electric field E. In (b) the linear polarization results to be an approximation of the nonlinear polarization.

Second-order nonlinear optical interactions

Consider the second order term of the nonlinear polarization given by the Eq.(1.2):

$$P^{(2)}(t) = \varepsilon_0 \chi^{(2)} E(t)^2 \,. \tag{1.3}$$

Second-order nonlinear optical interactions can occur only in non centro-symmetric crystals, that is, in crystals that do not display inversion

symmetry ($P(-E)= -P(E)$). Since liquids, gases, amorphous solids (such as glass), and even many crystals do display inversion symmetry, $\chi^{(2)}$ vanishes identically for such media, and consequently they cannot produce second-order nonlinear optical interactions. SH can also occurs at the surfaces of the medium, since here there is a breaking in the translational symmetry. On the contrary, third-order nonlinear optical interactions can occur both for centro-symmetric and non centro-symmetric media.

Let us consider the nonlinear interaction of two optical fields, at frequencies ω_1 and ω_2, incident upon a nonlinear medium characterized by a non-null nonlinear susceptibility $\chi^{(2)}$. The total incident field can be represented in the form:

$$E(t) = E_1 e^{-i\omega_1 t} + E_2 e^{-i\omega_2 t} + c.c.. \tag{1.4}$$

By substituting the Eq.(1.4) into the Eq.(1.3) we find:

$$\begin{aligned} P^{(2)}(t) = \chi^{(2)}[&E_1^2 e^{-i2\omega_1 t} + E_2^2 e^{-i2\omega_2 t} + 2E_1 E_2 e^{-i2(\omega_1+\omega_2)t} + \\ &+ 2E_1 E_2^* e^{-i2(\omega_1-\omega_2)t} + c.c.] + 2\chi^{(2)}\left[E_1 E_1^* + E_2 E_2^*\right]. \end{aligned} \tag{1.5}$$

We see from Eq.(1.5) that different frequency components are present in nonlinear polarization, each of which describes a different physical process such as second harmonic generation (SHG, 2ω), sum-frequency generation (SFG, $\omega_1+\omega_2$), difference-frequency generation (DFG, $\omega_1-\omega_2$) and optical rectification (OR). The complex amplitudes of the various frequency components are given by:

$$P(2\omega_1) = \chi^{(2)} E_1^2 \text{ , } P(2\omega_2) = \chi^{(2)} E_2^2 \text{ (SHG)}$$

$$P(\omega_1 + \omega_2) = 2\chi^{(2)} E_1 E_2 \text{ (SFG)}$$

$$P(\omega_1 - \omega_2) = 2\chi^{(2)} E_1 E_2^* \text{ (DFG)}$$

$$P(0) = 2\chi^{(2)}\left(E_1 E_1^* + E_2 E_2^*\right) \text{ (OR)}$$

However, not all these components will be present with a considerable intensity in the radiation generated by nonlinear interaction. The nonlinear polarization can efficiently produce an output signal only if a certain condition is satisfied: the phase-matching (PM) condition (which is discussed in a following section). Usually, no more than one frequency component can satisfy this condition at the same time. Beside these, the study of second-order processes has also been concerned with other non linear effects; one

among all, the optical solitons, or localized electromagnetic pulses, that can propagate long distances in nonlinear media without undergoing shape changes [Bec03].

The nonlinear polarization tensor

In the previous section we have taken the fields P and E to be scalar quantities. More generally, one needs to deal with the vector nature of the fields. In such case the quantities $\chi^{(n)}$ become tensors of order n+1 and the Eq.(1.2) becomes:

$$P_i = \sum_j \varepsilon_0 \chi_{ij} E_i + \sum_{jk} \varepsilon_0 \chi^{(2)}_{ijk} E_j E_k + \sum_{jkl} \varepsilon_0 \chi^{(3)}_{ijkl} E_j E_k E_l + \ldots , \tag{1.6}$$

where the indices i, j, k, l vary on the components x, y, z. In Eq.(1.6) we have assumed that the polarization depends only on the instantaneous value of the electric field strength. The assumption that the medium responds instantaneously implies (through the Kramers-Krönig relations) that the medium must be lossless and dispersionless. In [Boy08] the reader can find how to generalize these equations for the case of a medium with dispersion and loss. If the dispersion of the nonlinear susceptibilities can be neglected, all n+1 indices in the tensor $\chi^{(n)}$ are interchangeable. This result is known as the Kleinman's symmetry condition [Kle62]. Under this condition, it is practical to introduce a the *nonlinear tensor*, largely used in nonlinear optics:

$$d_{ijk} = \frac{1}{2}\chi^{(2)}_{ijk} .$$

We now assume that d_{ijk} is symmetric in last two indices (intrinsic permutation symmetry [Boy08]) and introduce the contracted *3x6* matrix d_{il} operating on the sum $E_{1j}E_{2k}$ column tensor, namely:

$$\begin{pmatrix} P_x \\ P_y \\ P_z \end{pmatrix} = 2 \begin{pmatrix} d_{11} & d_{12} & d_{13} & d_{14} & d_{15} & d_{16} \\ d_{21} & d_{22} & d_{23} & d_{24} & d_{25} & d_{26} \\ d_{31} & d_{32} & d_{33} & d_{34} & d_{35} & d_{36} \end{pmatrix} \begin{pmatrix} 2E_{1x}E_{2x} \\ 2E_{1y}E_{2y} \\ 2E_{1z}E_{2z} \\ 2(E_{1y}E_{2z} + E_{1z}E_{2y}) \\ 2(E_{1x}E_{2z} + E_{1z}E_{2x}) \\ 2(E_{1x}E_{2y} + E_{1y}E_{2x}) \end{pmatrix}, \tag{1.7}$$

where we have replaced the subscripts j and k by a single symbol according to the prescription:

$$xx=1,\quad yy=2,\quad zz=3,\quad yz=zy=4,\quad xz=zx=5,\quad xy=yx=6.$$

When Kleinman symmetry is valid, not all of the 18 elements of d_{il} in Eq.(1.7) are independent. For instance, by permuting first and second subscript indices we can have for the complete tensor d_{ijk} that $d_{xyy}=d_{yxy}$, which means that $d_{12}=d_{26}$ in the contracted tensor d_{il}. By applying this argument systematically, one finds that d_{il} has only 10 independent elements. Moreover, any crystalline symmetries of the nonlinear material can reduce this number further. In ZnO, for example, the d_{il} tensor is given by [Ger09]:

$$d_{il}=\begin{pmatrix} 0 & 0 & 0 & 0 & d_{15} & 0 \\ 0 & 0 & 0 & d_{15} & 0 & 0 \\ d_{31} & d_{31} & d_{33} & 0 & 0 & 0 \end{pmatrix}.$$

Practically, by choosing the convenient field polarization one has to consider only one or few components of the whole nonlinear susceptibility tensor. If for example we simply work with the field E_z, only the component d_{33} needs to be considered. However, in other cases, once the nonlinear interaction is known, it can be represented in terms of single effective nonlinear coefficient d_{eff} [Boy08] inferable by the tensor formulation in (1.7) with simple algebraic manipulation.

The electromagnetic formulation of nonlinear interaction

In a more general way we can write the polarization vector $\mathbf{P}$ as a sum of a linear term and a nonlinear one:

$$\mathbf{P}=\mathbf{P}_{\mathrm{L}}+\mathbf{P}_{\mathrm{NL}}=\varepsilon_0\chi\mathbf{E}+\mathbf{P}_{\mathrm{NL}}. \tag{1.8}$$

Writing the Maxwell's equations including explicitly the polarization term $\mathbf{P}$, yields:

$$\begin{aligned} \nabla\times\mathbf{H}&=\frac{\partial\mathbf{D}}{\partial t}=\frac{\partial}{\partial t}\left(\varepsilon_0\mathbf{E}+\mathbf{P}\right), \\ \nabla\times\mathbf{E}&=-\mu_0\frac{\partial\mathbf{H}}{\partial t}, \end{aligned} \tag{1.9}$$

where μ_0 is the magnetic permeability of vacuum. This can be taken equal to unity everywhere because the magnetic response of natural materials fades out in the optical frequencies [Yar67]. For the sake of simplicity we have supposed that the conductivity of the medium $\sigma = 0$. Taking into account the expression in Eq.(1.8) we can rewrite the first of the Eqs.(1.9) as:

$$\nabla \times \mathbf{H} = \varepsilon \frac{\partial \mathbf{E}}{\partial t} + \frac{\partial \mathbf{P}_{\mathrm{NL}}}{\partial t}, \tag{1.10}$$

where $\varepsilon = \varepsilon_0(1+\chi) = \varepsilon_0 \varepsilon_r = \varepsilon_0 n^2$ (being n the index of refraction of the medium). Taking the curl of the second of the Eqs.(1.9) and substituting the term $\nabla \times \mathbf{H}$ with the expression in Eq.(1.10), we obtain:

$$\nabla^2 \mathbf{E} - \mu_0 \varepsilon \frac{\partial^2 \mathbf{E}}{\partial t^2} = \mu_0 \frac{\partial^2 \mathbf{P}_{\mathrm{NL}}}{\partial t^2} \tag{1.11}$$

where we have used the vectorial relation $\nabla \times \nabla \times \mathbf{E} = \nabla \nabla \cdot \mathbf{E} - \nabla^2 \mathbf{E}$ with $\nabla \cdot \mathbf{E} = 0$ The Eq.(1.11) is named *nonlinear wave equation*. In this form, it is clear that the nonlinear polarization plays a fundamental role in the description of nonlinear optical phenomena. It acts, in fact, as a source radiating in a linear medium characterized by the permittivity ε .

A multitude of second-order effects can be studied by considering the interaction between three different waves. Consider an electromagnetic field $E(\mathbf{r},t)$ composed by the superposition of three waves oscillating at ω_1, ω_2 and ω_3 respectively:

$$E(\mathbf{r},t) = E_1(\mathbf{r})e^{-i\omega_1 t} + E_2(\mathbf{r})e^{-i\omega_2 t} + E_3(\mathbf{r})e^{-i\omega_3 t} + c.c. = \sum_{n=1,2,3} E_n(\mathbf{r})e^{-i\omega_n t}, \tag{1.12}$$

where $\omega_{-n} = -\omega_n$ and $E_{-n} = E_n^*$. The corresponding i-th component of the second-order polarization obtained by substituting the Eq.(1.12) into Eq.(1.3) is:

$$P_{\mathrm{NL}}(\mathbf{r},t) = \chi^{(2)} \sum_{n,m} E_n(\mathbf{r}) E_m(\mathbf{r}) e^{-i(\omega_n + \omega_m)t}, \tag{1.13}$$

which corresponds, into the wave equation (1.11), to a radiation source composed by harmonic components of frequencies that are sums and differences of original frequencies ω_1, ω_2 and ω_3. Substituting the Eqs.(1.13) and (1.12) into the Eq.(1.11), we obtain the single differential equation:

$$\sum_n \nabla^2 E_n(\mathbf{r}) e^{-i\omega_n t} + k_n^2 E_n(\mathbf{r}) e^{-i\omega_n t} = -\mu\chi^{(2)} \sum_{n,m} (\omega_n + \omega_m)^2 E_n(\mathbf{r}) E_m(\mathbf{r}) e^{-i(\omega_n+\omega_m)t} ,$$

where $k_n^2 = \mu\varepsilon\omega_n^2$. If the frequencies ω_1, ω_2 and ω_3 are commensurate, for example one frequency is the sum of the other two, i.e., $\omega_3 = \omega_1 + \omega_2$, we can separate the last equation into three differential equations by equating terms oscillating at the same frequency. The result is a set of three coupled Helmholtz equations with source:

$$\begin{aligned} \left(\nabla^2 + k_1^2\right) E_1 &= -2\mu\omega_1^2 \chi^{(2)} E_3 E_2^* , \\ \left(\nabla^2 + k_2^2\right) E_2 &= -2\mu\omega_2^2 \chi^{(2)} E_3 E_1^* , \\ \left(\nabla^2 + k_3^2\right) E_3 &= -2\mu\omega_3^2 \chi^{(2)} E_1 E_2 . \end{aligned} \tag{1.14}$$

In the absence of nonlinearity, $\chi^{(2)} = 0$, the source terms vanish so that each of the three waves satisfies the Helmholtz equation independently, as expected in linear optics. Eqs.(1.14) are valid when the frequencies ω_1, ω_2 and ω_3 are distinct. However, they can be used in the limiting case for which $\omega_1 = \omega_2$ and $\omega_3 = 2\omega_1$, paying attention in choosing the correct nonlinear polarization terms. In such a case, we have only two independent coupled equations:

$$\begin{aligned} \left(\nabla^2 + k_1^2\right) E_1 &= -2\mu_0\omega_1^2 \chi^{(2)} E_3 E_1^* , \\ \left(\nabla^2 + k_3^2\right) E_3 &= -\mu_0\omega_3^2 \chi^{(2)} E_1^2 \end{aligned} \tag{1.15}$$

These equations constitute the starting point for the analytical study of the SHG process that will be discussed in the next section.

Optical second-harmonic generation

The first experiment showing nonlinear effects at optical frequencies goes back to the 1961 and it was performed by Franken, Hill, Peters and Weinreich [Fra61]. By focusing a ruby laser ($\lambda = 694nm$) on a crystalline quartz plate, they observed radiation at twice the input frequency (i.e., at $\lambda = 347nm$). In this section we present a mathematical description of the SHG process in a lossless bulk medium [Arm62].

For the sake of simplicity, we reduce the problem to one dimension, assuming that it is invariant along the x and y directions, i.e. $\partial/\partial x = \partial/\partial y = 0$ (see Fig.1.2). We consider also that the fields can be written

as $E_1 = E_1(z)e^{ik_1 z}$ and $E_2 = E_2(z)e^{ik_2 z}$. With these assumptions the first of the Eqs.(1.15) becomes:

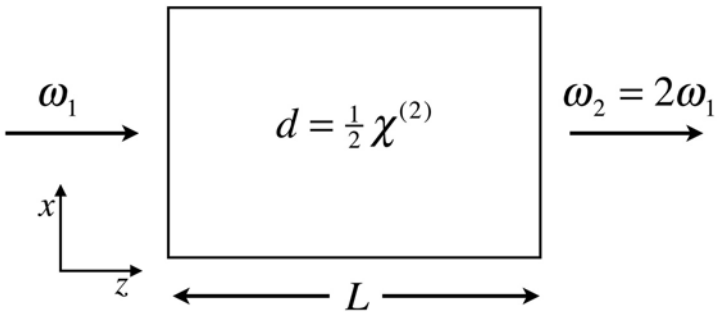

Figure 1.2. Second-harmonic generation schema.

$$\frac{d^2E_1}{dz^2}e^{ik_1 z} - 2ik_1\frac{dE_1}{dz}e^{ik_1 z} = -4\mu_0\omega_1^2 dE_2 E_1^* e^{-(k_2-k_1)z}. \tag{1.16}$$

Now, assuming the Slowly Varying Envelope Approximation (SVEA,) so that:

$$\frac{dE_1}{dz}k_1 \gg \frac{d^2E_1}{dz^2},$$

we get from Eq.(1.16):

$$\frac{dE_1}{dz} = -2i\omega_1\sqrt{\frac{\mu_0}{\varepsilon_1}}dE_2 E_1^* e^{-i\Delta kz}, \tag{1.17}$$

where $\Delta k = 2k_1 - k_2$ is the *phase mismatch* factor. Similarly, from the second of the Eqs.(1.15) we obtain:

$$\frac{dE_2}{dz} = -i\omega_2\sqrt{\frac{\mu_0}{\varepsilon_2}}dE_1^2 e^{i\Delta kz}. \tag{1.18}$$

In most of the experimental conditions, the power lost by the input beam due to the conversion to the SH frequency is negligible, i.e., $dE_1/dz \simeq 0$. This assumption takes the name of *undepleted pump approximation*. In these conditions, the SHG process can be analyzed by taking into account only the Eq.(1.18). Its solution, in absence of an input SH beam, i.e. $E_2(0) = 0$, and for a propagation length L inside the nonlinear crystal is:

$$E_2(L) = -i\omega_2\sqrt{\frac{\mu_0}{\varepsilon_2}}dE_1^2\frac{e^{i\Delta kL}-1}{i\Delta k},$$

which gives for the intensity I_2 the following expression:

$$I_2(L) = \frac{1}{2}\sqrt{\frac{\varepsilon_2}{\mu_0}}\left|E_2(L)\right|^2 = \frac{1}{2}\sqrt{\frac{\mu_0}{\varepsilon_2}}\omega_2^2 d^2 \left|E_1^2\right|^2 L^2 \frac{\sin^2\left(\Delta kL/2\right)}{\left(\Delta kL/2\right)^2}.$$

The conversion efficiency η is thus:

$$\eta(L) \equiv \frac{I_2(L)}{I_1} = 8\left(\frac{\mu_0}{\varepsilon_0}\right)^{\frac{3}{2}} \frac{\omega_1^2 d^2 I_1 L^2}{n^3} \frac{\sin^2\left(\Delta kL/2\right)}{\left(\Delta kL/2\right)^2}, \tag{1.19}$$

where we took $\varepsilon_1 \simeq \varepsilon_2 \simeq \varepsilon_0 n^2$.

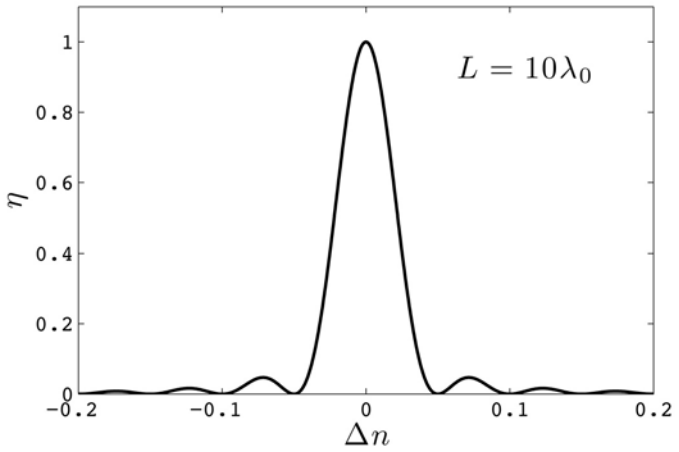

Figure 1.3. Normalized conversion efficiency as a function of the refractive index mismatch after a propagation length $L = 10\,\lambda_0$.

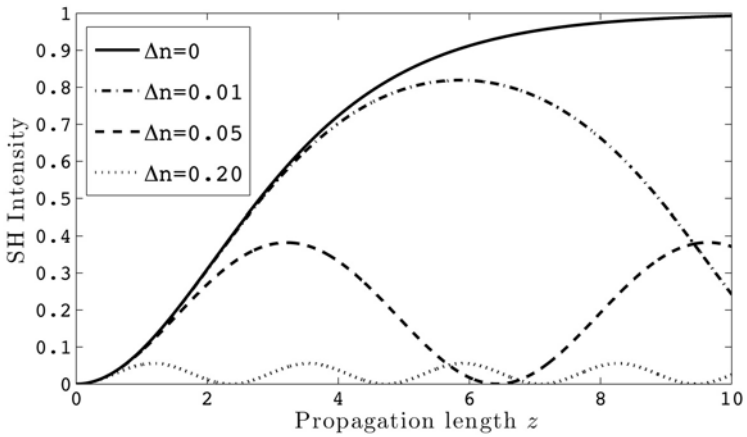

Figure 1.4. Normalized second-harmoic intensity versus the propagation distance z for different values of Δk

If

$$\Delta k = 0 \tag{1.20}$$

(or equivalently $\Delta n = 0$ in 1D approach), the *sinc* function in (1.19) assume its maximum and constant value. Then the conversion efficiency is only and directly proportional to d^2, to L^2 and to the total the intensity of the pumping beam. On the other side, if $\Delta k \neq 0$, the Eq.(1.19) predicts a dramatic decrease in the conversion efficiency (see Fig.1.3). Moreover, the *sinc* term is no longer constant, giving rise to an oscillating behavior with the propagation distance (see Fig.1.4). In the figure it is also possible to see how the larger is the phase mismatch the lower is the SH conversion efficiency.

In the previous analysis it was assumed that the input intensity at ω was not affected by the SH conversion process. This assumption limits the validity of the results to situations where the amount of the converted energy is small in comparison to the total fundamental power. If the undepleted pump approximation does not hold we must solve simultaneously the coupled Eqs.(1.17) and (1.18), that we rewrite here in a more suitable form:

$$\begin{aligned} \frac{dA_1}{dz} &= \kappa A_2 A_1^* e^{-i\Delta kz}, \\ \frac{dA_2}{dz} &= \kappa A_1^2 e^{i\Delta kz}, \end{aligned} \tag{1.21}$$

where $A_i = \sqrt{n_i} E_i, i = 1,2$ are defined as $|A_i|^2$ is proportional to the intensity of the corresponding wave, and the coupling constant κ is:

$$\kappa = -2i\omega_1 \sqrt{\frac{\mu_0}{n_1^2 n_2}} d ,$$

It follows from the Eqs.(1.21) that:

$$\frac{d}{dz}\left(|A_1|^2 + |A_2|^2\right) = \frac{d}{dz}\left(A_1 A_1^*\right) + \frac{d}{dz}\left(A_2 A_2^*\right) = 0 , \tag{1.22}$$

which is a direct consequence of the energy conservation. The Eqs.(1.21) can be easily solved numerically, using the Eq.(1.22) as a test of the goodness of the results.

The system of equations (1.21), or more generally the system (1.9), has a general solution consisting of the solution of the homogeneous system plus one particular solution of the inhomogeneous system driven by the

nonlinear polarization term [Blo62]. It can be formally expressed (considering only the SH field) as

$$\mathbf{A}_2 = \left(\mathbf{A}_{2\mathrm{hom}} e^{i\mathbf{k}_{2\mathrm{hom}} \cdot \mathbf{r}} + \mathbf{A}_{2\mathrm{inhom}} e^{i\mathbf{k}_{2\mathrm{inhom}} \cdot \mathbf{r}} \right) e^{-i\omega_2 t} . \tag{1.23}$$

In a general dispersive medium we find $\mathbf{k}_{2\mathrm{hom}} \neq \mathbf{k}_{2\mathrm{inhom}}$. For plane waves the amplitude $\mathbf{A}_{2\mathrm{hom}}$ of the homogeneous solution can be found imposing the boundary conditions. For other general situations, the shape of this solution has been widely studied and investigated. All the theory exposed in this and following sections of this Chapter concern only with this homogeneous component. In particular, the researchers are usually interested in searching that peculiar working condition that allows an enhancement of the conversion efficiency. This working condition is explained in the next section. In the general case, however, the conversion efficiency, and thus the generated SH intensity, is very low.

On the other side, the shape of the inhomogeneous solution has been almost ignored during last decades. It is very difficult to find an analytical formulation that describes its behavior. Moreover, since it represents only a *particular* solution, it has been thought that it could be always neglected respect to the homogeneous solution.

The general expression (1.23) of the SH solution is a crucial point for this thesis work. We will in fact focus our attention on those general regimes of low conversion efficiency and study the behavior of both the homogeneous solution (in the Part II) and the inhomogeneous solution (in the Part III).

Phase-matching condition

According to the Eq.(1.19), a prerequisite for efficient SHG is that the relation (1.20) is satisfied, which means that $k_2 = 2k_1$. This relation requires that both the SH and fundamental beam have the same *phase velocity* and can be written more generally for a 2D space as

$$\mathbf{k}_2 = 2\mathbf{k}_1 . \tag{1.24}$$

The above vectorial relation takes the name of *perfect phase matching (PM) condition*. The PM condition essentially requires conservation of linear momentum to sustain a mutual interaction over extended regions of space

between the fundamental and the generated harmonic field. The perfect PM condition (1.24) is a particular case of the general *PM condition*,

$$\mathbf{k}_2 - 2\mathbf{k}_1 - \Delta\mathbf{k} = 0 \tag{1.25}$$

when the phase mismatch factor is null, $\Delta\mathbf{k} = 0$. In Fig.1.5(a) is sketched the *collinear* case, namely where the two fundamental beams lie in the same direction and are overlapped. This is not the only possible situation, since *noncollinear* situations are also possible, as for example illustrated in Fig.1.5(b). If two fundamental beams are launched at different directions, there is not, at first sight, a privileged direction for the generation of the SH. Since the magnitude of the SH k-vector is fixed by the index of refraction and the wavelength, $|\mathbf{k}_2|=n_2\omega_2$, it can only end on the green dashed arc of circumference in Fig.1.5(b). However, as it is clear from the figure, the phase mismatch vector $\Delta\mathbf{k}$ will assume the lower extension in the direction of the geometrical sum $\mathbf{k}_1 + \mathbf{k}_1'$. This will be always the direction of the generated SH in a homogeneous material.

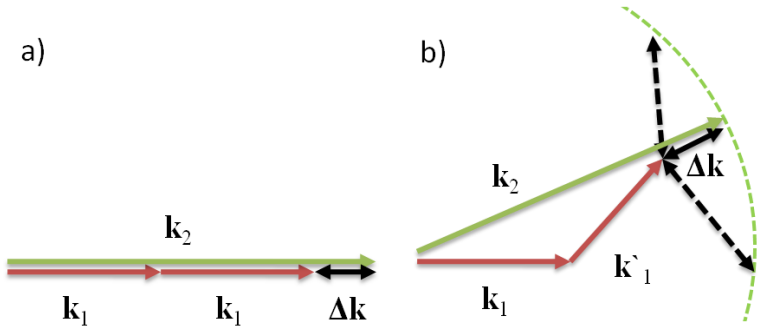

Figure 1.5. (a) Collinear SHG. (b) Noncollinear SHG.

When the perfect PM condition is satisfied, accordingly to Eq.(1.19), the conversion efficiency grows with the square of the propagation length *L*. The absence of a saturation level is due to the fact that we have assumed an undepleted pumping wave. As we saw in the 1D case, if $\Delta\mathbf{k} \neq 0$, the SH conversion efficiency quickly decrease. In that case the SH wave generated at a given point z_1, having propagated to some other point z_2, is not in phase with the SH wave generated at z_2. The result is the interference described by the factor $\sin^2(\Delta kL/2)$ in Eq.(1.19).

One half of the length separating two adjacent peaks of this interference pattern is called the *coherence length*, and it is defined as

$$l_c \equiv \frac{\pi}{\Delta k} = \frac{\pi}{k_2 - 2k_1} = \frac{\lambda}{4|n_2 - n_1|},$$

where λ is the free space wavelength of the fundamental beam. The coherence length l_c represents the maximum (homogeneous) crystal length that is useful in producing the SH power. Typically in nonlinear materials the difference in indexes of refraction at the fundamental and SH, Δn, is of the order of 10^{-1} to 10^{-2}. The coherence length is then only few wavelengths long. The intensity of the generated SH increases during the first coherence length, where the energy flows from the fundamental frequency to the SH. If the length of the nonlinear material is further increased, the energy flow changes its sign thus returning energy from the SH to the fundamental field (FF). After $2l_c$ the energy of the SH is zero. Unfortunately in nature *does not exist* materials with $\Delta n = 0$. The dispersive dependence of the index of refraction with the wavelength prevents the PM relation (1.24) to be naturally fulfilled. However, as we will see in the next section, a numbers of techniques can be implemented to externally force, or at least to approach, the perfect PM condition.

Phase-matching techniques

In the previous section we have seen that the PM condition is a necessary condition for an efficient SHG. PM does not generally occur in nature because of the refractive index normal dispersion. However, various methods have been proposed that attempt to bring the interacting waves closer to ideal perfect PM conditions. Here we will provide a briefly review.

One technique consists in using the natural birefringence of uniaxial crystals. When an optical wave propagates in isotropic crystals, the electrons displacement takes place in the direction of the applied field. In a birefringent crystal, however, the electrons will move in a direction imposed by the crystalline structure. As a result the resulting polarization vector is not parallel to the electric field and the solutions of the wave equation propagate with fixed polarization inside the crystal. In Fig.1.6(a) it is shown

an optical wave with an arbitrary polarization entering in a birefringent crystal with a k-vector non-parallel to the crystal axis. Inside the medium the ordinary and extraordinary polarization components split and follow two different propagation angles given by the different indexes of refraction for the two polarizations. In Fig.1.6(b) it is shown the diagram of the indexes of refraction varying the propagation direction inside such kind of crystal for both the ordinary and extraordinary polarizations and for both the FF and SH wavelengths. It is clear how it can be possible to found a particular propagation direction ϑ where the ordinary polarized FF has the same index of refraction of the extraordinary polarized SH (in the case of negative uniaxial or vice versa for the positive uniaxial crystals).

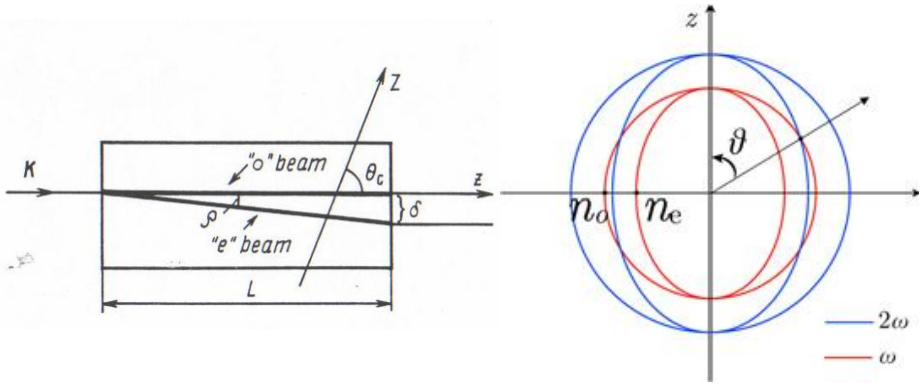

(a) (b)

Figure 1.6. (a) Scheme of the propagation of a generally polarized beam inside a birefringent crystal. (b) The indices' ellipsoid projection of a negative uniaxial ($n_e<n_0$) crystal. Propagation along the θ direction allows the PM condition $n_e(2\omega)=n_0(\omega)$.

Another way, proposed for the first time by Armstrong *et al.* in 1962 [Arm62], is the *quasi-phase-matching* (QPM) technique (although is was not experimentally obtained until 1992 [Fej92] to do technological reasons). It consists in periodically modulate the nonlinear coefficient of the material every coherence length. This is done by opportunely pooling the material with an external applied electrical field. Since the quadratic nonlinearity is given by a local displacement or asymmetry inside the crystal unit cell, the applied field forces the unit cell to rearrange in such a way to adapt its

polarization direction accordingly. In Fig.1.7 is reported a typical realization scheme for the case of $LiNbO_3$.

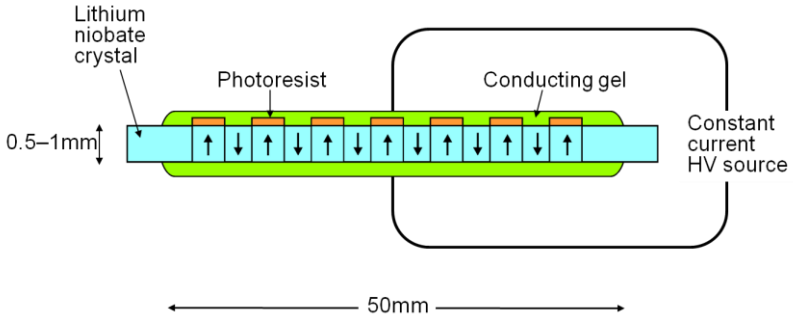

Figure 1.7. QPM technique scheme for a typical case of $LiNbO_3$ crystal. A photoresistive mask allows the change of the sign of the nonlinearity only inside selected regions.

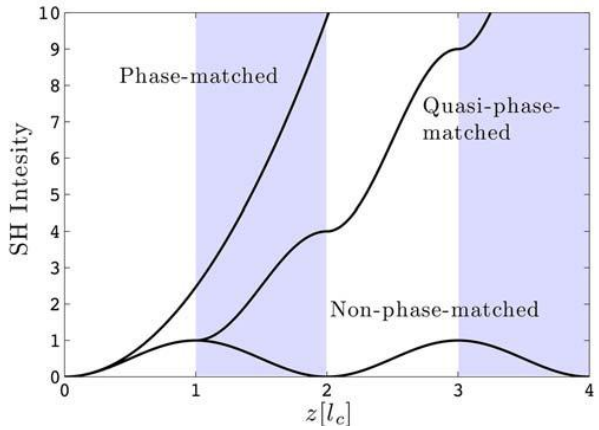

Figure 1.8. SH intensity for PM, non-PM and QPM strucures. By inverting the sign of $\chi^{(2)}$ in the highlighted region it is possible to artificially recover the PM between the fundamental and SH waves, so that the generation gets larger by increasing the length of the crystal.

The presence of the chromatic dispersion implies that after a length of l_c a π phase difference sets in between the nonlinear polarization source term and the generated SH field. If the crystal length is larger than l_c, the polarization interferes in a detrimental way with the SH field and the energy is converted back to the FF until a 2π difference of phase is reached. Using QPM, a π phase difference between FF and SH is artificially introduced at each multiple of l_c by periodically inverting the sign of $\chi^{(2)}$. In this way the phase difference always produce an energy transfer from the

FF to the SH, achieving efficiencies close to those obtained in phase-matched crystals (see Fig.1.8).

QPM can be also understood in terms of *momentum conservation*. The phase mismatch is compensated through an external momentum provided by the material. It is given by the reciprocal nonlinear lattice vector $G=\pi/l_c$, that result from the periodic modulation of the medium and it can be shown that it applies directly in the PM relation as

$$\Delta\mathbf{k}_{QPM} = \Delta\mathbf{k} - \mathbf{G} = 0 . \tag{1.26}$$

Another PM mechanism, proposed by Bloembegen and Sievers [Blo70] and experimentally demonstrated by Van der Ziel *et al.* [Zie79], uses periodical distribution of dielectric materials to induce a bending of the photon dispersion curve near the SH frequency. It was shown that the effective coherence length may be increased and even perfect PM can be achieved at the band edge of a semiconductor multilayer structure. Sakoda *et al.* [Sak96] proposed in 1996 a 2D structure that allows both the PM and the increase of the fundamental and SH density of states. Looking at the expression (1.19), it is clear that the enhancement of the FF intensity increases the conversion efficiency. Before Sakoda, several studies have been conducted to embed the nonlinear source in a Fabry-Pérot cavity, in order to enhance the harmonic conversion efficiency.

External cavity configurations were early envisaged by Armstrong *et al.* [Arm62], and experimentally demonstrated in the pioneering paper of Ashkin *et al.* [Ash66]. To enhance the efficiency of the SHG generation further, doubly resonant cavities, i.e., resonant both at the pump and at the harmonic frequencies can be used [Ou93]. As far as a practical device was concerned, a monolithic concept of a doubly resonant cavity was desirable [Ber97], because of the practical aspects of compact size. However, in all these cases, the resonant properties were obtained in detriment of the PM condition. In this context, the work of Sakoda was of extreme importance, because for the first time it was proposed a solution that allows simultaneously PM and field enhancement at both, fundamental and harmonic frequencies. In 1997 Scalora *et al.* have also shown that an exact PM and, high localization and overlapping of fields can be achieved by exploiting the anomalous dispersion of finite one-dimensional periodic

structures, at the edges of their transmission band gaps [Sca97]. This work represented the first significant step into the direction of the integration of nonlinear optical devices.

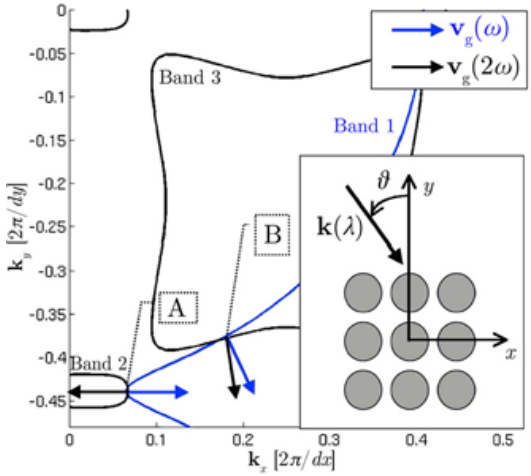

Figure 1.9. Iso-frequency curves for the fundamental wavelength (blue curve) inside the PC sketched in the inset. The black curves are the SH iso-frequency curves for $k_{2\omega}/2$. At points A and B the PM condition is fulfilled for specific angles of incidence.

Photonic crystals (PC) are structures where the linear index of refraction can be modulated along 1, 2 or 3 directions. As we saw in the previous section, the condition for an efficient SH conversion relies on matching the wave vectors at fundamental and SH frequencies. In the PC structures the consequent anisotropy of the dispersion curves provides a way to control the propagation direction of the generated harmonic. Moreover, in PCs the group velocity $\mathbf{v}_g$ and the wave vector $\mathbf{k}$ are not necessarily collinear. As a result, in condition of PM, the SH generated field can propagate in a completely independent direction, depending on the structure of iso-frequency curves. For example, in [Cen06b] the author numerically demonstrates the angular and frequency SH superprism. A PC consisting in a rectangular lattice of air holes embedded in GaN was used. The iso-frequency curves of such a PC are shown in Fig.1.9. Small angular variations or a small wavelength detuning of the FF induces large shifts of the SH emission.

SHG in supercollimating regime has also been recently studied [Nis08]. By exploiting flat regions of iso-frequency curves at both, fundamental and SH frequency, extremely narrow collimated beams (of the width of few wavelengths) can be used to enhance the SHG process in quadratic-nonlinear photonic crystals. In conclusion, although a large number of works concerning SH have been published since its discovery, a meager quantity dealt with the emission control of the generated harmonics. This is probably due to the fact that the principal difficulty to overcome was historically the low conversion efficiency.

2D Nonlinear photonic crystals

While the SHG in traditional PC is achieved by the *zeroing* of the phase mismatch $\Delta\mathbf{k}$, another strategy could be to *compensate* it by adding external momentum and generalizing the idea of the QPM. The first detailed work on such idea was written only recently by Berger [Ber98] and we will faithfully refer to it throughout this overview. The resulting structure is the first step versus the 2D disordered nonlinear structures studied in the Part I.

Let us consider a two dimensional structure that present a space-independent linear dielectric constant, but has a periodic second-order nonlinear coefficient. These kinds of devices are better known in literature as nonlinear photonic crystals (NLPC). The 1D case of a NLPC is the well-known QPM structure. In fig.1.10 it is shown schematically an example of a 2D nonlinear structure under study. It reminds a 2D linear PC; in this case the linear susceptibility is constant but there is a spatial modulation of the $\chi^{(2)}$ nonlinear susceptibility tensor.

Various demonstrations of QPM have been already performed (for a review, see [Fej92]). For instance, GaAs waveguides with periodic (100) and (-100) oriented zones were recently demonstrated [Yoo96], and periodically poled lithium niobate (PPLN) [Mye95] or periodic poled KTP [Kar97] have recently become some of the most attractive nonlinear materials for optical parametric oscillators.

In 1D QPM structures, for GaAs waveguides as for PPLN, the 1D periodicity of the nonlinear susceptibility is defined by the design of a metallic grating. In the case of GaAs waveguides, the grating is used as a mask for a reactive ion etching step [Yoo96], and in the case of PPLN, the grating is an electrode for ferroelectric domain reversal. Though these techniques are very different, they both use a metallic grating, defined by electron-beam lithography, which defines the pattern of the QPM structure. Both techniques can be generalized to the 2D structure presented in Fig.1.10.

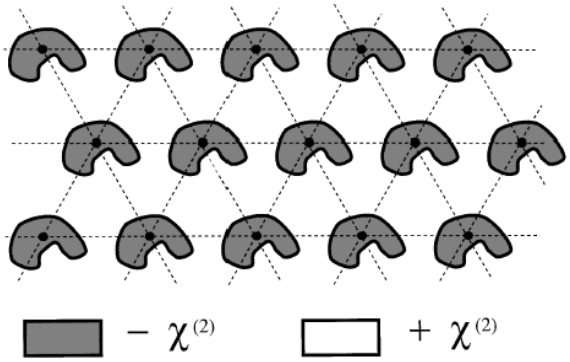

Figure 1.10. Schematic picture of a 2D nonlinear crystal. The material presents a translation invariance perpendicular to the figure, and is invariant by translation in a 2D lattice (here a triangular lattice). The linear susceptibility is constant in the whole material but the sign of the second-order susceptibility $\chi^{(2)}$ presents a given pattern in the unit cell [Ber98].

Let us assume that a plane wave at the frequency ω propagates in the transverse plane of a 2D crystal that is perpendicular to the translation axis of the cylinders, of arbitrary section. Let us recall that the linear refractive index is constant in the whole structure. This ensures that multiple reflections, leading to PBG effects, are not present. In this 2D structure, the problem can be considered as scalar [Vil92], which simplifies the notations. For instance, in the case of a 2D PPLN crystal, fundamental and harmonic waves are TM polarized, i.e., with the electric field in the translational direction. Although they are constant in space, the linear dielectric constants are assumed to be different at ω and 2ω, this dispersion being the source of phase mismatch. An efficient SHG process in the $\chi^{(2)}$ crystal is

obtained if a quasi-plane-wave at the harmonic frequency is observed to increase at a large scale, compared to the coherence length l_c and to the $\chi^{(2)}$ period order. We already saw that the Eq.(1.18) well describe the evolution of the SH field under well-established approximations as SVEA and undepleted pump and for plane wave and quasi-plane waves.

The nonlinear susceptibility can be written as a Fourier series,

$$\chi^{(2)}(\mathbf{r}) = \sum_{\mathbf{G}\in \mathrm{RL}} \kappa_{\mathbf{G}} \cdot \exp(-i\mathbf{G}\cdot\mathbf{r}) \tag{1.27}$$

where the sum is extended over the whole 2D reciprocal lattice (RL). Note the explicit dependence on the spatial coordinate **r**. Inserting this expression in Eq.(1.18), the increase of the SH field appears to be related to a sum of

$$\exp\left[i\left(\mathbf{k}^{2\omega} - 2\mathbf{k}^{\omega} - \mathbf{G}\right)\mathbf{r}\right].$$

The QPM condition appears then as the expression of the momentum conservation. It corresponds to the generalized PM condition shown in Eq.(1.26)

$$\mathbf{k}^{2\omega} - 2\mathbf{k}^{\omega} - \mathbf{G} = 0 \tag{1.28}$$

For 1D QPM, the phase mismatch can be compensated in a structure of period d if the spatial frequency of the structure, $2\pi/d$, is equal to a multiple of the l_c [Fej92]. In contrast to this, QPM in a 2D $\chi^{(2)}$ photonic crystal involves a momentum taken in the 2D RL. The possibilities of QPM are not only n-fold degenerate (thanks to the symmetry of the n-order lattice), but new QPM orders appear in the 2D crystal which are not multiples of the fundamental QPM process, opposite to the 1D situation. Two examples of 2D QPM processes are shown in Fig.1.11 (left): the fundamental process, which involves the shortest possible **G** vector, and a 2D QPM process with a momentum transfer $\sqrt{3}$ times greater, which is impossible in a 1D structure.

The 2D QPM order can be labeled with two integer coordinates, given in the ($\mathbf{G}_1$, $\mathbf{G}_2$) basis of the RL. In Fig.1.11, for instance, 2D QPM processes of orders [1, 0] and [1, 1] are represented. However, the related conversion efficiencies depends on the Fourier coefficients of Eq.(1.27), which depends on the shape of the $\chi^{(2)}$ pattern at the unit cell level, and is generally not the same for different vectors of equal modulus in the RL.

Using some trigonometry, Fig.1.11 leads to

$$\lambda^{2\omega} = \frac{2\pi}{|\mathbf{G}|}\sqrt{\left(1-\frac{n^{\omega}}{n^{2\omega}}\right)^2 + 4\frac{n^{\omega}}{n^{2\omega}}\sin^2\theta} \qquad (1.29)$$

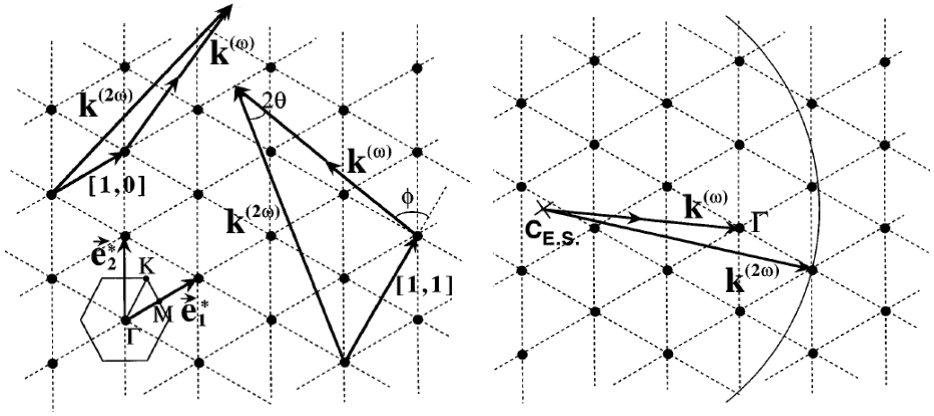

Figure 1.11. (left) Reciprocal lattice of the structure of Fig.1.10, with the 2D QPM processes of order [1, 0] and [1, 1] shown schematically. The first Brillouin zone with the usual G, M, and K points is represented on the left. (right) Nonlinear Ewald construction: The center of the Ewald sphere is located $|k_{\omega}|$ away from the origin of the RL and the radius of the sphere is $|k_{2\omega}|$. If a point of the RL is located on the Ewald sphere, PM occurs for the SHG process [Ber98].

where $\lambda^{2\omega}$ is the SH wavelength inside the material and 2θ the walk-off angle between $\mathbf{k}^{\omega}$ and $\mathbf{k}^{2\omega}$. More generally, this equation gives the direction of coherent radiation at the wavelength $\lambda^{2\omega}$ for a phased array of nonlinear dipoles having a phase relation fixed by the propagation of the pump. Eq.(1.29) appears then as a *nonlinear Bragg law*, and is a generalization for nonlinear optics of the Bragg law. It gives the direction of resonant scattering at the wavelength $\lambda^{2\omega}$ of a plane wave with vector $\mathbf{k}^{\omega}$ by a set of nonlinear dipoles. If the medium has no dispersion, $n^{\omega} = n^{2\omega}$, Eq.(1.29) is reduced to the well known Bragg law, which expresses the resonant scattering direction by a periodic set of scatterers,

$$\lambda = \frac{4\pi}{|\mathbf{G}|}\sin\theta = 2d\sin\theta$$

where d is the period between two planes of scatterers. In the case $n^{\omega} = n^{2\omega}$, the nonlinear emission follows the same behavior as a linear scattering: in both cases the direction of propagation is given by the Huyghens-Fresnel principle, given the phase relation between the scatterers.

The analogy with x-ray diffraction by crystals is useful for understanding the different possibilities offered by 2D QPM. Fig.1.11 shows a modified Ewald construction corresponding to Eq.(1.29) [Ewa69]. This figure follows the same principle as the usual Ewald construction, except for the fact that the radius of the Ewald sphere $|\mathbf{k}^{2\omega}|$ is greater than the distance $|\mathbf{k}^{\omega}|$ between its center and the origin of the RL. As in the case of x-ray diffraction, for a given pump wave vector $\mathbf{k}^{\omega}$, there is in general no reciprocal vector $|\mathbf{k}^{2\omega}|$ on the Ewald sphere. This means that the 2D QPM is a resonant process which can be obtained by varying either the angle of propagation of the pump or the wavelength. It is interesting to note that for specific angles and wavelengths several points can be located simultaneously on the Ewald sphere. In such a case of multiple resonances, SH beams can be generated simultaneously in different directions in the plane, in a similar way as the linear diffraction in several order beams by a diffraction grating.

Multiple resonances were already observed in the QPM SHG spectrum arising from the different reciprocal vectors $G_{m,n}$ of the quasi-periodic optical superlattice. The 2D RL indexing of the quasi-periodic 1D structure is the fundamental difference from the usual 1D periodic structure, and this difference is the reason for multi-wavelength frequency conversion. The 2D indexing comes from the fact that the 1D quasi-periodic lattice is nothing but the projection of a 2D periodic crystal on a 1D axis. This follows the well known geometrical construction of quasi-crystalline structures.

Third harmonic generation

Another important set of nonlinear effects are those leading to the *third harmonic* (TH) *generation.* This can be obtained directly due to the cubic nonlinearity of the material and/or due to the combination of fundamental and SH beams still via the quadratic nonlinearity, the so called *cascaded* third harmonic generation (THG). In the first case three photons of the FF annihilate to create directly a TH photon ($\omega+\omega+\omega \rightarrow 3\omega$). In the second case a two-step process occurs: first two photons of the FF

annihilate to create a SH photon (ω+ω→2ω) and then one photon from the FF and one photon from the SH combine to create a TH photon (ω+2ω→3ω).

From Eq.(1.2) it is possible, with little effort, to derive some of the consequences of the inclusion of the $\chi^{(3)}$ in the expansion of the relation between the electric and the induced polarization fields. As we saw in (1.6), the term $\chi^{(3)}$ is in general a 3+1 order tensor. This notwithstanding, for the purpose of this work and considering the values of the crystals we will use, we can adopt the isotropic assumption and take it as a scalar. We now consider a nonlinear polarization made by second and third order terms of the Eq.(1.2):

$$P_{NL}(t) = \varepsilon_0 \chi^{(2)} E(t)^2 + \varepsilon_0 \chi^{(3)} E(t)^3 \tag{1.30}$$

and a total field of the form

$$E(t) = E_1 e^{-i\omega_1 t} + E_2 e^{-i2\omega_1 t} + E_3 e^{-i3\omega_1 t} + c.c. \; . \tag{1.31}$$

By substituting the Eq.(1.31) into the Eq.(1.30) we find:

$$\begin{aligned} P_{NL}(t) = {} & e^{-i\omega_1 t}\varepsilon_0[\chi^{(2)} 2E_1^* E_2 + \chi^{(3)} |E_1|^2 E_1] + \\ & e^{-i2\omega_1 t}\varepsilon_0\left[\chi^{(2)} E_1^2 + \chi^{(3)} |E_1|^2 E_2\right] + \\ & e^{-i3\omega_1 t}\varepsilon_0\left[\chi^{(2)} 2E_1 E_2 + \chi^{(3)} E_1^3\right] + ... + c.c. \end{aligned} \tag{1.32}$$

In this expression we took only the leading terms considering that the SH and TH fields are far less intense with respect to the FF.

We see from Eq.(1.32) that new physical processes arise due to the contribution of the first two harmonics (E_1 and E_2) to the third one (E_3) and vice versa. The most famous effect is the *intensity dependent refractive index* due to the term $\chi^{(3)} |E_1|^2 E_1$ where the FF acts directly on itself producing a local variation of the index of refraction proportional to its intensity. To practically appreciate this effect taking into account typical values of $\chi^{(3)}$, propagation distances much longer than the typical crystal length used in this work are needed.

Our attention, on the other hand, is focused on the two terms

$$e^{-i3\omega_1 t}\varepsilon_0\left[\chi^{(2)} 2E_1 E_2 + \chi^{(3)} E_1^3\right]$$

representing a driving field at a the frequency $3\omega_1$. The first one is responsible of the cascaded THG, and the second one of the proper THG. In the first one, the generation of the field with three times the fundamental

wavelength is the result of the mutual interaction of the first two harmonics fields via the quadratic nonlinearity of the material. This is a purely $\chi^{(2)}$ effect. In the second one the THG is the result of only the fundamental beam via the third order nonlinearity. In principle the TH can be generated from the two *sources* at the same time and the effects can be linearly superimposed. Usually the two following situations occur: 1) the material presents inversion symmetry, $\chi^{(2)}=0$, thus there is only THG; 2) the material has a non null $\chi^{(2)}$ value. In this case the *cascaded THG is generally predominant*.

Now the PM relation can be generalized as follow

$$\begin{aligned} \mathbf{k}_2 - 2\mathbf{k}_1 - \Delta\mathbf{k}_{SH} &= 0 \\ \mathbf{k}_3 - \mathbf{k}_2 - \mathbf{k}_1 - \Delta\mathbf{k}_{TH} &= 0 \\ \mathbf{k}_3 - 3\mathbf{k}_1 - \Delta\mathbf{k}_{cascTH} &= 0 \end{aligned} \tag{1.33}$$

Note that the PM condition is different for the two THG processes since in general $\Delta\mathbf{k}_{TH} \neq \Delta\mathbf{k}_{cascTH}$. All the discussions made on the previous paragraphs are easily extended. For example, in the case of collinear interaction of all fields, we can define three coherence lengths

$$l_{c,SH} \equiv \frac{\pi}{\Delta k_{SH}}$$

$$l_{c,TH} \equiv \frac{\pi}{\Delta k_{TH}}$$

$$l_{c,cascTH} \equiv \frac{\pi}{\Delta k_{cascTH}}$$

that give us an idea on the behavior of each interaction. The smaller is the Δk, the longer is the propagation distance where the energy flow keeps the monotonic growing behavior for such interaction. The relations (1.33) are in general vectorial, thus any combination of those vectors in the space will be useful to achieve a PM situation. As we already saw, they are momentum conservation relations. From this point of view $\Delta\mathbf{k}$ represents a *missing momentum* that we can externally provide to the interaction. To add momentum we need to include an oscillating action of an appropriate frequency and, as we saw before, for example the way the QPM technique pursues is to physically alternate the sign of quadratic nonlinearity of the crystals. This is not the ideal solution, since the square wave modulation

will introduce higher orders perturbations, but so far it is the only way to practically realize it.

1.2. Ferroelectric materials

NLPCs can be artificially produced, with the same tecniques of the 1D QPM. Despite of this, in this work we are more interested in the *naturally occurrences* of the nonlinear domains inversion, for reasons that will be clear in the next Chapter. The best case of such *as-grown* nonlinear structures is represented by the ferroelectric crystals. Even if they are more often studied for their linear properties of spontaneous polarization, the root of the nonlinear properties dwells in the same ground. We will thus briefly introduce here a typical linear description of these crystals. For a deeper study the reader can refer for example to the DoITPoMS website (Dissemination of IT for the Promotion of Materials Science), of the University of Cambridge, from which this paragraph draws on information from.

The ferroelectric effect was first observed by Valasek in 1920 [Val20], in the Rochelle salt. This has molecular formula $KNaC_4H_4O_6 \cdot 4H_2O$. The effect was then not considered for some time, and it wasn't until a few decades ago that they came into great use. Nowadays, ferroelectric materials are used widely, mainly in memory applications. To be ferroelectric, a material must possess a spontaneous dipole moment that can be switched in an applied electric field, i.e. *spontaneous switchable polarisation*. This is found when two particles of charge q are separated by some distance $\mathbf{r}$. The dipole moment $\boldsymbol{\mu}$ is thus $\boldsymbol{\mu} = q\mathbf{r}$.

In a ferroelectric material, there is a net permanent dipole moment, which comes from the vector sum of dipole moments in each unit cell, $\Sigma\boldsymbol{\mu}$. This means that it cannot exist in a structure that has a centre of symmetry, as any dipole moment generated in one direction would be forced by symmetry to be zero. Therefore, ferroelectrics must be *non-centrosymmetric*. This is not the only requirement however. There must also

be a spontaneous local dipole moment which can leads to a macroscopic polarisation, but not necessarily if there are domains that cancel completely. This means that the central atom must be in a non-equilibrium position. For example, consider an atom in a tetrahedral interstice as in Fig.1.12.

In Fig.1.12(a) the structure is said to be non-polar. There is no displacement of the central atom, and no net dipole moment. In Fig.1.12(b) the central atom is displaced and the structure is polar. There is now an inherent dipole moment in the structure. This results in a *polarisation*, which may be defined as the total dipole moment per unit volume, i.e. $\mathbf{P}=\Sigma\boldsymbol{\mu}/V$. When the materials that are polarised along a unique crystallographic direction, certain atoms are displaced only along this axis, leading to a dipole moment along it. But, depending on the crystal system, there may be few or many possible displacing axes.

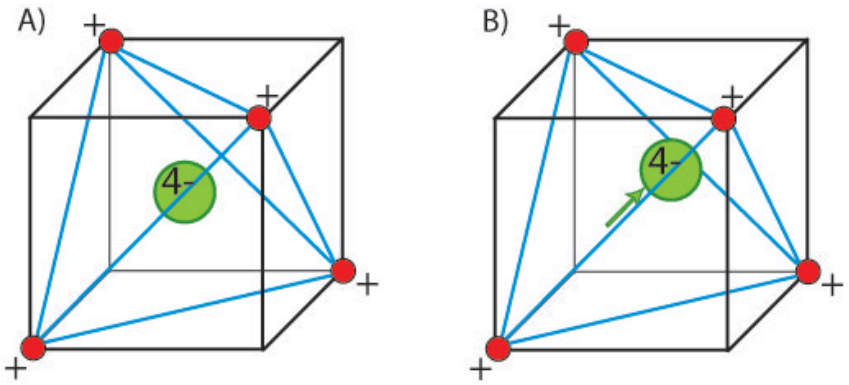

Figure.1.12. An example of tetrahedral crystal stucture. In (a) the central atom is exaclty centrally located while in (b) it is slightly displaced. As a consequence the crystal will be *polar*.

Since it is the most common and easy to see, let us examine a tetragonal system that $BaTiO_3$ forms when cooled from the high temperature cubic phase, through the Curie temperature (T_c=120°C). In this system, the dipole moment can lie in 6 possible directions corresponding to the original cubic axes. In a ferroelectric crystal, it is likely that dipole moments of the unit cells in one region lie along one of the possible six directions while the dipole moments in another region lie in a different one. Each of these regions is called a *domain*, and a cross section through a crystal can look like as sketched in Fig.1.13.

A domain is a homogenous region of a ferroelectric crystal, in which all of the dipole moments in adjacent unit cells have the same orientation. In a newly-grown single crystal, there will be many domains, with individual polarisations such that there is no overall polarisation. The polarisation of individual domains is organised such that polarization vector heads are held near the neighbouring tails (Fig.1.13). This leads to a reduction in stray field energy, because there are fewer isolated heads and tails of domains. This is analogous to the strain energy reduction found in dislocation stacking. Domain boundaries are arranged so that the dipole moments of individual domains meet at either 90° or 180°. In a polycrystal, where there are more than one crystallographic grain, the arrangement of domains depends on grain size. If the grains are fine (<<1μm), then there is usually found to be one domain per grain. In larger grains there can be more than one domain in each grain. Fig.1.13 shows a micrograph of the domains in a single grain. In this grain, the domains are twinned in such a way as to reduce the overall stray electric field energy.

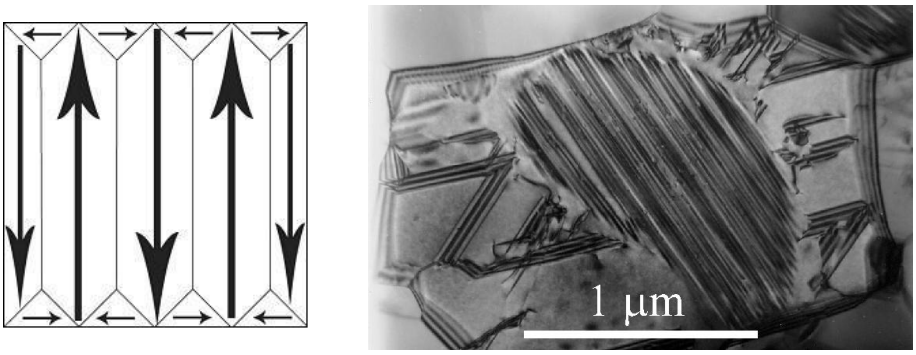

Figure 1.13. (left) Sketch of the domains formation when a ferroelectric crystal is cooled down to the Curie temperature. (right) Micrograph of the domains in a single grain This micrograph is reproduced from the DoITPoMS Micrograph Library.

In the presence of an external electric field E a polarised material lowers its energy by $-P \cdot E$, beeing P the polarisation. Any dipole moment which lies parallel to the electric field lowers its energy, while moments that lie perpendicular to the field increase its energy and moments that lie anti-parallel are even higher in energy ($P \cdot E$). This introduces a driving force to

minimise the free energy, such that all dipole moments align with the electric field.

Let us start by considering how dipole moments may align in zero applied field; since the horizontal direction is crystallographically unique, the dipole moment is stable either aligned to the left of to the right. These two moments are stable, because they sit in potential energy walls. The potential barrier between them can be represented on a free energy diagram (Fig.1.14). This material is considered to be homogenous.

If the polarisation points left then we have the situation in fig.1.14(a). The electric field consequently alters the energy profile, resulting in a "tilting" of the potential well, Fig.1.14(b). An increase in the electric field will result in a greater tilt, and lead to the dipole moments switching, Fig.1.14(c).

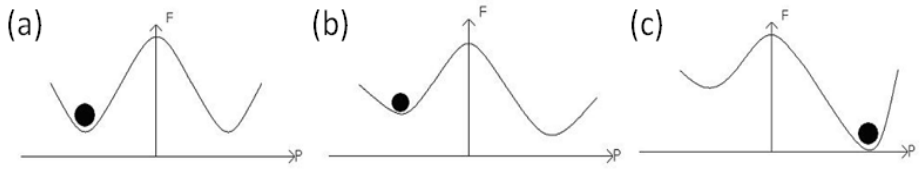

Figure 1.14. Free energy diagram. This scheme represents the potential barrier between the two stable positions (left and right versus on the horizontal direction) of the dipole moments.

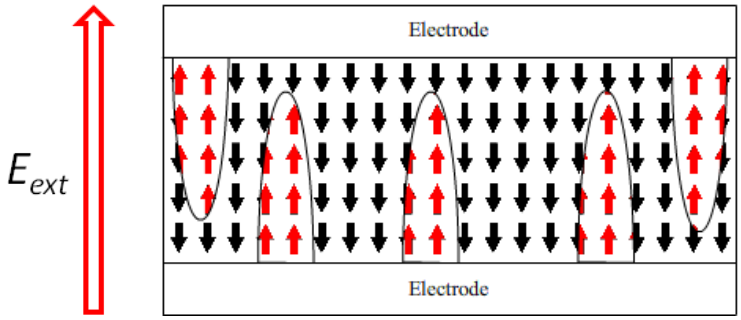

Figure 1.15. Snapshot of the inhomogenous nucleation process that happen when a reversed external electric field E_{ext} is applied on a fully polarized crystal. The arrows represent the local direction of the polarization.

We can now look at the more realistic scenario in which domains form. Consider a material which is fully polarised, so that all of the dipole

moments are aligned in the same direction. Then if we apply a reversed electric field over it, new domains with a reversed polarisation starts to nucleate *inhomogenously*. This requires a certain amount of time, in the same manner as any nucleation process. When the fluctuating nuclei reach a certain critical radius, they grow outwards, forming needle-like structures. When they reach the other side of the ferroelectric, they begin to grow outwards (Fig.1.15).

This dynamics explains the origin of the hysteresis loop. The removal of the field will leave some polarisation behind. Only when the field is reversed, also the polarisation starts to lessen and new, oppositely poled, domains form. They grow quickly however, giving a large change of polarisation for very little electric field. But to form an entirely reversed material, a large switching field is required. This is mainly due to defects in the crystal structure but it is also due to stray field energy. The polarisation of the material goes from a coupled pattern, with 180° boundaries, to a state in which many heads and tails are separated. This leads to the increase in stray field energy. Therefore, to attain this state, lots of energy has to be put in by a larger field. In Fig.1.16 it is shown how a minor hysteresis loop fits into the major loop above. There are three sections to this curve: 1)reversible domain wall motion; 2) linear growth of new domains; 3) new domains reaching the limit of their growth.

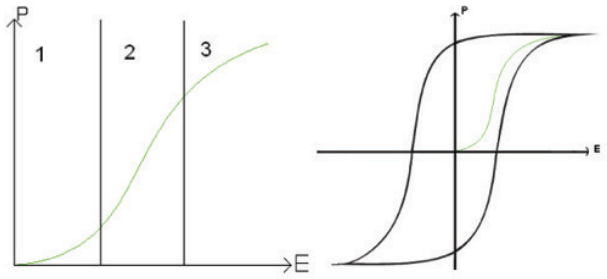

Figure 1.16. Hysteresis loop due to the nucleation process. It is possible to distinguish three sections: 1)reversible domain wall motion; 2) linear growth of new domains; 3) new domains reaching the limit of their growth.

Let us consider one of the most well-known ferroelectrics, barium titanate, ($BaTiO_3$). In Fig.1.17 it is shown its crystallographic strucure. The temperature T_C at which the spontaneous polarisation disappears is 120º.

Above T_C, barium titanate has a cubic structure. This means it is centro-symmetric and possesses no spontaneous dipole. With no dipole the material behaves like a simple dielectric, giving a linear polarisation. Below T_C, it changes to a tetragonal phase, with an accompanying movement of the atoms. The movement of Ti atoms inside the O_6 octahedra may be considered to be significantly responsible for the dipole moment.

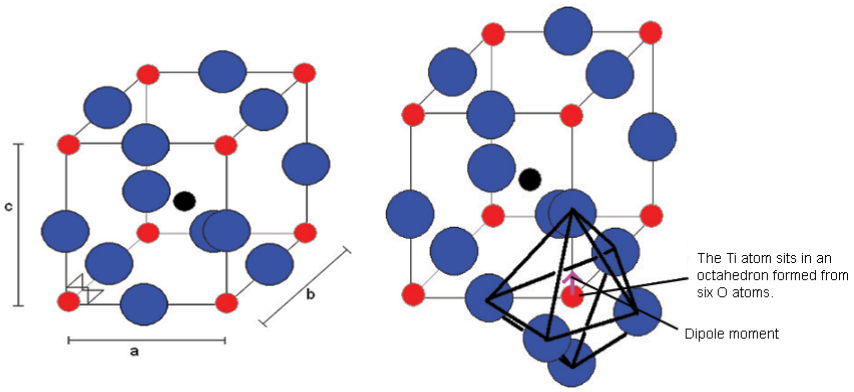

Figure 1.17. Crystallographic strucure of the barium titanate ($BaTiO_3$). The oxygen (blue) and titanium (red) atoms surround the barium (black) atom. On the left are reported the *a*,*b* and *c* lattice parameters and on the right is highlighted the octahedronal structure that the O_6 atoms form around the Ti atom.

Cooling through T_C causes the cubic phase of barium titanate to transform to a tetragonal phase with the lengthening of the *c* lattice parameter (and a corresponding reduction in *a* and *b*). The dipole moment may be considered to arise primarily due to the movement of Ti atoms with respect to the O atoms in the same plane, but the movement of the other O atoms (i.e. those O atoms above and below Ti atoms) and the Ba atoms is also relevant. The switching to a cubic structure is the reason for the polarisation spontaneously disappearing above T_C.

Barium titanate has two other phase transitions when we cool it further, each of which enhances the dipole moment. The phase which is reached after cooling to ~0°C from tetragonal is orthorhombic. And then rhombohedral below -90°C. All of these ferroelectric phases have a spontaneous polarisation based to a significant extent on movement of the Ti atom in the O_6 octahedra represented in Fig.1.18.

In conclusion, their intrisic propertiy to be *non-centrosymmetric* makes the ferroelectric crystals good candidate to possess non vanishing quadratic nonlinearity. The movement of the central atom is responsible of the breaking of the traslational symetry along one certain line. If the nucleation of the domains happens to be with an opposite polarization direction along this same line, there is little influence on the linear properties of the material, being both verses stable positions for the free energy diagram. However, fixing an external reference (for example an external linearly polarized electrical field), the sign of the $\chi^{(2)}$ nonlinearity appears to change value along with the change of the direction of the spontaneous polarization.

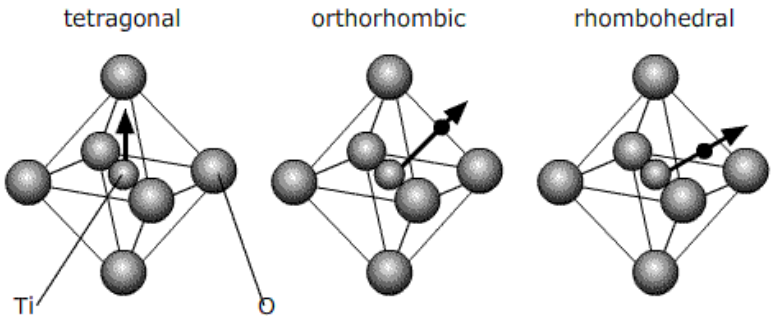

Figure 1.18. Spontaneous polarisation corresponding to the different phase transitions of the $BaTiO_3$. The direction of the polarization is given by the direction of the movement of the Ti atom.

1.3. Numerical tools

The field of the nonlinear optics is characterized by a high degree of complexity that does not allow many analytical solutions for the equations ruling the propagation. Few exceptions can be reported in the case of plane waves and *easy* modulation of the material properties. To have a more realistic representation of the light interaction and to have a large degree of freedom in the design of the linear and nonlinear properties of the material, one needs to resort to a numerical approach. However this is not a *unique*

choice, but, depending by the actual type of interaction, it needs to be carefully selected considering its *approximations* and *assumptions*.

The role of the numerical calculations in this thesis work is crucial. On one side (Part II), it was important to have a numerical correspondence and confirmation of the forecast made on simple PM schemes or statistical methods. On the other side (Part III), the experiments were not even thinkable without a prior numerical study of the phenomenon. For these reasons, we want to briefly explain here the strategy and the practical numerical set-up we used, even if a detailed description is outside the scope of this work.

The set of equations (and their mathematical form) chosen to describe the physics is strictly related with the following numerical method selected to resolve them. In the next section we present a derivation of the Maxwell's equations for the pulsed regime, in contrast to the more common plane wave approach used in text so far. For the sake of clarity they will be first considered in a one-dimension space domain plus the time coordinate and with specific assumptions and approximations. Even this form of the equations has a good validity and it has been widely used in other works, it is not the final form we used throughout this work.

It follows a schematic description of the numerical technique that we use to numerically solve this equations system. The method is called split step time domain Fast Fourier Transformed Beam Propagation Method (split step FFT-BPM) and has been manually implemented. As it will be clear later in the text, it presents both advantages and drawbacks respect to other more used numerical methods (such as for example Finite Difference Time Domain, FDTD), but it can reach the same level of accuracy. The main advantage is its easy *nonlinear* customization depending on the actual propagation characteristics.

Finally, in the following section, we will introduce the real and complete set of equations we solved for the purposes of this work.

It is worth noting that we did not resort to the very common SVEA because in critical situations, as for example propagation at big angles or examination of new phenomena, it can bring to numerical artifacts that are hardly separable from the physics results.

Equations in pulsed regime

We chose λ_0 =1μm as the reference wavelength and adopt the following scaling: $\xi = z/\lambda_0$ is the scaled longitudinal coordinate; $\tau = ct/\lambda_0$ is the time in units of the optical cycle; $\beta = 2\pi\tilde{\omega}$ is the scaled wave vector; $\tilde{\omega} = \omega/\omega_0$ is the scaled frequency, and $\omega_0 = 2\pi c/\lambda_0$, where c is the speed of light in vacuum. Gaussian units will be used in this section. We assume the fields can be decomposed as a superposition of harmonics with envelope and fast oscillating terms, of the type

$$\begin{aligned}
\mathbf{E} &= \hat{\mathbf{x}}\sum_{\ell}\left(\mathrm{E}_{\ell\omega}(z,t)\,e^{i\ell(k_0 z-\omega_0 t)} + c.c.\ \right)\\
\mathbf{H} &= \hat{\mathbf{y}}\sum_{\ell}^{\infty}\left(\mathrm{H}_{\ell\omega}(z,t)\,e^{i\ell(k_0 z-\omega_0 t)} + c.c.\right)\\
\mathbf{D} &= \hat{\mathbf{x}}\sum_{\ell}\left(\mathrm{D}_{\ell\omega}(z,t)\,e^{i\ell(k_0 z-\omega_0 t)} + c.c\ \right)\\
\mathbf{P}_{NL} &= \hat{\mathbf{x}}\sum_{\ell}\left(\mathrm{P}_{\ell\omega}(z,t)\,e^{i\ell(k_0 z-\omega_0 t)} + c.c\ \right)
\end{aligned} \tag{1.34}$$

with $\ell = 1,2,3$ for the first three harmonics respectively. Moreover, the displacement field may be related to the electric field by expanding the complex dielectric function as a Taylor's series in the usual way:

$$\varepsilon(z,\omega) = \varepsilon(z,\omega_0) + \frac{\partial\varepsilon(z,\omega)}{\partial\omega}\Big|_{\omega_0}\left(\omega-\omega_0\right) + \frac{1}{2}\frac{\partial^2\varepsilon(z,\omega)}{\partial\omega^2}\Big|_{\omega_0}\left(\omega-\omega_0\right)^2 + \ldots \tag{1.35}$$

It follows that a simple constitutive relation may be written to relate each harmonic to its relative displacement field, and it is relatively easy to show that [Lan60]:

$$\frac{\partial D_{\ell\omega}(z,t)}{\partial t} = \left\{ \begin{aligned} &-i\omega_0\varepsilon_{\ell\omega}(\omega_0)\,\mathrm{E}_{\ell\omega} + \left[\frac{\partial[\,\omega\varepsilon_{\ell\omega}(\omega)\,]}{\partial\omega}\right]_{\omega_0}\frac{\partial \mathrm{E}_{\ell\omega}}{\partial t} + \\ &\qquad + \frac{i}{2}\left[\frac{\partial^2[\,\omega\varepsilon_{\ell\omega}(\omega)\,]}{\partial\omega^2}\right]_{\omega_0}\frac{\partial^2 \mathrm{E}_{\ell\omega}}{\partial t^2} + \ldots \end{aligned} \right\} e^{-i\ell\omega_0 t}. \tag{1.36}$$

Substituting the field description like in (1.34) and taking into account (1.35) and (1.36), in scaled form Maxwell's equations for the ℓ^{th} harmonic take the following form:

$$\begin{aligned}
&\alpha_{\ell\tilde{\omega}}\frac{\partial \mathrm{E}_{\ell\tilde{\omega}}}{\partial\tau}+i\frac{\alpha'_{\ell\tilde{\omega}}}{4\pi}\frac{\partial^2 \mathrm{E}_{\ell\tilde{\omega}}}{\partial\tau^2}-\frac{\alpha''_{\ell\tilde{\omega}}}{24\pi^2}\frac{\partial^3 \mathrm{E}_{\ell\tilde{\omega}}}{\partial\tau^3}+\ldots= \\
&\quad =i\ell\beta\left(\varepsilon_{\ell\tilde{\omega},\xi}\mathrm{E}_{\ell\tilde{\omega}}-\mathrm{H}_{\ell\tilde{\omega}}\right)-\frac{\partial \mathrm{H}_{\ell\tilde{\omega}}}{\partial\xi}+4\pi\left(i\ell\beta\mathrm{P}_{\ell\tilde{\omega}}-\frac{\partial \mathrm{P}_{\ell\tilde{\omega}}}{\partial\tau}\right) \\
&\gamma_{\ell\tilde{\omega}}\frac{\partial \mathrm{H}_{\ell\tilde{\omega}}}{\partial\tau}+i\frac{\gamma'_{\ell\tilde{\omega}}}{4\pi}\frac{\partial^2 \mathrm{H}_{\ell\tilde{\omega}}}{\partial\tau^2}-\frac{\gamma''_{\ell\tilde{\omega}}}{24\pi^2}\frac{\partial^3 \mathrm{H}_{\ell\tilde{\omega}}}{\partial\tau^3}+\ldots= \\
&\quad =i\ell\beta\left(\mu_{\ell\tilde{\omega},\xi}\mathrm{H}_{\ell\tilde{\omega}}-\mathrm{E}_{\ell\tilde{\omega}}\right)-\frac{\partial \mathrm{E}_{\ell\tilde{\omega}}}{\partial\xi}
\end{aligned} \tag{1.37}$$

where

$$\alpha_{\ell\tilde{\omega}}=\frac{\partial[\,\tilde{\omega}\varepsilon_{\ell\tilde{\omega}}(\xi)\,]}{\partial\tilde{\omega}}\Big|_{\omega_0}$$

$$\gamma_{\ell\tilde{\omega}}=\frac{\partial[\,\tilde{\omega}\mu_{\ell\tilde{\omega}}(\xi)\,]}{\partial\tilde{\omega}}\Big|_{\omega_0}$$

and the symbol ' denotes a derivative with respect to frequency; together with $\varepsilon_{\ell\tilde{\omega}}$ and $\mu_{\ell\tilde{\omega}}$, $\alpha_{\ell\tilde{\omega}}$ and $\gamma_{\ell\tilde{\omega}}$ are also complex functions of frequency and of the spatial coordinate. Moreover, in deriving Eqs.(1.37) we have assumed that the background medium is isotropic, and that pulses do not diffract. The latter restriction simply means that transverse beam width remains many wavelengths wide at all times. This limitation can easily be lifted by allowing the fields to vary along the transverse coordinate [Sca05, Sca05b, Sca05c, Sca06, Sca06b]. More importantly, our description of the fields as the product of an envelope function and a carrier wave vector and frequency is a mere matter of convenience, primarily because it allows one to follow the detailed dynamics of each harmonic, and to explore the impact of each term on the dynamics. However, it should be noted that although this field decomposition constitutes the foundation of the SVEA, it should not per se be misconstrued as an approximation, because (1.34) do not yet contain restrictions on the envelope functions.

While in principle the number of linear dispersion terms (temporal derivatives of the fields) and/or the number of harmonics one retains to describe the system may be arbitrarily large, in practice one must work with a finite number of them. Of course, truncating the number of time derivatives or the number of harmonics is equivalent to making some kind of approximation.

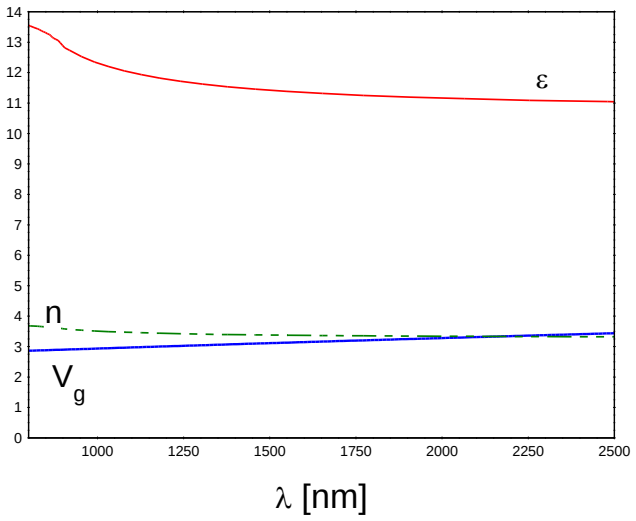

Figure 1.19. Dispersion relation of GaAs. Note that in whole intesting range we can approximate the group velocity V_g relation with a first order Taylor's expansion. The second order dispersion length, gives an idea to estimate when the second order effect become important. It can be of the order of centimeters or meters for typical interaction values.

Using this approach, we typically consider a medium only a few hundred wavelengths thick. Under these conditions, it is more than sufficient to neglect third and higher harmonics, and to neglect second and higher temporal derivatives that arise from linear material dispersion (Fig.1.19). Therefore, it is clear that the calculations may be simplified by truncating nonlinear polarization term at the SH fields without appreciably impacting the dynamics.

In terms of linear material dispersion, typical material dispersions and/or relatively short propagation distances make it possible to neglect second and higher order temporal derivatives, *without* the need to perform a SVEA in time [Sca06, Sca97, Cen01]. That is to say, it can easily be demonstrated that in the visible range and near IR ranges, for typical dielectric and semiconductor materials the second order dispersion length, defined as

$$L_D^{(2)} \sim \tau_p^2 / |k''|,$$

where τ_p is pulse duration and $k'' = d^2k/d\omega^2$, can easily be a few centimeters for a pulse only a few tens of femtoseconds in duration. After

these considerations, the dielectric constant in Eq.(1.35) can be accurately represented by the first two leading terms, even if a pulse were only a few optical cycles in duration. Of course, the truncation of (1.35) at the second term becomes a material characterization, not an approximation imposed on the envelope function. Therefore, under most circumstances of interest that involve pulse propagation in relatively thin media, (1.37) may safely and accurately be recast as follows [Sca06]:

$$\begin{aligned}\alpha_{\ell\tilde{\omega}}\frac{\partial \mathrm{E}_{\ell\tilde{\omega}}}{\partial\tau} &\approx i\ell\beta\left(\varepsilon_{\ell\tilde{\omega},\xi}\mathrm{E}_{\ell\tilde{\omega}}-\mathrm{H}_{\ell\tilde{\omega}}\right)-\frac{\partial \mathrm{H}_{\ell\tilde{\omega}}}{\partial\xi}+4\pi\left(i\ell\beta\mathrm{P}_{\ell\tilde{\omega}}-\frac{\partial \mathrm{P}_{\ell\tilde{\omega}}}{\partial\tau}\right)\\ \gamma_{\ell\tilde{\omega}}\frac{\partial \mathrm{H}_{\ell\tilde{\omega}}}{\partial\tau} &\approx i\ell\beta\left(\mu_{\ell\tilde{\omega},\xi}\mathrm{H}_{\ell\tilde{\omega}}-\mathrm{E}_{\mathrm{l}\tilde{\omega}}\right)-\frac{\partial \mathrm{E}_{\ell\tilde{\omega}}}{\partial\xi}.\end{aligned} \tag{1.38}$$

In summary, in addition to the assumptions that the linear background medium is isotropic and diffraction is neglected, the final Eqs.(1.38) for the ℓ^{th} harmonic contain the following simplifications: (i) second and higher-order, linear material dispersion terms are neglected; (ii) third and higher harmonics are also neglected. As written, (1.38) provide an accurate physical picture of the dynamics, including boundary conditions and all orders of reflections, even for pulses that are just a few wave cycles in duration.

The integration of (1.38) is carried out for pulses whose durations varied from a few optical cycles up to several picoseconds, with indistinguishable results in all cases investigated. In addition to having more control over each term, Maxwell's Eqs.(1.38) are written in a form that allows the use of the classic fast Fourier transform, beam propagation method [Sca94], appropriately modified to include all orders of reflections and feedback in the time domain. The advantage to use a spectral method is mainly that in the transformed domain it involves only multiplication of linear operators; it is unconditionally stable, with no known issues relating to phase or amplitude errors, and thus not prone to the generation of any numerical artifacts; it can easily be extended also to the multidimensional domain almost effortlessly [Sca05b, Sca05c].

Split step FFT beam propagation method

In this section we explain the solving algorithm used to solve Eqs.(1.38) following the seminal work in [Sca94]. For simplicity, we will treat only the first two harmonics $\ell = 1,2$. For this reasons the start point is a system of four coupled equations for the electric and magnetic fields of the fundamental pulse, at ω frequency, and the SH pulse, at 2ω frequency:

$$\begin{aligned}
&\alpha_{\tilde{\omega}} \frac{\partial \mathrm{E}_{\tilde{\omega}}}{\partial \tau} = i\beta\left(\varepsilon \mathrm{E}_{\tilde{\omega}} - \mathrm{H}_{\tilde{\omega}}\right) - \frac{\partial \mathrm{H}_{\tilde{\omega}}}{\partial \xi} + 4\pi\left(\mathrm{i}\beta\,\mathrm{P}_{\tilde{\omega}} - \frac{\partial \mathrm{P}_{\tilde{\omega}}}{\partial \tau}\right) \\
&\gamma_{\tilde{\omega}} \frac{\partial \mathrm{H}_{\tilde{\omega}}}{\partial \tau} = i\beta\left(\mu \mathrm{H}_{\tilde{\omega}} - \mathrm{E}_{\tilde{\omega}}\right) - \frac{\partial \mathrm{E}_{\tilde{\omega}}}{\partial \xi} \\
&\alpha_{2\tilde{\omega}} \frac{\partial \mathrm{E}_{2\tilde{\omega}}}{\partial \tau} = 2i\beta\left(\varepsilon \mathrm{E}_{2\tilde{\omega}} - \mathrm{H}_{2\tilde{\omega}}\right) - \frac{\partial \mathrm{H}_{2\tilde{\omega}}}{\partial \xi} + 4\pi\left(2\mathrm{i}\beta\,\mathrm{P}_{2\tilde{\omega}} - \frac{\partial \mathrm{P}_{2\tilde{\omega}}}{\partial \tau}\right) \\
&\gamma_{2\tilde{\omega}} \frac{\partial \mathrm{H}_{2\tilde{\omega}}}{\partial \tau} = 2i\beta\left(\mu \mathrm{H}_{2\tilde{\omega}} - \mathrm{E}_{2\tilde{\omega}}\right) - \frac{\partial \mathrm{E}_{2\tilde{\omega}}}{\partial \xi}
\end{aligned} \tag{1.39}$$

They include the effects of dispersion and the quadratic nonlinear term that are responsible of the coupling between the first and third equations. The couplings between the first and the second and between the third and the fourth equations are due to the intrinsic tridimensional nature of Maxwell's equations. In fact our case is only a special case of general pulse propagation feature if we consider a TEM polarization with electric field along x-axis during normal incidence. In all this treatment the indications of the spatial and temporal dependence are dropped except when they are necessary for the comprehension.

We will focus our attention only in the first equation, being with a similar procedure for the others. With a simple handling the first of (1.39) becomes

$$\frac{\partial}{\partial \tau}\mathrm{E}_{\omega} = \frac{1}{\alpha_{\omega}}\left[-\frac{1}{\mathrm{E}_{\omega}}\frac{\partial \mathrm{H}_{\omega}}{\partial \xi} + i\beta\left(\varepsilon - \frac{\mathrm{H}_{\omega}}{\mathrm{E}_{\omega}}\right) + \frac{i4\pi\beta\chi^{(2)}\mathrm{E}_{\omega}^{*}\mathrm{E}_{2\omega}}{\mathrm{E}_{\omega}}\right]\mathrm{E}_{\omega} \tag{1.40}$$

where we have expressed the nonlinear term and neglected its temporal derivative. It is possible to show that this term does not affect the accuracy of the method for a pulse at least longer than some optical cycles. Formally it is possible to recast Eq.(1.40) as

$$\frac{\partial}{\partial\tau}\mathrm{E}_\omega = \frac{1}{\alpha_\omega}\left[\hat{D}+\hat{V}\right]\mathrm{E}_\omega \tag{1.41}$$

where

$$\hat{D} = -\frac{1}{\mathrm{E}_\omega}\frac{\partial \mathrm{H}_\omega}{\partial\xi}$$

$$\hat{V} = i\beta\left(\varepsilon - \frac{\mathrm{H}_\omega}{\mathrm{E}_\omega}\right) + \frac{i4\pi\beta\chi^{(2)}\mathrm{E}_\omega^{*}\mathrm{E}_{2\omega}}{\mathrm{E}_\omega}$$

are particular operators referred respectively to a propagation in the free space and in the medium. The solution of (1.41) has the form

$$\mathrm{E}_\omega(z,\tau+d\tau) = \mathrm{E}_\omega(z,\tau)\exp\left(\frac{1}{\alpha_\omega}\left[\hat{D}+\hat{V}\right]dt\right)$$

that, at first order becomes

$$\mathrm{E}_\omega(z,\tau+d\tau) = \mathrm{E}_\omega(z,\tau) + \frac{\partial \mathrm{E}_\omega(z,\tau)}{\partial\tau}d\tau =$$

$$= \mathrm{E}_\omega(z,\tau) + \frac{1}{\alpha_\omega}\left[\hat{D}+\hat{V}\right]\mathrm{E}_\omega(z,\tau)d\tau + \Theta(d\tau^2).$$

If now we sum and subtract the term $\mathrm{E}_\omega(z,\tau)/\alpha_\omega$ it takes the following form

$$\mathrm{E}_\omega(z,\tau+d\tau) = \mathrm{E}_\omega(z,\tau)\left(1-\frac{1}{\alpha_\omega}\right) + \frac{\mathrm{E}_\omega(z,\tau)}{\alpha_\omega}\left(1+\left[\hat{D}+\hat{V}\right]d\tau + \Theta(d\tau^2)\right)$$

that is, at the second order, the same as

$$\mathrm{E}_\omega(z,\tau+d\tau) = \mathrm{E}_\omega(z,\tau)\left(1-\frac{1}{\alpha_\omega}\right) + \frac{1}{\alpha_\omega}e^{\hat{V}d\tau}\left(e^{\hat{D}d\tau}\mathrm{E}_\omega(z,\tau)\right).$$

Operator $\hat{D}$ involves a spatial derivative and it can be evaluated in the spatial Fourier domain

$$\hat{\tilde{D}} = -ik_\omega\frac{\tilde{\mathrm{H}}_\omega}{\tilde{\mathrm{E}}_\omega},$$

thus, the full integration step is

$$\mathrm{E}_{\omega}(z,\tau+d\tau)= \mathrm{E}_{\omega}(z,\tau)\left(1-\frac{1}{\alpha_{\omega}(z)}\right)+\frac{1}{\alpha_{\omega}(z)}e^{\hat{V}d\tau}FT^{-1}\left[e^{\hat{\tilde{D}}d\tau}FT\left[\mathrm{E}_{\omega}(z,\tau)\right]\right]. \quad (1.42)$$

Thank to this formulation it is possible now to split the problem in three steps: *i)* propagation in free space, accounting for the operator $\hat{D}$, *ii)* propagation in nonlinear medium, accounting for the operator $\hat{V}$ and *iii)* counting of the dispersive effect through the factor α_{ω}. All the equations of the set (1.39) need to be casted in this form and integrated at the same time. The detailed numerical treatment of the integration strategy can be somewhat tedious and it is outside the scope of this thesis work. This notwithstanding, we want to give a hint at least on how the free space propagation step is integrated.

We can start from the observation that the solution $\mathrm{E}^{(1)}(q,d\tau)=\mathrm{E}(q,0)e^{\hat{D}d\tau}$ of the equation $\partial E/\partial\tau=\hat{D}E$ can be expressed in the form

$$\mathrm{E}^{(1)}(q,\tau)=\mathrm{E}(q,0)+\int_0^{\tau}\hat{D}\mathrm{E}(q,\tau')d\tau' \quad (1.43)$$

where q is the transformed spatial coordinate. The integral represents the area under the curve $\hat{D}\mathrm{E}(q,\tau)$ between the two times 0 and τ. If we consider a time step $d\tau<<1$, the eq.(1.43) can be written as

$$E^{(1)}(q,d\tau)\simeq E\ (q,0)-\frac{ikd\tau}{2}\left[H\ (q,d\tau)+H\ (q,0)\right] \quad (1.44)$$

with a second order error. From the second of the Eqs.(1.39) we can obtain a similar equation for the H field

$$H^{(1)}(q,d\tau)\simeq H(q,0)-\frac{ikd\tau}{2}\left[E(q,d\tau)+E(q,0)\right]. \quad (1.45)$$

Substituting (1.45) into (1.44), after some algebraic manipulation we finally have

$$E^{(1)}(q,\tau+d\tau)\simeq E(q,\tau)\frac{\left(1-ik^2d\tau^2/4\right)}{\left(1+ik^2d\tau^2/4\right)}-\frac{ikd\tau H(q,\tau)}{\left(1+ik^2\delta\tau^2/4\right)} \quad (1.46)$$

where the field at the time step $\tau+d\tau$ is fully calculated with fields quantities at time τ.

Full vectorial equations

To maintain a high degree of generality we have performed numerical simulations of pulse propagation with a Maxwell-Lorentz system of equations in two dimensions, without resorting to either slowly varying or undepleted pump approximations. The numerical model is similar to that used in previous section with the addition of a transverse coordinate to include diffraction and propagation in a two-dimensional plane. In the previous paragraph the modeling of the material characteristics was limited to the inclusion in the equations system of only the first two orders of the material dispersion. Throughout this thesis work we actually include all higher order dispersion terms by adopting a more generic Lorentz oscillator model to describe material dispersion and, for simplicity, we assume a TM-polarized incident pump and generated fields. Depending on the actual case treated (namely the nonlinear tensor of the crystal used) different interactions can be implemented. In a two-dimensional propagation domain this means we will have an electromagnetic field composed by two electric components along the plane (y, z) and one magnetic component along the direction x perpendicular to the plane and to the material interface. In a very general way, the fields may be written as a superposition of harmonics as follows:

$$\begin{aligned}
\mathbf{H} &= \hat{\mathbf{x}}\sum_{\ell=1}^{\infty}\left(H_x{}^{\ell\omega}(z,y,t)+c.c\ \right)=\hat{\mathbf{x}}\sum_{\ell=1}^{\infty}\left(\mathcal{H}_x{}^{\ell\omega}(z,y,t)\,e^{i\ell(kz-\omega t)}+c.c\ \right)\\
\mathbf{E} &= \hat{\mathbf{y}}\sum_{\ell=1}^{\infty}\left(E_y{}^{\ell\omega}(z,y,t)+c.c\ \right)+\hat{\mathbf{z}}\sum_{\ell=1}^{\infty}\left(E_z{}^{\ell\omega}(z,y,t)+c.c\ \right)= \qquad (1.47)\\
&= \hat{\mathbf{y}}\sum_{\ell=1}^{\infty}\left(\mathcal{E}_y^{\ell\omega}(z,y,t)\,e^{i\ell(kz-\omega t)}+c.c\ \right)+\hat{\mathbf{z}}\sum_{\ell=1}^{\infty}\left(\mathcal{E}_z^{\ell\omega}(z,y,t)\,e^{i\ell(kz-\omega t)}+c.c\ \right)
\end{aligned}$$

where $\mathcal{H}_x^{\ell\omega}(z,y,t)$, $\mathcal{E}_y^{\ell\omega}(z,y,t)$ and $\mathcal{E}_z^{\ell\omega}(z,y,t)$ are generic, spatially- and temporally-dependent, complex envelope functions; k and ω are carrier wave vector and frequency, respectively, and ℓ is an integer. As we already stated, these equations are a convenient representation of the fields, and no *a priori* assumptions are made about the field envelopes. We have also assumed that a TM-polarized incident field generates similarly polarized harmonics. The linear response of the medium induced by an external applied field is described by a Lorentz oscillator model [Lor06]:

$$\ddot{\mathbf{P}} + \gamma\dot{\mathbf{P}} + \omega_0^2\mathbf{P} = \frac{Ne^2}{m}\mathbf{E}\ . \tag{1.48}$$

The solution in Fourier space is given by

$$\varepsilon(\omega) = 1 - \frac{\omega_p^2}{\omega^2 + i\gamma\omega - \omega_r^2}$$

We have assumed that

$$\mu(\omega) = 1.$$

The parameters γ, ω_p, and ω_r are the damping coefficient, the plasma and resonance frequencies, respectively. This model is not restrictive and different equations can be added, for example, to model negative index materials that require a magnetic response. The second and third order nonlinear polarization is assumed to be

$$\mathbf{P}_{NL} = \varepsilon_0\chi^{(2)}\mathbf{E}^2 + \varepsilon_0\chi^{(3)}\mathbf{E}^3. \tag{1.49}$$

As an example, each field component yields nonlinear polarization terms at the fundamental and harmonics frequencies as follows:

$$\begin{aligned}
\mathcal{P}_{NL}^{\omega}(y,z,t) &= 2\varepsilon_0\chi^{(2)}\left(\mathcal{E}_{2\omega}^{*}\mathcal{E}_{3\omega} + \mathcal{E}_{\omega}^{*}\mathcal{E}_{2\omega}\right) + \\
&+ 3\varepsilon_0\chi^{(3)}\left(|\mathcal{E}_{\omega}|^2\,\mathcal{E}_{\omega} + \mathcal{E}_{2\omega}^{2}\mathcal{E}_{3\omega}^{*} + \mathcal{E}_{3\omega}\mathcal{E}_{\omega}^{*2} + 2|\mathcal{E}_{2\omega}|^2\,\mathcal{E}_{\omega} + 2|\mathcal{E}_{3\omega}|^2\,\mathcal{E}_{\omega}\right) \\
\mathcal{P}_{NL}^{2\omega}(y,z,t) &= \varepsilon_0\chi^{(2)}\left(\mathcal{E}_{\omega}^{2} + 2\mathcal{E}_{\omega}^{*}\mathcal{E}_{3\omega}\right) + \\
&+ 3\varepsilon_0\chi^{(3)}\left(|\mathcal{E}_{2\omega}|^2\,\mathcal{E}_{2\omega} + 2|\mathcal{E}_{3\omega}|^2\,\mathcal{E}_{2\omega} + 2\mathcal{E}_{2\omega}^{*}\mathcal{E}_{3\omega}\mathcal{E}_{\omega} + 2|\mathcal{E}_{\omega}|^2\,\mathcal{E}_{2\omega}\right) \\
\mathcal{P}_{NL}^{3\omega}(y,z,t) &= 2\varepsilon_0\chi^{(2)}\mathcal{E}_{2\omega}\mathcal{E}_{\omega} + \\
&+ \chi\varepsilon_0^{(3)}\left(\mathcal{E}_{\omega}^{3} + 6|\mathcal{E}_{2\omega}|^2\,\mathcal{E}_{3\omega} + 3|\mathcal{E}_{3\omega}|^2\,\mathcal{E}_{3\omega} + 3\mathcal{E}_{2\omega}^{2}\mathcal{E}_{\omega}^{*} + 6|\mathcal{E}_{\omega}|^2\,\mathcal{E}_{3\omega}\right).
\end{aligned} \tag{1.50}$$

Assuming that polarization and currents may be decomposed as in Eqs.(1.47), we obtain the following 2D Maxwell-Lorentz system of equations for the ℓ^{th} field components, in the scaled two-dimensional space $(\tilde{y},\xi)$ plus time (τ) coordinate system:

$$
\begin{aligned}
&\frac{\partial \mathcal{H}_x^{\ell\omega}}{\partial \tau} = i\beta_\ell \left(\mathcal{H}_x^{\ell\omega} + \mathcal{E}_z^{\ell\omega} \sin\theta_i + \mathcal{E}_y^{\ell\omega} \cos\theta_i \right) - \frac{\partial \mathcal{E}_z^{\ell\omega}}{\partial \tilde{y}} + \frac{\partial \mathcal{E}_y^{\ell\omega}}{\partial \xi} \\
&\frac{\partial \mathcal{E}_y^{\ell\omega}}{\partial \tau} = i\beta_\ell \left(\mathcal{E}_y^{\ell\omega} + \mathcal{H}_x^{\ell\omega} \cos\theta_i \right) - 4\pi (\mathcal{J}_y^{\ell\omega} - i\beta_\ell \mathcal{P}_y^{\ell\omega}) + i4\pi\beta_\ell \mathcal{P}_{y,NL}^{\ell\omega} \\
&\qquad - 4\pi \frac{\partial \mathcal{P}_{y,NL}^{\ell\omega}}{\partial \tau} + \frac{\partial \mathcal{H}_x^{\ell\omega}}{\partial \xi} \\
&\frac{\partial \mathcal{E}_z^{\ell\omega}}{\partial \tau} = i\beta_\ell \left(\mathcal{E}_z^{\ell\omega} + \mathcal{H}_x^{\ell\omega} \sin\theta_i \right) - 4\pi (\mathcal{J}_z^{\ell\omega} - i\beta_\ell \mathcal{P}_z^{\ell\omega}) + i4\pi\beta_\ell \mathcal{P}_{z,NL}^{\ell\omega} \\
&\qquad - 4\pi \frac{\partial \mathcal{P}_{z,NL}^{\ell\omega}}{\partial \tau} - \frac{\partial \mathcal{H}_x^{\ell\omega}}{\partial \tilde{y}} \\
&\frac{\partial \mathcal{J}_y^{\ell\omega}}{\partial \tau} = \left(2i\beta_\ell - \gamma \right) \mathcal{J}_y^{\ell\omega} + \left(\beta_\ell^2 + i\gamma\beta_\ell - \beta_r^2 \right) \mathcal{P}_y^{\ell\omega} + \frac{\pi\omega_p^2}{\omega_0^2} \mathcal{E}_y^{\ell\omega} \\
&\frac{\partial \mathcal{J}_z^{\ell\omega}}{\partial \tau} = \left(2i\beta_\ell - \gamma \right) \mathcal{J}_z^{\ell\omega} + \left(\beta_\ell^2 + i\gamma\beta_\ell - \beta_r^2 \right) \mathcal{P}_z^{\ell\omega} + \frac{\pi\omega_p^2}{\omega_0^2} \mathcal{E}_z^{\ell\omega} \\
&\mathcal{J}_y^{\ell\omega} = \frac{\partial \mathcal{P}_y^{\ell\omega}}{\partial \tau} \\
&\mathcal{J}_z^{\ell\omega} = \frac{\partial \mathcal{P}_z^{\ell\omega}}{\partial \tau}
\end{aligned}
\tag{1.51}
$$

In Eqs.(1.51), the functions $\mathcal{J}, \mathcal{P}, \mathcal{P}_{NL}$ refer to linear electric currents, polarization, and nonlinear polarization, respectively. The coordinates are scaled so that $\xi = z/\lambda_0$, $\tilde{y} = y/\lambda_0$, $\tau = ct/\lambda_0$, $\omega_0 = 2\pi c/\lambda_0$, where $\lambda_0 = 1\mu m$ is just reference wavelength; γ, $\beta_{\ell\omega} = 2\pi\ell\omega/\omega_0$, $\beta_r = 2\pi\omega_r/\omega_0$, ω_p, are the scaled damping coefficient, wave-vector, resonance and electric plasma frequencies for the ℓ^{th} harmonic, respectively. θ_i is the angle of incidence of the pump field. The equations are solved using the split step FFT-BPM that advances the fields in time. Its strategy has been just explained in the previous section. Since the oscillator's equations are solved simultaneously with Maxwell's equations through the coupling action of the terms $\mathcal{E}_y^{\ell\omega}$ and $\mathcal{E}_z^{\ell\omega}$, all orders of material dispersion are taken into account. Furthermore, no explicit boundary conditions are required because they are implicitly included in the solution of the equations.

Part I

Chapter 2

SHG in disordered nonlinear domains structures

2.1. State of the art

In Chapter 1 we saw that, out of the PM condition, the generated SH field propagates in the material with different phase velocity with respect to the FF. In addition, when beam and/or pulsed propagation are considered, the different directions of the k-vectors and/or the different group velocities will make the SH inevitably walk-off (spatially or temporally) by the FF after a certain time. This directly interrupts the SH energy provision. Some

studies tried to compensate, for example, the temporal dispersion by engineering material dispersion slope to modify the pulse group velocity. Fortunately, in the majority of the cases the spatial extension of the pulses/beams is bigger, or at least of the same order, than the samples dimension. In this case there is not enough time/space for the walk-off to happen. To give a rough idea, a 3 nanoseconds pulse is of the order of one meter in spatial extension and a 3 picoseconds pulse is of the order o 1mm.

The main issue to assess is thus the phase velocities difference, and this is what we are really interested in. This difference results from the normal dispersion of the material that imposes different refractive indices at the two wavelengths. The parameter that better gives us the idea of the scale of this phenomenon is the coherence length. After *one coherence length* from the material entry surface, the two harmonic beams have already completely lost their phase synchronization and the energy of the generated SH cannot be further increased. Moreover, during the second coherence length the SH energy return back to the FF. Depending on the material and on the tuning of the beam, the coherence length can sensibly vary, but it is always on the micro- or even nano-scale, and the *bulk* efficiency of the generated SH outside the PM condition unlikely reaches appreciable values.

As outlined in Chapter 1, one of the well known methods to go beyond this limit is the QPM technique. It was practically achieved for the first time by Fejer *et al.* [Fej92]. By periodically changing the sign of the quadratic nonlinearity one can externally correct the phase delay of the SH every coherence length distance during the propagation. This allows a mono-directional energy flow from the FF to the SH. While the high efficiency of the method is not under discussion, we want to underline here some of the drawbacks. For example, it is clear that a crystal can be *pooled* (namely quasi-phase-matched) only for one specific wavelength interaction and for one nonlinear process each time. The QPM bandwidth is in general very narrow and it makes the overall alignment and tuning processes very critical. For this reason also, the method is thought to be proficient with continuous wave, while it loses nominal efficiency with short pulsed

interaction where the spectral bandwidth can span up to hundreds of nanometers.

During last ten years several attempts were made to gain some degree of freedom trying to obtain large bandwidth keeping, at the same time, the SH conversion efficiency at reasonable levels. An easy modification of the classical QPM technique consists in superimpose different periodicities along the one dimensional poling. Alternatively it is also possible to play with the frequency chirp and/or duty factor of the nonlinearity's variation (see for example [Ari10] for a complete review). However, the most important achievement was probably the stepping from an intrinsic 1D QPM geometry to a more feasible 2D geometry, introducing the NLPC [Ber98] (see Chapter 1). Here the periodicity is spread in a two dimensional plane. For this reason, to be fully characterized, it needs not only a reciprocal vector (RV) *value* but also a RV *direction*. The generation process is more complex because different RVs $\mathbf{G}$ with different directions and magnitudes can contribute either to the same interaction or facilitating different SH emission. The main difference with the classical QPM is essentially that the NLPCs allow the SHG at different (designable) angles. To loose the constrain of the (still present) narrow bandwidth, some authors proposed the introduction of some degree of disorder in the perfectly ordered poled structure. For example in [She07] the square-based periodicity of the nonlinear pooling was rotationally perturbated with a random rotation of the unit cell (see Fig.2.1).

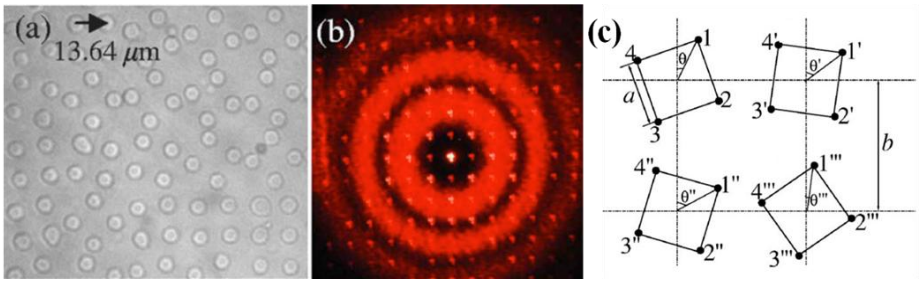

Figure 2.1. (a) Micrograph of etched domain structure used in [She07], (b)reciprocal vectors detected with He–Ne laser, (c) Schematic picture showing how the short-range ordered structure is created by placing randomly oriented basic units on a square lattice of period b [She07].

The result is that the RVs distribution acquires an effective relatively broad area that can be used to PM more easily the SH interaction. At this stage, the position of the reversed nonlinear domains forming the pseudo-periodicity still needs to be somehow designed. This requires an effort that can be not negligible for long samples and for in-series production devices. On the other side, the broadening of the **G** vectors spectrum can be still not enough to reach that degree of freedom as ideally desired.

The last step that connects this branch of investigation to the present work was the discovery of the fact that the domains the ferroelectric crystals naturally present (see Chapter 1) are not only regions where the *linear* polarization assumes an opposite direction. Even if this does not change the linear index of refraction, it affects as a consequence also the *nonlinear* polarization. The sign of the $\chi^{(2)}$ keeps alternating throughout the sample along the change of the direction of the linear polarization. This is true only for the *as-grown* crystal, namely without any artificial poling subsequent to their growing. Since the linear value of the index of refraction is homogeneous, in last analysis we can refer to these materials as quadratic NLPC consisting of *antiparallel ferroelectric nonlinear domains with randomized sizes and positions*. In the next section we are going to overview their main characteristics and the experimental set-up where they are typically used.

2.2. Random nonlinear domains crystals

One of the ferroelectric crystal that posses random inverted nonlinear domain is Strontium Barium Niobate (SBN). This crystal shows needle-like domains distributed parallel to the optical axis. Fig.2.2 shows different views of such crystal obtained by different techniques. The pictures show the domain structure of the crystal as it grows naturally in chemical laboratories. In the first case (left) the boundaries of the domains have been made visible by selective chemically etching the surface of the sample [Ber98b, Mol08]. In the second case (right) the graphs were obtained by

using the SH nonlinear microscopy [She10]. The figures depict the domain structure as seen perpendicular (first row) and along (second row) to the optical c-axis which coincides with the longer dimension of the domains.

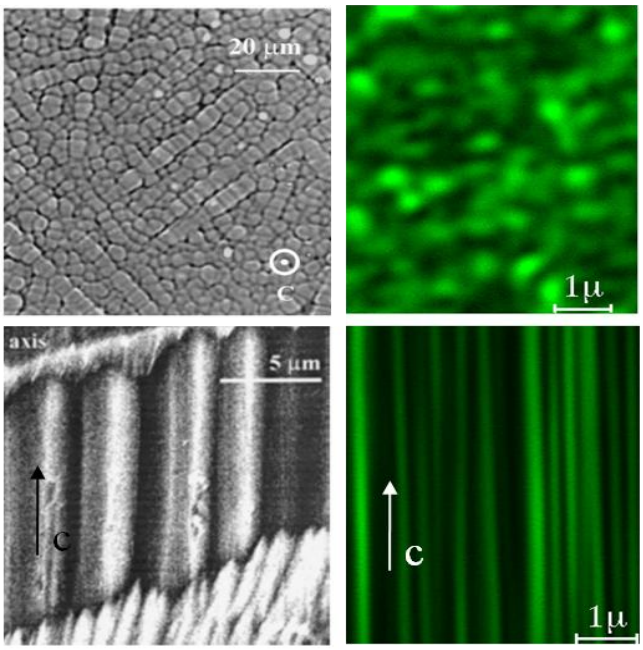

Figure 2.2. (left) Optical micrograph revealing the 2D distribution of the alternate ferroelectric domains on the a–b plane (perpendicular to the c axis, on the top) and along c-axis (on the bottom) of a SBN crystal after selective chemical etching [Mol08]. (right) multi-domain structure of another SBN sample as visualized by the SH nonlinear microscopy; viewing area perpendicular (top) and parallel (bottom) to the optical c-axis [Wan10].

The as-grown domain pattern depends on a variety of factors that can span from the type of crystal, to the growing method, passing through the electric voltage applied and the thermal history. The dimension of the domains can be unpredictable. In [Soe05] a number of different imagine techniques are reviewed showing that, in last analysis, it is not easy to visualize the nonlinear domains without having a prior knowledge on the strucure.

For example, Fig.2.3, shows the bar chart representing the domain distribution as the crystal shown in Fig.2.2(left). These bar charts are typically used to characterize the random domain pattern. However, when one uses images as these there are still a number of unanswered questions. For example, is the etching process able to show *all* the domains, even the

smaller ones? How many domains are there in one grain? How is the sign of the nonlinearity for each domain?

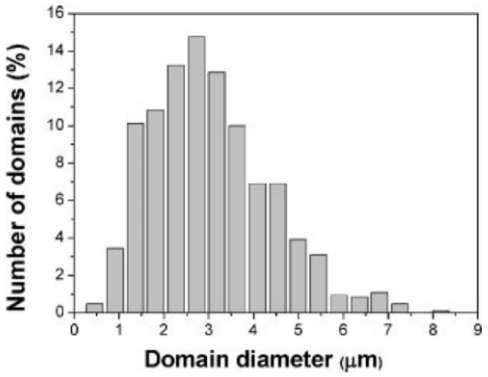

Figure 2.3. Histogram showing the domain diameter distribution of the optical micrograph in Fig.2.2 (left).

For this reason, the starting point of our work will be to have a clear and deep nonlinear crystal characterization using a a *reversed-engineering* approach. Starting with the far field experimental visualization of the generated SH from real crystals, we design *guess structures* and numerically model the laser light propagation through them. We proceeded until we obtained the same far field emission for both numerical and experimental data, namely the same nonlinear structure. Even if this method is precise, it is extremely time consuming and cannot be applied to systematical analysis of big amount of samples. Despite that, it allowed us to validate a more simple and fast statistical method that takes into account the domains pattern as a whole ignoring the individual domain specification.

Notwithstanding this initial lacking of information we can describe the main features of the domain pattern, also aided by images as in Figs.2.2.

- Firstly, the domains have all identical linear properties. Some variation of the linear index can be present between two domains of different $\chi^{(2)}$ sign due to the strong variation of the polarization. However, the magnitude of this variation is of the order of 10^{-2}-10^{-3} [Woi01, Gai09].
- Domain sizes in the x-y plane can vary from few nanometers to tens of microns and their packing is random. On the other hand, the coherence

length for the SHG varies between 0.1 and 1.5μm. The harmonic generation in this structure is therefore generally based on higher order phase-matching, especially for the non-collinear cases which require smaller grating periods than the forward PM.

- The domains are elongated along the crystal c-axis. This leads to a finer modulated structure in the x-y plane compared to modulation along the c-axis, which is of significantly larger scale. We will consider the system as two-dimensional since it has been proved that the structure in c direction has practically no impact on the effects observed in experiments [Kaw98].
- Due to the tetragonal unit cell of the crystal, the needle-like domains are either parallel or anti-parallel ferromagnetic orientated along the crystal c-axis. Thus the sign of the second-order nonlinearity $\chi^{(2)}$ changes from domain to domain in the x-y plane. This provides a *natural* two-dimensional poled structure. The term "natural" is here used in the sense that it is not technical designed and controlled, even if the growing process, the type of material and the history of the crystal can strongly affect the distribution.

The scheme shown in Fig.2.4 illustrates the comparison between a periodically poled and the disordered 2D ferroelectric as-grown crystal. In the first one is clear the periodicity of the sign of the nonlinear domains while no such single period is evident in the second case and apparently no single periodicity dominates the formation. The disordered modulation provides a continuous set of PM gratings with various periods and in all directions of the x-y plane. As a result, for any fundamental wavevector $\mathbf{k}_\omega$ of light propagating through the crystal there will be also a matching grating vector $\mathbf{G}$ in this plane to fulfill the phase-matching condition $\mathbf{k}_{2\omega}=2\mathbf{k}_\omega + \mathbf{G}$. Furthermore, this is not limited to SHG but is equally valid for any other second-order parametric process such as sum frequency mixing or difference frequency mixing [Boy08].

Since the probability for different periods varies only slowly, the directly linked SHG efficiency as a function of the fundamental wavelength can be considered as practically constant over the range of several

nanometres. As a result, the disordered domain structure provides *achromatic* PM, meaning that all frequencies (in the transparency range of the crystal) are converted with equal efficiency. Achromatic PM is a property highly desirable for all-optical devices that could convert different wavelengths in the same material with equal efficiency. It also proofs very useful in systems with tunable laser wavelength, where the strength of the SH response from the unpoled SBN is independent of the adjusted wavelength. Furthermore, no angular or temperature tuning of the crystal is needed when the working wavelength is changed.

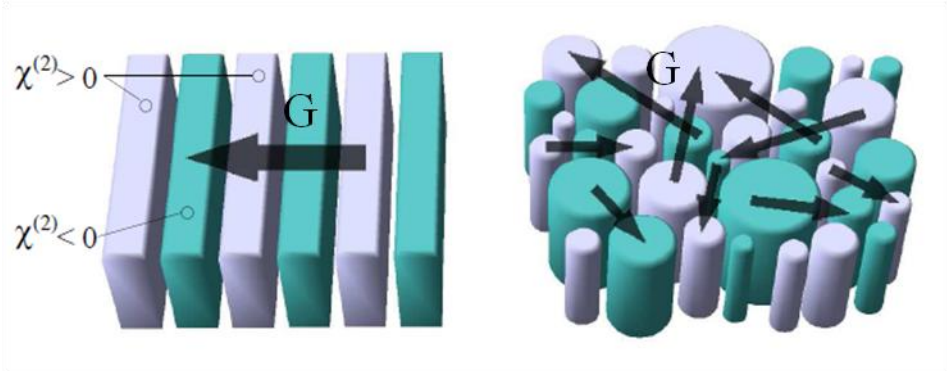

Figure 2.4. Schematic comparison of a strictly periodic structure to natural domain poling in SBN. The grey arrows illustrate grating vectors [Fis08].

It is important to point out at this point that the main drawback of such high degree of freedom is a rather low conversion efficiency. However, a low conversion efficiency means also a low depletion of the FF. This aspect is of particular importance for measurement applications where the FF has to be analyzed with minimal distortion and losses.

The most interesting applications of achromatic PM are probably found in the context of ultra-short pulses. Due to the fundamental uncertainty principle, the spectral bandwidth of a pulse naturally increases as the pulse duration becomes shorter. This relation is known as the time-bandwidth product of a laser pulse and the corresponding limiting factor can be calculated with the Fourier transform.

The strength of the SH generating process depends on the polarization of the fundamental light wave with respect to the principal axis of this crystal. As discussed in Chapter 1, this process is governed by the second-

order electric susceptibility $\chi^{(2)}$ which varies strongly along the different crystal axis. SBN belongs to the 4mm (C_{4v}) crystal class, and possess non-zero components $d_{31}\approx 9.4$ pm/V, $d_{15}\approx 6.76$ pm/V and $d_{33}\approx 17.7$ pm/V [Cha00](data for 1064 nm fundamental wavelength). This means that the highest conversion efficiency will be achieved for light polarized along the c-axis since it makes use of the largest tensor element d_{33}. Hence the wavevector of the corresponding FF stands normal to the c-axis ($k_\omega \perp z$) and the light is propagating in the x-y plane. On the other hand, the orientation of the wavevector within this plane has no impact on the efficiency. Along any propagation direction in the plane the build-up of the SH field depends solely on the PM condition, which is isotropic in x and y since the disorder of the domain structure has no directional preference. Accordingly the position of the non-zero elements in the tensor, it is clear that a linear polarization of the FF along any of the crystal axis will lead to extraordinary polarized SH emission. Ordinarily polarized SH light can only be generated from mixed polarization states of the fundamental, as we will show in a following section.

Planar SHG, k perpendicular to z

Moshe Horowitz and Baruch Fischer studied the broadband SHG in SBN already in the early 90's [Hor93]. Yet the interest in this technique suffered under the rather low conversion efficiency in this material, and the relevance of this approach for ultra-short pulses was not commonly recognised. The more recent development of sources for laser pulses with only femtoseconds duration changes this situation in two ways: one is the need for a broader PM bandwidth for ultra-short pulses, the other is the fact that the concentration of the pulse energy in such a short event leads to extremely high peak intensities.

It is very interesting to shortly review the work done in [Fis08] to briefly explain this kind of interaction. The experimental setup consisted of a femtosecond oscillator providing 150fs long pulses at 76Mhz of repetition rate and 0.5W of average power, which is tunable within the range of 700 to 900 nm. A lens with 50 mm focal length focused the input beam on an

unpoled SBN crystal of the dimensions 5×5×10 mm. All sides of the crystal were polished, allowing the observation of the SH radiation from different directions. The power of the SH emission was measured with a regular power meter, while the spectral properties of the fundamental beam and the SH radiation were monitored by a spectrometer with an average resolution of 0.3 nm.

The fundamental beam is propagating perpendicular to the domain orientation (z-axis) as shown in Fig.2.5(a). All available grating vectors for PM thus lie in the x-y plane, resulting in a SH emission in theoretical all directions of this plane. However, the PM diagram in Fig.2.5(b) makes evident that for an increasing angle between the SH wave vector and the direction of the FF, the reciprocal grating vector **G** has to become longer. This means that the required grating periods have to become smaller, for large angles $\varphi >> \pi/2$ even smaller than the fundamental wavelength.

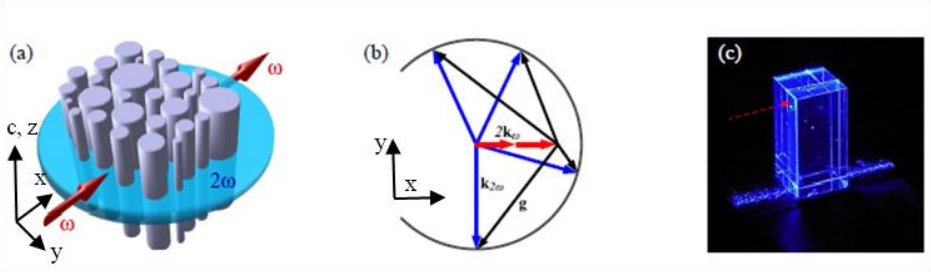

Figure 2.5. SH emission for a beam propagating in the x-y plane of the SBN crystal. (a) Schematic representation of the domain orientation to the FF, leading to the PM condition depicted in (b), where red and blue arrows indicate the fundamental and SH wave vector, respectively, and grey arrows stand for the reciprocal grating vector. The four cases are exemplary only, QPM is given in all direction in the x-y plane. (c) Photo of the SH emission in experiment, where the blue lines are either reflections or scattering of the SH at the sample holder and the crystal facets. The red arrow represents the fundamental beam [Fis08].

Consequently, the SH emission for large φ is due to a higher order processes than the forward PM, leading to a relative weaker SHG. The SH light scattering at the crystal input facet in Fig.2.5(c)(left crystal facet in photo) is forward SH reflected at the crystal output facet (right side). Nonetheless, the photo shows clearly in this case a rather homogeneous distribution of the SH signal in all directions of the x-y plane.

The femtosecond conversion efficiency can be calculated as the ratio of the generated average SH output power and the average input power of the fundamental. The observed maximum efficiency of the SHG process is close to 0.1%. The radiation coming out from the top surface and recorded by the power meter is only a fraction of the whole signal emitted in this plane. Due to the total internal reflection almost half of the generated SH light is trapped inside the crystal and only the emission at the angles 90±23° is collected by the power meter. After accounting for the whole generated SH signal, the total conversion efficiency for the fundamental propagating in the x-y plane is estimated to be about 0.38%.

Conical SHG, k parallel to z

For a FF propagating along or under a small angle to the crystal domain orientation (c-axis), the same two-dimensional modulation leads to a very different PM situation compared to the conditions for a FF propagating in the x-y plane. As it is depicted schematically in Fig.2.6(a), the SH is no longer emitted in a plane but in the form of a cone [Tun03]. The infinite set of reciprocal PM vectors now lies in a plane perpendicular to the propagation direction. The diagram in Fig.2.6(b) shows the effect of the PM condition for a beam propagating exactly in direction of the c-axis: since the available grating vectors are restricted to the normal of the fundamental wave vector, the cone angle φ depends directly on the phase mismatch between the fundamental and the SH wave. Fig.2.6(c) extends this description for small angles α of the fundamental beam with respect of the c-axis. It shows that the axis of the emitted SH cone always coincides with the crystal c-axis, independent of α, the fundamental wavelength or the phase mismatch. However, the cone angle is affected by all of these, as can be seen from the longitudinal and transverse PM conditions that can be written as

$$k_{2\omega}\cos\varphi = 2k_{\omega}\cos\alpha$$
$$k_{2\omega}\sin\varphi \pm 2k_{\omega}\sin\alpha = \left|\mathbf{G}_i\right|.$$

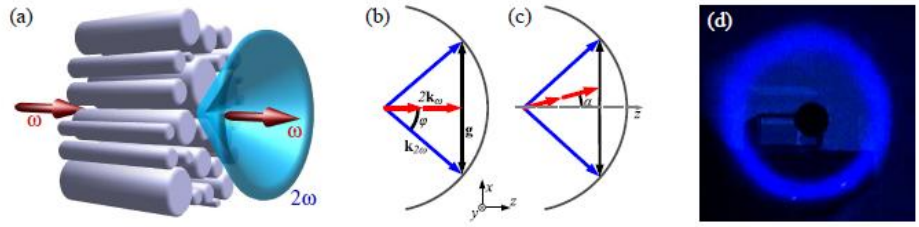

Figure 2.6. Propagation of the FF along the crystal c-axis leads to a conical SH emission. (a) Schematic representation of the SH emission geometry to the domain orientation; (b,c) diagrams illustrating the PM condition for the beam propagating (b) exactly along and (c) under an angle α to the c-axis. (d) Photo of the conical emission in experiment scattered through a thin piece of paper. The black dot in the middle is a metal plate stopping the fundamental beam [Fis08].

Due to the continuous set of grating vectors $\mathbf{G}_i$ in the x-y plane the transverse PM condition is always fulfilled. Furthermore, the homogeneous intensity distribution of the SH cone, which can be seen in the photo of the experiment in Fig.2.6(d), clearly confirms the isotropy of the PM in the disorded structure. Also, due to the radial symmetry of the SHG geometry, the conical emission is always radially polarised [Tun03]. The longitudinal PM condition determines the cone angle. Together with the refraction at the crystal surface, the external cone angle θ has a strong dependence on the fundamental wavelength. To give an example, for a fundamental wavelength of 860nm the full external angle (2θ) measured at low powers is 130°.

After having discussed the two cases for $k_\omega \perp z$ and $k\omega \parallel z$ separately, it should be mentioned that the angle φ increases monotonically with the angle α between the propagation direction of the fundamental wave and the crystal c-axis. Consequently, the cone opens in a gradual transition, until in the extreme case of $\alpha=\pi$, meaning $k_\omega \perp z$, the cone is transformed into a plane.

Planar SHG, noncollinear pumps

Since the PM scheme requires that two photons of the fundamental beam annihilate to generate one SH photon, it is also interesting to study what happens if the two photons are provided with different characteristics, for example at different direction or with different polarization. To implement this idea the following experimental set-up has been used

[Tru07]. A 8 nanosecond Nd:YAG system at 1064nm (repetition rate 10 Hz) was arranged to deliver two beams (denoted as A and B) with total energy of 3 mJ and diameter of 5 mm (FWHM). The beams intersected in the unpoled SBN crystal at the external angle 4º. Due to the extremely long pulse duration compared with the crystal lenght, for our purpose we can see the beams as stationary plane waves. The two beams were loosely focused in the crystal. Beam paths were chosen such that counter-propagating pulses would meet in the central part of the SBN crystal. The polarization orientation of entering beams A and B are controlled by λ/2 wave plates. The geometry of the experiment is shown in Fig.2.7.

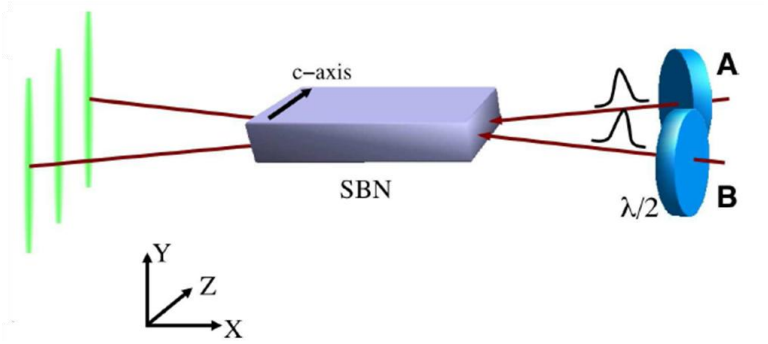

Figure 2.7. Scheme of the experiment in [Tru07].

In Fig.2.8(a) they are shown three photographs of forward emitted SH signals observed in the experiment. The three pictures (left to right) represent the case of 1)extraordinary polarized fundamental beams, 2)perpendicularly polarized fundamental beams (A-extraordinary;B-ordinary) and 3)ordinary polarized fundamental beams. The SH signal is emitted in a form of three well resolved lines. The side lines (numbered 1,3,4,6,7,9) represent SH emitted separately by each fundamental beam. The middle lines (numbered 2,5,8) appear only when both beams A and B are simultaneously present and hence represent the non-collinear SHG by the two beams. The polarization state of each SH lines is indicated as ”e” (extraordinary) or ”o” (ordinary). Note that all but one (line 5) outputs are extraordinary polarized. The presence of this particular ordinary polarized signal defies the previous claims that in SBN crystal only extraordinary SH signal could be generated [Hor93]. This line appears as a result of

$$E_{1A}O_{1B} \rightarrow O_2$$

interaction that is governed by the same component d_{32} responsible for

$$O_{1A}O_{1B} \rightarrow E_2$$

process. However since the phase mismatch for the former interaction is larger the emitted signal is weaker than that of the latter process.

PM conditions for SH signals are shown in Fig.2.8(b). They can be represented in vector form as

$$\mathbf{k}_{1A} + \mathbf{k}_{1B} + \mathbf{g} = \mathbf{k}_2$$

where $\mathbf{k}_{1A}$ and $\mathbf{k}_{1B}$ represent fundamental waves, $\mathbf{k}_2$ is SH and $\mathbf{g}$ is one of the grating vectors provided by the random character of nonlinear medium. As it is seen from the PM diagram, $\mathbf{g}$ vectors have different sizes and orientation, but they always lie in a x-y plane. This is in contrast to single uniform QPM structures with only a fixed set of grating vectors available.

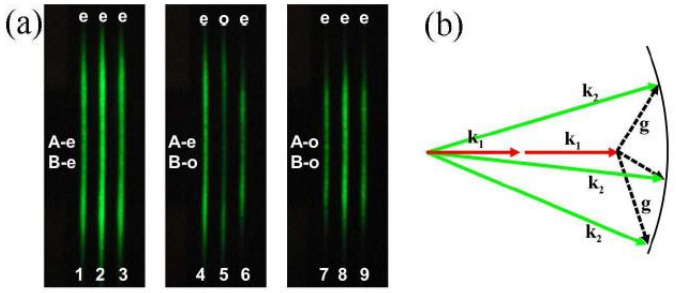

Figure 2.8. (a) SH signal (lines) in the nanosecond experiment obtained for different polarization orientations of the fundamental beams A and B. (b) Illustrative diagram of the PM conditions for generation of the SH scattered light (single beam case); g are grating vectors that compensate the bulk phase mismatch [Tru07].

Due to the randomness of the SBN media a pool of grating vectors with different magnitudes and orientations are available for PM. This enables PM in extremely broad wavelength range and SH emission in broad angular range as it seen in the photos in figure Fig.2.8(a). The angular distance between the maxima is of the order of 10 degrees. Moreover, this continuum of infinite number of grating vectors allows simultaneous PM of several SH processes. For instance in Fig.2.8 we observe simultaneous PM of collinear and non collinear processes. It has also been shown that the polarization

properties of these processes can be used to determine the relative strength of two relevant components of the second order nonlinearity d_{32}/d_{33} [Tru07].

2.3. The role of ferroelectric domains structure

Recent experiments with random domain SBN crystals demonstrated that the emission pattern of the generated waves may differ drastically from sample to sample, being either spatially homogeneous or exhibiting distinct intensity peaks (see for example Fig.2.5 and 2.8) [Fis06, Tru07]. This behavior points towards the difference in the actual distributions of ferroelectric domains in different samples. Observations of random domains ranging from tens of nanometers to few microns have been reported in the literature [Ter02, Shv08, Gai09, Rom02,]. Moreover, it has been even suggested that the domain walls induced light scattering of the fundamental wave plays significant role in the SH generation [Mol08]. In order to obtain a better understanding of the nonlinear interaction in random media, in this section we study theoretically and numerically the role of the domain distribution on the efficiency and transverse characteristics of the SH emission in a quadratic random crystal. The numerical simulations obtained are supported by our experimental evidence of the SH emission.

Modeling random ferroelectric domain pattern

We have developed a model to describe and simulate our quadratic crystals with random 2D ferroelectric domain distribution, considering the domains as *building blocks*. We follow the characteristics of the experimentally reported structures in SBN crystals [Gai09, Mol08].

To mimic the process of domain formation we adopt the following strategy. Firstly, we assume that the individual domains (our building blocks) have form of rods with a circular transverse profile. While the assumption about circular shape follows from the experimental observations [Rom01], it is in fact not that critical because, as we see below, the

macroscopic pattern of nonlinearity distribution consists of regions of opposite sign of the nonlinearity which may have very complicated (not necessarily circular) shape. As we consider light propagation and emission in the plane perpendicular to the longer dimension of the domain only their transverse structure is taken into account here. A Gaussian distribution of the domain sizes is chosen with a certain mean diameter (ρ_0) and variance (σ). Using this distribution a number of domains is randomly generated and randomly placed in a rectangular area representing the size of the sample. In all the cases discussed here at least two thousand domains were used to create a random domain pattern. The domains number that takes part in the process may depend on the geometry of the interaction. As a rule of thumb this number should be large compared to the actual size of the input optical beam [Leg01].

In the next step we randomly assign at each domain a particular sign of the nonlinearity (positive/negative). Some particular 2D domains patterns for different choice of statistical parameters are shown in Fig.2.9(top left) and in the top row of Fig.2.10. The black and white colors denote the antiparallel oriented domains with opposite signs of the quadratic nonlinearity. These kind of generated patterns are then directly used in the numerical simulations.

A completely random assignment leads sometimes to large agglomeration of domains with the same sign of the $\chi^{(2)}$ nonlinearity. This agglomeration leads to artificial small G vectors in the reciprocal space. In Fig.2.9 (top left) we depict a typical case of domain pattern where large areas of domains agglomeration occur (for example as indicate in the red circles). These areas act effectively as a single domain distorting the real distribution. In Fig.2.9 (top right) we depict its relative spatial spectrum. The white circle indicates the place where the G vectors should be more gathered considering the nominal mean domain value (indicated by “a” in this case). It is clear from this picture that the G vectors of the structure are in general much smaller than the expected value. This effectively corresponds to larger spatial oscillation of the sign of the $\chi^{(2)}$ distribution. In the same figure (bottom row) we also show two different possibilities to describe this domain pattern with a bar chart. In the first case (left) the

number of domains while in the second case (right) the *area of the domains* as a function of the domain width are considered. The two bar charts give two different outputs starting from the same domain distribution. This is a clear example of the inadequacy of this method to describe this kind of structure.

To avoid the negative effect of the domain agglomeration, and to create structures with very fine domain pattern, the sign of each particular domain was assigned taking into account the signs of its closest neighborhood, such as in Figs.2.10(a) and (b). The algorithm implemented here integrates the area close to the domain under study; if in this area there is a prevalence of positive $\chi^{(2)}$ sign, a negative sign will be chosen and vice versa. As a comparison, in Fig.2.10(c) it is also reported the same domain distribution as in Fig.2.10(b) but allowing some degree of agglomeration. The non occupied zones among the domains are considered to form the domain walls and they amount to around 10% of the whole area of the sample which is in agreement with the experimental observations in similar poled structures [Ale96]. In the region of the domain walls the nonlinearity is assigned a null value. However, we allowed in this region for a small linear refractive index change of the order of 10^{-3} to account for the strong discontinuity of the vector of spontaneous polarization [Ale96, Woi01]. This weak linear index variation will produce a linear scattering of light. We will talk about this effect later in this section.

The insets in Fig.2.10(a) and Fig.2.10(b) depict corresponding histograms of the domain size and correspond to the following parameters: (a) ρ_0=0.3μm, σ=0.05μm; (b) ρ_0=0.3μm, σ=0.1μm. Such histograms were previously used to characterize actual samples of as grown SBN crystals with disordered domain pattern [Mol08] but do not contain all the needed information on the distribution. For example, it is not possible to retrieve the distribution of the sign of the nonlinearity. Moreover, as we already have shown before, the histograms can be ambiguous since it is possible to choose either the diameter or the area of the domains as discriminating parameter. Moreover notice how, starting from the same statistical parameters, it is possible to draw two completely different random patterns (Fig.2.10(b,c)) by either allowing or avoiding the agglomeration.

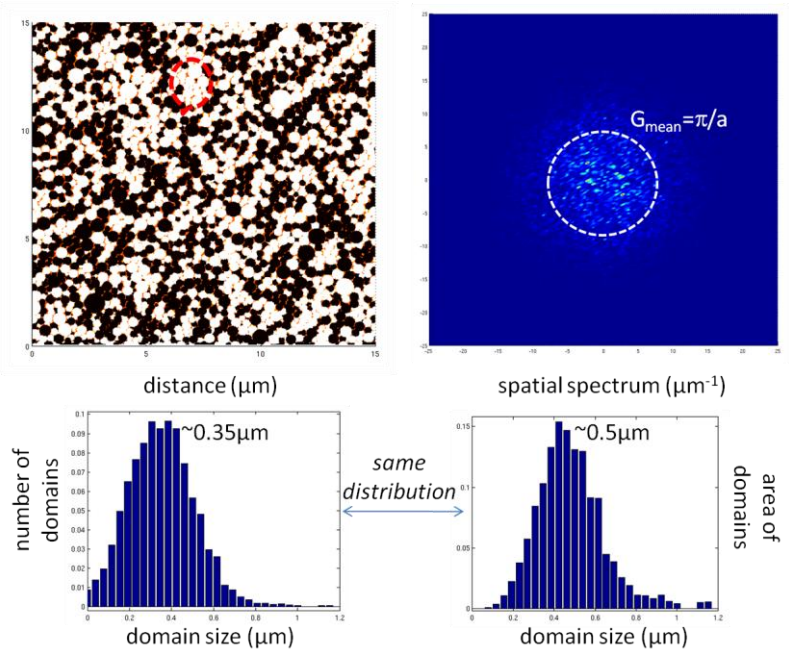

Figure 2.9. (top left) Example of domain distribution with strong agglomeration of domain with the same sign of nonlinearity (marked in red). (Top right) Spatial spectrum indicating that the spatial periodicities possessed by the structure are smaller than the nominal one. (Bottom row) Two different realizations of bar charts of the same structure.

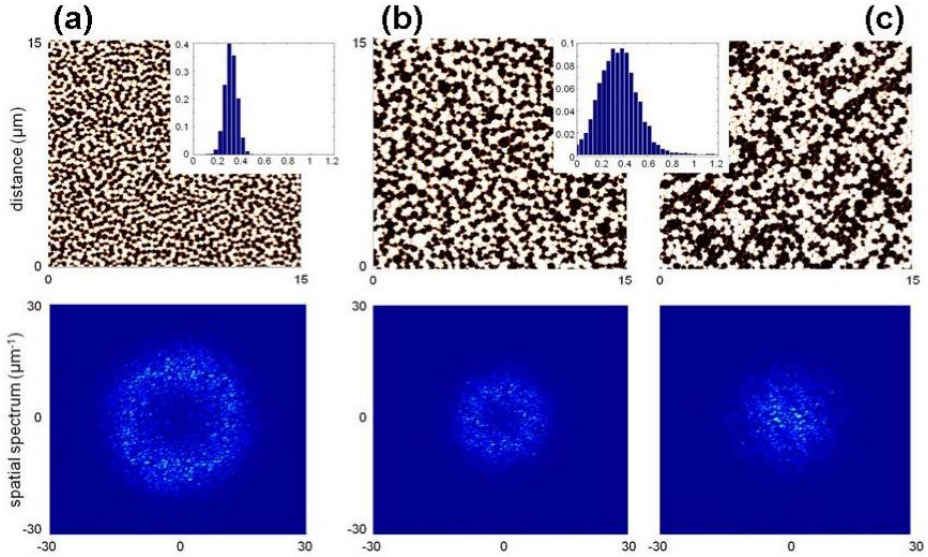

Figure 2.10. Examples of particular realizations of the random domain pattern. (a) ρ_0=0.3μm, σ=0.05μm, (b) ρ_0=0.3μm, σ=0.1μm, (c) ρ_0=0.3μm, σ=0.1μm with agglomerations of the domains. The insets depict histograms of the resulting domain diameters. Bottom row: corresponding spatial Fourier spectrum of the domain patterns. Note that the agglomeration of domains shown in (c) results drastically changes its spatial Fourier spectrum and hence will have a strong impact on SH emission.

SH emission forecast

In order to fully characterize the domain pattern as a QPM nonlinear photonic structure we use the spatial Fourier spectrum of the nonlinearity distribution. Such spectrum represents the domain of reciprocal vectors $\mathbf{G}$ which will be employed to fulfill the PM condition $\mathbf{k}_2 - 2\mathbf{k}_1 - \mathbf{G} = 0$ which determines the direction and efficiency of the quadratic process. Here $\mathbf{G}$ can be expressed as $\mathbf{G} = (2\pi/\Lambda)\ \mathbf{n}$ where Λ represents periodicity along the generic direction $\mathbf{n}$. In this particular case we can consider a *virtual* periodicity made by two adjacent domains with a different sign of the nonlinearity.

In the bottom row in Fig.2.10 we depict the modulus of the square of the Fourier spectrum corresponding to the domain patterns shown in the top row. In these graphs the strength of the spectral components is directly represented by their brightness. It is clear that different domain distributions lead to drastically different structure of the reciprocal space which, as we will show later, will subsequently affect the SH emission. This property has been used to control the shape of the generated SH beam in specially designed structures [Qin08, Ell09]. As it is clear from the bottom row of Fig.2.10(a,b), a real spatially random domain pattern leads to a circularly shaped Fourier spectrum. The radius of the circle will be directly related to the mean domain size and its width from the radius will be related with the standard deviation. In particular, domain distributions with narrow (broad) standard deviation lead to the correspondingly narrow (broad) width of the reciprocal distribution of the $\mathbf{G}$ vectors. Domain distributions with small (big) mean domain size lead to the correspondingly large (small) radius of the circular distribution. As comparison, the bottom row of Fig.2.10(c) depicts the spatial Fourier spectrum of the distribution with large rate of domains agglomeration. Here the structure consists effectively of large area domains of the size of the agglomerated areas, and consequently its spatial spectrum shrinks toward very small components.

In order to see how the particular nonlinear structures affect emission of the SH we need to consider the PM condition. In Fig.2.11 we plot the three particular scenarios associated with the random domain structures.

The green circle represents possible directions of the SH k-vector while the yellow ring represents the more considerable region of the reciprocal vectors **G** provided by the randomness of the domain pattern. As the pattern is isotropic so is the distribution of the **G** vectors.

The most efficient SH emission is expected to occur in the directions determined by the intersection of the green circle and yellow ring where the PM conditions are fulfilled with the stronger coefficients of the reciprocal spectrum. It is clear that, because of availability of isotropically oriented **G** vectors, the generation of the SH is expected to be non-collinear and with a broad spatial distribution of the intensity.

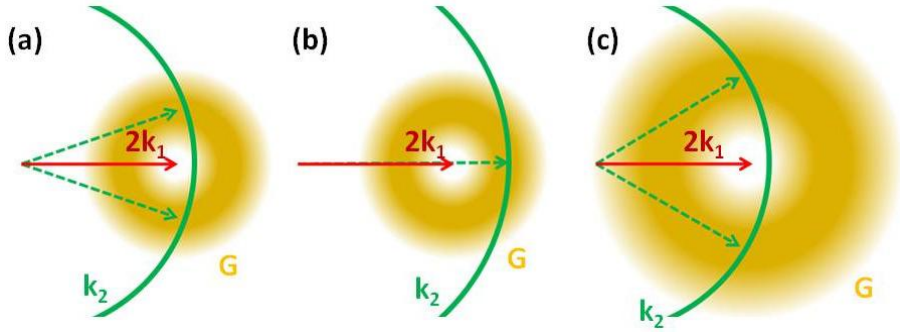

Figure 2.11. Diagram illustrating few possible scenarios of the PM condition for the SH emission in medium with disordered ferroelectric domain structure. Dashed green arrows indicate possible directions of strong emission of SH. (a-b) same disordered domain distribution, different wavelengths of the fundamental wave λ_F (λ_F is shorter in case (b)); (c) random domain distribution with the mean value significantly smaller than in cases (a-b)

The two cases shown in Fig.2.11(a-b) correspond to identical domain pattern but they differ in the wavelength of the fundamental wave. Hence, in the first case (a) the SH is expected to be emitted predominantly in two angular directions. On the other hand the same structure used with shorter fundamental wave (as in Fig.2.11(b)) should lead to mostly forward emission centered around the direction of the fundamental wave. Finally, the domain pattern with much smaller average size is expected to lead to strongest emission oriented at large angles as in Fig.2.11(c). As the geometric regions of the strongest PM shown in these three examples differ significantly one may expect this property to be reflected in the SH emission pattern. However, the actual spatial intensity distribution of the generated SH wave

will be determined not only by the PM condition but also by the strength of the nonlinearity for the particular emission direction which is strongly affected by the randomness of the system.

In order to explore this further we employ the statistical approach of Dolino [Dol72] and Le Grand [Leg01]. In this approach the intensity of the SH wave generated in the medium consisting of randomly distributed antiparallel domains can be expressed as

$$I_{2\omega} \propto I_{\omega} d_{eff} f(q, \rho_0, \sigma) \tag{2.1}$$

where I_{ω} is the intensity of the fundamental wave and d_{eff} is the effective $\chi^{(2)}$ nonlinearity which depends on material parameters and geometry of the interaction. The function $f(q, \rho_0, \sigma)$ represents the effect of disorder in the domain distribution

$$f(q, \rho_0, \sigma) = \frac{4L}{q^2} \cdot \frac{1 - e^{-\rho_0^2 \sigma^2}}{1 + e^{-\sigma^2 q^2} + 2\cos(q\rho_0) e^{-\sigma^2 q^2/2}}. \tag{2.2}$$

where L is the propagation distance and $q = |\Delta k|$ is the absolute value of the phase mismatch. The linear dependence of $I_{2\omega}$ on propagation distance is the signature of disorder which makes the process of SH build-up to be incoherent [Ray04, Mor01, Mor04, Shu08]. As the phase mismatch parameter q is in our geometry of interaction uniquely linked to the angle between propagation direction of the SH and fundamental waves, the relation (2.1) provides, in fact, angular distribution of the SH intensity.

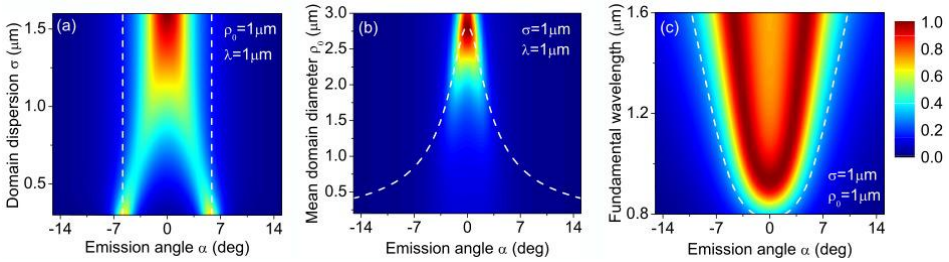

Figure 2.12. Theoretically predicted angular distribution of the SH emission in the quadratic crystal with random domain distribution (Eq.(2.1)). (a) constant average domain diameter ρ_0=1μm, (b) constant dispersion σ=1μm. In all simulations we assumed λ_F =1μm. (c) The effect of varying of the wavelength of the fundamental wave on the emission angle of the SH. Here ρ_0=1μm and σ=1μm. In all graphs the dashed line represents phase PM with a single reciprocal vector $|\mathbf{G}_{mean}| = \pi/\rho_0$.

The contour plots in Fig.2.12 illustrate the relation Eq.(2.1) as a function of emission angle and/or statistical parameters of the domain distribution. From Fig.2.12(a) it is evident that for low domain dispersion the structure is almost perfectly periodic leading to very directed transverse emission determined by the PM condition which in this case is satisfied in two particular directions of the SH. As the domain dispersion increases the more **G** vectors contribute towards the PM which results in a forward emission of the SH. Plot in Fig.2.12(b) illustrates the effect of the mean value of the domain diameter. For fine domain pattern (at given dispersion) many **G** vectors participate in the SH generation leading to very broad emission. As the average domain diameter increases the SH emission becomes less spread approaching the forward emission for large ρ_0. Finally, in Fig.2.12(c) we demonstrate the effect of varying the wavelength of the fundamental wave on the SH generation. In this particular example $\rho_0 = \sigma = 1\mu m$.

The dashed line in all graphs in Fig.2.12 represents emission of the SH determined solely by the PM condition taking into account only one reciprocal vector

$$|\mathbf{G}_{mean}| = 2\pi / \Lambda = 2\pi / 2\rho_0 = \pi / \rho_0$$

corresponding to the mean diameter of the domains. It is clear while this simplified approach is sufficiently accurate for weak disorder it leads to erroneous results for high degree of randomness of the periodic structure. In addition it cannot be used to determine the spatial distribution of the emitted SH.

Numerical simulations

To test the above discussed analytical predictions we resorted to numerical simulations of SHG in random domain structures. We numerically solved the Maxwell`s equations assuming that the random quadratic medium (for example as in Fig.2.8 or Fig.2.9) is illuminated with a Gaussian fundamental pulse. We used the material parameters which correspond to those of as-grown SBN crystals [Woi01]. For example at

800nm and 1064nm the indexes of refractions are n_{ext}=2.25 and 2.22, for the extraordinary polarization, and n_{ord}=2.28 and 2.25, for the ordinary one.

It should be stressed here that Vidal and Martorell [Vid06] were perhaps the first ones to investigate numerically SH emission in multi-domain crystal. They considered only 1D structure and used the matrix transfer approach. Our simulations of full Maxwell equations were conducted using optical pulses and finite beams in two dimensional medium. Therefore we could describe SH emission at arbitrary angle and did not have to perform statistical averaging in order to obtain relevant physical quantities such as the energy of the generated waves.

To simulate the light propagation through SBN crystal we use the numerical model discussed in the Chapter 1. Contrary to the most common nonlinear numerical codes, the one implemented here is able to solve the complete 2D vectorial Maxwell's equations in the time domain without SVEA. For this reason all angles of propagation and/or diffraction are allowed. Furthermore, no undepleted pump approximation is used.

A number of numerical simulations have been performed with different working conditions. The fundamental pulse length in the plane of the nonlinear domain was in the range 6-30 optical cycles. We varied the fundamental wavelength from 790nm up to 1550nm. The data for the index of refraction were obtained fitting the Sellemier's equation with the coefficient as in [Woi01] to a general Lorentz curve. In Fig.2.13 we show the results of some of these simulations obtained assuming the λ_F=800,1064nm. In this figure the plots in the left column depict the spatial intensity distribution of the fundamental and generated SHs for three different random samples. The statistical parameters of the domain distribution are: (b) ρ_0=3μm, σ=0.3μm, λ_F =1.064μm, here the sample is bigger to arrange an enough number of domains; (c) ρ_0=0.9μm and σ=0.1μm, λ_F =1.064μm; (d) ρ_0=0.3μm and σ=0.05μm, λ_F =0.800μm.

Middle column shows the transverse structure of the fundamental and SHs in the spatial Fourier space (or equivalently, in the far field) and the plots in the right column depicts the energy of the fundamental and SHs as a function of the time of propagation. In the Fig.2.13(a) is depicted the typical propagation of the fundamental pulse. Initially located in the air, it

impinges normally in the sample. Due to the index mismatch, part of the pulse is backward reflected and the remaining is forward propagating in the material. The k-spectrum of the fundamental field shows a very narrow peak with coordinates $k_x = 2\pi/\lambda$ and $k_y = 0$ during the first part of the propagation in the air and $k_x = 2\pi n(\lambda_F)/\lambda_F$ and $k_y = 0$ after entering in the material, where $n(\lambda_F)$ is the index of refraction at the fundamental frequency.

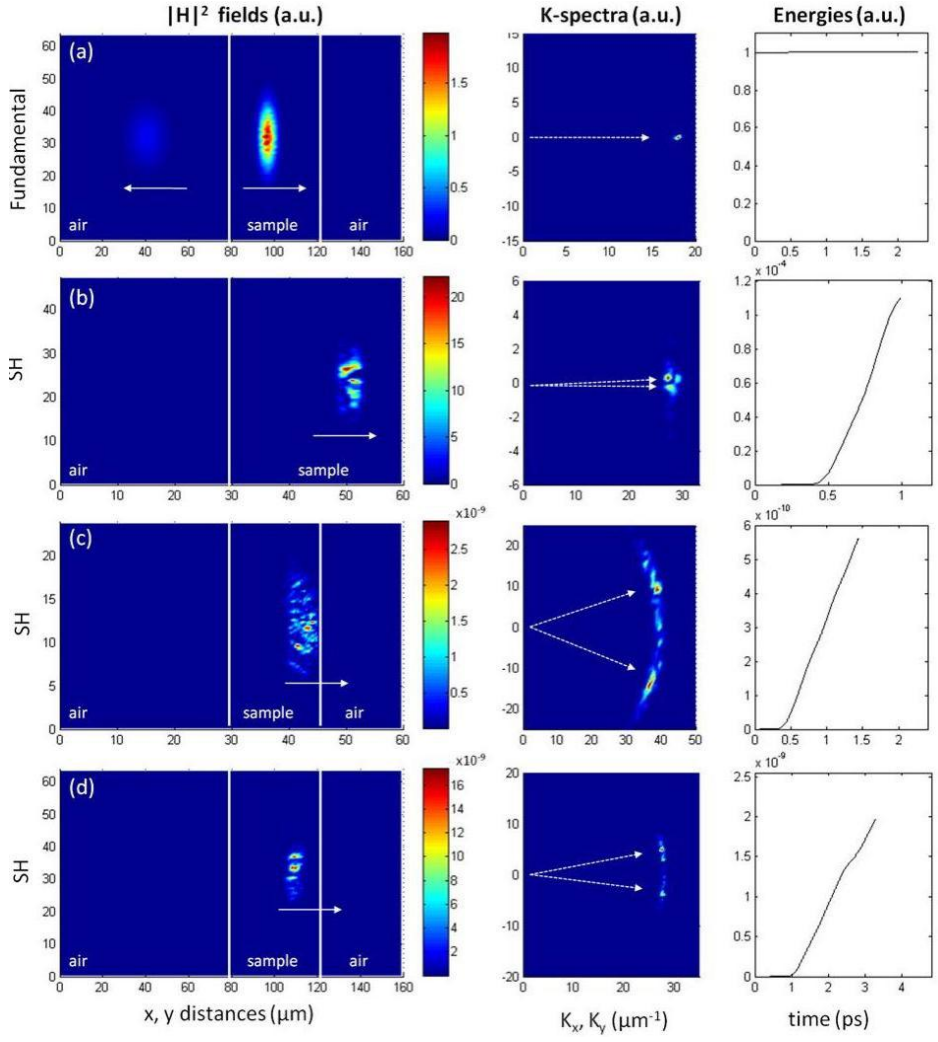

Figure 2.13. Numerical simulations - generation of the SH by a femtosecond laser pulse in a disordered structure. Left column: Spatial intensity distribution of the fundamental (a) and SHs (b-d) for three different random samples in three different numerical simulations. Middle column - the structure of the interacting waves in the spatial Fourier space. Right column - energy of the fundamental and SHs as a function of the time of propagation.

Since the efficiency of the nonlinear process is low, the energy of the fundamental is practically constant during the propagation in the SBN.

The graphs in Fig.2.13 demonstrate dramatic variations in the far field of the emitted SH depending on the characteristics of the domain pattern. Note the differences in the emission angles in cases (b), (c) and (d) which correspond to the domain distributions from large to small average domain sizes, namely 3, 0.9 and 0.3μm. The angular distribution of the intensity of the generated SH fields reflects the spatial distributions of the domains. As expected, the energy of the generated SH clearly displays a linear-like growth. This is indication of the incoherent character of the build-up of the SH and is in full agreement with earlier experiments and theoretical prediction [Ray04, Mor01, Mor04]. The difference in the maximum reached values of the SH fields and energies is due to the different input intensities of the fundamental as initial condition. For example, in the simulation in Fig.2.13(b) the input intensity is three orders of magnitude higher than the simulation in Fig.2.13(c).

The full investigation process for all the distributions considered consisted in four steps (Fig.2.14):

1. We firstly generate the domain distribution fixing ρ_0 and σ. Bar chart and spatial spectrum are recovered (a);
2. With the G distribution obtained in the spatial spectrum we make a forecast on the SH angle of emission θ_{mean}. This is done simply using the PM relation and the algebraic cosine law (b)

$$\cos\theta_{mean} = \frac{k_{2\omega}{}^2 + (2k_\omega)^2 - G_{mean}^2}{2k_{2\omega}(2k_\omega)};$$

3. We feed the complete spatial domain patter into the Maxwell's equations and numerically simulate the complete SH emission distribution (c);
4. Finally we test experimentally and record the SH emission from the real sample (d).

From the comparison among the analytical forecast, numerical results and experimental recorded signals we are able to determine with a good level of confidence the actual domain distribution characteristics possessed by the sample.

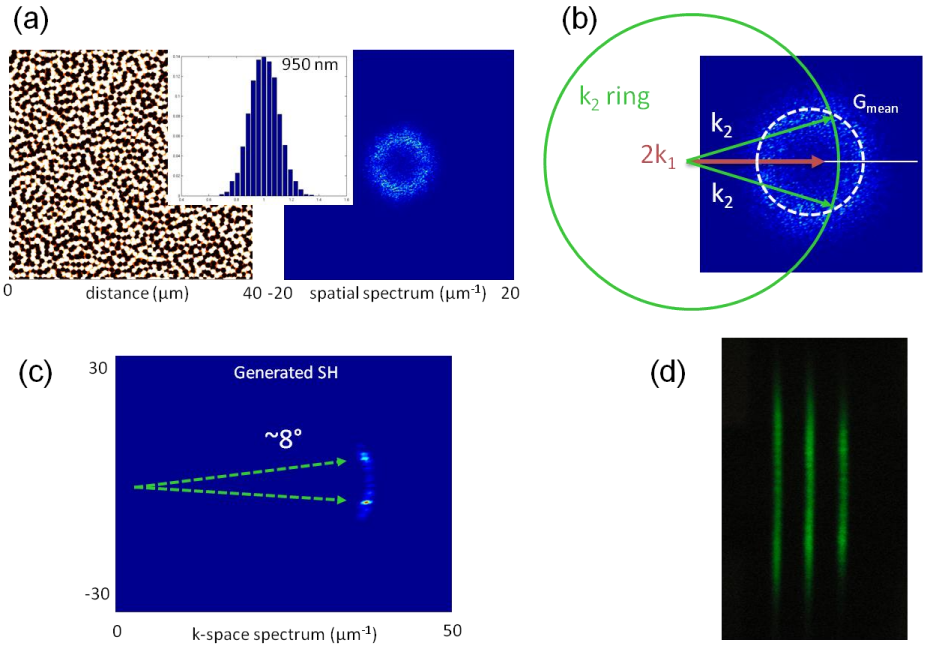

Figure 2.14. Full investigation step. (a) Design of the domain pattern; (b) forecast of the emission using the PM relation; (c) Numerical simulations of SHG; (d) Experimental verification.

In Fig.2.15 we report more examples of the generated SH. In these three cases we directly compare the spatial characteristic of the structures (on the left) with the generated SH signal (on the right). Notice how the changes in G distribution directly affect the generation of the SH. In all the three cases the domain mean value is practically the same. Thus it is possible to verify how this method is also able to appreciate the difference in the SH emission due to the variation of the parameter σ.

Comparing the numerical simulations with the analytical predictions, Eq.(2.1), we find them in very good agreement. Therefore the simple statistical approach appears to be a powerful tool in predicting spatial distribution of the generated harmonic in media with disordered domain structure. This suggests that experimental observation of SH pattern can be employed to obtain information about the degree of the disorder of the ensuing domain structure. This aspect is currently being experimentally investigated.

To give an idea of the power of this method, as it follows from the results of this study we can evaluate that to have SH light propagating at

the transverse and backward directions the sample needs to possess nonlinear domains at least of the order of 10-50nm. This consideration is very important as far as the choice of the domain visualization technique with appropriate resolution is concerned [Soe05].

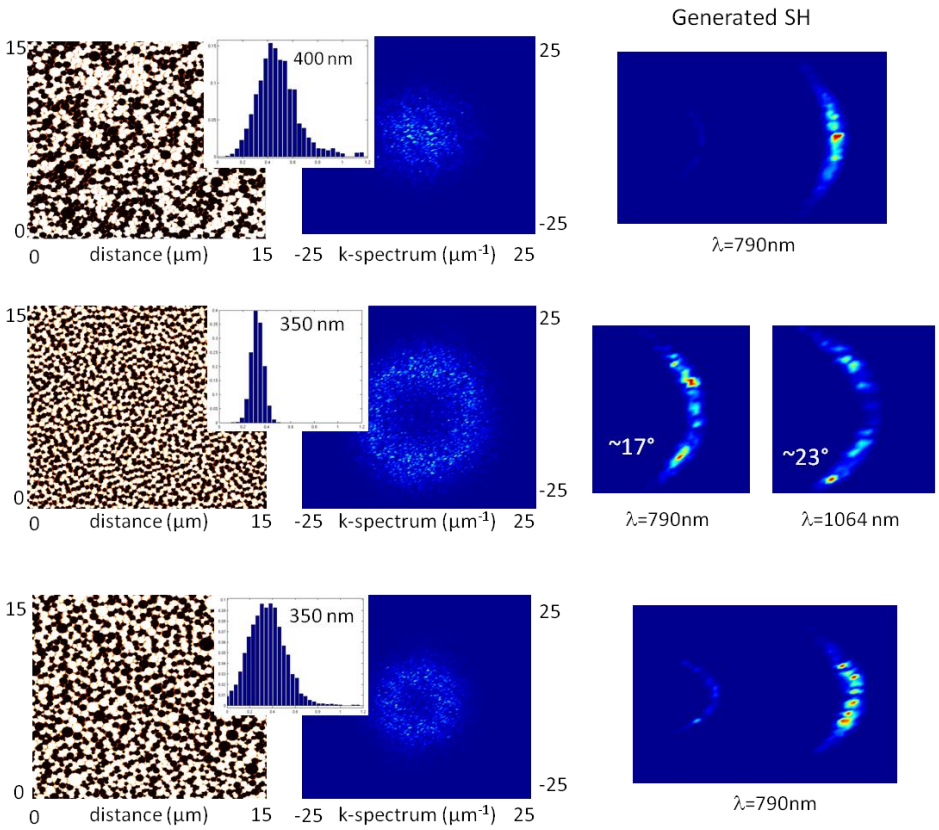

Figure 2.15. Numerical SH generation (right) from different structures (left) at different wavelengths. Since the mean domain value is practically unchanged, the differences in the SH emission are due to the different value of the parameter σ.

Finally, we would like to comment on the role of the light scattering on the SH emission. Due to the discontinuity in the direction of spontaneous polarization between domains a small jump of the linear index of refraction is present in the area of the domain walls. For instance, according to [Woi01] this index modulation is $\Delta n_{\lambda=852nm} = 1.0\times10^{-4}$ and $\Delta n_{\lambda=404nm} = 2.6\times10^{-3}$. Obviously the strength of light scattering induced by the domain walls will be at least one order of magnitude weaker for infrared than for visible light.

Thus, the SH light will always experience stronger scattering than the fundamental wave while propagating in the same sample.

It has been suggested before that the wide angle emission of the SH in experiments with multi-domain SBN crystals could be attributed to the emission of the SH signal by scattered fundamental beam [Mol08]. To test this hypothesis we included the effect of index variation in the domain walls in our numerical simulations. In fact all graphs depicted in Fig.2.13 have been obtained assuming the index jumps at fundamental frequency of $\Delta n = 0.01$. No appreciable effect in both fundamental beam nor the SH has been observed. This confirms that the transverse emission of the SH is caused solely by the spatial modulation of the nonlinearity resulting from the random domain pattern. However, it should be stressed that in the situation when the strong scattering of the SH is present it may indeed affect its overall intensity distribution.

Chapter 3

Cascading THG in disordered nonlinear domains structures

3.1. Introduction

Theoretically, the frequency limitations of SH and/or TH generation processes are only set by the crystals transparency. A peculiarity of ferroelectric crystals is the fact that they possess a very wide transparency window. For the case of SBN it ranges from λ=0.4μm to approximately 4 or 6μm (the specifications of manufacturers differ in this point); in Fig.3.1 it is plotted the measurement of the absorption within the range of our interest.

This characteristic of SBN made it possible to easily tune our IR laser at 1500nm wavelength and to observe TH generated at 500nm.

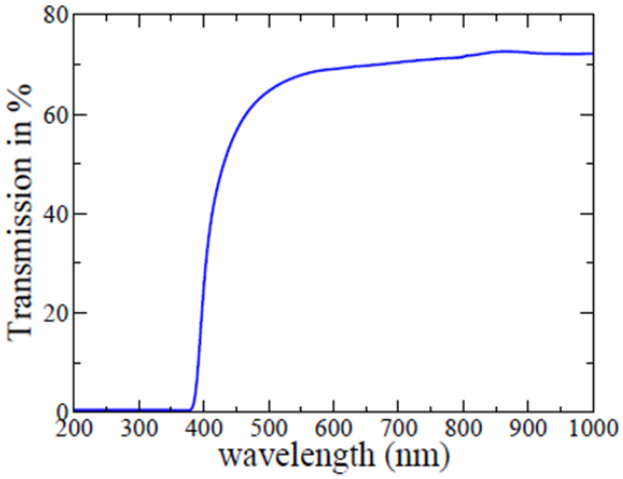

Figure 3.1. Trasparency window of SBN [Fis08].

It has been previously demonstrated that periodically poled quadratic nonlinear media can be used in THG. The process is not a $\chi^{(3)}$ THG, but it is based on cascading of two quadratic effects: SHG followed by sum frequency mixing [Pfi97, Sal05, Fuj07, She09]. Because these two independent processes have to occur at the same time, two different PM conditions should be satisfied simultaneously. Obviously, this requires prior knowledge of all involved wavelengths, in order to manufacture a desired structure. For such application working with a random quadratic medium is an advantage since it will automatically PM any parametric process simultaneously, provided the degree of randomness is high enough.

In this section we present what it is, to our knowledge, the first quantitative and systematic experimental analysis on cascaded THG in unpoled SBN crystals with disordered ferroelectric domain structure. Actually, the first observation of THG in such medium has been reported by Molina *et al.* [Mol08] but since the generated signal was very weak only qualitative observations were conducted. In our case, thanks to the surprisingly high intensity signal we experimentally recorded, we could make a detailed study on the TH emitted properties. We discuss the spatial

distribution of the generated TH signals, as well as their polarization properties and compare them with the theoretical model.

We worked in both collinear and noncollinear set-up to cover a big portion of the experimental possibilities. The last but not the less important reason to investigate the THG is the fundamental importance that the influence of a *quadratic* nonlinear perturbation can play with a *cubic* material response.

3.2. Collinear setup

Esperimental set-up

In Fig.3.2(a) is sketched our experimental set up. The source is a fiber laser providing a 400fs pulse at a wavelength of 1500nm. The measured peak power reaches a value of 20kW at 5MHz repetition rate. The half waveplate (WP) has the function of linearly polarize the beam. The input polarization of the beam can be varied from ordinary to extraordinary by adjusting the WP. The beam is focused by an 8cm focal length lens (L) onto the face parallel to the c-axis of a sample of unpoled SBN crystal. A band-pass filter (BPF) separates the fundamental beam and its harmonics so their corresponding powers and spatial intensity distribution can be measured and recorded onto a CCD camera from the screen located 22mm behind the crystal. In addition, a polarizer (P) enables measurements of the ordinary and the extraordinary components of the generated harmonics.

When the linearly polarized fundamental beam is launched into the SBN crystal, the SH and TH beams are readily observed. We chose the extraordinary polarization since the efficiency here is maximum (see the previous sections). However, the random character of the ferroelectric domain distribution results in low conversion efficiency for both harmonics. For an average fundamental input power of 27mW, the powers of the SH and the TH are 40μW and 11nW, respectively. We have measured the dependence of the power of the TH as a function of the power of the

fundamental beam. The results are depicted in the plot in Fig.3.2(b). As expected, the experimental points follow faithfully the cubic fit (solid red line). It is worth stressing here that in order to determine possible contribution of the direct THG via the third order nonlinearity we run a test experiment using a single domain SBN crystal. Such SBN crystal has symmetry inversion, thus $\chi^{(2)}=0$.

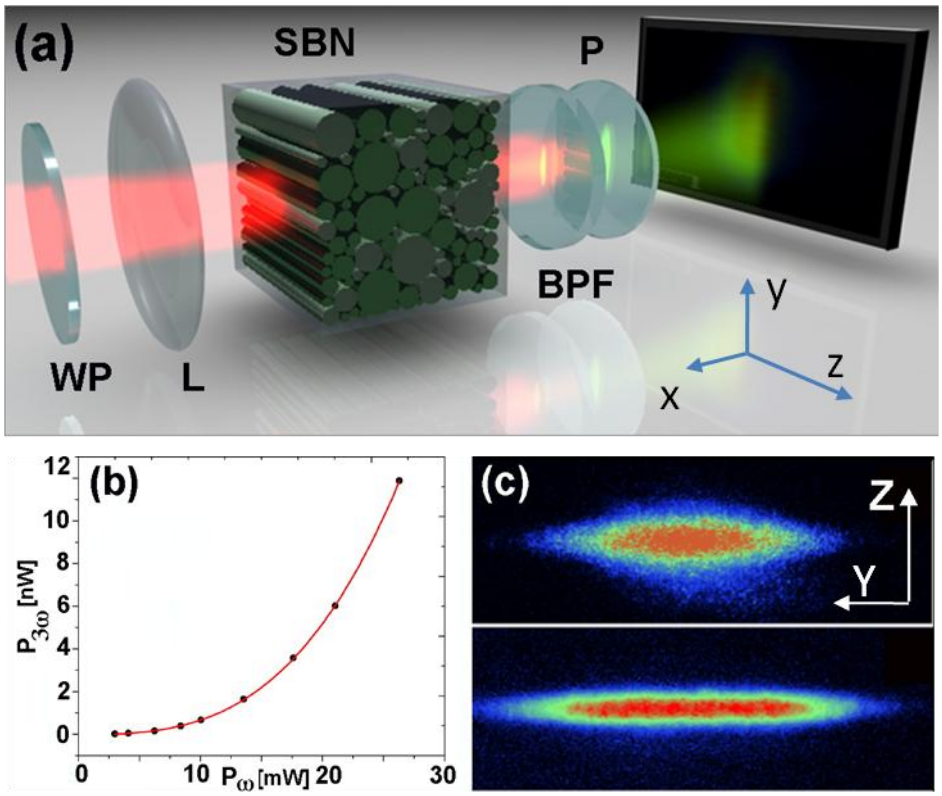

Figure 3.2. Schematic of the experimental setup. The multi-domain structure of the SBN sample is schematically shown. L lens, WP half wave-plate, BPF band pass filter, P polarizer . (b) Power of the third harmonics vs. the input power of the fundamental beam (measured with Ophir Laser Power Head PD300-UV, accuracy ±3%). Solid line represents a cubic fit. (c) Experimentally recorded transverse intensity distribution of the second (top) and third (bottom) harmonics.

The TH generated from this crystal can only come from a $\chi^{(3)}$ effect because there is not cascaded THG. Since *no third harmonic signal had been detected* under the same experimental conditions we are confident that the observed TH emission in a random domain SBN was indeed only a result of the cascaded $\chi^{(2)}$ process. The images in Fig.3.2(c) depict the spatial light

intensity distribution of both, SH and TH beams (for an extraordinary polarized fundamental wave). As the emission region is small (hundred microns) compared to the crystal-screen distance, these images represent the far field (or spatial spectrum) of the emitted waves. It is clearly visible that compared to the SH, the TH trace is narrower along the vertical (z or c) axis but at the same time broader along the horizontal (y) axis.

Phase matching relation

While the narrowing of the TH intensity can be attributed to the smaller spatial overlap between the fundamental and the SH waves, the elongated y-trace is directly related to the domain randomness and its role in the PM process. To explain this let us first recall that the formation of the TH is a result of two cascaded quadratic processes: SHG

$$E_{2\omega} \propto \hat{d}_{eff}^{(1)} E_{\omega}^{2} \tag{3.1}$$

and sum frequency generation in which the TH of the input field is formed by mixing of the fundamental and SH waves:

$$E_{3\omega} \propto \hat{d}_{eff}^{(2)} E_{\omega} E_{2\omega}, \tag{3.2}$$

where $\hat{d}_{eff}^{(1)}$ and $\hat{d}_{eff}^{(2)}$ represent the effective nonlinearity of the SBN for the constituent processes. These processes involve simultaneous fulfillment of two PM conditions which are schematically illustrated in Fig.3.3. The random domain distribution provides a broad set of reciprocal wavevectors ($\mathbf{G}_m$ - formally determined by the Fourier spectrum of the domain structure) that are used to PM the SHG (Fig.3.3). These vectors are represented in the graph by the orange disk with the dashed-line circle representing the mean value of the $|\mathbf{G}_m|$ distribution. Then the PM condition is satisfied in the area of intersection of this disk with the green ring representing the spatial direction of the wave-vector of the SH $\mathbf{k}_{2\omega}$. As a result, the generation of the SH is non-collinear with broad spatial distribution of the intensity. The second constituent process involves the interaction between the directed fundamental beam and the already spatially distributed SH. The angular emission of the latter is now determined by the intersection of the big circle (with the radius $|\mathbf{k}_{3\omega}|$) with a disk of the reciprocal vectors $\mathbf{G}_m$. Since the randomness contributes to both cascaded processes by providing the

reciprocal $\mathbf{G}_m$ vectors, the resulting spatial distribution of the generated TH is broader than that of the SH (angle $\phi_3 > \phi_2$). It should be stressed here that because of randomness of nonlinearity the above described generation of SH and TH can be realized for broad spectral range of the fundamental wave. This was confirmed in different experiments with fundamental wave in the range 1200nm - 1550nm.

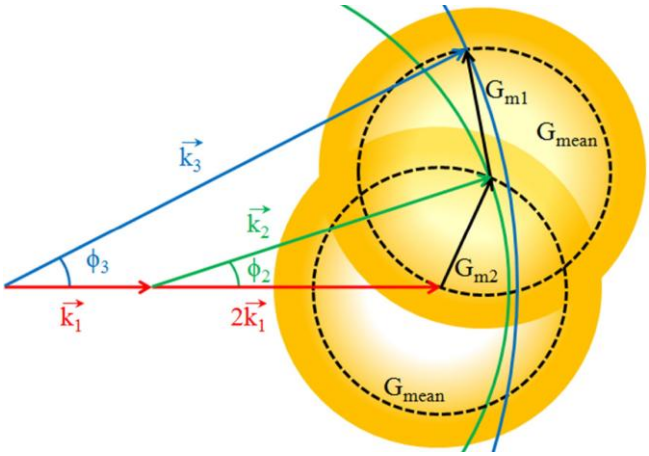

Figure 3.3. Diagram of the PM for cascaded THG in random SBN crystal. Reciprocal vectors G_{m1} and G_{m2} phase match the SH and TH generation, respectively. Note the broadening of the emission angle for the THG.

Polarization properties

Next we study the polarization properties of the emitted harmonics. To this end we record the power of both ordinary and extraordinary components of generated SH and TH as a function of the azimuthal angle α. The results of this measurement are shown in Fig.3.4, where the experimental data is represented by dots and triangles. The graph in Fig.3.4(a) shows the power dependence of the extraordinary component of the SH. Interestingly, in our experiments the ordinary component of SH is negligibly weak hence, the SH is always extraordinary polarized. On the other hand, the TH contains both, ordinary and extraordinary components. Their dependence on polarization of the fundamental wave is displayed in Fig.3.4(b). Clearly, the strongest SH and TH signals are recorded for an extraordinary fundamental wave. The ordinary generated TH is approximately eight times smaller for the same input power. The solid

curves in both graphs represent the theoretical predictions which are obtained by considering all possible processes contributing towards the generation of SH and TH.

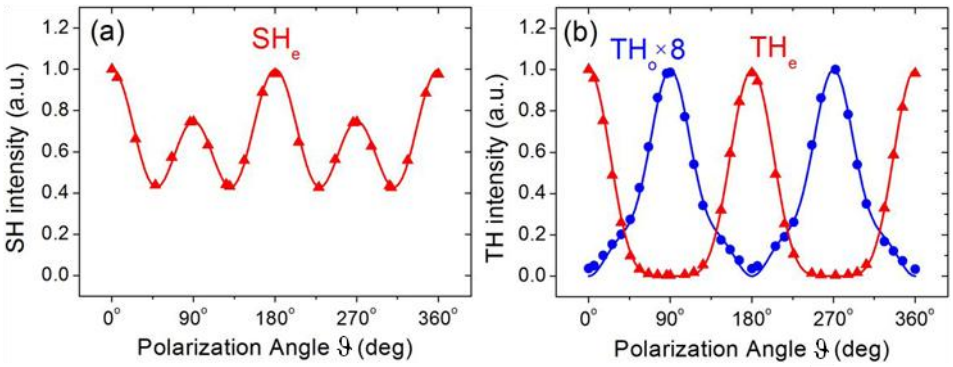

Figure 3.4. The power of the ordinary (blue) and extraordinary (red) components of the SH (a) and TH (b) as a function of the input polarization angle of the fundamental beam. 0° corresponds to the extraordinary fundamental wave. Points - experimental data; lines - theoretical fit Eqs.(3.3).

We denote by O_j and E_j the ordinary and extraordinary components of the j-th wave (j=1,2,3 for the fundamental, SH and TH, respectively). Then, for arbitrary polarized fundamental wave, the SH and TH will, in principle, contain ordinary and extraordinary components.

We start with SHG. Its extraordinary component is formed via the following two processes: $E_1E_1 \rightarrow E_2$ and $O_1O_1 \rightarrow E_2$. On the other hand, the ordinary component of the SH is obtained via a single interaction, $E_1O_1 \rightarrow O_2$. The TH is formed due to mixing of photons from the fundamental and SH beams. In particular, the extraordinary component is created via the processes $E_1E_2 \rightarrow E_3$ and $O_1O_2 \rightarrow E_3$, while the ordinary component appears due to the wave mixing, $E_1O_2 \rightarrow O_3$ and $O_1E_2 \rightarrow O_3$. The strength of each of these nonlinear processes is determined by the corresponding effective nonlinearity (see next section). In homogeneous media, all these processes contribute coherently to the total amplitude of the generated harmonic. However, because of the disorder in the domain distribution, this is no longer the case.

As discussed earlier [Ray04], the disorder in a nonlinear crystal leads to the incoherent build up of the generated waves. As a result, the two

constituent processes in SHG, namely $E_1E_1 \rightarrow E_2$ and $O_1O_1 \rightarrow E_2$, are mutually incoherent. Such a breakup of mutual coherence between two constituent nonlinear processes has already been noticed in the studies of SHG in random crystals [Tru07]. However, the effect of randomness is even more profound. Since in our experiments only an extraordinary SH component is generated, the effective nonlinearity responsible for the interaction $E_1O_1 \rightarrow O_2$ is negligible. In homogeneous crystals, the effective nonlinearity is directly proportional to the relevant element of the $\chi^{(2)}$ tensor (see next section). The situation is more complex in media with random domains. As pointed out by Le Grand *et al.* [Leg01], the randomness generally weakens the strength of nonlinear interactions. Consequently, the constituent interactions involving different polarization states of the fundamental beam and its harmonics will be affected differently by the disorder. Introducing the ordinary and extraordinary intensity components of the fundamental beam as $I_\omega \cos^2 \vartheta$ and $I_\omega \sin^2 \vartheta$, respectively, and taking into account the mutually incoherent character of the contributing nonlinear processes, we present the intensity of the ordinary and extraordinary components of the SH and TH by the following relations,

$$\begin{aligned} I_{2\omega}^{(e)} &\propto I_\omega^2(\cos^4 \vartheta + R_1 \sin^4 \vartheta) \\ I_{2\omega}^{(o)} &= 0 \\ I_{3\omega}^{(e)} &\propto I_\omega^3(\cos^6 \vartheta + R_2 \sin^4 \vartheta \cos^2 \vartheta) \\ I_{3\omega}^{(o)} &\propto I_\omega^3(\sin^6 \vartheta + R_3 \sin^2 \vartheta \cos^4 \vartheta) \end{aligned} \qquad (3.3)$$

where the quantities R_1, R_2 and R_3 represent relative strengths of the constituent nonlinear processes. They are used as free parameters in fitting the formulas (3.3) to the experimental data, as shown in Fig.3.4. We found that the best agreement between experiment and theory is achieved for R_1=0.75, R_2=0.011 and R_3=1.1.

Numerical simulations

Finally, we study numerically the formation of TH radiation in disordered $\chi^{(2)}$ structure by solving directly the Maxwell equations as explained in the Chapter 1, assuming the propagation of the FF in a two-dimensional nonlinear medium with randomly distributed domains

(Gaussian distribution with mean value of 1μm and standard deviation of 0.1μm). The Fig.3.5 illustrates the dynamics of the process by depicting the SH and TH in a real and Fourier space, respectively. In this way, one can easily capture the spatial properties of the generated waves. The difference in the angular emission for both SH and TH is clearly visible. It is worth noting that the same simulations conducted for a single domain crystal (with the same nonlinearity) did not produce any TH signal.

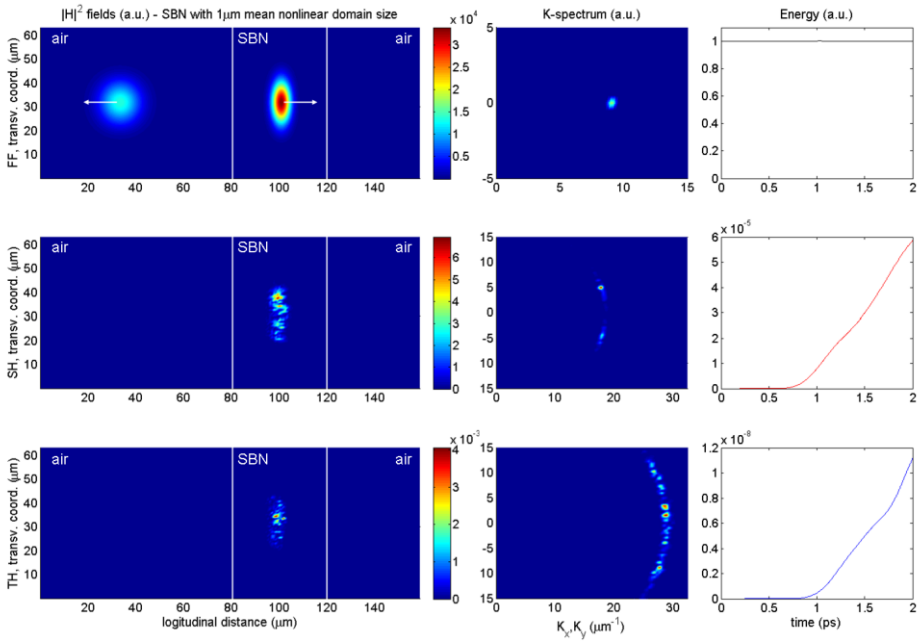

Figure 3.5. Numerical results. Generation of the SH and TH by a femtosecond laser pulse in a disordered structure. Left column: Spatial intensity distribution of the fundamental, SH and TH (from the top to bottom). Middle column- the transverse structure of the interacting waves in the Fourier space. Note the much broader emission angle for the third harmonics. Right column - energy of the fundamental, SH and TH as a function of the time of propagation of the fundamental pulse in the SBN crystal.

The Fig.3.5 depicts a snapshot during the propagation of a FF inside a SBN crystal. Due to the index mismatch, a portion of the field is backward reflected. The forward propagating portion generates SH and cascaded TH. Notice the typical shape of the generated field (on the left) that mirrors the domains distribution covered by the fundamental pulse. From the k-spectra we can clearly see the direction of propagation and/or the k-vector composition (that will produce a similar far field image). For the FF only a

single peak in the forward direction is present. For the SH, it is possible to clear distinguish two peaks at a fixed angle that well agrees with the domains statistical distribution (see Chapter 2). The TH, on the other hand, presents more broad distribution that well agrees with the experimental recorded image. From the energy diagrams we can verify that the FF is undepleted. The linear behavior for the generated SH and TH confirms the incoherent nature of those two signals.

3.3. Noncollinear setup

Experimental set-up

We describe now the theory and experiment results obtained for the noncollinear set-up case. Here we decided to use a new solution respect to the one used in the previous section. The set-up will be here implemented with a *bi-prism* that hardwarely split the input fundamental beam into two beams converging with and angle 2α. This presents the disadvantage that it is impossible to vary the angle of the two beams inside the crystal (without changing the optical components), but it is more useful from the practical point of view because the set-up does not need a delay line and in general a delicate alignment. This decision also, goes toward the idea of the integration and simplification for a future real device application. As we will see in the last section, as far as the application for pulse monitoring and characterization is concerned, the nonlinear interaction in the disordered crystal involves two beams (pulses) intersecting at small angle inside the disordered medium.

In this part of the work we extend our studies by considering simultaneous SHG and THG via cascading. This is particularly relevant for interactions involving fundamental waves at the telecommunication wavelengths since cascading leads to the emission of the TH in the visible part of the spectrum, far from the absorption edge of the commonly used quadratic crystals. We investigate polarization properties of the emitted

harmonics and model them using the concept of effective nonlinearity and taking into account the role of spatial randomness of the antiparallel ferroelectric domains. We support our experimental results with direct simulations of the Maxwell's equation in random quadratic medium as explained in the first Chapter.

The experimental setup is shown in Fig.3.6. As a light source we used an optical parametric amplifier (TOPAS) generating 150fs pulses (λ=1500nm, 250Hz rep rate) with total energy of 0.788mJ and beam diameter 5mm (full width at half maximum). The beam was propagating through the half-waveplate (WP) in order to control its polarization, and then after focusing with a 100mm cylindrical lens (L) was incident on a bi-prism (BP) converting the incoming beam into two symmetric beams which then intersected at the angle of $2x\alpha=2x2.344^{o}$ inside the SBN crystal (Fig.3.6(b)). In the experiment, the orientation of the crystal was such that both beams propagated in the x-z plane, close to its crystallographic x-axis and nearly perpendicularly to the longer dimension of the domains (coinciding with the optical axis), as illustrated in Fig.3.6(a). Interaction of these two beams inside the crystal resulted in the emission of SH and TH waves whose far field in the forward direction was recorded using a CCD camera located behind the SBN crystal.

In the experiment the input polarization of the fundamental beam was varied from ordinary to extraordinary by adjusting the half wave-plate (WP). Band-pass filters (not shown) placed in front of the CCD camera were used to separate the fundamental beam and its harmonics so their corresponding spatial intensity distribution could be separately recorded. In addition, a polarizer (not shown) located behind the SBN sample enabled measurements of the ordinary and the extraordinary components of the generated harmonics.

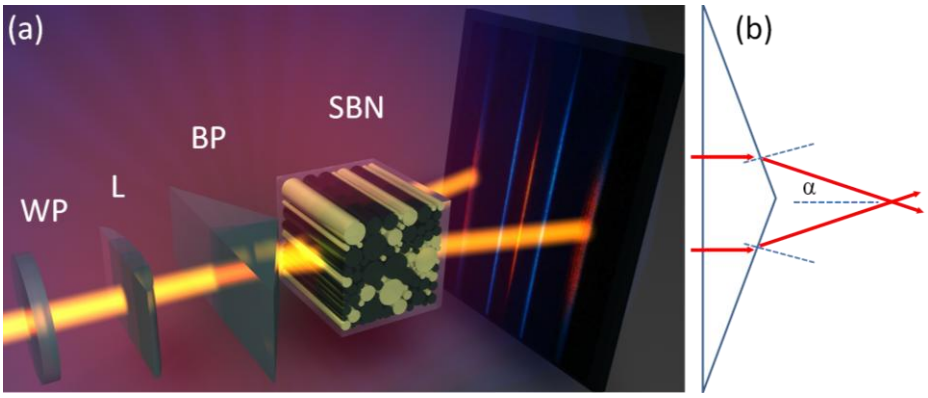

Figure 3.6. (a)Schematic of the experimental setup. The multi-domain structure of the SBN sample is schematically shown. WP- half wave-plate, L- cylindrical lens, BP- bi-prism. (b) Top view scheme of the bi-prism.

When the two intersecting linearly polarized fundamental beams propagate in the sample of the SBN crystal, the nonlinear interaction in the crystal leads to the emission of both, SH and TH. In our previous works with the fundamental wavelength of 1.064μm or 0.8μm the TH could not be observed since it was above the absorption edge of the medium. On the contrary, now it falls in visible part of the spectrum and its intensity was high enough to be measured and characterized.

Because of the randomness the overall generated signals were rather weak. The total emitted power of the SH and TH reached 35μW and 16nW, respectively. Typical harmonic intensity pattern observed on the screen is depicted in Fig.3.7. It consists of seven lines oriented perpendicularly to the optical c-axis of the crystal. The three lines denoted as SH1, SH2 represent the SH while the four lines marked as TH1 and TH2 represent the TH waves. The two SH signals (denoted as SH2) represent waves emitted due to the interaction of fundamental photons from each constituent FF. On the other hand, the central line (SH1) is a result of interaction of fundamental photons from both FF's.

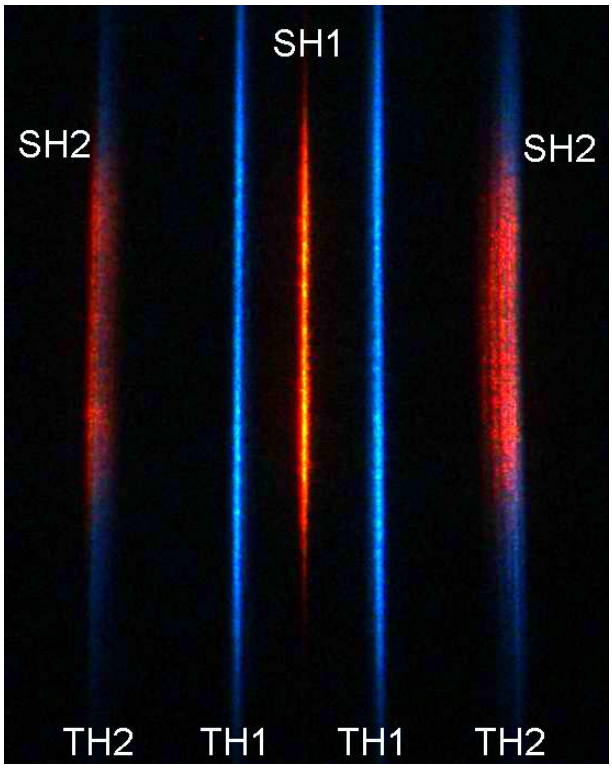

Figure 3.7. Experimentally recorded planar emission of the SH and TH.

Phase matching relation

Fig.3.8(a) illustrates the PM condition for this process in the x-z plane. In this case the $\mathbf{G}_i$ denotes one of the reciprocal vectors provided by the randomness. Fig.3.8(b) depicts the PM in the 3-dimensional (3D) setting. The number of differently oriented reciprocal vectors $\mathbf{G}$ located on an arc defined by the magnitude of the wave vector ($\mathbf{k}_{2\omega}$) of the SH reflects the planar emission of SH forming a vertical line on the screen.

When such generated SH photons interact with photons from the fundamental beams via the sum frequency mixing, the outcome is cascaded THG. Due to the presence of two noncollinear fundamental beams and three SH signals, the TH emission acquires the *four-line pattern*. Similarly to SH generation, the sum-frequency mixing also utilizes the reciprocal wave-vectors $\mathbf{G}$ to fulfill its corresponding PM conditions. In typical fabricated structures the simultaneous PM of two such processes would require careful

design of the ferroelectric domain pattern and would work for only one set of frequencies.

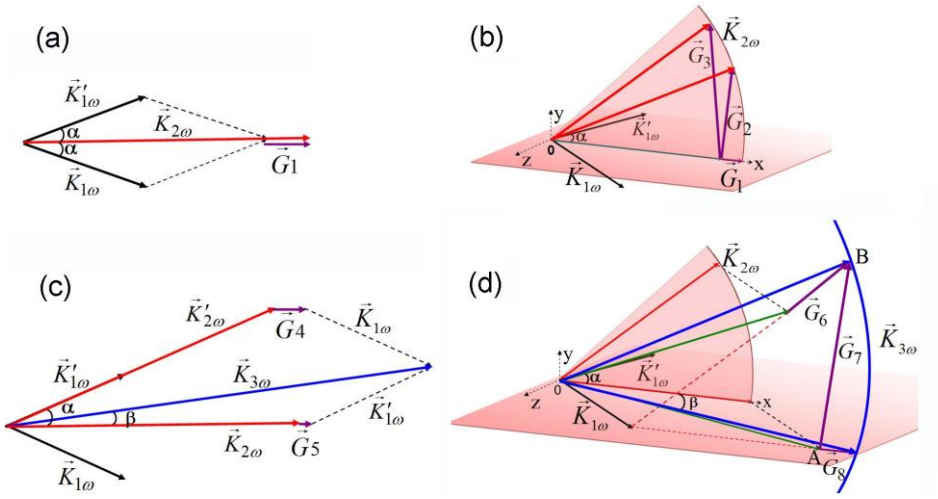

Figure 3.8. Diagrams illustrating the PM scenarios for the SHG (a-b) and cascaded THG (c-d) generation in random SBN crystal in the presence of two FF. G_1...G_8 represent reciprocal vectors provided by the randomness of the nonlinearity. See text for details.

Here, the randomness ensures that there are always reciprocal vectors available which can phase match practically all quadratic processes for broad spectrum of the fundamental waves. The emission of the four TH lines can be explained by considering again the respective PM conditions of the underlying wave mixing mechanism. In particular, the two lines denoted as TH2 are formed by the interaction of the fundamental beam with its corresponding SH (SH2). On the other hand, the TH signal marked as TH1 is emitted via two different processes which are illustrated in Fig.3.8(c). The first one involves fundamental wave $\mathbf{k}_{1\omega}$, the SH signal $\mathbf{k}'_{2\omega}$ originating from the second fundamental wave $\mathbf{k}'_{1\omega}$ and the reciprocal wave-vector $\mathbf{G}_4$. The resulting TH signal is emitted in the direction indicated by the vector $\mathbf{k}_{3\omega}$. However, this TH signal will also receive contribution originating from the interaction of the auto-correlation SH signal (with the wave-vector $\mathbf{k}_{2\omega}$) with one of the fundamental wave $\mathbf{k}'_{1\omega}$ employing the reciprocal vector $\mathbf{G}_5$. Graph in Fig.3.8(d) illustrates the full 3D character of the interaction leading to the emission of the TH in a form of the line TH1. As can be seen in this figure, the TH emission in a particular direction is due to the

contributions of the SH signals in all directions. Also a single SH signal will contribute to the TH emission in different spatial directions.

Experimentally recorded image of the emission lines (see Fig.3.7) shows that the spatial (vertical) extent of the third harmonic is significantly larger than that of the second harmonic. This is a consequence of the fact that in each of the quadratic processes such as SHG or sum frequency mixing the randomness of the nonlinearity results in delocalized emission of the generated frequency (see also [Sti10, Pas10]). As the TH is formed via cascading of two quadratic processes its spatial distribution is broader than each of the constituent interactions.

Polarization properties

The strength of the nonlinear interaction in quadratic media is determined by the effective nonlinearity which itself is a function of polarization of the interaction waves. Hence, by studying the polarization characteristics of the emitted harmonics one can extract information about details of the particular interaction process.

To really understand the polarization properties of the emitted signals we need to have a look closely to the polarization tensor of the SBN (with a group symmetry 4mm)

$$\begin{pmatrix} P_x \\ P_y \\ P_z \end{pmatrix} = \begin{pmatrix} 0 & 0 & 0 & 0 & d_{15} & 0 \\ 0 & 0 & 0 & d_{24} & 0 & 0 \\ d_{31} & d_{32} & d_{33} & 0 & 0 & 0 \end{pmatrix} \begin{pmatrix} E_x^{(1)} E_x^{(2)} \\ E_y^{(1)} E_y^{(2)} \\ E_z^{(1)} E_z^{(2)} \\ E_y^{(1)} E_z^{(2)} + E_z^{(1)} E_y^{(2)} \\ E_x^{(1)} E_z^{(2)} + E_z^{(1)} E_x^{(2)} \\ E_x^{(1)} E_y^{(2)} + E_y^{(1)} E_x^{(2)} \end{pmatrix}, \tag{3.4}$$

where the notation $E^{(1)}$ and $E^{(2)}$ stands for the two fields making the interaction, being them two FFs or a FF and a SH. The detailed analysis can be tedious, but we want to give here an example that explains the procedure. From Fig.3.8(a) we can set the first step of interaction between two collinear FFs written in coordinate (y,x,z) as follow

$$\begin{aligned} E^{(1)} &\to E_\omega \left(0, \cos\vartheta, \sin\vartheta\right) \\ E^{(2)} &\to E_\omega \left(0, \cos\vartheta, \sin\vartheta\right) \end{aligned}.$$

Following the scheme in Eq.(3.4), the in-plane polarization components will have the following form

$$\begin{aligned} P_x &= 0 \\ P_y &= d_{24}E_\omega^2 \cos\vartheta\sin\vartheta \\ P_z &= d_{32}E_\omega^2 \cos^2\vartheta + d_{33}E_\omega^2 \sin^2\vartheta \end{aligned} \quad .$$

For example for $\vartheta = 0$ (ordinary polarized input) we get

$$E^{(1)}, E^{(2)} \to E_\omega(0,1,0)$$

thus

$$\begin{aligned} P_x &= 0 \\ P_y &= 0 \\ P_z &= d_{32}E_\omega^2 \end{aligned} \quad ,$$

namely extraordinary polarized polarization. The second step of interaction will be thus between the following fields

$$\begin{aligned} E^{(1)} &\propto E_\omega(0, \cos\vartheta, \sin\vartheta) \\ E^{(2)} &\propto E_\omega^2\left(0,\, d_{24}\cos\vartheta\sin\vartheta,\; d_{32}\cos^2\vartheta + d_{33}E_\omega^2\sin^2\vartheta\right) \end{aligned} \quad . \tag{3.5}$$

The scheme in Eq.(3.4) now takes the particular form

$$\begin{pmatrix} P_x^{TH} \\ P_y^{TH} \\ P_z^{TH} \end{pmatrix} \propto \begin{pmatrix} 0 & 0 & 0 & 0 & d_{15} & 0 \\ 0 & 0 & 0 & d_{24} & 0 & 0 \\ d_{31} & d_{32} & d_{33} & 0 & 0 & 0 \end{pmatrix} \begin{pmatrix} 0 \\ E_y^{(1)}E_y^{(2)} \\ E_z^{(1)}E_z^{(2)} \\ E_y^{(1)}E_z^{(2)} + E_z^{(1)}E_y^{(2)} \\ 0 \\ 0 \end{pmatrix} \tag{3.6}$$

and consequently the polarization components can be written as

$$\begin{aligned} P_x^{TH} &= 0 \\ P_y^{TH} &\propto d_{24}\left(E_y^{(1)}E_z^{(2)} + E_z^{(1)}E_y^{(2)}\right) \\ P_z^{TH} &\propto d_{32}E_y^{(1)}E_y^{(2)} + d_{33}E_z^{(1)}E_z^{(2)} \end{aligned} \quad . \tag{3.7}$$

Substitutions Eqs.(3.5) in (3.7), after some algebra we finally get the following expression

$$\begin{aligned} P_y^{TH} &\propto E_\omega^3\left[d_{24}d_{32}\cos^3\vartheta + d_{24}\left(d_{33}+d_{24}\right)\cos\vartheta\sin^2\vartheta\right] \\ P_z^{TH} &\propto E_\omega^3\left[d_{33}^2\sin^3\vartheta + d_{32}\left(d_{33}+d_{24}\right)\sin\vartheta\cos^2\vartheta\right] \end{aligned} \quad . \tag{3.8}$$

In the experiment we varied the azimuthal angle ϑ (ϑ is the angle with respect to y-axis of the sample) of the linearly polarized fundamental

wave from zero to 360º, while measuring the power of the extraordinary and ordinary components of the emitted harmonics. The results of these measurements are shown in Fig.3.9, where the experimental data are represented by filled and open circles for the central (SH1, TH1) and peripheral (SH2, TH2) harmonic signals, respectively. Fig.3.9(a) and (b) show the dependence of the ordinary and extraordinary component of the SH and TH on polarization of the fundamental beam. The plots show that the polarization properties of the SH and TH beams do not depend on the particular emission directions. This is because the angle between two fundamental beams is relatively small.

The solid lines in Fig.3.9 represent the theoretically predicted dependence. It has been obtained by considering all possible processes contributing towards the SH and TH signals, in the way outlined in Eq.(3.8). Then, for arbitrary polarized fundamental beams, SH and TH will contain ordinary and extraordinary components. In case of, e.g. SH1 SHG, its extraordinary component is formed via the following two processes:

$$E_1E'_1 \rightarrow E_2 \text{ and } O_1O'_1 \rightarrow E_2.$$

On the other hand, the ordinary component of the same SH signal is obtained via the following interaction:

$$E'_1O_1 \rightarrow O_2 \text{ and } E_1O'_1 \rightarrow O_2.$$

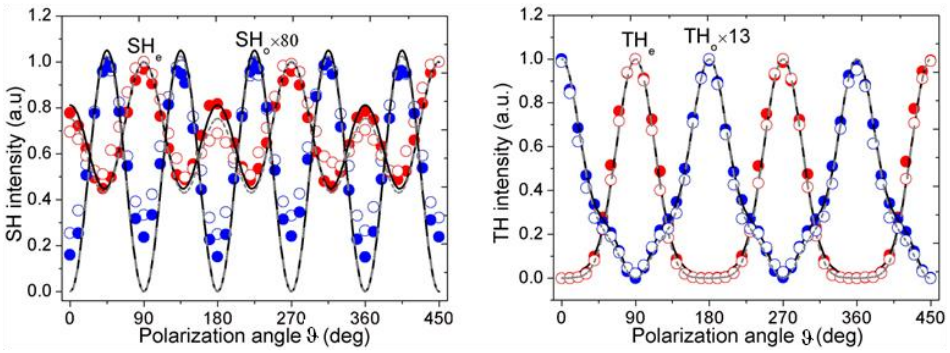

Figure 3.9. Intensity of the SH (left) and TH (right) signals as a function of the polarization angle of the input fundamental beams. Filled and open circles denote the experimental points for the central (SH1, TH1)and peripheral (SH2, TH2) harmonic signals, respectively. The solid line represents theoretical fit (Eqs.(3.9)). The red and blue colors refer to the extraordinary and ordinary components of the corresponding harmonics.

The TH is formed due to mixing of photons from the fundamental and SH beams. In particular, for the light emitted into the TH1 line, its extraordinary component is created via the following processes:

$$E_1E_{2SH2} \rightarrow E_3 \text{ and } O_1O_{2SH2} \rightarrow E_3$$
$$E'_1E_{2SH1} \rightarrow E_3 \text{ and } O'_1O_{2SH1} \rightarrow E_3$$

while the ordinary component appears due to the following interaction:

$$E_1O_{2SH2} \rightarrow O_3 \text{ and } O_1E_{2SH2} \rightarrow O_3$$
$$E'_1O_{2SH1} \rightarrow O_3 \text{ and } O'_1E_{2SH1} \rightarrow O_3.$$

In analogous way one can identify all remaining processes contributing towards the SH2 and TH2 emissions. All these interaction processes are inferable from the polarization tensor in (3.4).

Unlike homogeneous media where all these processes contribute coherently to the total amplitude of the generated harmonic, the randomness of nonlinearity induced by multi-domain structure makes these constituent processes mutually incoherent. Therefore one can show that the intensities of SH and TH depend on the polarization angle ϑ of the fundamental beam as follows

$$\begin{aligned} I_{2\omega}^{(e)} &= I_{\omega}^{2}(sin^4\vartheta + R_{21}\cos^4\vartheta) \\ I_{2\omega}^{(o)} &= I_{\omega}^{2}(R_{22}\cos^2\vartheta\sin^2\vartheta) \\ I_{3\omega}^{(e)} &= I_{\omega}^{3}(\sin^6\vartheta + R_{31}\cos^4\vartheta\sin^2\vartheta) \\ I_{3\omega}^{(o)} &= I_{\omega}^{3}(cos^6\vartheta + R_{32}\cos^2\vartheta\sin^4\vartheta) \end{aligned} \qquad (3.9)$$

where R_{2j}, (j=1,2) and R_{3k} (k=1,2) denote the strengths of the constituent nonlinear processes and are determined by the corresponding effective nonlinearity.

It is worth noting that the effective nonlinearity for all constituent processes depends not only on the material parameters, polarization and geometry of interaction but is also affected by the disorder as it has been shown by Le Grand *et al.* [Leg01]. We have extended this theory to cascaded processes. It appears that disorder generally weakens the strength of the quadratic interaction and its effect depends on the phase mismatch of the process. In fitting the theoretical formulas to the experimental data we used the following values for the R_{2j} and R_{3k} parameters: R_{21}=0.75, R_{22}=4.10 and

R_{31}=0.25, R_{32}=1.40 for the harmonic lines SH1 and TH1; R_{21}=0.82, R_{22}=4.20 and R_{31}=0.04, R_{32}=1.31 for the harmonic lines SH2 and TH2.

Notice, as example, how the last two equations of the set (3.9) are obtained simply taking the square of each terms in the Eqs.(3.8). The good agreement of the fit with the experimental results in Fig3.9 is the clear mark of an incoherent superposition of the generated fields. Indeed, if the field were coherently growing, their intensities would be proportional to the total square of the polarization terms, namely $\left(P_y^{TH}\right)^2$ and $\left(P_z^{TH}\right)^2$. This will give rise to mixing product terms that will drastically change the shape of the recorded curves.

Numerical simulations

Finally, we investigated numerically the SHG and THG in disordered quadratic media with two intersecting fundamental beams with Gaussian spatial and temporal profiles. Starting from Maxwell's equations and considering monochromatic stationary waves we can write the generic and well known equation describing the electromagnetic interaction that for the transverse-electric case, for example, holds as

$$\nabla^2 \mathbf{E}_j - k_{0j}^2 n_j^2 \mathbf{E}_j = \mu_0 \omega^2 \mathbf{P}_{NL,j}\,, \tag{3.10}$$

where $k_{0j} = \omega_j / c$, ω_j is the frequency, n_j is the index of refraction and j=FB1, FB2, SH, TH discriminates for the two noncollinear fundamental beams, SH and TH respectively. The Gaussian fundamental beams, assumed to be undepleted, are tuned at 1500nm, are 24μm in diameter and impinge at the nonlinear medium at an internal angle α=±2.35° with respect to the x-axis. The SH and TH nonlinear polarizations can be simply expressed as

$$\begin{aligned} \mathbf{P}_{NL,SH} &= \epsilon_0 \chi^{(2)}(x,y)\left[\mathbf{E}_{FB1}^2 + \mathbf{E}_{FB2}^2 + 2\mathbf{E}_{FB1}\mathbf{E}_{FB2}\right] \\ \mathbf{P}_{NL,TH} &= 4\epsilon_0 \chi^{(2)}(x,y)\left[\left(\mathbf{E}_{FB1} + \mathbf{E}_{FB2}\right)\mathbf{E}_{SH}\right] \end{aligned} \tag{3.11}$$

where we neglected the cubic nonlinearity and did not impose any constrain on the 2D spatial distribution of the $\chi^{(2)}$ nonlinearity.

The equations were solved with a standard 2D finite element method (COMSOL Multiphysics) considering several realizations of Gaussian distributions of the nonlinear domain pattern. As example, in Fig.3.10 we report the case of domain distribution with 1μm mean value and 0.15μm standard deviation. Plots in Fig.3.10 depict the far field intensity at the exit surface of the medium of both, SH and TH signals. The different emission angles are due to the noncollinear PM conditions and are in good agreement with the discussion above. For the peripheral emission lines, the SH and TH overlap as in the experiment while for the centrally emitted (TH1) TH, the simulated emission angle is $\beta=1.70^{o}$, corresponding very well to the measured angle of 1.7^{o}. It is clear from these plots that the signals corresponding to the noncollinear interactions are always strongest than those originating from the collinear interaction. This effect, also clear from the experimental data, results from the fact that the corresponding effective second order nonlinearity is at least four times stronger in the former case. Varying the parameters of the domain distribution (i.e. mean value and standard deviation) does not affect the positions of the peaks but only changes the relative emitted intensity, since it will only change the number of **G** vectors available to satisfy that particular phase matching relation.

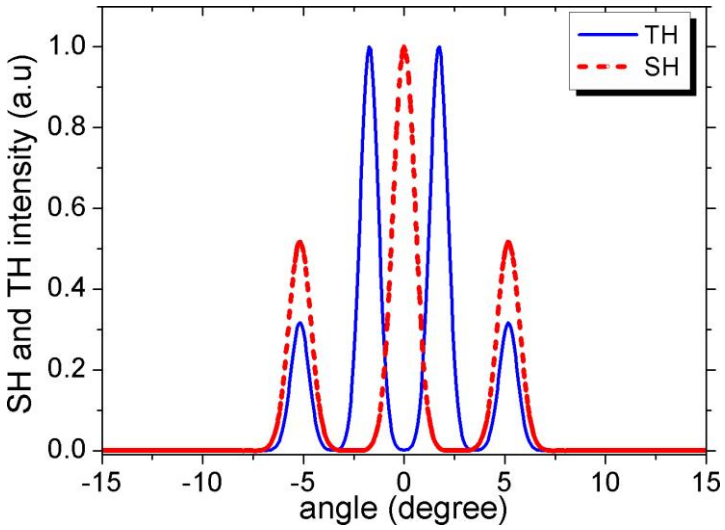

Figure 3.10. Numerically simulated far field intensity of the SH (red-dashed) and TH (blue-solid) generated via interaction of two fundamental waves in SBN crystal with random domain distribution.

Chapter 4

Pulsed dynamics in disordered nonlinear domains structures

4.1. Introduction

The use of ultrashort optical pulses has nowadays become an essential tool in a rapidly increasing number of applications in both research and industry. Important examples include the measurements of the dynamics of complex DNA molecules, monitoring of chemical reactions, optical communications, and laser micromachining. For the success of such applications, it is essential to obtain a precise knowledge of the duration and stability of the laser pulses. The existing techniques of ultrashort pulse

measurements usually rely on optical gating between the pulse and its replica that is typically realized through a nonlinear optical process, e.g. parametric process of the generation of the SHs [Die89, Tre97, Iac98, Dor02, She84].

Among the different schemes for optical gating, noncollinear SHG is known as one of the best methods for single-shot pulse-duration measurements [Gyu79, Kol81, Salt82, Sal82, Jan77, Rem88, Sal87, Wya81, Akt03, Sza83, Ish85, Sal86, Rag01, Col99, Dub94, Sac01]. In this method, two beams cross at a small angle inside a quadratic nonlinear crystal and, if the PM conditions are fulfilled, a SH beam is generated in the forward direction. The spatial shape of the generated SH beam represents the correlation function of the interacting ultrashort pulses.

It is well known that to obtain an efficient SHG the PM condition has to be fulfilled. Since the angular, frequency, or temperature conversion bandwidth utilized in these techniques is quite narrow (it decreases with the crystal length), this requires careful selection and alignment of the crystals used in a particular application. However, in disordered media SHG PM is possible over a broad frequency bandwidth, being limited only by the transparency region of the crystal, and it does not require angular or thermal crystal tuning [Hor93].

In this Chapter we show that the planar SHG resulting from the non-collinear interaction of a pulse with its own replica represents the autocorrelation of the pulse. Since the fundamental pulse broadens with the propagation inside the crystal due to material dispersion, the autocorrelation trace will widen correspondingly. This effect can be also used for the chirp characterization of the input femtosecond pulses. The broad conversion bandwidth provided by the random QPM process makes possible to use the same crystal for different wavelengths without need of realignment.

4.2. Short pulses characterization

Phase-matching conditions

In earlier works on parametric processes in unpoled SBN crystals, it was considered mainly *collinear* pump interaction schemes [Fis06, Fis07, Sal08]. For a single fundamental beam propagating along or perpendicular to the optical axis (which coincides with the domain orientation) the PM condition results in SH radiation emitted in a form of a cone or a plane. For counter propagating pumps being either perpendicular to [Fis07] or directed along the z-axis [Sal08] the SH signal is also emitted in a form of a plane. Here, we consider two fundamental beams propagating in crystallographic plane x-z of the SBN crystal and forming angles $-\alpha$ and $+\alpha$ with the x-axis. Then the general vectorial PM condition for SHG is written as $\mathbf{k}_2 = \mathbf{k}_1' + \mathbf{k}_1 + \mathbf{G}$, where $\mathbf{k}_1$, $\mathbf{k}_1'$ and $\mathbf{k}_2$ are the wave vectors of the fundamental and SH waves, respectively, and $\mathbf{G}$ represents one of the reciprocal vectors available from the infinite set of vectors provided by a disordered NLPC. The PM conditions which require 3D consideration are visualized in Fig.4.1(a). The blue arc defines the geometrical place of the $\mathbf{k}_2$ direction. All reciprocal vectors $\mathbf{G}$ are situated in the x-y plane. If we consider a complete random distribution of the nonlinear domains, $\mathbf{G}$ vectors can take any length and direction within this plane. We notice that all possible PM triangles determine that the SH radiation is emitted in the form of a plane coinciding with the crystal x-y plane.

Because the SH signal is generated in the area where the pulses from each fundamental beam overlap, the width of the emission region is directly related to the pulse length and beam size (see Fig.4.1(b)). Let us consider two distinct limiting cases:

1. interaction of *long pulses*, when the pulse width $\tau ? 2\rho\tan\alpha / u$, where α is the angle between each of the beams and the crystal x-axis, ρ is the beam radius, and u is the speed of light in the crystal. the SH radiation is generated from the volume overlap of the two fundamental beams and the width of the emission area Δz is defined as $\Delta z = 2\rho / \cos\alpha$. In this situation the pulse duration has

no connection with the area of the generated SH. This corresponds to the situation depicted in Fig.4.3(a).

2. interaction of *short pulses* when $\tau = 2\rho\tan\alpha / u$. In this case the SH emission area is defined by the *temporal overlap* of both pulses and has form of a thick line with the width of $\Delta z = \tau u / \sin\alpha$ (see Fig.4.2). This relation is valid for identical rectangular pulses with the duration τu and width 2ρ. This situation corresponds to the situation depicted in Fig.4.1(b) or Fig.4.3(b).

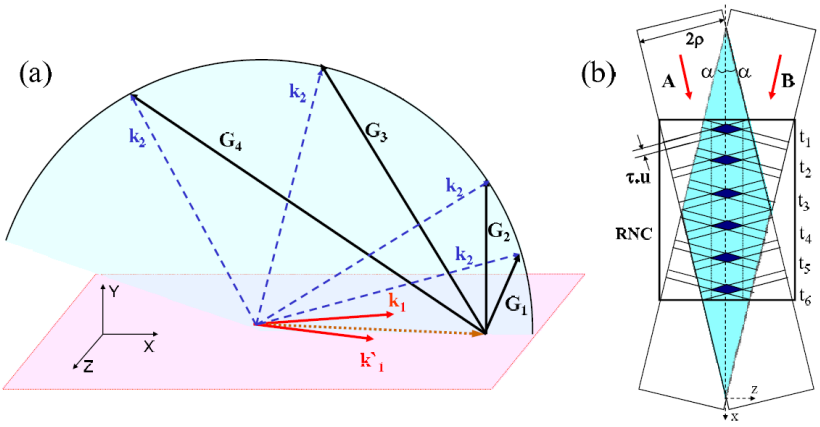

Figure 4.1. (a) Schematic of the PM diagram demonstrating the planar emission of the SH wave via interaction of two noncollinear pumps with bisector coinciding with crystal x-axis. **G**i being the reciprocal vectors of the disordered nonlinear crystal. (b) Overlap of the beams **A** and **B** and the overlap of the short pulses forming a narrow line inside the crystal.

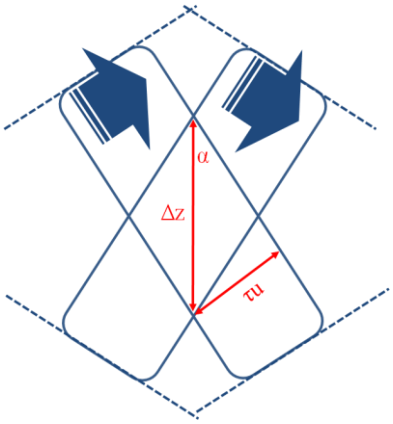

Figure 4.2. Schematic of the relation between the overlapping region and the pulse duration for the short pulses case.

In the case of Gaussian pulses, the width of the SH emission area will be $\sqrt{2}$ smaller [Jan77]

$$\Delta z = \tau u / \left(\sqrt{2}\sin\alpha\right) \tag{4.1}$$

leading to following relation $\tau = \Delta z\sqrt{2}\sin\alpha / u$. This is the well-known formula for the pulse duration single-shot measurements by noncollinear SHG experiments, see for example [Jan77, Sal81, Ish8510]. The difference is that in the traditional pulse-duration measurement techniques the recording of the SH trace is performed in forward direction, integrated over the crystal length. This is due to the fact that PM conditions are only fulfilled in the forward direction. In the situation considered here, we deal with an emission also in the transverse direction, due to the specific for this type of media omnidirectional *random quasi phase matching* [Bau04]. Therefore, the two-pulse overlapping volume is moving towards the output face, resulting in a SH line as illustrated in Fig.4.1(b). Monitoring transversely the width of this line along the crystal length can now provide an additional information about the pulse evolution inside the SH crystal.

Theoretical model

In order to take full advantage of this set-up and to be able to handle all the characteristic of the propagation, we need to consider a theoretical model. We assume that the two fundamental beams have a Gaussian spatial and temporal profile and cross at an angle 2α inside the crystal. The corresponding amplitudes can be written as:

$$\begin{aligned} A_1 &= A_{10}\exp\left(-\frac{z_1^2}{2\rho^2}\right)\exp\left(\frac{-(t-x_1/u)^2}{2T^2}\right) \\ A_2 &= A_{20}\exp\left(-\frac{z_2^2}{2\rho^2}\right)\exp\left(\frac{-(t-x_2/u)^2}{2T^2}\right), \end{aligned} \tag{4.2}$$

where (x_1, z_1) and (x_2, z_2) are the coordinates in reference systems oriented along the propagation direction of each one of the beams (Fig.4.3), $u=c/n$ is the speed of light in the crystal. T is the pulse-width at $1/e$ levels in intensity.

By introducing a common coordinate system for both beams, corresponding to the x- and z-axis (x,z) (Fig.4.3) we calculate the SH field

generated in the crystal. Assuming that PM is provided by the random QPM process [Bau04], the SH amplitude is proportional to the nonlinear polarization at doubled frequency:

$$B(x,z,t) \propto P_{2\omega}^{(2)} \propto d_{eff}^{(2)} A_1 A_2. \tag{4.3}$$

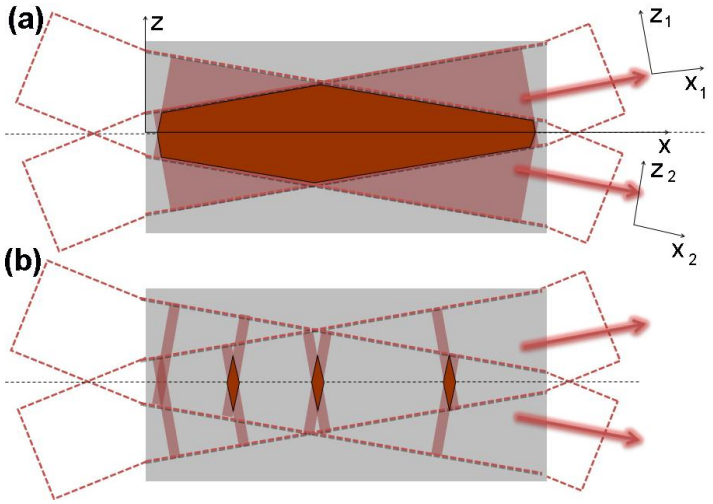

Figure 4.3. Beam superposition inside the SBN crystal for two limiting cases of (a) long pulses and (b) short pulses. For the case (b), as beams propagate the emission region moves along the x-axis giving rise to the recorded trace.

The generated SH signal recorded by a CCD camera represent a cross-correlation function of two interacting pulses. Therefore, in case of Gaussian pulses, the SH field can be represented as

$$\begin{aligned} B(x,z,t) = B_0(x) \exp\left(-\frac{z^2 \cos^2\alpha + x^2 \sin^2\alpha}{\rho^2} \right) \\ \times \exp\left(-\frac{(tu - x\cos\alpha)^2 + z^2 \sin^2\alpha}{u^2 T_c^2(x)} \right), \end{aligned} \tag{4.4}$$

where α denotes the half angle between the wave-vectors of the two intersecting fundamental beams inside the crystal and $B_0(x)$ is an amplitude that will be defined below.

The initial velocity of each spectral component is [Agr07]

$$u(0,t) = e^{-\frac{(1+iC)}{2}\frac{t^2}{T^2}}, \tag{4.5}$$

with C the initial chirp at the entrance of the crystal. With propagation inside the crystal the pulses experience broadening due to material dispersion, that depends on the initial chirp of the pulse. We have considered this effect assuming a chirped pulse in a medium with group velocity dispersion β_2 by formally replacing in Eq.(4.4) the pulse duration, T, by the *complex pulse duration*, T_c [Agr07],

$$T_c^2 = [T^2 - i\beta_2 x(1+iC)](1+iC)^{-1}. \tag{4.6}$$

In such case

$$B_0(x) \propto d_{eff}^{(2)} A_{10} A_{20} / [1 - i\beta_2 x(1+iC)/T^2]. \tag{4.7}$$

Figure 4.4(a) illustrates emission of the SH (central peak, in blue) via the noncollinear interaction of the overlapping pulse fronts of the two fundamental beams inside the crystal as described by Eq.(4.4) in condition of *big* radii ($\rho >> uT/2\tan\alpha$) of the beams.

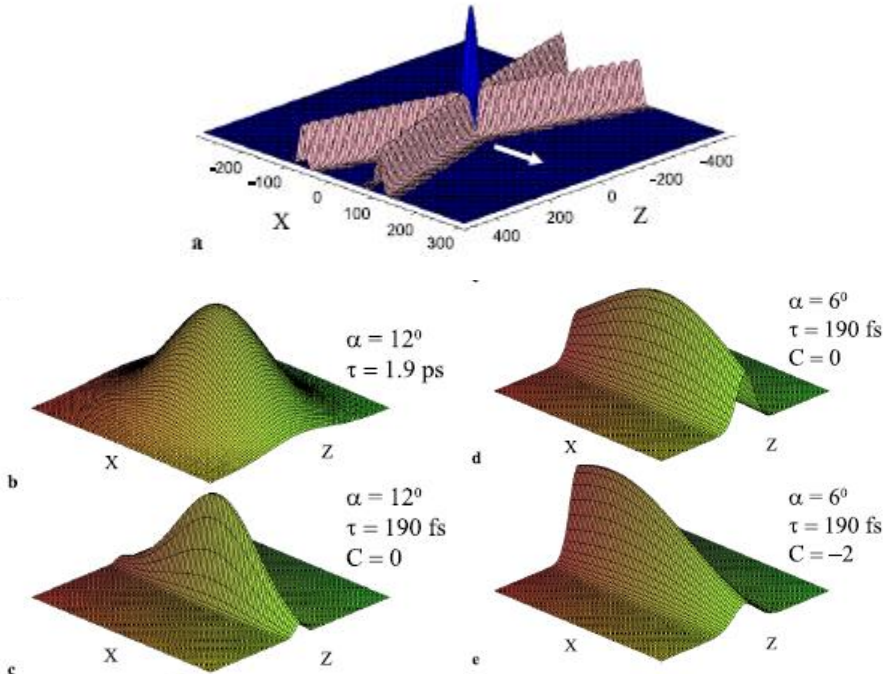

Figure 4.4. (a) Emission of the SH wave (central peak, blue) via the noncollinear interaction of the overlapping fundamental pulses inside the crystal, as described by Eq.(4.4). Background emission of the SH wave by each beam is shown as well. In this simulation, the beam radii are considered much bigger than $uT/2$ tan α, with 2α being the angle between the beams inside the crystal. (b-e) Theoretically evaluated snap-shot of the spatial profiles of the SH signal for different pulse durations and chirp parameters.

The graph also shows the background emission of the SH (in pink) by each individual beam. Only in the region of pulse overlap, a much stronger SH signal is emitted. Since the detected signal corresponds to an integration in the time domain, it results in a recorded continuous trace along the x-direction. The resulting SH intensity emitted from the overlapping of the fundamental beams is given by

$$I_{2\omega}(x,z) = \frac{T^4 I_{2\omega}(0)}{T_{ch}^4(x+L/2)} \exp\left(-\frac{2z^2\sin^2\alpha}{u^2 T_{ch}^2(x+L/2)}\right) \times \exp\left(-\frac{2z^2\cos^2\alpha + 2x^2\sin^2\alpha}{\rho^2}\right) \tag{4.8}$$

where

$$T_{ch}(x) = T\left[\left(1+\frac{C\beta_2 x}{T^2}\right)^2 + \left(\frac{\beta_2 x}{T^2}\right)^2\right]^{1/2}. \tag{4.9}$$

If the pulse is *long* the recorded trace corresponds to the second exponent of Eq.(4.8) and its shape (see Fig.4.4(b)) is defined only by the transverse dimensions of the beam and can not be used for estimation of pulse duration (Fig.4.3(a)). In the most interesting, from the practical application point of view, limit of very large ρ, the transverse profile of the SH trace along x is determined solely by the first exponent in Eq.(4.8). This case is illustrated on Fig.4.4(c,d,e) for two different angles between the two fundamental beams.

The thickness $\Delta z(x)$ of the SH trace depends directly on the pulse duration (as shown in Fig.4.1(b) and 4.3(b))

$$\Delta z(x) = \frac{uT_{ch}(x)}{\sqrt{2}\sin\alpha}. \tag{4.10}$$

If the width of the SH trace is measured at the input facet of the crystal (x=0) we obtain, (considering $T_{ch}(0)=T$) a measure of the pulse duration,

$$T = (\sqrt{2}\sin\alpha)\Delta z(0)/u. \tag{4.11}$$

The same relation holds for the experimentally measurable FWHM of the pulse duration, τ, and the FWHM of the trace transverse profile,

$$\tau = (\sqrt{2}\sin\alpha_{ext})\Delta z_{FWHM}(0)/c. \tag{4.12}$$

Additional information about the pulse can be obtained if the SH trace is recorded along the nonlinear crystal. Depending on the values of the group velocity dispersion β_2 and the initial chirp of the pulse C the width of the trace may became dependent on the distance measured from the entrance surface. For β_2 and C having the same sign, the trace width will grow constantly with the increase of distance from the front surface, while for β_2 and C of the opposite signs, this width will first reach its minimum at certain distance and will start growing afterwards. The case of negative β_2=-466 fs²/mm and C=-4 is shown on Fig.4.4(e). As can be seen from Eqs.(4.9) and (4.10) for known β_2 it is sufficient to measure the width of the trace at a distance x from the crystal entrance in order to determine the initial chirp of the pulse:

$$C = \frac{\sqrt{(4\Delta z(0)^2 \Delta z(x)^2 / u^4)\sin^4\alpha - (x\beta_2)^2}}{x\beta_2} - \frac{(2\Delta z(0)^2 / u^2)\sin^2\alpha}{x\beta_2}. \qquad (4.13)$$

Comparing Fig.4.4(d) and Fig.4.4(e) we note that the chirp may strongly affect the spatial profile of the recorded SH field, which can be also used in analyzing the properties of the input pulses.

Experimental results and discussion

Two types of experiments have been conducted by using light sources with different wavelengths and pulse durations. In the first experiment we used a Nd:YAG laser delivering 8 ns pulses at 1064 nm wavelength with repetition rate of 10 Hz. This experiment is representative of the situation where the pulse duration is too long and the recorded image cannot be used to measure the pulse duration. A large emission SH area has been experimentally recorded (Fig.4.7(a)), but it is non representative of the pulses duration.

In the second experiment the fundamental pulses are generated by a femtosecond MIRA (Coherent) oscillator tuned to 810 nm, with an approximate pulse duration τ =180 fs and repetition rate 76 MHz. The schematic representation of this experimental geometry is displayed in Fig.4.5. The incoming infrared laser beam is split into two equal parts (with

the amplitudes E_A and E_B) which are incident at an unpoled SBN crystal (5x5x10 mm, all sides polished) under an acute angle such that the two beams intersect in the central part of the crystal. The externally measured intersection angle $2\alpha_{ext}$ in different measurements is in the range of 20-28°. A variable delay line in one of the arms ensures that the two pulses coincide inside the crystal.

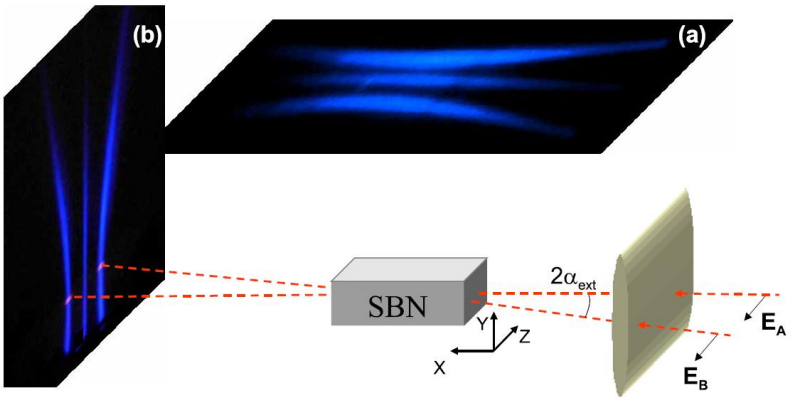

Figure 4.5. Photographic images of the SH emission in the transverse (a) and forward (b) directions via noncollinear waves interaction. The middle line in both photos corresponds to the planar SH emission as a result of the mixing of the two beams/pulses A and B (λ_F= 810 nm). These central traces disappear if one of the input beams (A or B) is blocked or if the pulses do not overlap inside the crystal. The two arcs on both sides of the central lines represent the conical emission from each individual pump beam.

We note that it is essential to have a large beam width in the plane of the crossing angle in order to fulfil the requirement for *short pulse* nonlinear interaction discussed above. For this reason, the beams are focused in the crystal with a cylindrical lens (f=10 cm), resulting in beam transverse dimension in the range of 2.2x0.43 mm. The path lengths of both incident beams are adjusted to ensure that the propagating pulses meet inside the crystal. In the experiments, the polarization vectors of both pump beams are chosen to be extraordinary, being directed along the crystallographic z-axis. The generated SH radiation is also polarized along z indicating the interaction of the type e_{AeB}-e_{SH}. This interaction gives the highest efficiency compared with other two possible geometries, namely o_{AoB}-e_{SH} and o_{AeB}-o_{SH}. In this notation, '*e*' means an extraordinary wave and

'*o*' an ordinary wave. The 4mm point symmetry group of the SBN crystal determines nonzero components of the second-order nonlinearity tensor $\hat{d}^{(2)}$. Since the direction of the fundamental beams is close to or coincides with the crystallographic x-axis, the relevant $\chi^{(2)}$ component for $e_A e_B$-e_{SH} is d_{33} (see previous Chapter).

The SH signal can be detected by a CCD camera imaging the crystal x-z plane from above or in front of the crystal. In the first case, the camera can record the evolution of the SH signal along the propagation of the fundamental beams from the entrance to the output of the sample. The photos in Fig.4.5 illustrate experimentally observed (a) transversely and (b) forward emitted SH signal for the noncollinear interaction of the fundamental beams in the SBN crystal. In each photograph, the central line appears only if two femtosecond pulses overlap inside the crystal. Blocking one of the beams or introducing a relatively large delay (> 2 ps) for one of the pulses makes this line to disappear. The two arcs located symmetrically on each side of the central trace represent the conical emissions from each individual pump beam [Fis06, Mol08, Tun03]. They are formed as a result of the collinear interaction of the fundamental photons within each beam. The internal cone angle β is defined by the PM conditions similar to that discussed in [Fis06, Tun03] but modified to account for an arbitrary position of the fundamental beam with respect to the x-axis. Actually, the cone angle β can be found from the relation [Fis06, Tun04]

$$\beta = \cos^{-1}\left[\left(2k_1/k_2\right)\sin\alpha\right]. \tag{4.14}$$

Based on the internal angle α corresponding to the present experiment, we obtain that the external cone angle $\beta = 79½$.

Fig.4.6 shows the AC trace measured for the case of 810nm fundamental waves. As both pulses enter the crystal simultaneously, the trace is located centrally inside the geometrical region of the overlap of both incoming beams. The plot on the right depicts a detailed profile of the AC trace. In the presence of a temporal delay between the fundamental pulses, the AC line will shift transversely to left or right by $\delta z = u\delta t / 2\sin\alpha$ (see Fig.4.9(a)). This lateral shift can be used to calibrate the AC measurements. On the right hand side of Fig.4.6, a digitized trace from the region close to

the entrance side of the crystal is shown. According to Eq.(4.1), its width gives the FWHM pulse duration of 193 fs .

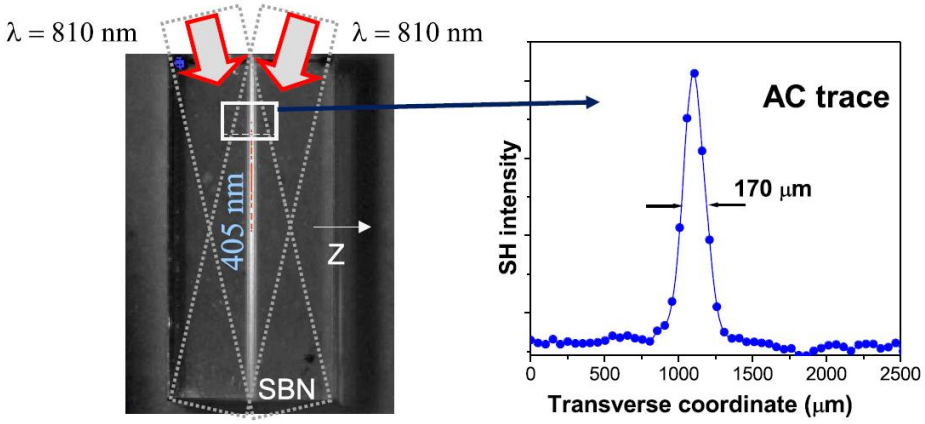

Figure 4.6. (left) The AC trace of transversely emitted SHG from two intersecting fundamental beams. (right) Detailed profile of the AC trace.

In Figs.4.7 we comparate the two experiments. For long (8 ns) pulses (Fig.4.7(a)) the trace fills the entire overlapping area of the beams. In this particular experiment the intersection angle $2\alpha_{ext}$ ~22°. On the other hand, in the case of femtosecond pulses (see Fig.4.7(b)) the trace has a form of a narrowline located inside the area of an overlap of both beams. In this case, the thickness of the trace directly reflects the pulse duration, with intensity distribution representing the AC function of the pulses.

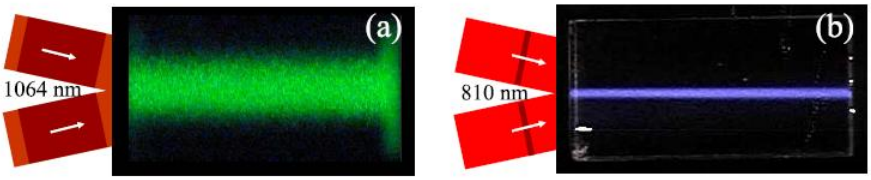

Figure 4.7. (a-b) Comparison of the thicknesses of the planar SH emission in the case of (a) nanosecond and (b) femtosecond pulses;

It should be stressed that since the SH signals originating from each individual beam are emitted in a cone, it is possible to separate them from that coming from overlapping pulses which is generated in a plane. This makes the measurement virtually background-free as illustrated in Fig.4.8. Fig.4.8(a) shows the background-free autocorrelation trace recorded by the camera pointing vertically at the crystal. The images in Figs.4.8(b,c) depict SH signals emitted by each separate beam. These images were obtained by *tilting* the camera at an angle corresponding to the conical emission of the SH by each fundamental beam.

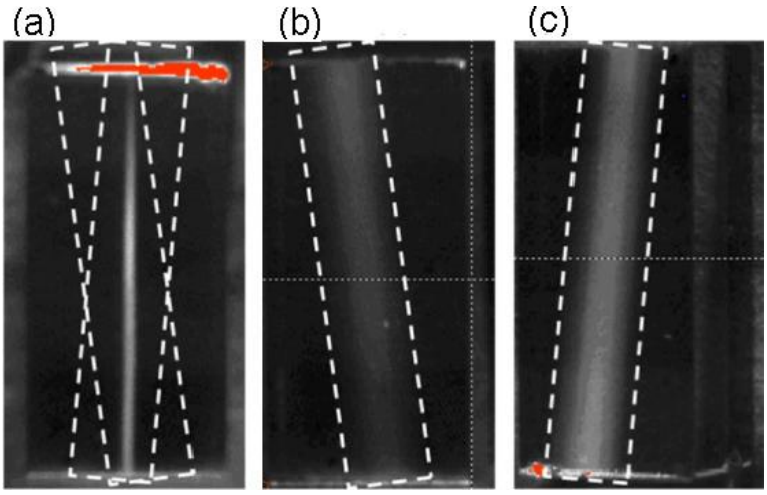

Figure 4.8. Recorded SH traces corresponding to (a) noncollinear planar SHG and (b,c) single beam SHG. To obtain the images (b) and (c), the imaging system is rotated in the y-z plane.

The photo in Fig.4.9(c) illustrates the experimental observation of the SH cross-correlation trace originating from interaction of a single pulse in a one beam with *two consecutive pulses* in the other beam. This pulse doublet is obtained by splitting the original femtosecond pulse utilizing the difference in the velocities of the orthogonally polarized pulses in a birefringent lithium niobate crystal [Fis07]. In this case the interaction results in a formation of two parallel SH traces separated by a distance corresponding to the temporal separation of both pulses. The same argomenations can be used to interpreter the AC trace in case of one the two beams presents double peaked strucure or if it is made by a train of pulses.

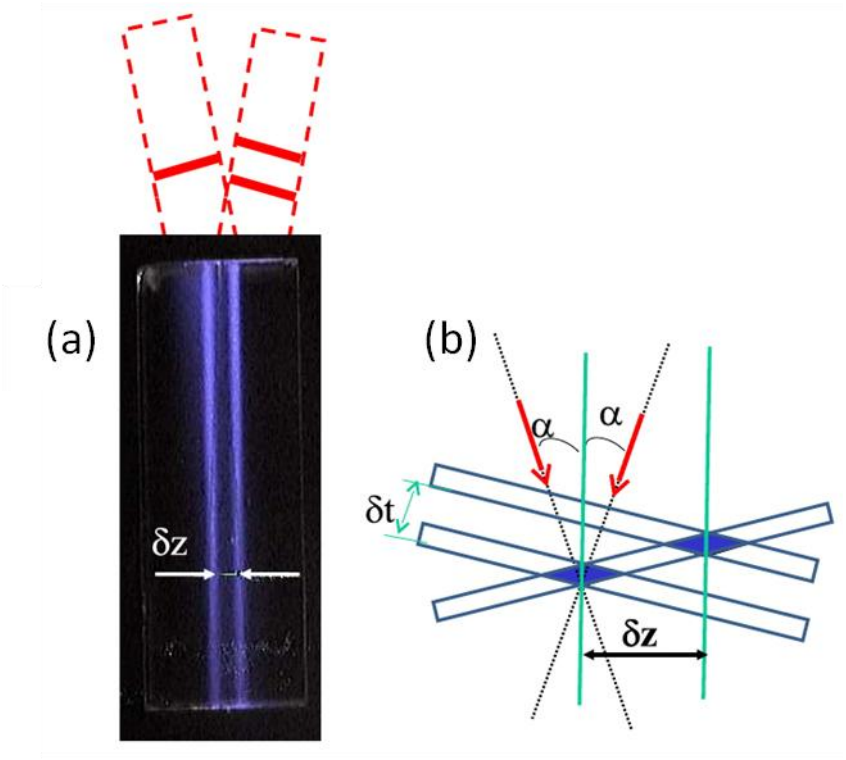

Figure 4.9. (a) Experimental observation of the formation of cross-correlation trace, when one of the fundamental beams carries a sequence of two consecutive pulses; (b) Schematic illustration of this process.

The temporal delay between the pulses is 837fs. Graph in Fig.4.9(b) depicts schematic of this process. The accuracy of this measurement depends on the resolution of the imaging system which can be easily controlled by choosing the proper magnification. In our experiments all autocorrelation traces were recorded using a standard CCD camera. To asses the accuracy of our method we compared its results with those obtained by the commercial Grenouille autocorrelator. We found very good correspondence in pulse measurements. For instance, for a Grenoullie reconstructed FWHM of 272.2 fs, our method gave 276 fs. As was mentioned above, the noncollinear SHG geometry discussed here enables us not only to determine the pulse width but also to obtain information about the initial pulse chirp. To this end, we should measure the transverse width of the autocorrelation trace at different distances from the front entrance facet of the crystal and then use equation Eq.(4.10) and Eq.(4.13) to calculate the

chirp parameter C. We demonstrate this in our experiments using pulses with different initial chirps, realized through different alignment of the laser. The results are shown in Fig.4.10, which depicts the width of the autocorrelation signal (data points) as a function of propagation distance. The lines represent a theoretical fit (using Eq.(4.10)) from which the chirp parameter C is found. The insets show corresponding autocorrelation traces.

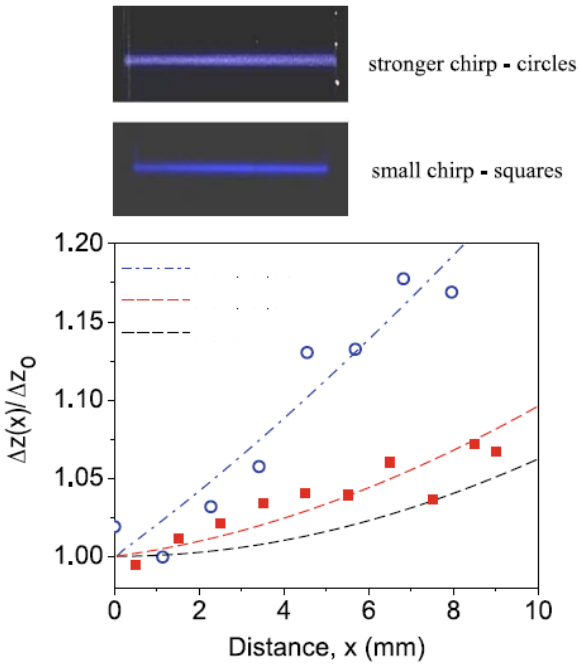

Figure 4.10. (top) Two typical autocorrelation traces recorded in the regime of weak and strong chirp. (bottom) Evaluation of pulse chirp by measuring the transverse width of the SH trace at different locations inside the crystal. Dashed lines represent theoretically calculated evolution of the SH signal for three different values of the incident chirp.

An additional advantage of using random QPM with respect to other usual nonlinear techniques is that we can obtain a SH signal for different polarizations of the input beam without any further alignment. As expressed in Eq.(4.3), the resulting SH signal is proportional to $d_{eff}^{(2)}$.

The symmetry of the SBN crystal allows for three different interactions, namely (eee), (ooe), and (eoo) [Tru07]. The large bandwidth of the random QPM process allows to simultaneously phase match all these

processes, so we can obtain a SH planar emission for different input beam polarizations. The most effective SH emission, however, takes place for the extraordinary beams since the (eee) interaction is driven by the largest coefficient d_{33}.

In conclusion, we have demonstrated that, by employing random QPM in an SBN crystal, we can realize non- collinear planar SH generation. By imaging the SH emitted in the transverse direction, we have determined the pulse duration and the initial linear pulse chirp. In addition, such type of nonlinear media can be used for nonlinear optical interactions with multiple input wavelengths or input polarizations without any further alignment or angular tuning due to available broad bandwidth provided by the random nonlinear photonic structure.

Conclusions of Part I

Phase matching is a crucial point for efficient nonlinear interactions, but unfortunately it is not a natural condition in common materials. Different techniques that assure this phase matching condition share the common limitation of the reduced bandwidth. In the same time, a specific design of the structure is useful only for one particular nonlinear interaction and well defined polarizations of the interacting beams. In this work we studied new aspects related with the nonlinear interaction in random and disordered nonlinear photonic crystals. We show that these structures provide a very broad PM, both in wavelength as well in angular domain, the only limitation being the transparency window of the material. This topic is extremely new and it is characterized by high complexity since it needs to merge fundamental knowledge from structured materials and linear, nonlinear and statistical optics. We approached the problem to the best of

our ability using the tools of theoretical study, numerical analysis and experimental verification.

In Chapters 2 and 3 we analyzed the SH and TH emissions from the SBN crystal, which is the natural material with the $\chi^{(2)}$ modulation of the *random* NLPC. We verified in detail that the pattern and the characteristics of the experimentally measured signals are in good agreement with both the forecast made by the PM scheme and the numerical simulations of the full vectorial Maxwell's equations, that we have obtained with our 2D nonlinear propagation model specially adapted to simulate these kind of random structures. We showed that cascaded processes in such structures are also possible with simultaneous fulfillment of PM for SHG and sum frequency generation.

We also proved that this nonlinear interaction can be used to characterize the random distribution of the material. In Chapter 2 we proposed a different approach to the modeling and visualization of the nonlinear domains. Due to the technical difficulties to obtain unambiguous images of the nonlinear structures, we approached the problem from the opposite side, numerically providing guess structures and iteratively adapting them to the experimentally obtained SH emission. In this way the statistical parameters are univocally fixed regardless of the growing method or crystal manipulation.

This study has been performed by a non commercial numerical code that solves the Maxwell's equations in their complete form and advances the fields in time. The numerical method does not rely on any of the usual approximations (such as SVEA, undepleted pump, etc…) giving us a very good confidence on the results obtained. This is in opposition on the other code more usually employed to solve this kind of noncollinear interaction. The presence of light generation at big angles respect to the FF propagation direction (as for example the transverse and backward SHG) requires careful implementation of the numerical code and does not permit the inclusion of strong approximations (such as SVEA) that will produce numerical artifacts. In addition to the electromagnetic pulse propagation simulations, we implemented a numerical tool that automatically generates disordered structures that mimic the ferroelectric crystals features. These

structures were then studied in the spatial Fourier space and analyzed with the PM scheme.

To our knowledge this work is the first one where a lot of issues related to the emission from these structures are systematically assessed. As an example, the *transverse* SHG in both collinear and non collinear schemes has been widely investigated and explained. The whole study embodied in Chapters 2 and 3 is a valid base where future works can build a systematic study and investigation device-oriented. The knowledge of how the nonlinear domains collectively operate gives a unique opportunity to their artificial and/or post-production engineering based on specific on-demand SH emission characteristics. The comparison between simulations and experiments allows us to interpret different emission patterns opening the possibility 1)to control the light emission by the proper design of the nonlinear domains and 2)to characterize the material by the study of the nonlinear emission.

Finally, in Chapter 4 we present a first practical application of our new acquired knowledge on these materials. We deepen the observation made in Chapter 2, shifting to the pulsed regime. We gave theoretical bases and experimental verification for the practical and easy determination not only of the fundamental beam pulse duration, but also of the initial chirp possessed by the beam. This put this method is complementary respect with other well-know methods as FROG, Grenouille and SPIDER. In fact, our theory does not present any limitation on the measurable pulse duration, giving us the possibility to characterize ultrashort pulses down to few optical cycles. In this regime the other commercial methods either are not usable or require very careful set up and alignment. Moreover, the set up is very easy and robust and does not require particularly expensive tools.

The shift of the pulse measurement from hundred-of-femtoseconds limit (as in this work) down to few-femtoseconds level, presents however two main critic points. The first one concern with the difficult handling of so short pulses and it is not peculiar of only our method. Few-optical cycles pulses propagate in fact with very strong dispersion in both the nonlinear crystal and in all other optical components (as for example in the beam splitter). This demands a very accurate characterization of all the optical

elements and a smart design of the experimental set-up. The second critic point is illustrated in Fig.4.6. The overlap between the two fundamental fields that generates the SH trace has a transversal dimension that depends directly on the duration of the fundamental pulses. To correctly record this trace we need to have an image with an appropriate graphical sampling. For few-optical cycles pulses, this sampling can be quite severe. To solve this issue, in principle, it can be enough to provide an adequate magnification trough the optical system of the recording camera.

Both the critic points have a *technological* nature and we are confident that it will be possible to find satisfying solutions. Recently we re-proposed the experiments illustrated in the last section of this Chapter, where we have experimentally tested our set up for 70fs pulses with promising results. Our future goal is to perform the experiment with 10fs source laser, finally proving the great potentiality of our method. If we will be successful, this will give a new tool to the scientific world, academic and industry, to easily fully characterize the recently introduced ultrashort pulse sources. These are, in fact, finding some problems to be widely commercialized mainly due to the lacking of a (cheap) feedback characterization tool.

Part II

Chapter 5

Phase Locked Harmonic Generation

5.1. State of the art

In 1961, with the generation of the SH light using a beam from a ruby laser, Franken and his collaborators experimentally discovered SHG, and so nonlinear optics was born [Fra61]. Since then, SHG has become one of the most investigated and discussed nonlinear optical processes. Although the conversion efficiency reported at the time was quite small, the advent of PM techniques [Gio62, Mak62] has made it possible to significantly boost SHG conversion rates. Countless, detailed theoretical studies of SHG have appeared since the seminal work by Armstrong *et al.* [Arm62] and Bloembergen *et al.* [Blo62] in 1962. In fact, during the last four decades the study of SHG has mushroomed and evolved to the point that non-linear $\chi^{(2)}$

processes are so well understood that are there are very few chances for more surprises to be revealed, at least from the theoretical point of view.

Because the primary reason to investigate SHG has consistently been the achievement of efficient frequency doubling, the emphasis has been on phase matched interactions between the fundamental and the SH beams. PM is a condition that essentially requires conservation of linear momentum that allows continuous energy flow from the pump to the SH, generating high efficiency signal. However, this is a condition that does not generally occur naturally, and so the literature abounds with contributions that contain techniques and stratagems attempting to circumvent a naturally occurring phase mismatch, in order to bring the interacting waves closer to ideal, phase matched conditions [Gio62, Fej92, Sap05, Boy66, Pet05, Web86, Sid96, Rei03, Ste96, Dag06, Gal00, Con99, Fuj06, Sca97, Cen01, Wan01, Kry95, Liu06, Xu03, Orl96].

The systematic study of nonlinear propagation phenomena at or very near PM conditions has resulted in relatively few studies of SHG and related propagation phenomena in a phase mismatched environment. In fact, from time to time workers have been confronted with situations where, in addition to the usual SH beam, a second component was observed. For example, the general solution for SHG from a boundary layer discussed in [Arm62, Blo62] (see Chapter 1) is revealed as being composed of a reflected signal, and two forward propagating components, one displaying a k-vector that is a solution of the homogeneous wave equation (i.e. the expected wave vector at the SH frequency), and the other a k-vector that is the solution of the inhomogeneous wave equation, equal to twice the pump wave vector. Shapiro [Sha68] in 1968 noted: "SHG spectra consisted of two parts: a part matched across the breadth of the laser fundamental … and a portion which remained fixed in frequency and coincided with the laser fundamental peak." The author thus appreciated that there were two SH components, but did not elaborate further on his findings.

In 1969, in a mathematical treatment Glenn [Gle69] provided a general solution of the SH field that also showed two contributions, one arising as a surface term, traveling with the characteristic group velocity expected at the second harmonic frequency, and a second component that instead appeared

to travel with the group velocity of the fundamental beam. These findings notwithstanding, workers' attention remained focused on efficient energy conversion schemes, via the implementation of QPM [Fej94].

In 1987, Manassah *et al.* [Man87] theoretically showed that, in the weak conversion efficiency regime and in the presence of group velocity dispersion, the SH signal was characterized by a double-peaked structure. The effect was attributed to an interplay between $\chi^{(2)}$ and $\chi^{(3)}$ processes, and self- and cross-phase modulation that occurred during the interaction. Then in 1990, Noordam *et al.* [Noo90] reported that under conditions of a phase and group velocity mismatch, the SH signal indeed displayed two prominent features. In their words: "This letter is ... the first report on the observation of double-peak shapes due to group velocity difference between the fundamental and the generated SH".

In the years that followed, the phenomenon was again reported theoretically and experimentally. The high-intensity regime and the relatively high conversion efficiencies (up to 3.5%) however required that the interaction be placed in a context of competing second and third order processes [Mal97]. Su *et al.* [Su06] introduced additional theoretical and experimental evidence that a purely second order process could lead to a double-peaked structure in the time domain profile of the SH beam. The effect was attributed to induced group velocity dispersion (GVD), under conditions of negligible group velocity mismatch (GVM). As the pump and SH beam co-propagate, they argued, the pump is able to impress its dispersive properties on the SH pulse, a process that may be viewed as induced effective dispersion.

Also recently, the double-peaked structure in the SH signal was discussed theoretically in the context of femtosecond pulse propagation in a birefringent nonlinear material, under phase mismatched conditions [Mle99]. In that study, the authors used a finite difference time domain (FDTD) method to solve Maxwell's equations in the presence of a material discontinuity that separated vacuum from a nonlinear medium. The result suggested that the SH signal splits into two components, one that travels at the pump's group velocity, and a second component that walks off,

consistent with all previous predictions and observations of the phenomenon.

In the present investigation we perform a detailed study of the nature of this double-peaked pulsed SHG under conditions of phase and group velocity mismatch, and low conversion efficiencies and pump intensities, in bulk or structured nonlinear materials. We generally find qualitative agreement with all previous reports regarding the presence of a double-peaked SH signal, and a SH pulse that propagates at the pump's group velocity. Instead, our results provide additional insight into the dynamical aspects and the interpretation of the phenomenon, in that we find that the origin of the double-peaked structure resides in a phase-locking (PL) mechanism that characterizes not only SHG, but also $\chi^{(3)}$ processes, for example, as shown in reference [Ako02], where PL mechanism was first discussed in the context of intense field propagation and filamentation in the atmosphere. We find that the two peaks consist of a first peak that quickly phase-locks to the pump pulse and propagates under the pump envelope at the pump's group velocity, and a second component that propagates with the characteristic group velocity of the SH frequency, which we can refer to as the normal component. At low intensities, the normal component propagates at the nominal group velocity given by linear material dispersion.

One point worthy of note is that the PL mechanism that we describe occurs for arbitrarily small pump intensities. For this reason we believe it is not a soliton effect, which usually relies on a threshold mechanism [Fej92, Kiv95, Con97, Con97b, Con98, Llu96]. In reference [Llu96], for example, the effect is discussed at length within the context of continuous wave beams, diffraction, and associated spatial soliton formation, in both seeded and un-seeded cases. The authors in fact coined the term *beam locking* to distinguish the phenomenon from other soliton-like effects that occur in $\chi^{(3)}$ media [Llu96]. In our case, we find that once the normal component separates, the PL is complete, the interaction between the waves ceases, and in the absence of pump focusing, the energy of the second harmonic pulse clamps.

Moreover, the introduction of a physical boundary with vanishingly small index discontinuity, e.g. the pulse is made to cross from a non-zero $\chi^{(2)}$ region into a region free of nonlinearities, is enough to cause the phase-locked SH pulse to be released, and to begin a journey still in the forward direction but with a different group velocity. Thus it is important to stress that the nonlinear coupling is the link to activate the PL. In the region where, for some reasons, the nonlinear coupling is null either the phase locked harmonic is not generated, either, if it was previously generated, it becomes free to propagate accordingly to its wavelength dispersion characteristics.

The partial informations achieved at the time we started this thesis work were enough to give us a simple idea: the phase locked harmonic component, once generated, *reads the complex index of refraction* of the fundamental beam. This is in opposition to the fact that the normal harmonic component keeps reading the index of refraction given by the dispersion values at its own frequency. At that time this idea was only partially supported. Thus, our goal in this Part III will be to fully experimentally prove our idea, providing a systematic and detailed study.

In few words, let's consider a continuous beam at frequency 2ω that propagates with k-vector $2k_1$ (due to the PL mechanism). This can be seen as if the field is propagating in a medium with an *effective* index of refraction $n_2=2\omega/2k_1=\omega/k_1=n_1$, namely the same index of the fundamental beam. The more urgent task to accomplish was to give an experimental support to this idea and the results are explained in this and in the next Chapter. Here we tried to work with a smart working condition. Following our idea, if we tune the SH in a spectral region of the material dispersion where the absorption is strong, the difference in the two harmonics behaviors is pushed to the extreme consequence: the normal component should be completely absorbed while the PL component will be able to propagate undisturbed, provided that the fundamental beam is tuned in a transparent region. The experiment described in the following Chapter goes in this direction giving us the definitive proof.

As expected, the harmonics conversion efficiencies are relatively small and this makes them not practically usable. A way to shift a bit the

importance of these results from the fundamental relevance to the real applicability is to try to enhance those efficiencies. Strong of the remarkable result achieved, we then made a step further considering the behavior of such component in a microcavity environment. In Chapter 7, we started with a theoretical study of a free standing cavity. As a second step, we set up an experiment to prove our finding first with a single mirror cavity, than with a high performance high-Q (double dielectric mirrored) microcavity.

Finally, in Chapter 8 we wanted to push even further our finding. We investigated what happens if one harmonic field is tuned in a region where the material shows metallic behavior. In fact here, the field should be not simply absorbed, but in principle no light propagation at all should be allowed due to the opposite signs between the magnetic permeability (always around 1) and the electric permittivity (assuming negative values in the UV range of most semiconductors). As we will show at the end of the Chapter 8, the PL phenomenon is so robust to even put in crisis conventional wisdom.

5.2. Role of phase matching in pulsed SHG

Phase Locking Theory

The dynamics of the PL mechanism can be traced back to the beginning of nonlinear optics. As outlined by Bloembergen in his seminal work [Blo62], energy transfer between the FF and its generated harmonic, far from the PM condition, always happens near the interface. The expression "*near the interface"* could acquire different connotations and/or meanings depending on the working conditions, such as the dimensions of the incident pulse and the sample. Generally speaking, assuming normal material dispersion and that all fields are tuned at frequencies below a material resonance, the generated harmonic fields will always experience dispersion such that they will tend to travel slower than the FF. The exchange of energy between the FF and its harmonics takes place within the walk-off distance, i.e. until the

harmonic pulse is no longer under the spatial influence of the FF pulse due to differences in group velocities. Of course, walk-off is best observed under conditions of large mismatch. In this situation it is easy to observe that when a pump pulse crosses an interface between a linear and a nonlinear medium there are always three generated SH and/or TH components. One component is generated backward into the linear medium (i.e. vacuum), due to the index mismatch between the materials that form the interface and the remaining two components are generated forward. The basis for understanding the generation of two distinct forward-moving signals can be found in the development of the mathematical solutions of the homogeneous and inhomogeneous wave equations at the harmonic frequencies [Blo62, Arm61] (see Chapter 1). In the linear case the wave equation has a homogeneous form. Depending on other approximations made (for instance SVEA, undepleted pump, etcetera) the solution is well known.

If a quadratic term is considered in the constitutive relation, in the way outlined in the Chapter 1, a SH field with double frequency arises from the material. This has a generally very low efficiency level if no other expedient is adopted. This newly generated field satisfies the same kind of wave equation, except that now a driving term is present on the right hand side. The resulting inhomogeneous form of the equation has a solution composed by the sum of the homogenous and inhomogeneous solutions, which is difficult to express analytically in the general case. This prediction of a two-component SH signals was later discussed and observed [Sha68, Gle69, Man87, Noo90, Ras97, Su06, Mle99].

Continuity of the tangential components of all the fields at the boundary leads to generation of the two forward-propagating components that interfere in the vicinity of the entry surface and immediately give rise to Maker fringes [Mak62]. It turns out that while the inhomogeneous component (inhomogeneous solution) is captured by the pump pulse and experiences the same effective dispersion of the pump, the homogeneous component (homogeneous solution) travels with the group velocity given by material dispersion. That is, this component has wave-vector

$$k_{2\omega}^{HOM} = n(2\omega)k_0(2\omega),$$

where

$$k_0(2\omega) = 2\omega / c$$

represents the free space wave-vector at the frequency 2ω, and exchanges energy with the pump until the inevitable walk-off. The inhomogeneous, phase locked, component has a wave-vector given by

$$k_{2\omega}^{INH} = 2n(\omega)k_0(\omega),$$

where

$$k_0(\omega) = \omega / c,$$

so that the wave-vector of the inhomogeneous components is precisely twice the pump's wave-vector

$$k_\omega = n(\omega)k_0(\omega).$$

The situation for the TH is analogous. Here the term *phase-locked* is used to emphasize the fact that the inhomogeneous component maintains the same phase relative to the FF beam for the entire propagation distance. In the limit of $\Delta n \rightarrow 0$, namely the difference between the indexes of refraction at the fundamental and the SH approaches zero, the two solutions merge into a single one. In the other cases, where $\Delta n \neq 0$, the two solutions interacts until they completely walk off. Consequently, to clearly distinguish the two components it is important to work with conditions very far from the PM and use very short pulses, which will faster the walk off process.

Even if it is possible, at least formally, to write the solution of the nonlinear Maxwell's equation for the SH as a sum of the homogeneous and inhomogeneous terms as we have shown in Section 1.1. In this work we numerically solve the whole system of the Maxwell's equations without imposing any form or limitation to the solution. Our theory predicts that the pump, tuned within a region of optical transparency of the material, captures and impresses its dispersive properties on portions of the generated SH and TH signals, which in turn behave as parts of the pump and co-propagate with the pump pulse for the entire length of the sample. As we will see better in the next Chapter, these general conclusions thus apply: if the medium is transparent at the pump frequency, then the material will be transparent for the generated inhomogeneous harmonic component. Similarly, if the medium absorbs the pump and is transparent

in the SH and TH ranges, the inhomogeneous components are absorbed and the normal components survive.

In absorbing materials [Cha65, Bur61, Bri94, Mar00, Ver02, Ram00, Che95], Maker fringes [Mak62] are observed as long as material absorption is small. At the same time, the amplitude of the transmitted beam is independent of sample thickness [Ram00]. Thus, both theoretical and experimental evidence suggest that the inhomogeneous component interacts with the normal SH component to produce Maker fringes. This interaction stops as soon as the normal component either is absorbed or walks off from the pump, leaving the inhomogeneous portion of the signal intact.

Even though many of these predictions and observations are not new, only recently we recast these phenomena that in ordinary, transparent materials were cast in terms of a PL mechanism that also characterizes higher order nonlinearities, as is the case in filamentation of high-intensity fundamental and TH beams in the atmosphere [Ako02].

In the present analysis we calculate the energy velocities of the generated pulses, defined as usual:

$$\mathbf{V}_e = \frac{<\mathbf{S}>}{<U>}; \tag{2.1}$$

the brackets mean a definite integral U is the energy density and S is the Poynting vector defined as

$$\mathbf{S} = \frac{c}{4\pi}\mathbf{E}\times\mathbf{H}.$$

The group velocity calculated as

$$V_g = \frac{\partial k}{\partial \omega} \tag{2.2}$$

is not adequate, because this value describes only the homogenous signal. Experimental and theoretical evidence [Sha68, Gle69, Man87, Noo90, Ras97, Su06, Rop07] shows that the pump and the phase locked pulses propagate at the same energy velocities. In confirmation of the fact that the phase locked generated fields behave in all respects as if they were pump fields, our calculations show that the proper energy velocities for the SH and

TH fields (that is to say, the velocity of the pump field) are recovered only if the Landau energies [Lan60]

$$U(z,t)=\frac{1}{8\pi}\left(\mathrm{Re}\left(\frac{\partial[\omega\varepsilon(\omega)]}{\partial\omega}\right)|\mathbf{E}|^2+\mathrm{Re}\left(\frac{\partial[\omega\mu(\omega)]}{\partial\omega}\right)|\mathbf{H}|^2\right) \quad (2.3)$$

are evaluated with the material parameters of the pump frequency. Therefore, we find that $\mathbf{V}_e$ is identical for all pulses only if *the generated inhomogeneous harmonic fields are attributed the material dispersion of the pump*. This finding cements the notion that phase locked pulses behave as the pump pulse does, and ultimately require to be treated as such in the application of boundary conditions. For this reason, in absorbing materials, discrepancies have been recorded between predictions and experimental results [Ver02, Ram00], even though there was a recognition that the two SH components propagate at different group velocities and peculiar phase properties [Kri04].

Numerical simulations and experimental results

To model simultaneous SHG and THG in ordinary materials we used the equation and the description stated in Chapter 1. As an example, in Fig.5.1 we illustrate a snapshot of a typical case of SHG and THG in a generic dispersive nonlinear material. We assume that the FF and the harmonic fields are tuned far enough from resonance to render absorption negligible. The incident peak pump power is chosen to be quite low, of the order of few W/cm^2, in such a way we can suppose null the effect of other nonlinear effects. The nonlinear coefficient is considered of the order of 1pm/V and the index of refraction are n_{FF}=3.3, n_{SH}=3.8 and n_{TH}=3.9, but these numbers do not limit the validity of the discussion. Fig.5.1 shows the fundamental beam after it already passed the entry interface of the material. It is possible to recognize both homogeneous and trapped inhomogeneous (or phase-locked) components for the SH and TH. The homogeneous component travels at a slower group velocity than the pump and eventually walks off. The pump and the trapped portions of the SH signal travel at the same energy velocity. Notice how the walk-off is faster

for the TH components rather than for the SH components due to the bigger difference in the group velocities.

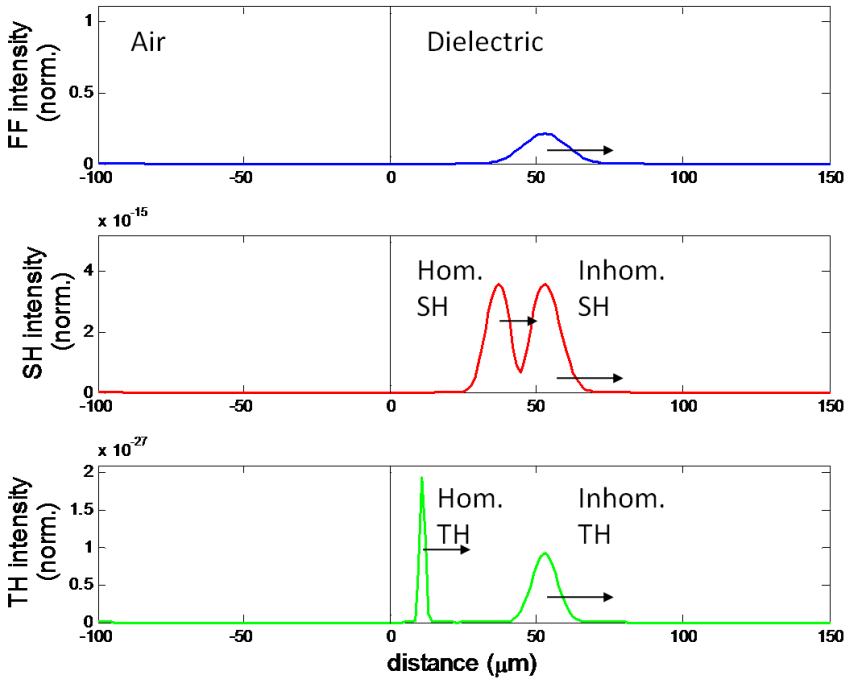

Figure 5.1. Snapshot of pump, SH and TH propagation into a generic dispersive material.

It is easier to separate and identify the different components of the fields if we depict the k-space power spectrum of the signals for a generic propagation moment as in Fig.5.1. In Fig.5.2 We find three components for the FF: a reflected signal in the air ($-k_{0\omega}$), a residual forward propagating signal into the air ($k_{0\omega}$) (due to the theoretical infinite extension of the Gaussian shape) and a forward propagating signal in the material (k_{ω}). For the SH and TH we find an analogue situation (with $-k_{02\omega}$, $k_{02\omega}$, $k_{2\omega}=k_{02\omega}n_{2\omega}$ and $-k_{03\omega}$, $k_{03\omega}$, $k_{3\omega}=k_{03\omega}n_{3\omega}$ respectively). All these signals have k-vectors as predicted by material dispersion. In addition to them we can clearly recognize the two inhomogeneous, phase locked, components at $2k_{\omega}$ and $3k_{\omega}$ respectively. These k-vectors do not respect the dispersion characteristics of the material, but they depend only by the propagation values of the FF. Note that the reflected signals are not visible in the Fig.5.1 just because

they have already propagated enough to be out from the visible spatial domain.

This scenario is completely generic. The relative intensities of the two generated components for each harmonic are on a comparable scale as long as the working conditions are far from the PM (in this particular case the phase mismatch is of the order of μm^{-1}). The positions of the peaks in the normal and k spaces are fixed by the dispersion values. Their amplitudes are slowly varying with the indexes mismatch of the materials forming the interface (air and a generic dielectric in this case).

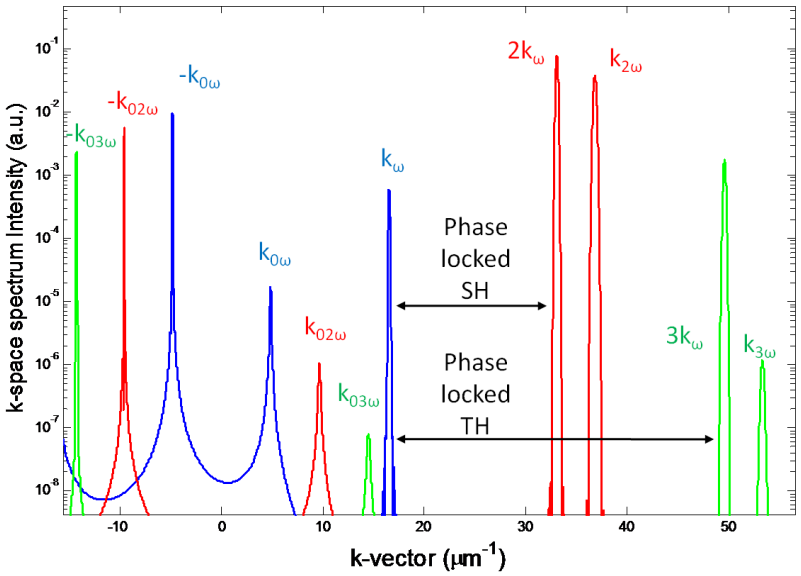

Figure 5.2. k-space spectrum of the fields depicted in Fig.5.1 (SH and TH field are out of scale).

The PL phenomenon did not attract much attention for a long period, basically due to the low conversion efficiency. Another reason is the difficulty of the inhomogeneous component to be manifest during the numerical simulations and the experiments.

There are two main evidences of its presence during the interaction: the two-component structure in the k-spectrum and the Maker fringes in the time domain. Regarding the first point, we need to note that the difference between $k_{2\omega}^{HOM}$ and $k_{2\omega}^{INH}$ can be very small in typical working

conditions. For example for a FF tuned at 1.2μm and the following indexes of refraction n_{FF}=1.8 and n_{SH}=2.0 we only get

$$k_{2\omega}^{HOM} = 17.6\mu m^{-1}$$
$$k_{2\omega}^{INH} = 16.8\mu m^{-1}.$$

If we have again a look on Fig.5.2 we see that it can be very likely that the two components are almost completely overlapped and it can be quite difficult notice their actual composition.

On the other side, concerning the SH pulse structure in the time domain we can make another easy example. Let us consider a super-Gaussian pulse having a spatial extension of approximately 50μm, incident from vacuum on a dispersive generic positive index material (PIM) as in Fig.5.3. We are able to clearly discern the typical spatial modulation that characterizes the generated SH intensity due to the finite coherence length (on the order of few μm), as the pulse samples the material. Because the FF and SH pulses do not propagate far into the medium and because the spatial extension of the FF pulse is relatively long, the two pulses do not have enough time to experience walk-off. The assumed dispersion yields group velocities V_{FF}^{g} =c/3.27 and V_{SH}^{g} =c/4.08. In this case it is not possible to clearly see the temporal separation between the two SH components. This situation can be associated with picosecond pulse propagation in a few microns sample, while the situation in Fig.5.1 is typical of short femtosecond pulse propagation in millimeters long sample.

As a result, only recently with the broad availability of short duration laser sources the researchers must deal with the real structure of the generated harmonics. Ordinarily, the existence of a phase mismatched component leads to low energy conversion. The behavior of the energy in time is also indicative of the internal dynamic of the generated SH. In Fig.5.4 we show the SH energy as a function of time for two phase-mismatched situations: a case corresponding to the pulse depicted in Fig.5.3, where pulse walk-off has not yet occurred (red curve) and a case which describes the situation depicted in Fig.5.1 where the walk-off and the energy clamping process are complete (blue curve).

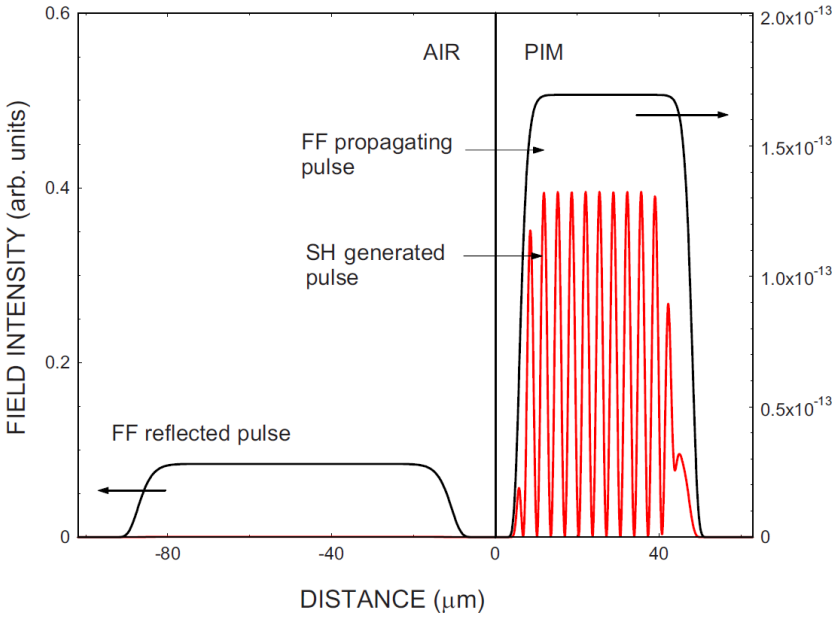

Figure.5.3. A picosecond super-Gaussian pump pulse (black, scale on left axis) propagates into a positive index material (PIM) having n_{FF}=1.8 and n_{SH}=2.0. The generated SH (red, scale on the right) presents Marker fringes due to the overlapped presence of the homogeneous and inhomogeneous components.

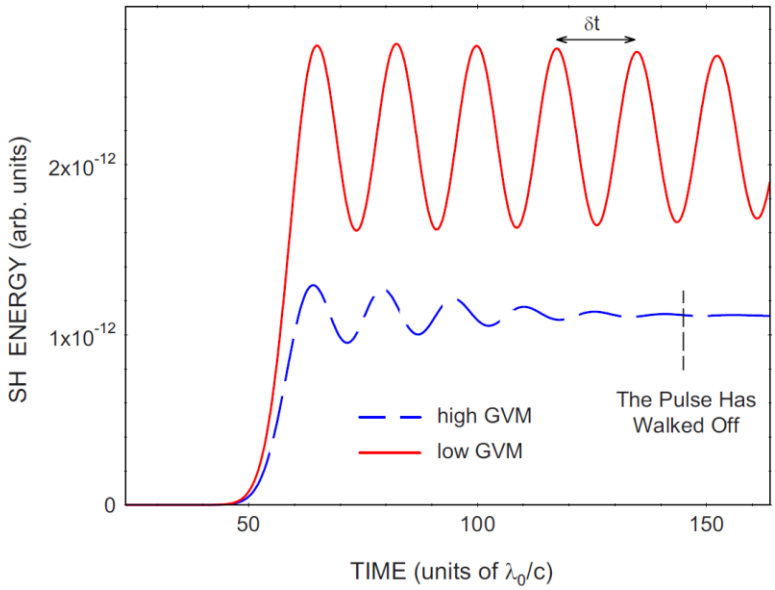

Figure.5.4. Comparison of energy vs time diagram for SHG under phase mismatched conditions. (blue curve) large GVM and (red curve) low GVM. The time interval δt correspond to the coherence length.

The two cases are generic and are distinguished by the group velocity dispersion (GVD) parameter that gives us the idea of the difference in the group velocity of the homogeneous SH pulse with the FF pulse (thus with the inhomogeneous SH pulse). Once the normal SH pulse separates, the SH energy quickly settles to a constant, steady state value. The PL is indeed a condition that prevents energy exchange to occur (we will give more details in the next Chapter). This is verified by monitoring the phase of the SH pulse as a function of time, at different longitudinal positions. It is a robust phenomenon that does not depend on any threshold intensity or a particular phase mismatch, and the outcome is also stable against the presence of absorption (as we will see in the next Chapter). The energy exchange diagram shown in Fig.5.4 suggests that the interaction evolves into a relatively simple phase link between the FF and the SH trapped pulse. It is apparent that the resulting dynamics comes about as a result of a relationship between the phases of the pulses, and not as a material feature.

To practically appreciate this double nature of the SH, it need a way to separate the two component either in time or in space. An experimental verification can be found in [Faz09] where this situation is analyzed in a two dimensional nonlinear crystal. A FF tuned at 800nm is launched at certain incident angle inside a $LiNb0_3$ crystal. The exit interface of a $LiNbO_3$ crystal was cut at 20^o respect to the orientation of the entry interface. The crystal is transparent for both the FF and the SH.

Extrapolating the previous discussion regarding the k-vector composition of the generated SH, at the exit interface we can expect two components propagating at two different output angles. The homogeneous component will propagate accordingly the Snell's law at its own dispersion values. The inhomogeneous component, on the other hand, will propagate in the same direction of the FF, so that the output angle will be determined by n_{FF}.

In Fig.5.5 are reported both numerical and experimental results. In the experiment, the fundamental beam impinges first normally to the entry interface, but it is then refracted at a certain angle at the exit accordingly to the Snell's law corresponding to n_{FF}. The generated SH is decomposed and

recorded in two spots: one refracts accordingly to the Snell's law at n_{SH} and the other faithfully follows the fundamental beam direction. Thus, the k-vector of the inhomogeneous SH has the same direction of the FF k-vector. We may conclude that the homogeneous SH "see" the index of refraction imposed by the dispersion value n_{SH} ($\neq n_{FF}$), but the inhomogeneous SH component "see" the same refractive index n_{FF} of the fundamental beam. In the same work ([Faz09]) it is also possible to find an experimental verification of the separation in time of the two SH components.

These numerical and experimental results show the behavior of the generated homogeneous and inhomogeneous harmonic components concerning the *real part* of the index of refraction. To have a full proof of our initial idea, we need a verification of their behavior concerning the *imaginary part* of the complex index of refraction. This will be the subject of the next section.

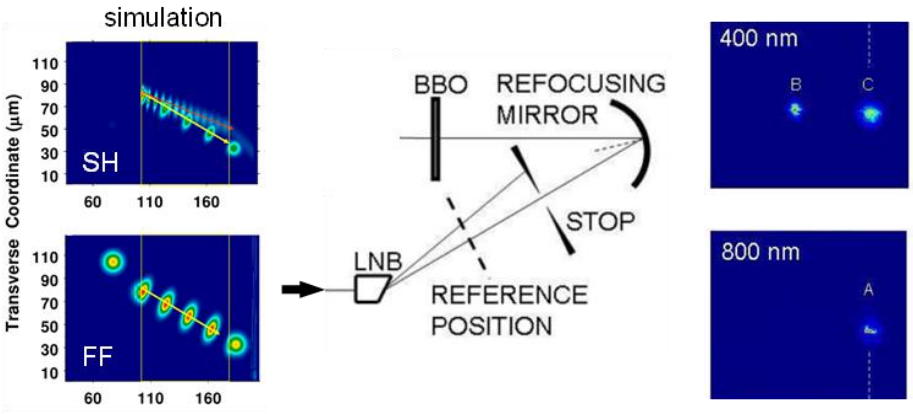

Figure.5.5. SH generation in a trasparet crystal ($LiNbO_3$) at a *not-normal* incidence angle. Numerical simulation (left), experimental set-up (center) and experimental recorded results (right). Two clear SH spot are recorded, one of those is at the same FF value [Faz09].

Chapter 6

Inhibition of absorption in opaque materials

6.1. Numerical Simulations

In the previous Chapter we studied the phase locked harmonic generation in a generic transparent medium. What happens now if a significant absorption is present at the SH wavelength? To say, do the homogeneous and inhomogeneous components still respond differently?

Since its inception in the early 1960s the study of nonlinear frequency conversion has focused on improving the efficiency of the process in transparent materials [Fra61, Gio62, Mak62, Arm62, Blo62, Sha68, Gle69, Man87, Noo90, Ras97, Su06]. Nonlinear conversion rates depend on factors such as phase and group velocity mismatch, peak pump intensity and nonlinear coefficient of the material. Linear absorption is considered

detrimental since it is assumed that the generated harmonics are reabsorbed. The question of harmonic generation in absorbing materials and/or semiconductors at frequencies above the absorption edge has previously been considered only in the context of measuring the nonlinear coefficients [Cha65, Bur61, Bri94, Mar00, Ver02, Ram00, Che95] thus with thin films or *in reflection* experimental set-up, but it has not been as widely studied as in the transparency frequency range. For example, the enhancement of THG in various types of glasses opaque to TH light was experimentally demonstrated [Ver02]. UV SHG above the absorption band edge in LiNbO3 [Ram00] as well as UV and X-ray [Che95] SHG in semiconductors have been reported. These works indicate that the subject of harmonic generation in absorbing materials is of interest partly for the purpose of realizing coherent sources, and because of the many potential applications that semiconductors find in optical technology.

A systematic examination of propagation phenomena and nonlinear frequency conversion below the absorption edge of semiconductors is still lacking primarily because these processes are thought to be uninteresting and inefficient, due to absorption and to the naturally high degree of phase mismatch. In this Chapter we dispel this notion, predict and experimentally observe the inhibition of absorption for femtosecond, SH and TH generated signals in a GaAs bulk substrate. If our analysis is consistent we expect that while the homogeneous components follow the dispersion characteristics of the material at the actual tuning, the inhomogeneous components will keep reading the complex index of refraction at the FF tuning, even if extremely different behavior will arise.

To answer to the initial question we now consider a propagation inside a 450μm thick GaAs substrate. The incident FF is tuned at 1300nm and has an intensity of ~160MW/cm^2. The pulse duration is of the order of hundred femtoseconds. The peak power is low enough to avoid shape changes due to self- and cross-phase modulation, and nonlinear pump absorption. We use the numerical model described in Chapter 1 to simulate the pulse propagation and the harmonic generation in this configuration. GaAs is transparent for the wavelengths above 900nm and strongly absorptive

below it, as it is possible to see in Fig.6.1. This means that both SH and TH signals are tuned well below the absorption edge of GaAs, at 650nm and 435nm, respectively. For a FF tuned at 1300nm, the characteristic absorption lengths of GaAs are typically much less than one micron. For example, transmittance through one micron of GaAs is ~10^{-4} at 532nm, and ~10^{-8} at 364nm. The plot in Fig.6.1 represents the complex index of refraction of GaAs as reported by Palik [Pal85]. The Lorentz parameters are thus chosen to reflect these data and, in particular, are ω_p=9.425, ω_r=2.98, and γ=0 for the pump (γ=0 effectively makes the medium transparent to the pump); ω_p=9.425, ω_r=2.98, and γ=0.5 for the SH; ω_p=9.425, ω_r=2.98, and γ=1.65 for the TH. The indexes of refraction for this tuning have the following values: n_{1300nm}=3.41, n_{650nm}=3.83+i0.18 and n_{433nm}=3.88+i1.55. The consequent phase mismatch for the SH is $\Delta k=4\pi(n_2-n_1)/\lambda_1$=4.06μm^{-1}. For a propagation in a L=450μm thick slab we can also estimate the parameter $\Delta kL=1.8x10^3$.

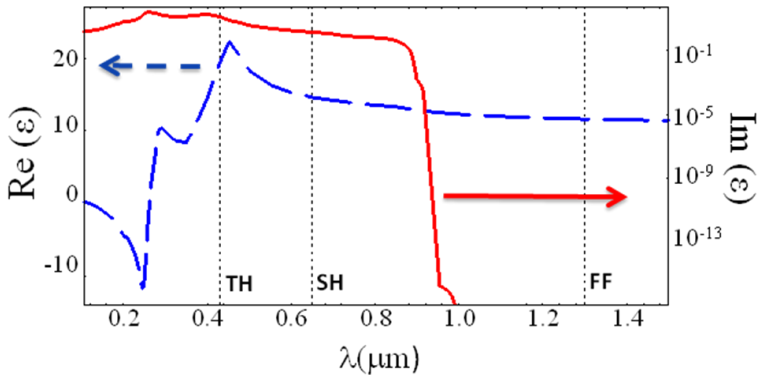

Figure 6.1. Real and immaginary part of GaAs as reported in Palik [Pal85]

For the sake of precision, we can note some discrepancy for the index at the TH among different reported values in literature and the value obtained here with the Lorentz model. This is due the high slope and high values of the complex dispersion curve around that wavelength. Moreover, the Lorentz model is used to model directly the permittivity of the material. To have a simple comparison between the absorption and not-absorption case as in the previous Chapter we only change the parameter γ. Real part of ε is

almost unaffected, while the imaginary part shifts from zero to a not negligible value. The index of refraction is then recovered by calculating the total square root of the complex ε. In the case of the TH wavelength, the high value of the imaginary part of ε sensibly changes the real part of the index of refraction. On the other end, the value of the real part of the index for the SH is practically insensible to the variation of γ. However, the validity of the whole following discussion it is not affected.

With these considerations in mind, in Fig.6.2 we show the pump and the trapped harmonic pulses propagating through a GaAs substrate. This situation is similar to that depicted in Fig.5.1. The dispersion values are comparable, but now a not negligible absorption at the harmonics wavelengths is present. The main difference is that now the homogeneous SH and TH components are completely absorbed few microns after the entry interface and only the inhomogeneous components propagates until the exit of the nonlinear medium.

In Fig.6.3, we depict the k-spectrum of the pulses shown in Fig.6.2. Also here we can note the absence of the homogeneous components; their spectral positions are marked by vertical red (SH) and green (TH) lines to better indicated their position. All their numerical values (in μm^{-1}) are shown in the following table.

FF in the *air*	$k_{0\omega} = \omega/c$	4.8
FF in the *GaAs*	$k_{\omega} = k_{0\omega}\, n_{\omega}$	16.5
SH in the *air*	$k_{02\omega} = 2\,\omega/c$	9.6
HOM SH in the *GaAs*	$k_{2\omega} = k_{02\omega}\, n_{2\omega}$	37.0
INHOM SH in the *GaAs*	$2k_{\omega}$	33.0
TH in the *air*	$k_{03\omega} = 3\,\omega/c$	14.5
HOM TH in the *GaAs*	$k_{3\omega} = k_{03\omega}\, n_{3\omega}$	55.1
INHOM TH in the *GaAs*	$3k_{\omega}$	49.5

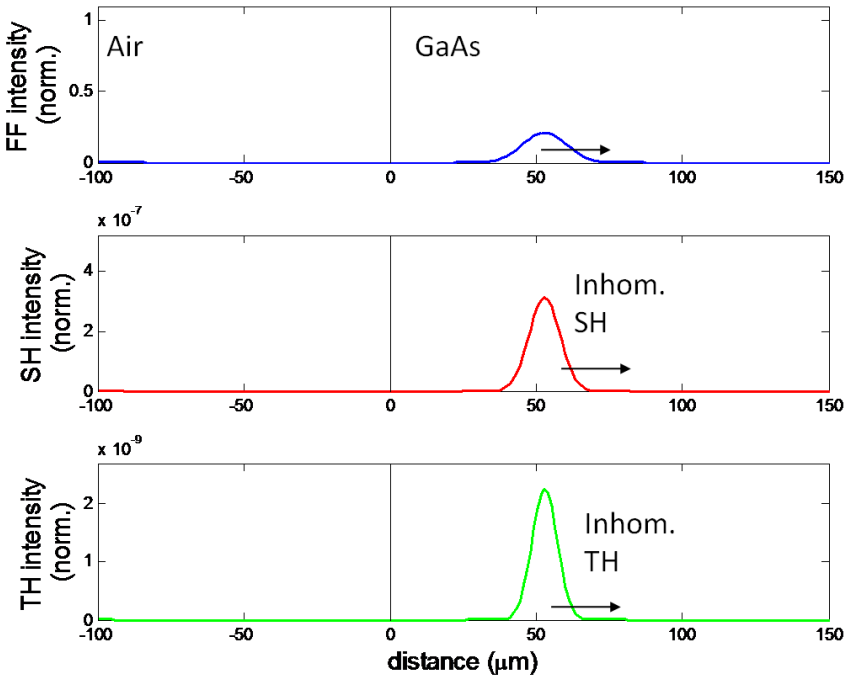

Figure 6.2. Snapshot of pump (tuned at 1300nm), SH and TH propagation into a GaAs slab. The SH and TH are tuned below the absorption band edge.

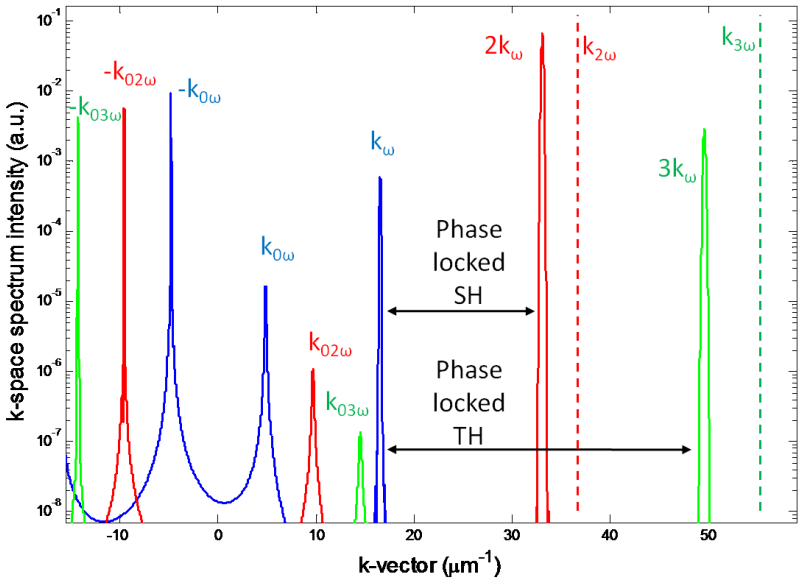

Figure 6.3. k-space spectrum of the fields depicted in Fig.6.2 for a propagation in GaAs (SH and TH field are out of scale).

These results definitively prove the possibility to generate and propagate SH and TH in opaque materials. This peculiar working condition is also quite interesting since it is possible to perfectly study the behavior of inhomogeneous component free from the homogeneous component in the background.

In Fig.6.4, we show the energy evolution of the pump and harmonic pulses inside and at the exit surface of the substrate. The FF and generated signals become stationary once the pump is completely inside the substrate. The energy exchange and the harmonic generation occur at entry (time ~150) and exit surfaces (time ~1200, corresponding to 450μm propagation distance), and the energies remain constant inside the substrate. At the exit surface, some SH energy is lost, while the TH signal nearly doubles in magnitude, although opposite behavior is also possible using slightly different material dispersion.

From this figure, one discerns that the SH and TH energies are generated at the entry surface and remain constant while the pulses transit through the sample. This is due to the fact that FF and harmonic fields are locked in phase. A spectral analysis of the signals shows that the frequency makeup of each pulse does not change with distance, an indication that no energy is exchanged. However, the pulses interact once again at the exit surface, where harmonic energy may be created (TH) and lost (SH).

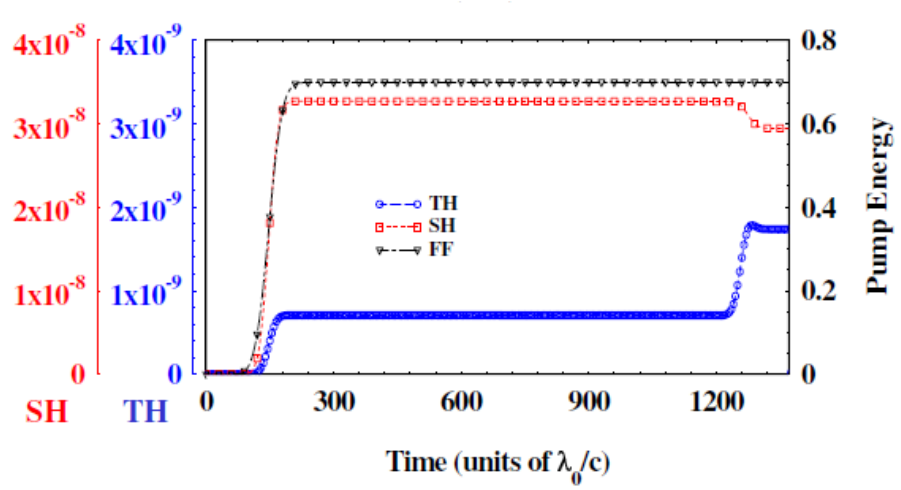

Figure 6.4. Pump (right axis) and harmonic (left axes) energies inside and to the right of the GaAs substrate.

6.2. Experimental results

Our calculations prove that the introduction of absorption causes the trapped harmonics to survive in the form of phase locked pulses. We have experimentally verified this phenomenon using the setup shown in Fig.6.5. An optical parametric amplifier pumped by ~100fs amplified Ti:Sapphire laser was used to deliver the pump pulses at 1300nm. We first filtered out all possible background component at the SH and TH wavelengths from the laser source by means of an equilateral dispersing prism. The collimated pump beam is incident onto the GaAs substrate at an angle of 20°. We chose GaAs mainly for two reasons. On one side it presents the absorption band edge in an useful position, so that we can use our IR lasers and record generated light in the absorptive range with not too much effort. On the other side it possesses a high nonlinear coefficient that reached values around 100pm/V. However, due to the $\chi^{(2)}$ tensor characteristics, this very high value is accessible only along one particular direction. Unfortunately, the growing direction of our crystals is turned by 90º, exactly where the $\chi^{(2)}$ coefficient is null. Choosing a propagation direction not normal to the crystal surface give us the possibility to use a quadratic coefficient that can vary in the range 0-100pm/V. 20º is a good compromise between the wish to get as much generated signal as we can and the need to not complicate too much the collinear experimental set-up. We expect to access to $\chi^{(2)}$~10pm/V.

After passing through the GaAs, the SH and TH fields were separated from the pump using a prism and lens/slit assembly. The moveable slit assembly provided a spatial filtering so that only one beam reaches the detection system. The signals were coupled to a spectrometer by means of a liquid light guide and were then measured using a near infrared photomultiplier (PMT) tube (for the pump) or liquid nitrogen cooled CCD array (for SH and TH).

The measured spectra for the pump and its first two harmonics are shown in Fig.6.6. The area under each spectrum corresponds to the measured energy (2.9μJ for pump, $3.7\text{x}10^{-8}$μJ for SH, and $7.3\text{x}10^{-9}$μJ for TH).

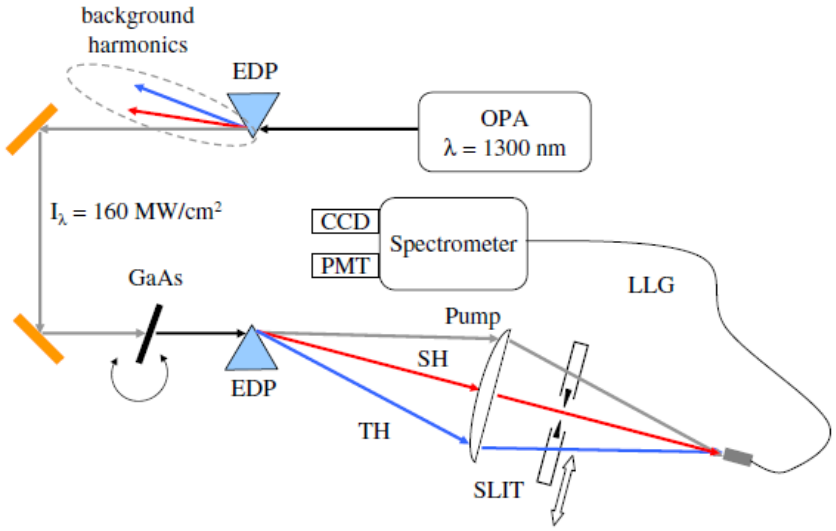

Figure 6.5. Experimental setup.

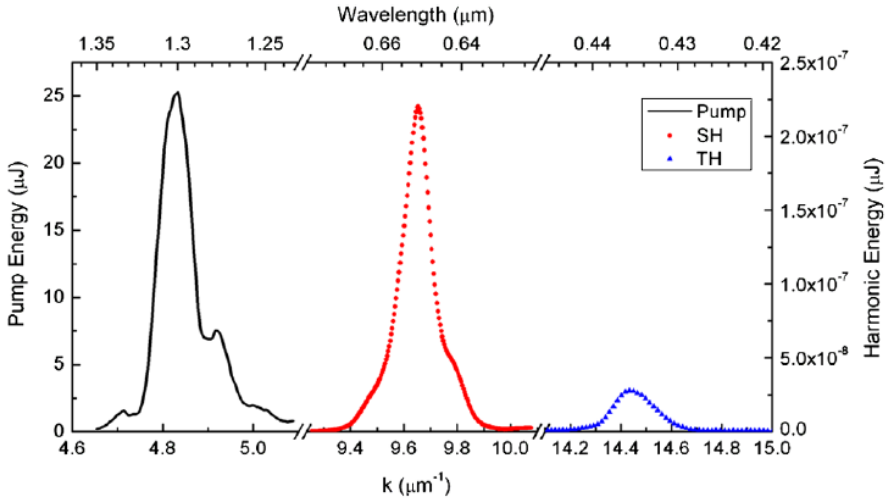

Figure 6.6. Measured spectra of the pump and the transmitted harmonics

Absolute values of the SH and TH energies were calibrated by sending laser beams of known power along the same optical paths and through the same detection system. We were therefore able to estimate the SH and TH conversion efficiencies to be 1.3×10^{-8} and 2.5×10^{-9}, respectively. Knowledge of the conversion efficiencies and pump transmittance data was used in the model to estimate $\chi^{(2)}\sim100$pm/V, and $n_2\sim10^{-12}$ cm²/W, respectively.

The results on the estimated $\chi^{(2)}$ is quite surprising. As outlined before, for our propagation direction we expect to access to a $\chi^{(2)}$ value of the order of only 10pm/V. This gave us the opportunity to realize that this experiment is *the first of the kind*. To our knowledge, nobody before never had the idea to try to record the generated harmonic signals in the *absorption spectral region* of the materials in transmission set-up. All the experimental $\chi^{(2)}$ values provided in the literature are measured in a reflection set-up, thus only partially accessing to the bulk nonlinear characteristics in this peculiar regime. Our estimated value of $\chi^{(2)}$ can be a hint that the dispersion curve of the quadratic nonlinear coefficient can reach higher levels respect those thought before. Indeed, after a careful research we finally found an experimental work [Ber03] where the authors measured $\chi^{(2)}$ coefficients in GaAs that can reach 500pm/V in the visible and UV spectral region. This confirms the validity of our experimental results.

Removing the GaAs sample from the beam path caused the conversion efficiencies to drop by a factor of twenty for the SH, and by a factor of two for the TH. The residual SH and TH signals come from the harmonic generation by any of the optical components present in the experimental set-up. As we pointed out before, the homogeneous components are absolutely negligible due to the high absorption and the long propagation distance.

The presence of *surface* generated SH and TH is a critic point often raised during the study and analysis of the results. At this stage the very good agreement between the experimental and numerical results do not leave much space for doubts regarding the origin of the generated signals. This notwithstanding, in a separate work [Sca10] we developed a detailed analytical model to evaluate the influence of other nonlinear sources, as for example electron gas pressure of surface currents. The main result is that at this scales the surface generated harmonic signals are not comparable with the bulk generated signals. In addition, as we will see later in the next Chapter, also experimental verifications are possible to confirm further this result.

Our theoretical and experimental results represent the evidence that absorption can be inhibited in opaque materials, well above the absorption edge of semiconductors and dielectrics alike. This dramatic result is due to a PL mechanism that causes the pump to trap and impress its dispersive properties to the generated harmonic signals. As a consequence, a GaAs substrate 450μm thick supports the propagation of red and violet light. Our results suggest that it is possible to achieve significant nonlinear frequency conversion at high frequencies, particularly towards the UV, using readily available sources and materials and that the still relatively low conversion efficiencies can be improved significantly in a cavity environment, where PL still holds. This will be the subject of the next Chapter.

Finally, as pointed out in Ref.[Zin07], accessing regimes that are outside the norm highlights the fact that our "understanding of nonlinear wave conversion phenomena is still far from complete", with many more surprises that are likely waiting to be revealed.

6.3. Pump undepletion

In the context of the inhibition of absorption at the harmonic wavelengths due to the PL mechanism, there is another aspect that is important to address at this point. That is to say, instead of the inhibition of absorption, it is possible at first sight to assume that the inhomogeneous component is indeed absorbed at the expense of the pump. The assumption of the flow of the energy from the FF to the inhomogeneous SH initially is indeed a valid option, but our investigations have shown that this does not occur. We numerically find that the energy in the SH signal remains constant regardless of our integration step. Should the inhomogeneous signal be continuously absorbed, pump depletion should manifest itself rather quickly, as the harmonics would represent a significant drain of energy. As a rough estimation, we can suppose that the SH is completely absorbed every absorption length (or skin dept, depending on the working

condition) of propagation. Consequently, every absorption length an amount of energy equivalent to the energy at the SH right after the entry surface of the material should flow monotonically from the FF to the inhomogeneous SH. Using the numbers achieved in the experiments in previous section it is needed a propagation distance of the orders of many centimeters before we could start to appreciate a depletion of the pump.

For this reason, as a clear example we want here to discuss a numerical case where we tune the FF beam at 800nm in the region of transparency (ε_{FF}= 2.64) of a virtual material, so that the SH is tuned to a wavelength range where the dielectric constant is negative (ε_{SH}= -5.5-i 3.3). This is an extreme case that in principle allows no propagating modes (see Chapter 8 for experimental results). The permeability is assumed to be μ=1. These dielectric constants correspond to indices of refraction n_{FF}(800nm)= 1.62 and n_{SH}(400nm)= 0.7 – 2.43i.

Under these working conditions the absorption length is extremely short. Indeed, since sign(ε) and sign(μ) are opposite, the material will behave as a metal. Here, supposing a bulk material, the most relevant propagation parameter is the skin depth. To evaluate the skin dept of the material at the SH, one may perform a simple numerical simulation using any of a number of commercially available codes, such as TFCalc or COMSOL. We tuned a plane wave at 400nm and made it impinging on a bulk material as detailed before. In Fig.6.7 we depict the field intensity near the entry interface. The intensity decreases to 1/e of its incident value in only 8nm.

Accordingly to our estimation, every 8nm or so the SH signal will have lost nearly all of its energy (a numerical value of $1.4\text{x}10^{-5}$ in this case). Thus, one may estimate that the FF field will be ~23% depleted after propagating 130microns inside the medium. In Fig.6.8 we report the energy of the FF pulse inside the material for both linear (where we set $\chi^{(2)}$=0) and nonlinear cases. The rise time corresponds to the time it takes the pulse to cross the interface. Materials parameters are such that pump transmittance by a single interface is ~94%. The figure clearly shows that total transmitted energy settles to about 94% after ~150 optical cycles have elapsed for both

cases. Since each optical cycle translates to a propagation distance of one wavelength, it is clear that the pump energy stays constant for hundreds of microns after crossing the interface.

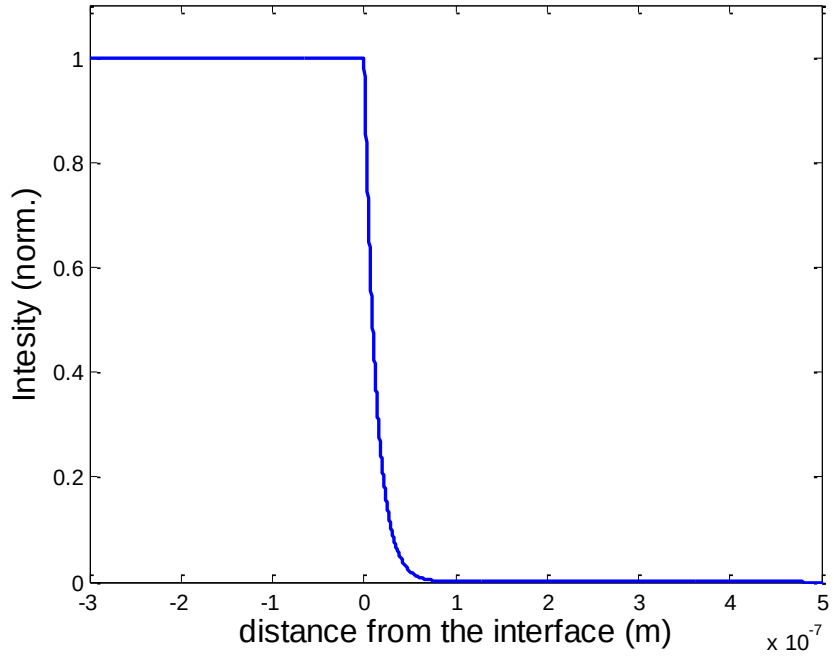

Figure 6.7. Intensity profile of a 400nm plane wave impinging on a material with ε_{SH}= -5.5-i 3.3 and μ=1.

This allows us to conclude that indeed the FF and the inhomogeneous SH do not exchange energy during the propagation, after an initial transient, even under the conditions where the SH field is tuned to the metallic region of the spectrum. Similar results are reported for THG in GaP (see Chapter 8).

In conclusion we outlined the general behavior of the generated harmonics from nonlinear material interface. Always present is the phase locked component with the peculiar characteristic to *not exchange energy with the FF field during the bulk propagation*. Its energy is fixed and generally orders of magnitude lower than the homogeneous component. This is because the usual working conditions tend to approach the PM situation

where a net flux of energy spills from the FF to the homogeneous component, making it difficult to observe the PL components.

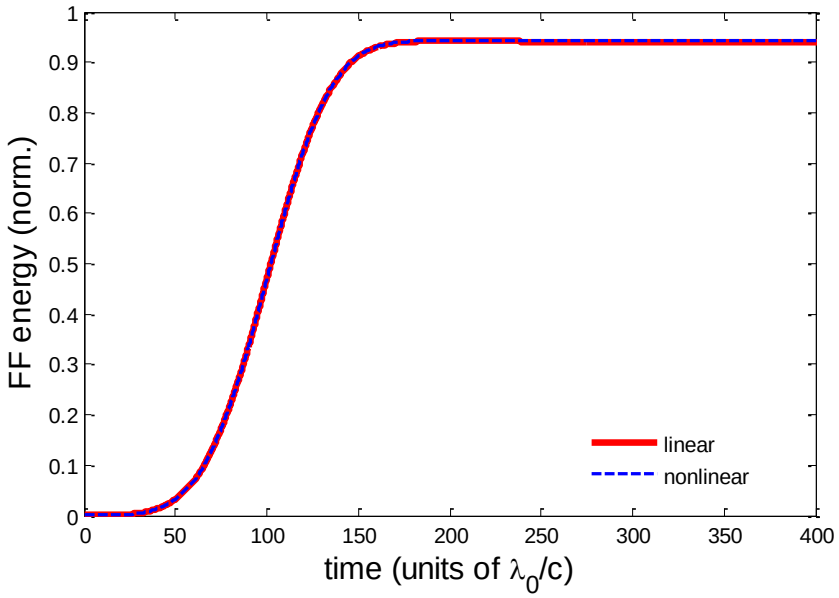

Figure 6.8. Energy profiles of the FF for both linear and nonlinear propagations in the case where the FF is tuned at 800nm with ε_{FF}= 2.64 and the SH is generated with ε_{SH}= -5.5-i 3.3. The two profiles are identical. The homogeneous SH component is promptly absorbed and the inhomogeneous SH component does not exchange energy with the FF.

Chapter 7

Field localization and enhancement in absorbing cavities

7.1. Introduction

In the previous Chapter, a systematic effort was initiated to study the dynamics of SH and TH generation in conventional transparent materials, but especially in opaque materials, under conditions of generally large phase mismatch, where the overall energy conversion efficiency of the harmonics is low. In this Chapter we want to assess the issue of the inhomogeneous phase locked harmonics behavior in a cavity environment. The goal is twofold: from one side we are searching for a fundamental confirmation of our theory on the phase locked harmonics; on the other side

we want to see if the phase locked signal could be intense enough to be readily and practically usable for applications.

The novelty of such field requires a step-by-step investigation to get a robust base where we can build our research. For this reason, we start with the simplest cavity structure: a free standing GaAs etalon. We have chosen this material for the reasons explained in the previous Chapter. However, the results can be extended to different nonlinear materials. Then we move in the second section to an experimental verification. Since the efficiencies involved are very low, we preferred to work with a slightly more efficient sample, namely a metallic mirrored GaAs slab. In the last section, finally, we study the efficiency of the phase locked component in high performance high-Q cavities. To mark in detail its trend, we prepared and analyzed four double dielectric mirrored GaAs samples with Q factor varying from 125 to 3830.

Before to start, it can be useful to briefly reassume the results achieved in the previous two Chapters. We showed experimentally that the imaginary part of the effective index of refraction that the inhomogeneous harmonics experience is equal to that of the pump. Then, it is easy to retrieve the information also for the real part. This may be done by performing a full spectral decomposition of the fields and by calculating the effective index of refraction $n_{eff}=c\langle k\rangle/\langle\omega\rangle$ as the ratio of expectation values,

$$\langle k\rangle = \int_{k=-\infty}^{k=\infty} k\,|H(\omega,k)|^2\,dk$$

and

$$\langle \omega\rangle = \int_{\omega=-\infty}^{\omega=\infty} \omega\,|H(\omega,z)|^2\,d\omega\,,$$

calculated in the sense of average quantities. The E field may also be used in the calculation. Once the imaginary part of the index is mapped onto the pump index of refraction, the real part of the index is obtained by performing a Kramers-Kronig reconstruction, which in turn yields a real part for the high harmonic field that is identical to the index of refraction for the pump field. Here the experimental data concerns the FF and the first

two harmonics, but due to the general nature of the phenomenon it is possible to easily extend the discussion to all the higher harmonics.

It is important to point out again that the two harmonic components (homogeneous and phase locked) have different nature and respond differently to the surrounding environment. The phase locked component travels locked in phase with the pump, and once its energy settles it does not exchange energy with the FF regardless of the propagation distance within the nonlinear medium. Every interface, linear or nonlinear (i.e. a discontinuous nonlinear coefficient) or perturbation in the linear and/or nonlinear characteristics of the material provokes a disengagement of the phase locked component from the fundamental and leads to energy exchange. On the other hand, the behavior of the homogeneous component is well known and relies only on the dispersive properties of the material at that frequency.

Hence it is straightforward to think of the possibility to completely separate the destinies of the two components, by letting them propagate in a situation where there is a substantial difference between the fundamental, SH and/or TH complex indices of refraction.

For example, in previous Chapter, a pump pulse was tuned in the transparent region of GaAs (1300nm). The SH and TH thus fall deep into the absorption region (650nm and 433nm), as can be seen in Fig.6.1, where the absorption spectra of GaAs can be clearly identified. In this situation SH and TH homogeneous components are completely absorbed within a few nanometers from the surface and the only observable SH and TH are the phase locked components. It then becomes clear that the survival of the harmonic fields can have significant consequences as it opens the door to new dynamical scenarios by allowing working conditions hitherto assumed inaccessible for absorbing materials, semiconductors in particular.

7.2. Free Standing Cavity

SH and TH localization

One may ask the following question: If the phase locked component experiences the same index of refraction of the FF pulse, how do the harmonic fields behave in a cavity designed to be resonant at the FF frequency? The answer is that the PL not only inhibits absorption at the harmonic wavelengths, but as we will show later, it also fosters the enhancement of harmonic generation by several orders of magnitude compared to the no-cavity case due to the double action of FF field localization and *anomalous harmonic field localization*. While the role of FF field localization is easily understandable, an explanation is needed to clarify the role of the harmonic field localization.

We can start to illustrate this concept with a simple free-standing GaAs etalon. Although GaAs is not required for our purposes (any absorbing nonlinear material will do) we choose to work under conditions similar to those chosen in the previous Chapter. In so doing one can first isolate and then focus attention on the phase locked component by studying its behavior in a cavity environment. A FF beam tuned at 1300nm generates SH and TH signals. The dispersion curves for GaAs (Fig.6.1) shows that it is transparent at wavelengths above 900nm and completely opaque below 900nm. The presence of the harmonic wavelengths in the opaque spectral range has been already clearly demonstrated in the previous Chapter.

Now let us reduce the optical thickness of the GaAs layer down to two FF wavelengths inside the material, so that the pump field resonates. The complex refractive index of GaAs is n_{1300nm}=3.41, n_{650nm}=3.83+i0.18 and n_{433nm}=3.88+i1.55, as reported by Palik [Pal85]. Conventional wisdom dictates that this structure should be resonant for the FF, but not for the SH and TH signals due to the optical thickness. More than this, the material is expected to absorb the wavelengths correspondenting to the SH and TH.

While this is true for the homogeneous components, the PL mechanism causes the phase locked components to resonate inside the cavity along with

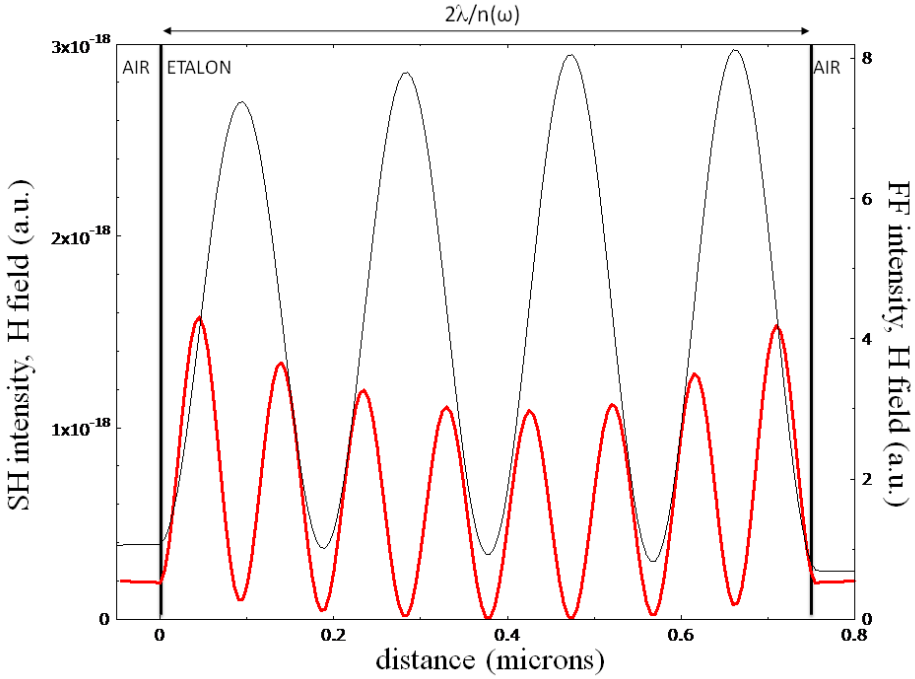

Figure 7.1. GaAs free standing etalon in air, two wavelengths thick. Fundamental (black, thin) and SH (red, thick) fields localization for 1300nm tuning. The SH propagates in phase with the FF.

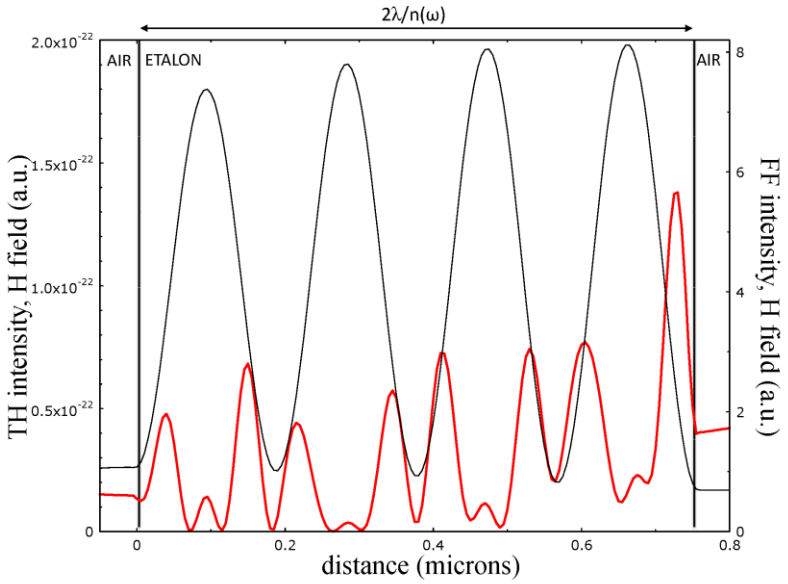

Figure 7.2. GaAs free standing etalon in air, two wavelengths thick. Fundamental (black, thin) and TH (red, thick) fields localization for 1300nm tuning. The TH propagates in phase with the FF.

the pump. For illustration purposes, in Figs.7.1 and 7.2 we report the results of a numerical calculation of the FF (thin line) and the harmonics (thick lines) inside the etalon. The figure represents the H fields of the FF, SH and TH for a certain snapshot during the propagation.

The calculations correspond to a general dynamical regime where a FF pulse more extended that the cavity length is impinging on the cavity from the air interface on the left and two harmonics are generated. These figures represent the situation with the actual values of the index of refraction of GaAs. As mentioned before, the homogeneous components are quickly absorbed while the phase locked components are free to resonate and become localized, following the pump. As a direct consequence, FF and harmonic fields propagate *in phase* with a typical cavity localization pattern and a consequent good overlap. To have a comparison, we have considered the same type of cavity, but we have artificially reduced the absorption of the material. This was done by restricting the values of absorption down to near zero at the harmonics wavelengths ($\gamma \rightarrow 0$). Under this (unrealistic) circumstance, the homogenous components are not absorbed and, in fact, dominate the dynamics. This behavior is clearly identified in the fact that the new harmonic field is *out of phase* and *does not overlap* the FF. These results are shown in Figs.7.3 and 7.4 for the SH and TH case, respectively.

To summarize, there are three notable elements that may improve SH and TH conversion efficiencies in an etalon: the localization of the FF, the localization of the harmonics fields, and the good overlap among them. Inhibition of absorption is accompanied by a pull of the harmonics, initially tuned far from any cavity resonance, into an effective resonant condition. The phenomenon will occur with any nonlinear absorbing material, including negative index material.

The example above is representative of a generic situation. To make a complete study of the behavior of the phase locked component in a cavity one needs to be more specific about the model under study and about the cavity considered.

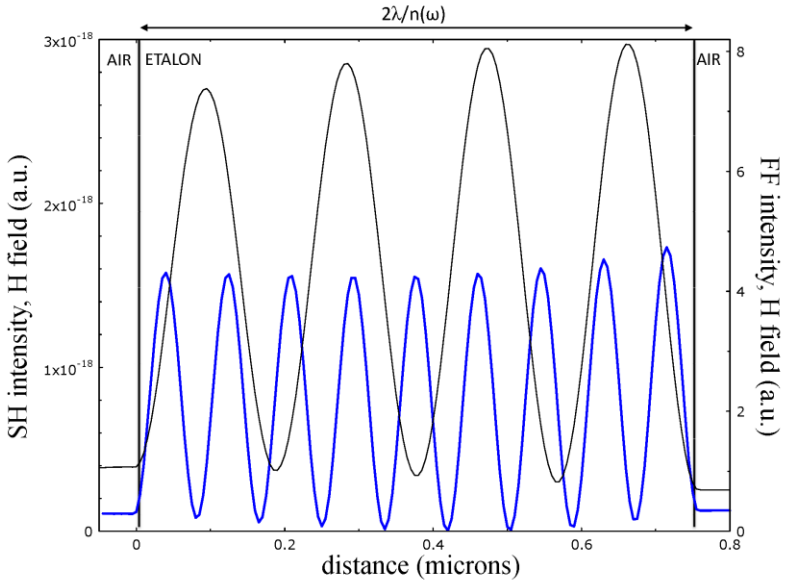

Figure 7.3. GaAs free standing etalon in air, two wavelengths thick. Fundamental (black, thin) and SH (blue, thick) fields localization for 1300nm tuning. In this case the absorption at the SH frequency is forced to zero. The SH is not propagating in phase with the FF owing to the presence of the homogeneous component.

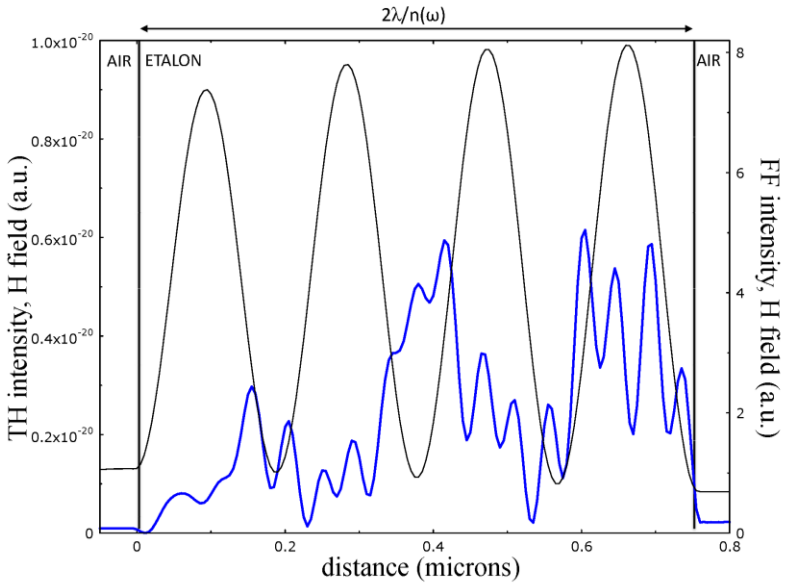

Figure 7.4. GaAs free standing etalon in air, two wavelengths thick. Fundamental (black, thin) and TH (blue, thick) fields localization for 1300nm tuning. In this case the absorption at the TH frequency is forced to zero. The TH is not propagating in phase with the FF owing to the presence of the homogeneous component.

The aim of this section is to discuss in some detail SH and TH behavior under unusual working condition of high absorption at the harmonic wavelengths using numerical solutions of the vectorial Maxwell's equations under pulsed conditions, as explained in Chapter 1.

Fig.7.5 represents our typical initial condition. The fundamental pulse is the on-axis cross section of a Gaussian-shaped pulse that has a spatial extension much larger than cavity size. The cavity is two FF wavelengths thick (in the material) $L=2\lambda/n(\lambda)=762.4$nm surrounded by air. The nonlinear coefficients are generically assumed to be $\chi^{(2)}\sim10$pm/V and $\chi^{(3)}\sim10^{-19}m^2/V^2$ accordingly the values found in literature. However, a different choice will not change the qualitative aspect of the results.

In fig.7.6 we report the calculated transmission spectrum of the structure. This cavity has a resonance at 1300nm (the FF wavelength), but no resonance features are present at the SH and TH wavelengths.

We have performed several calculations for different central carrier wavelengths λ(nm)= 1200, 1220, 1240, 1300, 1310, 1320, 1330, 1350, 1370. The frequency spectra of the FF, SH and TH signals are reported in the Fig.7.7. The input FF pulse is 30 optical cycles in duration, with a peak intensity of ~1GW/cm^2. There are two clearly visible maxima of generation at 650 and 433nm. As the tuning of the FF approaches the resonance wavelength (1300nm) the generation of both harmonics increases: while the fundamental is scanned across the resonance, the SH and TH fields are resonating as well.

Few considerations on the SH energy are useful. In Fig.7.8 we report three different energy conversion curves for propagation of pulses 10, 30 and 60 optical cycles in duration, respectively. The curves represent the total energy as a function of time. The SH pulse gains energy only when the FF pulse crosses an input or output interface. Once the FF pulse exits into vacuum, the energy of the SH stabilizes. As expected, pulses of longer duration tend to better resolve the resonance, and thus generate more SH signal.

As a comparison, in Fig.7.8 we also depict the energy conversion for propagation in a GaAs bulk medium under the same working conditions. It

is possible to evaluate a gain factor of approximately 4 between cavity and bulk situations. This value is in agreement with the poor quality factor of the cavity estimated around Q≅10.

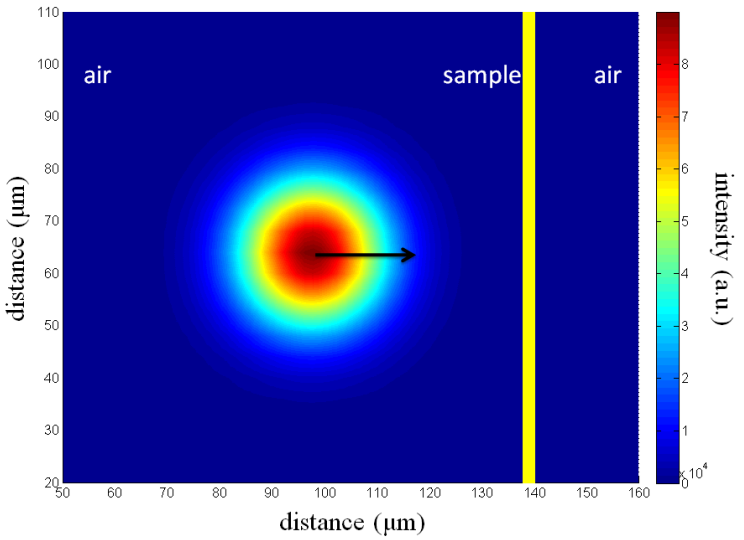

Figure 7.5. Initial condition of the calculation. A Gaussian shaped pulse is placed in the air and propagates toward the sample at normal incidence.

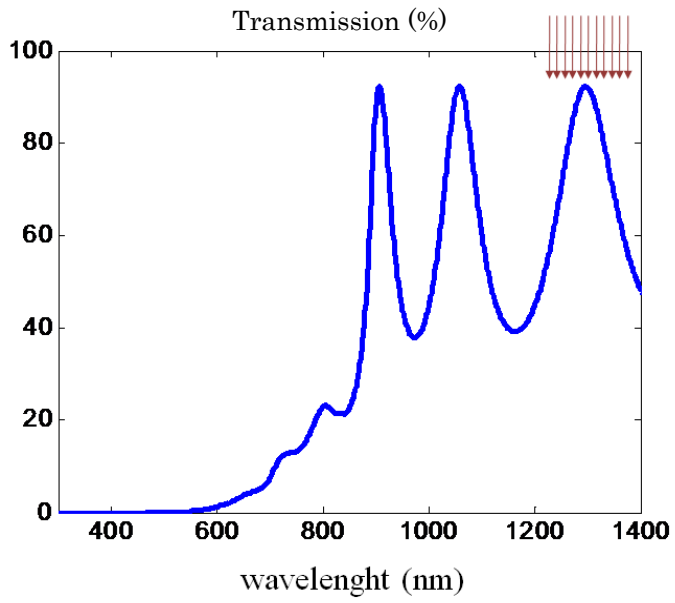

Figure 7.6. Calculated transmission spectrum of the structure. The scan of the resonance is marked.

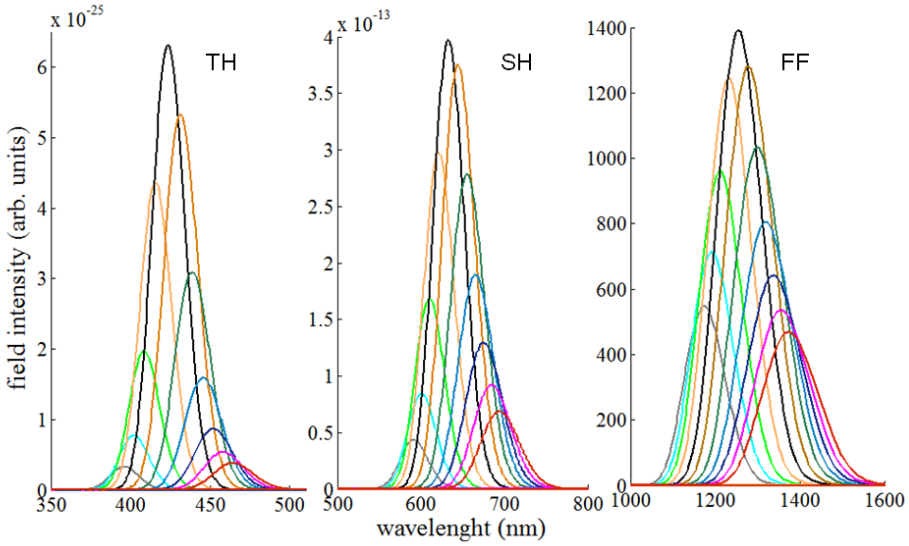

Figure 7.7. Calculated frequency spectra of the fundamental and of the generated SH and TH changing the tuning of the FF in proximity of the resonance marked in Fig.7.6 (1300 nm). The SH and TH fields experience the same resonance behavior of the FF, with maxima at 433nm and 610nm, respectively.

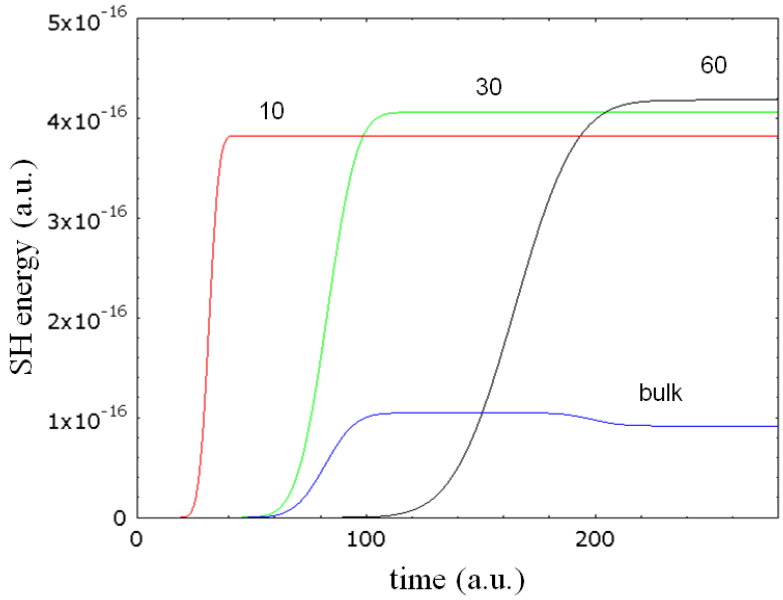

Figure 7.8. SH energy in function of the time for a FF pulse 10, 30 and 60 optical cycles long. As reference, the value for a bulk generation in the same working condition is reported.

The role of the cavity enhancement

In Fig.7.1 we saw how the phase locked SH is in-phase and well overlapped with the FF, while in Fig.7.3 we saw how the inhomogeneous component is out-of-phase and bad overlapped with the FF. These facts can be enough to hope in a higher enhancement of the phase locked components with respect to the homogeneous one. In addition, the opaque nature of the material at the SH wavelength has the role to get rid of this last component giving us the confidence that the signal we achieved in Fig.7.7 are indeed made by only the phase locked component. However the absorption of the material always needs some distance to have a complete effect and, in reality, for a structure as thin as the free standing etalon in this Chapter, we always expect some residual homogeneous SH and TH signals. Having a closer look to the transmission spectrum in Fig.7.6, for example, we can notice how the linear transmittance for the SH at 650nm is still assuming values of few percents, of the order of 2%.

The criticism that can be raised at this point is the following: even if a 2% of the homogeneous SH component is present in the interaction, can it be possible that this residual component is enhanced *faster* than the not-absorbed phase locked component in such a way the signal obtained in Fig.7.6 is made mainly by the homogeneous SH?

To better elucidate the aspects related with the interaction of a short pulse with a cavity environment we can now resort to a slightly simplified scheme. The role of the cavity is to enhance the value of the peak intensity of the impinging FF inside the structure. Thus, we can perform a set of numerical simulations in a transparent GaAs-like bulk similar to that in Fig.5.1, but now varying the value of the peak of the impinging FF.

In Fig.7.9 we depict a snapshot of the propagation in a GaAs-like material, where the absorption has been numerically turned off. We have used the exact parameters of GaAs, except the value of the absorption coefficient that is artificially fixed to zero. The top row represents the initial condition with a fundamental pulse 60 optical cycles long (~200fs) impinging on the material from air.

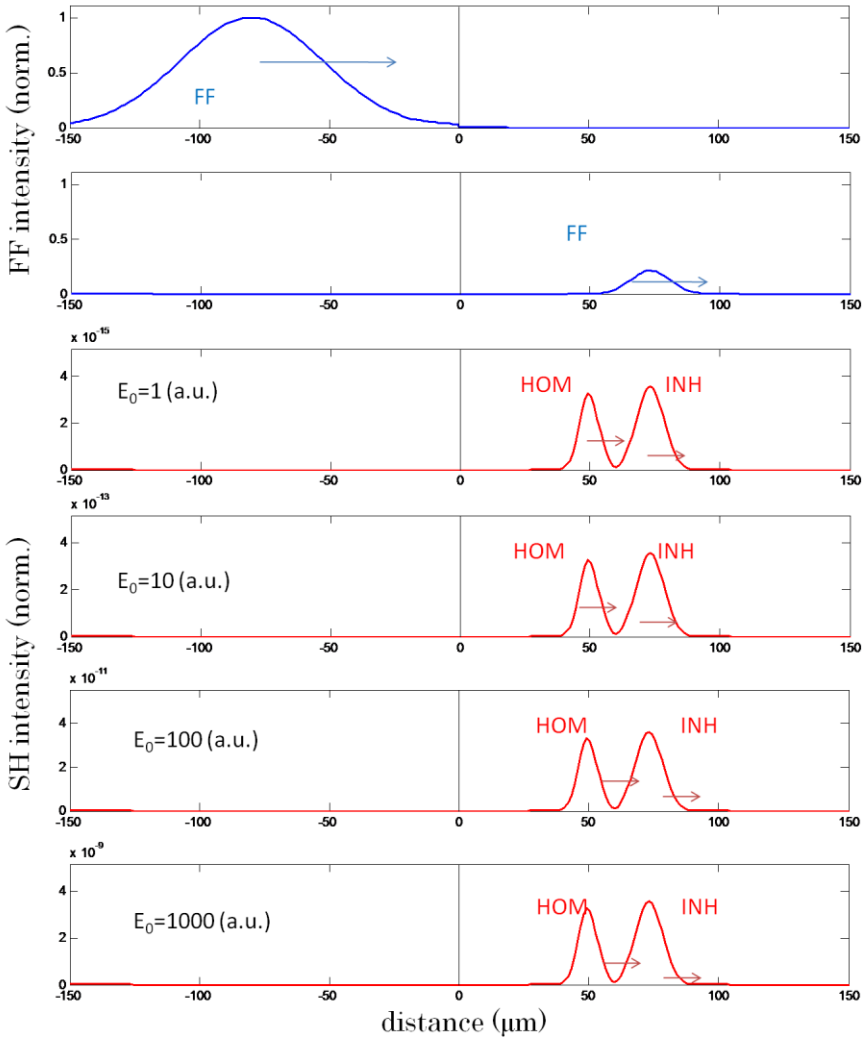

Figure 7.9. Propagation of FF (blue) and generated SH (red) for a not-absorbing GaAs-like material. From the top: FF initial conditions; FF after 75 μm propagation distance inside the material; generated SH at the same time for four different input FF levels.

The second row depicts the situation of the FF pulse after a propagation distance of 75μm inside the material. Due to the index mismatch (Air/GaAs), part of the FF pulse is reflected back into air. In the lower rows we depict the generated SH signal for 4 different values of the input FF intensity. The FF field is increased by one order of magnitude each time. As one can plainly ascertain from the figure, the two SH components are always present with comparable relative field amplitude.

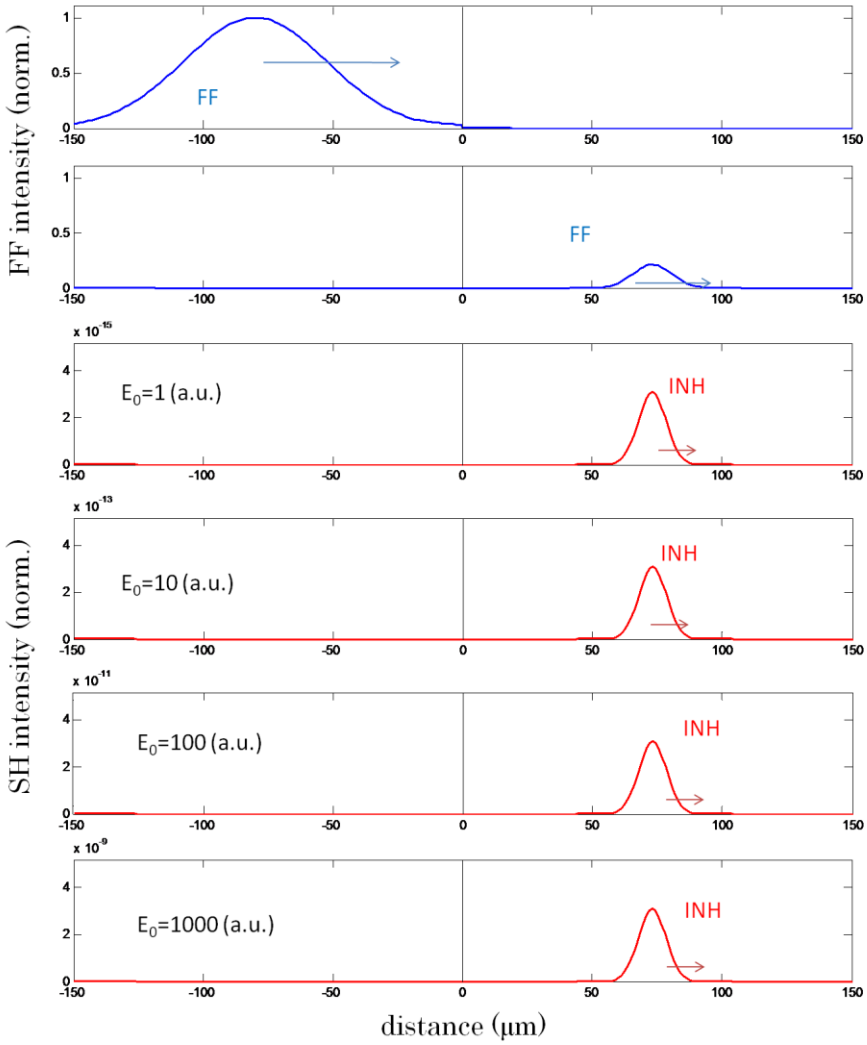

Figure 7.10. Propagation of FF (blue) and generated SH (red) in GaAs. From the top: FF initial conditions; FF after 75 μm propagation distance inside the material; generated SH at the same time for four different input FF levels.

If we were to detect the total SH generated in this transparent material we would have the signal made by the sum of inhomogeneous and homogeneous components. Approximately 50% of the detected signal will correspond to each of the two components. Increasing the input FF field does not change either the phase mismatch condition or the relative intensities of the two SH components. We observe that the peak intensities of the SH signals normalized to the FF input intensity peak (namely the SH

efficiency) grow quadratically with the incident input FF field intensity for *both* SH components. We will discuss this fact more deeply in the next section.

Let's now simulate the same situation, but using the actual GaAs data, namely taking absorption into account. The index of refraction at the SH wavelength yields an absorption length of approximately 100nm. In Fig.7.10 we report the results. The same considerations made above still apply. The only difference is that now the homogeneous SH component is completely absorbed near the entry interface. In contrast, the behavior of the inhomogeneous component is nearly unaffected because it experiences the same level of transparency as the pump field. In this case of *opaque* material, the detected signal at the output would be approximately 50% of the case of *transparent* material showed in Fig.7.9.

One may thus conclude that in the transparent phase mismatched condition, about half of the energy is stored in the homogeneous component and the other half resides in the inhomogeneous signal. On the other hand, in opaque material (at the harmonic wavelength), the energy stored in the homogeneous component is absorbed. If some residual signal is still present, it will never will grow faster that the inhomogeneous component.

k-vector distribution

To have a definitive answer to the problem posed above, it may also be useful to observe the spectral components of the generated field inside the cavity. Unfortunately, since the cavity length is very short compared with the pulse duration, it can be quite difficult to have a clear image of the two separated SH components in the k-space. The time the pulse experiences the cavity length is much less than the time the pulse freely propagates in the air, thus the k-components in the air always surround the other portion of the spectrum.

However, since at this stage we are more interested in qualitative results rather than in some exactly working condition, we can provide a clearer numerical result, very similar by just slightly more favorable than our previous working conditions. We simulate now a 1μm GaAs etalon for a

30fs FF field tuned at 1μm, while the SH is tuned to 500nm, where transmittance is less than 1 part in 10^4. In Fig.7.11 we presented the results in the k-space spectrum.

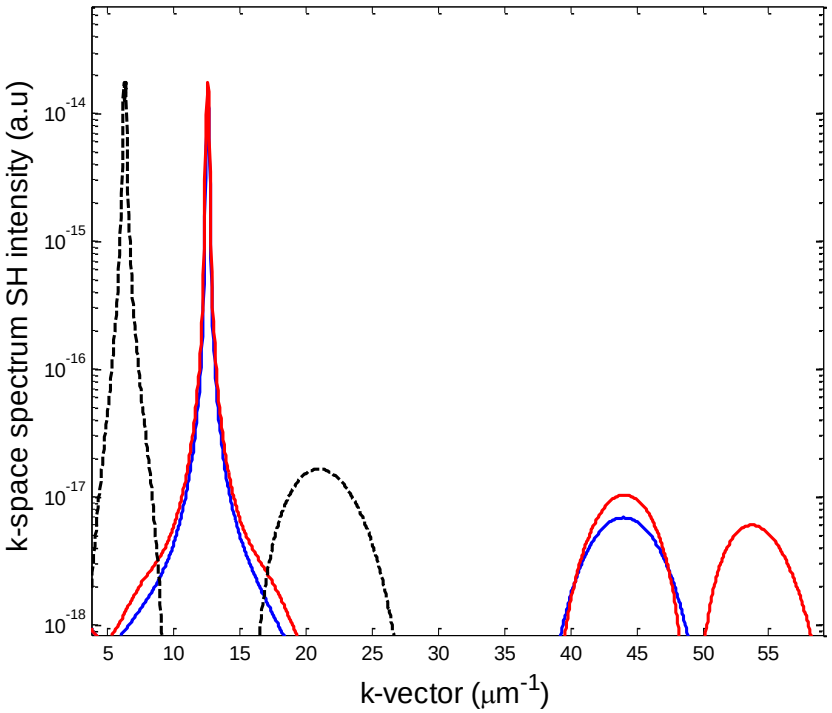

Figure 7.11. k-spectra of the propagation of 30fs FF tuned at 1μm in a GaAs 1μm cavity (dashed black, out of scale). Generated SH in the same GaAs etalon (blue) and generated SH in a GaAs-like cavity without absorption (red).

When the pulse impacts the structure all spectral components are present simultaneously. The black dashed curve is the FF, found mostly in free space (for this tuning $k_{0\omega}=6.3\mu m^{-1}$). We can also see the component related to the propagation into the material ($k_{\omega}=22\mu m^{-1}$). The red curve is the SH k-spectrum generated in the absorption-less GaAs-like material, and its spectrum contains: (1) the k-vector component that describes a SH field generated inside the cavity ($k_{02\omega}=12.6\ \mu m^{-1}$) and that immediately spills into the air; (2) the inhomogeneous k-vector component inside the etalon ($2k_{\omega}=44\ \mu m^{-1}$); (3) the homogeneous k-vector component in the material ($k_{2\omega}=53\mu m^{-1}$).

In summary, we have all the expected components when material absorption is absent.

In contrast, the blue curve represents the generated SH signal in the real GaAs. Please note that the part of the spectrum that corresponds to the homogeneous k-vector component is now missing, while the inhomogeneous component is almost unaffected. That is to say, the spectral decomposition of the fields clearly indicates the absence of the SH homogenous components, and the presence of the inhomogeneous SH signal. This is the definitive proof of the nature of the SH signal that survives inside an opaque cavity.

In conclusion, in this section the PL phenomenon was fully investigated in a cavity environment under pulsed dynamics, revealing the possibility to enhance harmonics conversion efficiencies thanks to the synergic action of the fields' localization. Finally, the theory has a generality wide enough to cover every situation where a harmonic field is generated. Thanks to the cavity environment a new range of possible applications are enabled, for example, frequency conversion towards the UV and XUV ranges.

7.3. Single metallic mirror cavity

Numerical calculations

In the previous section we highlighted the surprising behavior of SH and TH phase locked components with frequencies below the absorption edge by showing that, when the material is placed inside a cavity resonant only at the fundamental frequency, the PL mechanism not only inhibits absorption but also fosters the cavity localization of the generated harmonics, in such a way they perfectly overlap with the FF. We also start to discern the possibility that this localization will turn into an effective enhancement of the generated signals. Our interpretation is that this enhancement arises because of two complementary factors.

First, PL with a resonant pump (and in particular, the coincidence in the effective refractive index) pulls the harmonics into effective resonance

too, leading to field enhancement and increased energy exchange between the fields. In this regard, we note that the rate at which energy is transferred from a nonlinear source to a field at a harmonic frequency (for instance at frequency 2ω) is proportional to $\mathbf{J}_{2\omega} \cdot \mathbf{E}_{2\omega}$ at each point inside the material, where $\mathbf{J}_{2\omega}=-\partial \mathbf{P}_{2\omega}/\partial t$ is the current density and $\mathbf{P}_{2\omega}$ is the harmonic polarization induced by the FF. Since currents, polarization, and fields are local variables, the conversion efficiency depends on the strengths of both the FF and SH (or TH) fields at each point inside the cavity.

Second, if the cavity filled with the nonlinear medium is short (only a few wavelengths thick), the FF inside the medium *visits* the front and rear interfaces many times during the duration of a light pulse. As pointed out in the previous Chapter, in the opaque region it is just near the interfaces that energy can flow from the pump to the harmonic fields. Far from the interfaces, once the homogenous component is absorbed, the total energy of the phase locked component clamps and remains constant. In other words, both entrance and exit interfaces are constantly traversed by the FF and, as a result, the exiting harmonic fields are constantly generated by continuous interface crossings. The resulting field is also coherent with the fundamental since the pulse duration is much longer that the time needed to cross the entire etalon.

The conversion efficiency in the case of a simple etalon increases by only a small factor with respect to the case of a bulk medium, due to the fact that the Q factor of the cavity is relatively small. In this section we show that slight improvements to the cavity, for example, by adding a mirror at the back interface, can sensibly change the overall picture

To put into evidence the role played by the PL mechanism in a cavity configuration we have performed a numerical study aimed at finding the best possible conditions. We have considered two basic designs: a standard cavity with gold mirrors on both ends of the GaAs sample for simultaneous forward and backward SHG and a cavity with only the back mirror for backward SHG. Both configurations are schematically shown in Fig.7.12.

A plane wave FF of 100MW/cm^2 of average intensity impinges from the left side of the structure with an angle of 10^o with respect to the normal to

the surface. As we already explained before, the GaAs growing method makes the $\chi^{(2)}$ having the higher value in direction parallel to the entry surface while it is zero in the normal direction. A small incident angle, as in this case, will not be too detrimental for the characteristic set up of the cavity and will give us the possibility to access to a non vanishing value of the quadratic nonlinear coefficient. Thus, for these calculations we assume $\chi^{(2)}$~10pm/V.

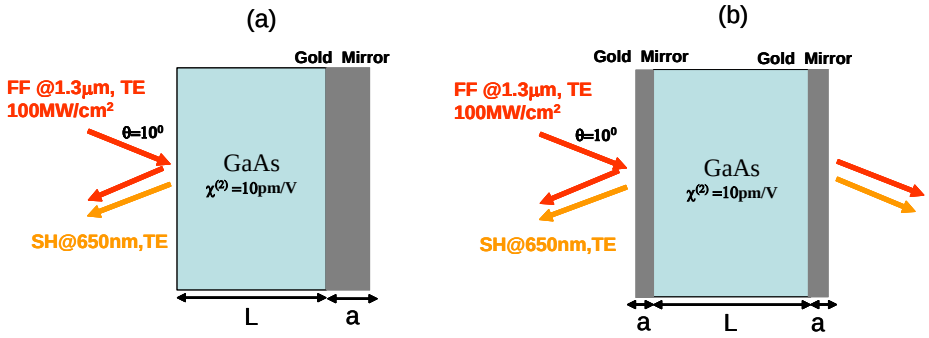

Figure 7.12. Schematic representation of the two geometries considered.

The thicknesses of the GaAs and of the mirrors will be for the moment parametrically indicated as L and a, respectively. The tuning of the FF is the same of the previous Chapter, namely with the FF at 1300nm with the generated SH below the absorption band edge at 650nm.

The SHG calculations have been performed using a standard Green function approach as detailed in [Mat05]. The length of the GaAs and the thickness of the mirrors have been varied simultaneously for both configurations and the corresponding SHG calculated. On the contrary to the previous case with the ideal free standing etalon, we now expect that the best performance will be achieved not exactly for an integer number of the FF wavelength into the material. This is mainly due to the asymmetry of the structures or to the presence of the metal. The GaAs length was thus varied in a range going from zero to an approximately three FF wavelengths in the material. The metal mirrors thickness was varied in a range from zero (no mirrors) to a convenient value depending on the structure.

The complex refractive indexes for GaAs and gold are taken from experimental measured data [Pal85] (also see previous Chapter). The results for the configuration in Fig.7.12(a) are shown in Fig.7.13, where the generated SH signal is reported as a function of both the GaAs and Au thicknesses. Due to the asymmetry of the structure, only the backward generated signal is considered. The emission behavior with respect to the variation of L (fixing a) is somehow periodic with a certain fraction of number of FF wavelengths into the material, as expected. However the best performance is achieved for L=645nm. Notice how this value is very close to 762nm that corresponds to two wavelengths of FF into a bulk GaAs. The emission behavior with respect to the variation of the thickness of the metallic mirror (fixing L) is slowly varying after a value of a=80nm.

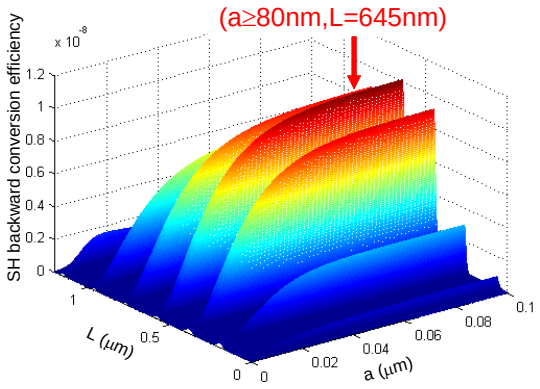

Figure 7.13. SH conversion efficiency vs. length of the GaAs and thickness of the back mirror for configuration in Fig.7.12(a). Backward generated signal.

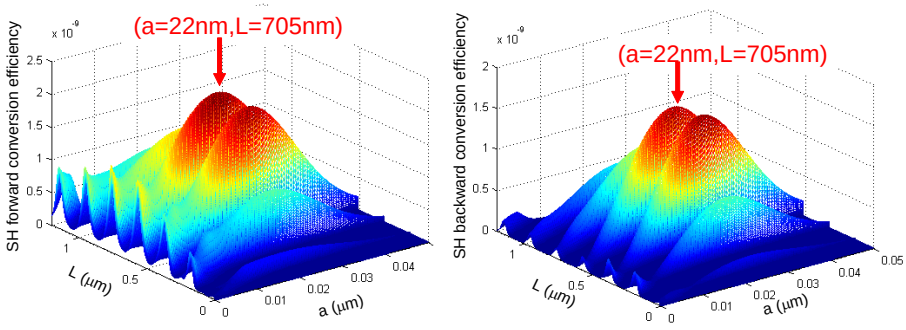

Figure 7.14. SH conversion efficiency vs. length of the GaAs and thickness of the mirrors for configuration in Fig.7.12(b). Backward(right) and forward (left) generated signals.

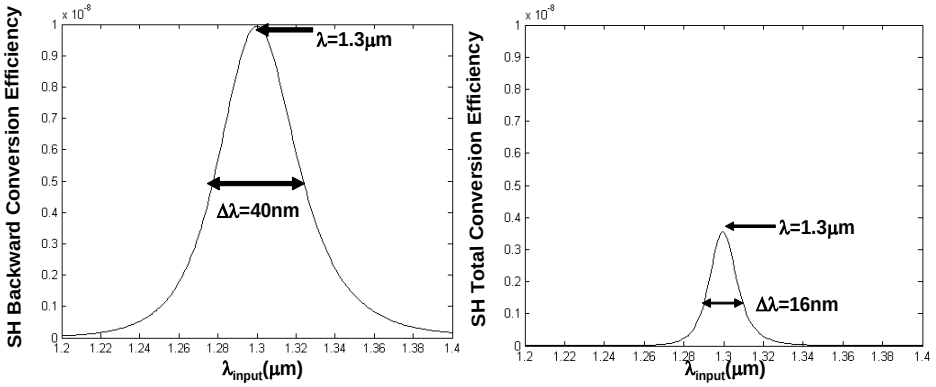

Figure 7.15. Spectral bandwidth of the SHG for configuration in Fig.7.12(a)(left) and in Fig.7.12(b)(right).

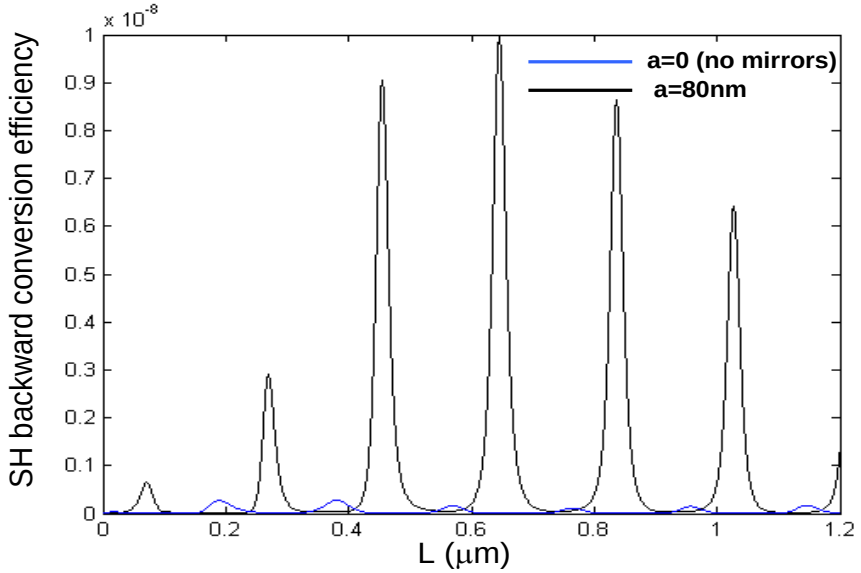

Figure 7.16. SHG from a simple GaAs etalon (no mirror) and from the same GaAs etalon plus a back mirror of 80nm.

The results for the configuration in Fig.7.12(b) are shown in Fig.7.14. In this case both backward and forward generated signals are considered due to the symmetry of the structure. They show the same kind of features with almost the same level of conversion efficiency. The emission behavior with respect to the variation of L (fixing a) is similar to the configuration in Fig.7.12(a), with a maximum value at L=705nm. The emission behavior with respect to the variation of the thickness of the metallic mirrors (fixing

L) presents a clear peak at a=22nm for both backward and forward configurations.

We note that for the configuration scheme in Fig.7.12(a) the best SH conversion efficiency, of the order of 10^{-8}, is obtained for a length of the GaAs of ~645nm and a length of the back mirror equal or greater than 80nm. On the contrary, in Fig.7.14 we note that the configuration in Fig.7.12(b) is far less efficient than the configuration in Fig.7.12(a), in fact we get a total (forward+backward) conversion efficiency of ~$3.5x10^{-9}$.

In Fig.7.15 we compare the spectral bandwidth of the SH emission as a function of the incident wavelength. From this figure it is evident that configuration in Fig.7.12(a) not only ensures a greater SHG, but also a better tunability.

It is important to spend few words about the crucial role played by the back mirror in the enhancement of the SH emission in the configuration in Fig.7.12(a). In Fig.7.16 we show the SH emission with and without the back mirror. The SHG with the back mirror is ~35 times greater than the SHG with no back mirror.

Experimental results

We now step to the experimental demonstration of our numerical prediction. We fabricate a structure following the optimum parameters found in the previous section for the configuration consisting of a GaAs layer having a back gold mirror as in Fig.7.12(a). The sample was fabricated using MOCVD to grow a 645 nm GaAs layer above a AlAs etch-stop layer, on top of a GaAs substrate. A gold mirror approximately 200nm thick was deposited onto the GaAs layer, aided by a few nanometers of Ti buffer layer to ensure good adhesion between the metal and the semiconductor. The structure was then glued upside down onto a silicon substrate using benzocyclobutene polymer. Finally, the GaAs substrate and the AlAs layer were removed using mechanical grinding followed by chemical etching. The structure is shown schematically in Fig.7.17(a). The calculated and measured linear reflectance from the sample, plotted in Fig.7.17(c), show

that the structure displays a resonance at the FF, 1300nm. However, the stack is not resonant at the SH and TH wavelengths.

In Fig.7.17(b) is reported in detail the experimental set up. We used a typical reflection measurement set-up. The source consists of ~100fs fundamental pulses from an OPA laser working at 1KHz repetition rate, with tunable wavelength between 1200 and 1600nm. The beam has a power of 200MW and was focused on the sample down to a ~0.5 millimeter spot size, with corresponding peak intensity of ~5GW/cm^2. The reflected signal was collected and analyzed with a spectrometer connected to a cooled Si CCD camera. Due to the nonlinearity of the material, SH and TH fields will be generated and recorded. Nine different measurements were performed from 1260nm up to 1420nm in 20nm wavelength steps (Fig.7.18). As references, the SH and TH signals generated from a simple gold mirror and a bulk GaAs sample, as well as the background illumination, were recorded with the same set-up and subtracted from the harmonic signals recorded with our sample. These references show clearly that surface SH and TH signals generated by the bulk GaAs and gold samples are negligible with respect to the harmonics generated by the cavity.

The SH and TH measured for each step of the fundamental tuning are shown in Figs.7.18(a) and 7.18(b), respectively. The vertical axis shows the conversion efficiency of each process. These results show that two generation peaks are clearly visible and, in particular, the maximum SH efficiency occurs at ~650nm and for the TH at ~435nm: this is remarkable proof that the harmonics display resonant behavior. The dashed curve represents the envelope of the fields obtained numerically in the continuous wave (CW) regime for the cavity in our experiment, and the agreement is very good when $\chi^{(2)}$~14pm/V and $\chi^{(3)}$~1.17x10^{-19}m^2/V^2. Due to field enhancement and overlap this time we recorded a SH conversion efficiency of order 1.5x10^{-7}.

The presence of the Ti layer, introduced as practical solution to a mechanical gold adhesion problem, unfortunately acts on the interaction in a detrimental way spoiling the sample structure scheme. However, even under these conditions conversion efficiencies are at least three orders of

magnitude larger than the SH signal generated by bulk GaAs under the same conditions (~10^{-10}).

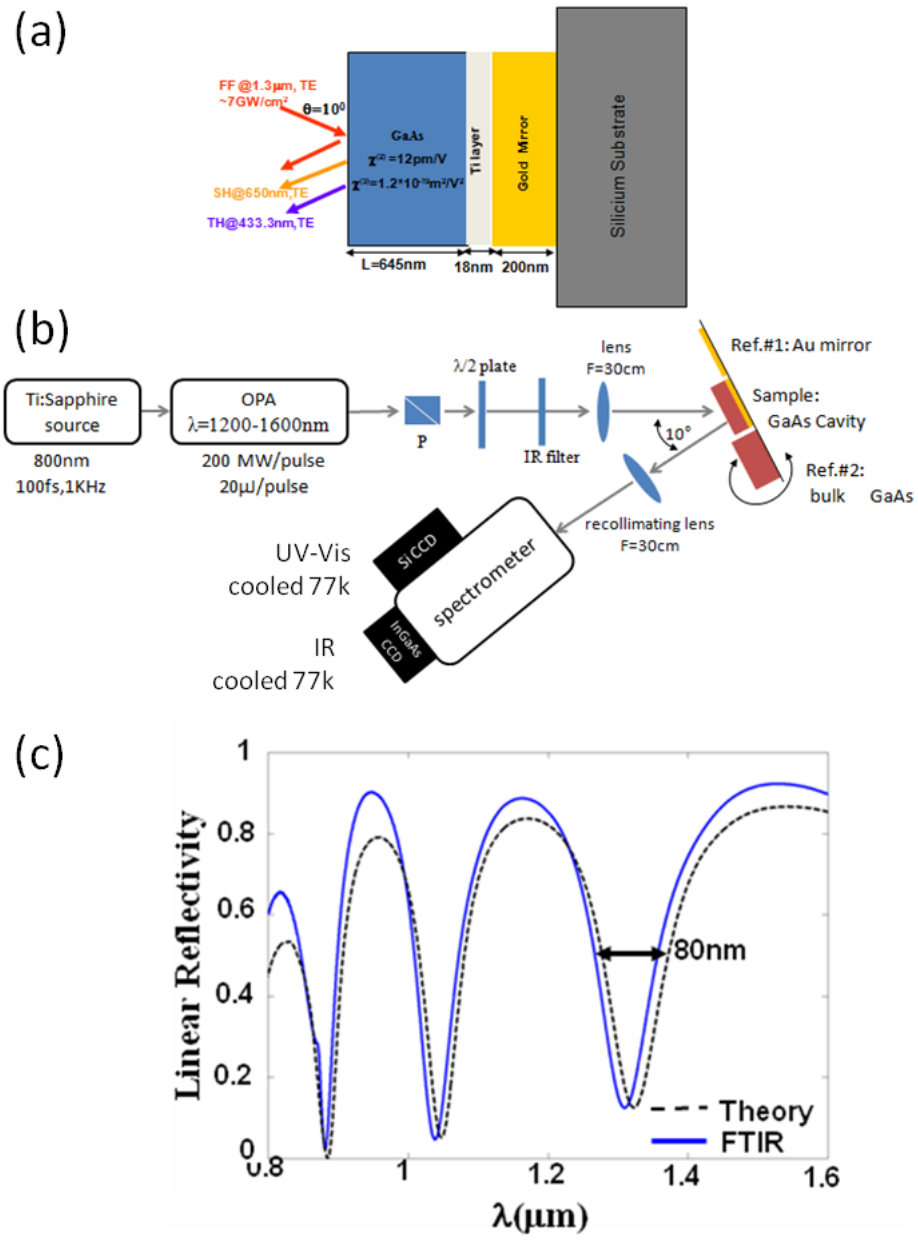

Fig.7.17. (a) Sample's scheme. (b) Experimental set-up. (c) Linear reflectivity of the sample taken by Fourier Transform Infrared Spectroscopy (FTIR) and comparison with theory.

With this consideration in mind, the estimated $\chi^{(2)}$ value can be actually under-estimated by almost one order of magnitude. This is in agreement with the study made on [Ber03] that found $\chi^{(2)}$ values of the order of hundreds pm/V for GaAs in the UV-VIS frequency range. Even more fascinating is the TH situation, where we recorded efficiencies of order of $1.4x10^{-8}$ under conditions of even higher absorption and *wrong* cavity length. This is a direct proof of the robustness of the PL mechanism.

The FF was recorded separately with a cooled InGaAs CCD camera. Neither the Si nor InGaAs CCD have a wide enough recording spectrum to be used at the same time to record FF and generated SH and TH. To evaluate the conversion efficiency scales in Fig.7.18 we used an independent HeNe laser source, whose signal could be measured at the same time with the Si CCD camera linked to the spectrometer and with a commercial power meter. In this way we were able to calibrate our recorded signals.

The consequences of this relatively simple experiment and calculations showed here open new possibilities to the examination of new optical phenomena in wavelength ranges that are far below the absorption edge. The results reported here have general validity, and apply well to semiconductors and dielectric materials alike, absorbing or not at the harmonic frequencies, as well as negative index materials, because the phase locked components do not experience the material dispersion characteristics at the harmonic wavelength. Finally, the right choice of materials based on the transparency window at the fundamental wavelength combined with cavity effects leads to relatively high nonlinear conversion efficiencies in GaAs at wavelengths well beyond the absorption edge, at 650nm and 433nm, respectively, with conversion efficiencies that are at least three orders of magnitude larger compared to bulk GaAs and can potentially be much higher. Our calculations show that conversion efficiencies may also be dramatically improved by sandwiching the GaAs etalon between distributed Bragg mirrors. This will be the subject of the next section.

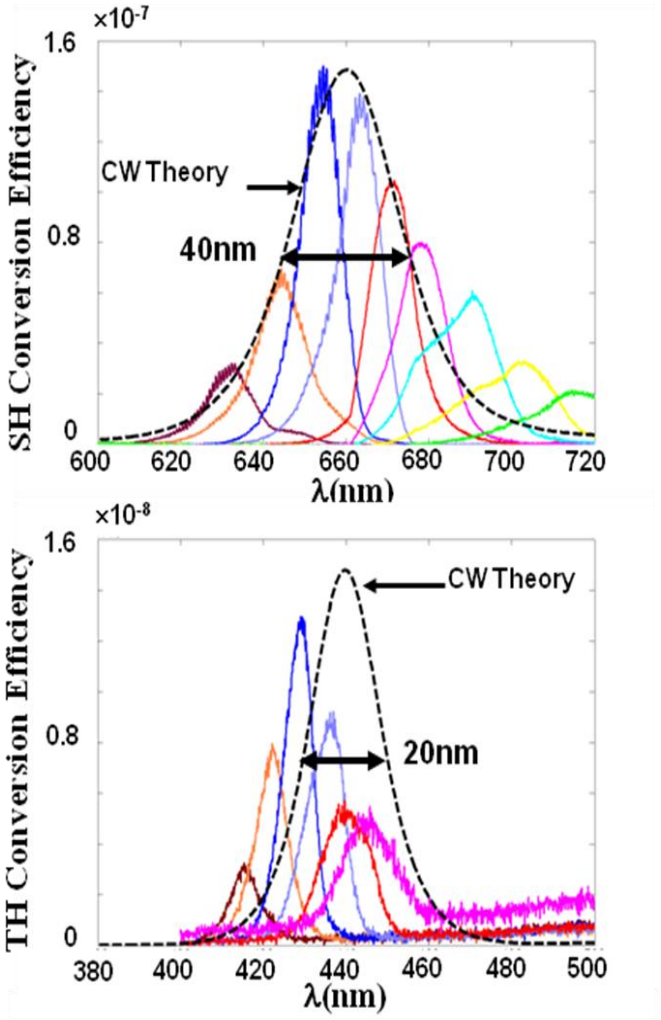

Figure 7.18. Experimental results for SH (c) and TH (d) signals. The dashed black curves represent the CW theory. The different curves represent the harmonic signals for different pump tunings (respectively from left to right 1260nm, 1280nm, 1300nm, 1320nm, 1340nm, 1360nm, 1380nm, 1400nm, 1420nm). We note that the bandwidths of the signals are in excellent agreement with the numerical predictions.

7.4. Double dielectric mirrored cavity

Defect microcavities

Before to describe our numerical results, we want to briefly remind here the main features of a Fabry-Perot type microcavity. To enhance the performance, multilayer films can be placed on both sides of the microcavity behaving like two perfectly parallel Bragg mirrors.

This kind of structure may be seen also as a *photonic crystal with a defect* that breaks the perfect symmetry of the structure and allows the localization of the light at certain frequencies within the forbidden bands.

Such microcavity type structures would trap inside any z-propagating light resonant with the cavity (see Fig.7.19). A specific mode corresponding to the photonic bang gap of the perfect periodic photonic crystal, that in principle should decay exponentially once it enters the crystal, may be trapped if its frequency coincides with one of the resonant frequencies of the cavity (see for example [Joa08] for more details). This light trapping results in a strong light localization within the defect.

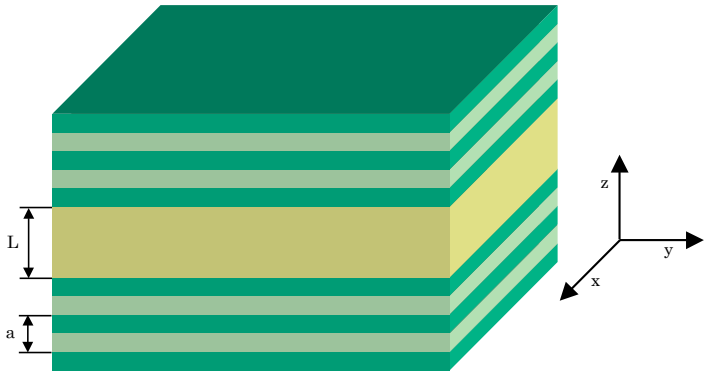

Figure 7.19. Schematic illustration of a photonic crystal with a defect, or microcavity. Defect modes appearing in such structure will be localized near the different colored layer that breaks the symmetry in the z-direction.

The reflectivity spectrum corresponding to such a microcavity is shown in Fig.7.20(a). A narrow band of frequencies that can propagate through the

crystal appears as a consequence of the introduction of the defect. The introduction of the defect results also in the appearance of a high energy density of the electric field at the defect site, which falls off exponentially as we move away from the defect. This high energy density can be used to enhance the interaction between light and matter, being especially useful when considering nonlinear interactions.

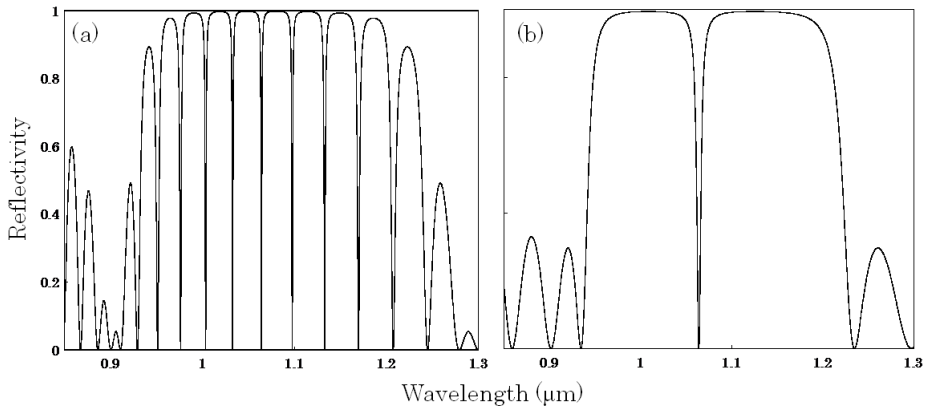

Figure 7.20. Reflection spectrum for a photonic structure made of 20 periods quarter wave Bragg mirrors (QWBM) structure with a defect. The thickness of the defect is equal to 1 μm (a) and to 10 μm (b)

For a fixed thickness L of the defect layer the peaks in transmission occur at wavelengths that satisfy the resonance condition: $\lambda = 2L\cos\theta / m$, where θ is the angle of incidence and m is an integer. When L is increased, several wavelengths may satisfy the resonance condition and the number of peaks increases as can be seen in Fig-7.20(b).

To decrease the width of the resonance it is possible to operate in two different ways: 1) increase the thickness of the defect keeping the same multilayer mirror structure or 2) increase the number of multilayer pairs in the mirror structure, keeping the same thickness of the defect. This last one is the strategy we used in our experimental set-up.

SH generation efficiency in high-Q cavities

In this section we want to pose the following question: is it possible to enhance SH in the phase mismatched regime using ordinary laser sources

and materials, up to a level that could rival harmonic generation from phase matched or quasi phase matched materials?

To take advantage of the inhibition of absorption of the phase locked SH component and find an affirmative answer to this question it is necessary to improve the nonlinear conversion efficiencies. As reported in the previous Chapter (and also in [Mak62, Jer70, Noo90, Su06, Kri04, Mle99]), using pump intensities of order 1GW/cm^2, conversion efficiencies from a single interface of GaAs or similar material is of order 10^{-10}. Presently we are not aware of analytical tools that might be used to infer the explicit expression of conversion efficiency for the phase locked component.

As a rough estimate of what one might expect in terms of conversion efficiency Fermi's golden rule provides a good practical procedure to follow. According to this rule, the spontaneous emission rate is [Fer50]:

$$\gamma = \frac{2\pi}{\hbar}\rho(\omega)|< f\,|\,\boldsymbol{\mu}\bullet\mathbf{E}\,|\,i>|^2, \qquad (2.1)$$

where $|f>$ and $|i>$ are final and initial states, respectively, ρ(ω) is the density of states, $\boldsymbol{\mu}$ is the dipole moment, and $\mathbf{E}$ is the local electric field. Both ρ(ω) and $|\mathbf{E}|^2$ are proportional to the cavity Q. As a result nonlinear conversion rates are proportional to Q^2. One should keep in mind that these estimates are just that, and that geometrical factors like field localization, dipole position and distribution inside the cavity intervene to alter these estimates through shape factors. In what follows we present results that confirm that this simple relation is a useful and practical tool to predict conversion efficiencies of the phase locked SH component.

In our experiment (in Fig.7.21(a) is sketched the set up) we used four different samples made of a 350nm thick GaAs layers sandwiched between different sets of distributed Bragg mirrors (Fig.7.21(b)). The samples were designed with 4, 6, 8 and 10 pairs of SiO_2(210nm)/Si_3N_4(120nm) layers on each side, respectively.

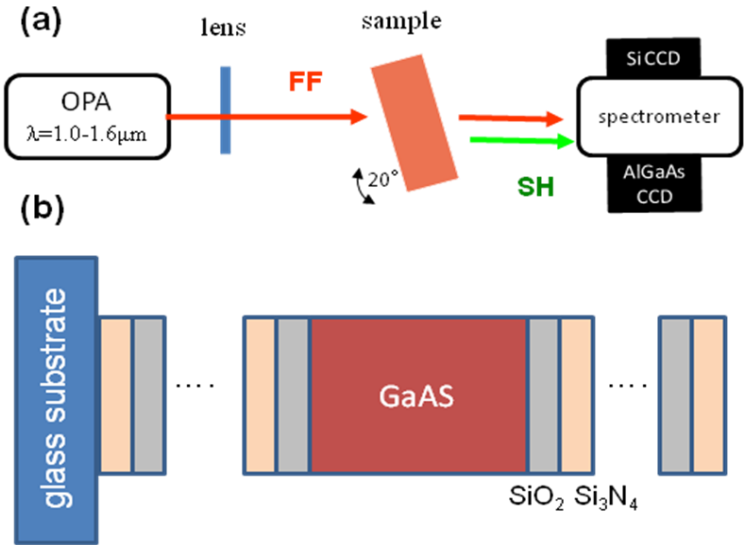

Figure 7.21: (a) Experimental set up and (b) Sample scheme.

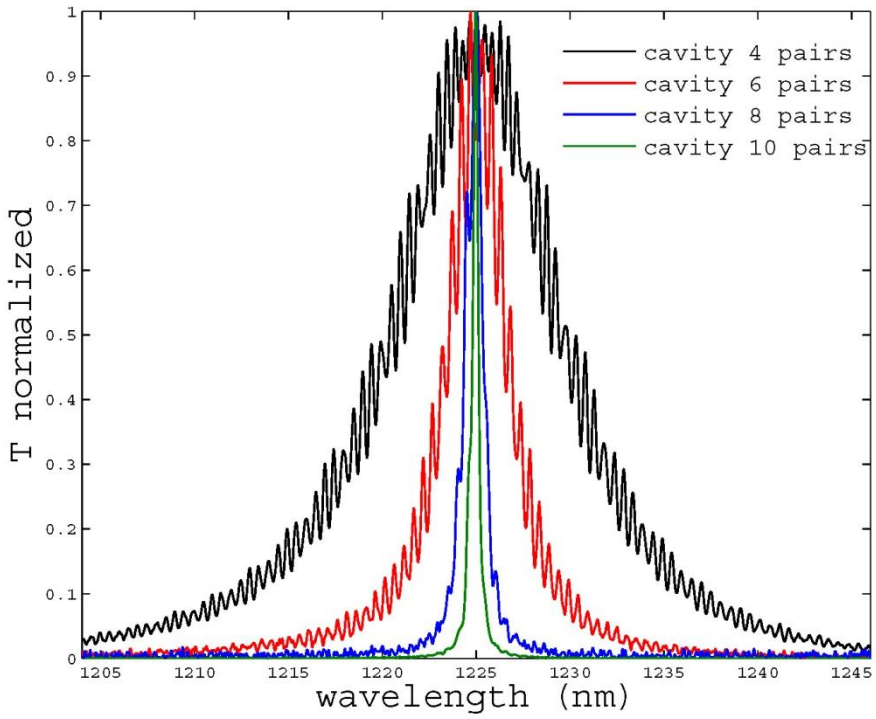

Figure 7.22. Samples transmission spectra. The transmissions of the samples are obtained from the transmission spectra of an ultrashort fs laser. The fast oscillations are due to the multiple reflections inside the 1mm glass substrate.

Each of these samples has a resonance centered at the same wavelength, but having different width due to their different quality factors. To ascertain the resonance shapes and widths we experimentally illuminated the samples with an ultrashort femtosecond pulse. The measured resonances are shown in Fig.7.22. The resonances are all centered at λ=1225nm and have widths (FHMW) of 9.3nm, 2.6nm, 1.2nm, and 0.32nm, respectively. The corresponding cavity Q factors, calculated as $Q=\lambda/\Delta\lambda$, are 125, 350, 1200 and 3830.

The difference between this kind of dielectric sandwich and the free standing GaAs etalon discussed in section 7.2 is that in this case the internal field is amplified by hundreds of times relative to the incident field. The linear properties of the stack are such that it is transparent at the FF wavelength and allows it to become localized, but it remains opaque for the SH (the transmission at 612nm is less than 5%). This guaranties that the observed SH signal consists of phase locked SH component only. In Fig.7.23 is reported the linear transmittance for the 6 pairs mirror sample. The blue curve is the transmittance of the real sample while in comparison the red curve is transmittance of a similar sample obtained numerically turning off the absorption inside the GaAs layer. Notice how the two structures behave identically at the FF wavelength, while the real sample starts to absorb for wavelength less than 900nm. The red curve gives us, on the other hand, an idea of linear gaps possessed by the whole multilayer structure due to the multi reflection inside the stack. These gaps will affect also the generated phase locked harmonics inside the GaAs layer, being them nonlinearly uncoupled with the FF inside the dielectric mirrors. In other words, after the inhomogeneous SH and TH are generated inside the absorptive GaAs layer thanks to the PL mechanism, their intensities at the exit of the sample will depend on the linear properties of the distributed Bragg mirrors. We then carefully designed the sample being sure that at least the generated SH will not experience a too low linear transmission. Unfortunately, inevitably the TH will fall in a band gap where the linear transmission approaches zero (see Fig.7.23). For this reason we will focus now only on the generated SH, leaving the study of the TH for a future work.

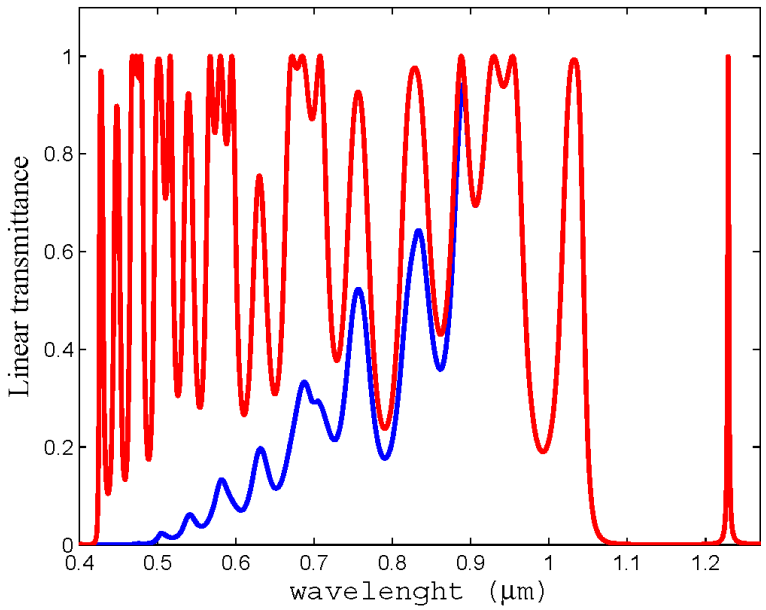

Figure 7.23. Linear transmission of the 6pair mirrors sample. (blue curve) real GaAs cavity structure. (red curve) GaAs-like structure without absorption.

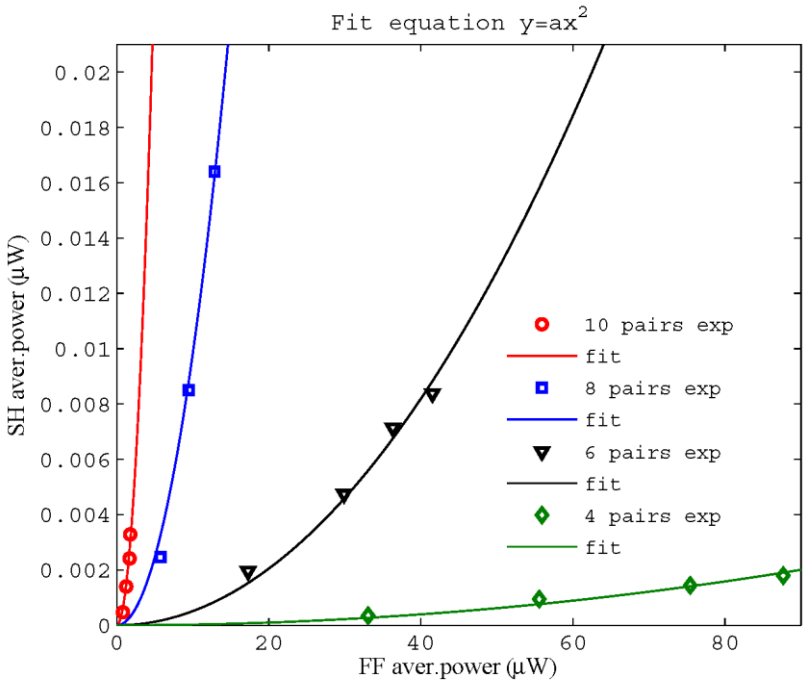

Figure 7.24. Experimentally measured behavior of the SH output power versus the input FF power for all 4 samples. The continuous lines represent the quadratic fit.

The FF pulse centered at λ=1225 nm was provided by a tunable OPA and was slightly focused down to a spot of about 500μm onto the sample. Its duration was fixed at 3ps and the intensity incident onto the sample was of the order of 10MW/cm^2. The transmitted signals at the FF wavelength were collected with a cooled AlGaAs camera, and the ones at the SH frequency were recorded with a Si detector. The sample is rotated 10^o degree to take advantage of the non vanishing $\chi^{(2)}$ in that direction.

The SH efficiency was normalized to the effective FF energy that finds its way inside the cavity. To account for the spectral width of the pulse, for each sample we calculated the overlap between the FF and the cavity spectra. In short, after we put the sample in place in the experimental set-up the laser source was shifted to shorter duration (around 80fs). This broad spectrum pulse is able to scan the effective transmission characteristics of the sample (Fig.7.22). Multiplying this spectrum for the spectrum of the 3ps pulse used during the experiment we can estimate how much FF energy has actually penetrated inside the cavity.

For each sample we first measured the behavior of the SH output power versus the input FF power (Fig.7.24). As shown in the figure, the SH follows a regular quadratic pattern. This is an indication that two-photon absorption and other non-linear effects are not affecting the generation process in an appreciable measure. Notice how the FF power range becomes smaller for higher Q cavities due to the smaller bandwidth of the resonance. At the same time, the enhancement of the FF field within the cavity increases with the reflectivity of the cavity's mirrors, leading to more efficient SH generation for higher-Q cavities. To operate in a safe region for all sample, we chose to extrapolate the SH efficiencies corresponding to 0.15MW/cm^2 of FF intensity. This corresponds more or less to the last experimental point for the 10-mirrors pairs sample in Fig.7.24.

Finally, in Fig.7.25 we report for each sample the SH conversion efficiency vs. cavity factor Q. The circles show the experimental points and the solid line is a quadratic fit of the data. The first circle marks the bulk emission (see Chapter 6). The results are thus in good agreement with the general estimate made previously in Eq.(2.1). The figure shows that it is possible to achieve efficiency of the order of 0.1% with external pump peak

intensities of order 10MW/cm^2, which for 3ps incident pulses leads to 0.15MW/cm^2 inside the cavity. This means that there is real potential for pump depletion with relatively low intensities (tens of MW/cm^2), provided the incident pulse resolves the resonance. In this particular situation the FF peak power was kept conservatively low to avoid two-photon absorption at the pump frequency, which can be considerable in GaAs at these wavelengths. Beyond this, the phase locked SH behavior is completely general and possible devices could be designed by choosing more appropriate materials, such as polymers, to outperform GaAs given the potential for much higher nonlinear coefficients [Ber03]. Finally, these results are easily extended to THG, as shown in the first section of this Chapter. In this particular case the cavity was not optimized for THG, which happened to be tuned inside a band gap of the stack.

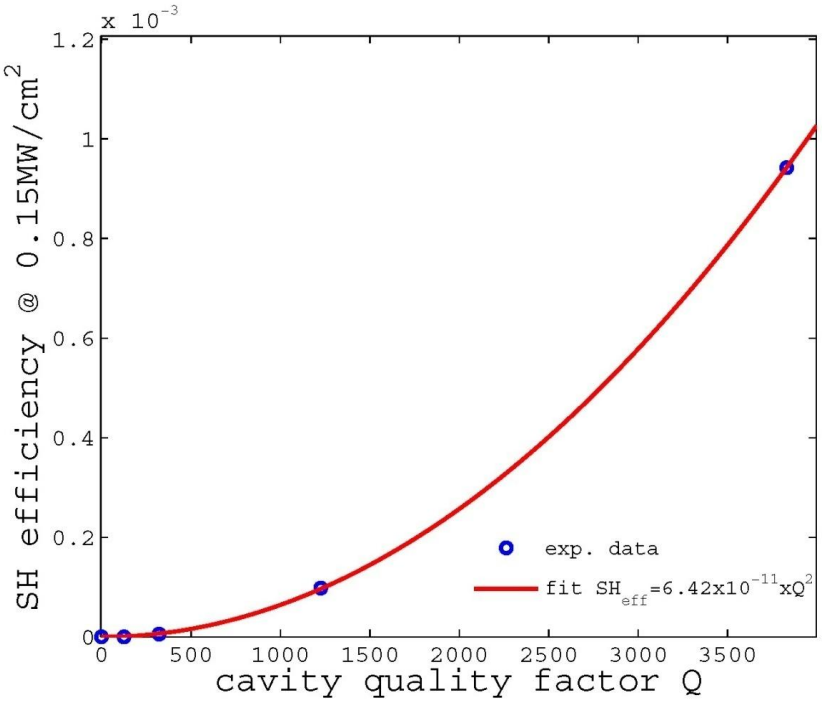

Figure 7.25. SH efficiency versus cavity Q factor, experimental data and quadratic fit. Due to the absorption regime at the harmonic wavelength, the SH is only made by the inhomogeneous component.

The role of the absorption

Accordingly the study for the free standing cavity, we are confident that the signals we recorded in the experiment are indeed made by only the inhomogeneous SH and TH components. Even if an enhancement of the residual homogeneous components is still present due to the not perfectly zero linear transmittance of the structure at those wavelengths, it keeps being negligible respect to the enhanced inhomogeneous signals.

However, since the absorption length is comparable with the thickness of the GaAs slab, we can make an additional last test as a further verification. In Fig.7.26 and Fig.7.27 we report the results of the numerical simulation of the FF propagation as in our experiment, through the 6 couples mirror structure. In the first case (Fig.7.26) the central cavity layer is made by a GaAs-like material without absorption. In the second case (Fig.7.27) we used the real data of the GaAs, taking into account the absorption. In the figures are reported three different snapshots of the FF and the relative generated SH. From the top, the first snapshot represents the initial condition with the FF pulse propagating in the air toward the sample. In the second snapshot the FF pulse is crossing the sample and, finally, in the third snapshot has completely left it beyond.

The only difference we can appreciate between the two figures is the level of the generated SH. In presence of absorption the intensity of the SH is almost half respect to the case without absorption. This is also confirmed by the monitor of the SH energy versus the propagation time plotted in Fig.7.28. This perfectly agrees with the discussion made previously in the section 7.2.

In conclusion, we experimentally demonstrated SH conversion efficiencies that approach 0.1% in an opaque GaAs cavity, using incident pump intensities of order 10MW/cm^2. We have also shown that the conversion efficiency of the inhomogeneous, phase locked SH component is a quadratic function of cavity-Q, namely the enhancement factor of the FF inside the cavity. These results show that high conversion efficiencies can be obtained in phase mismatched materials in ways that may also be practical.

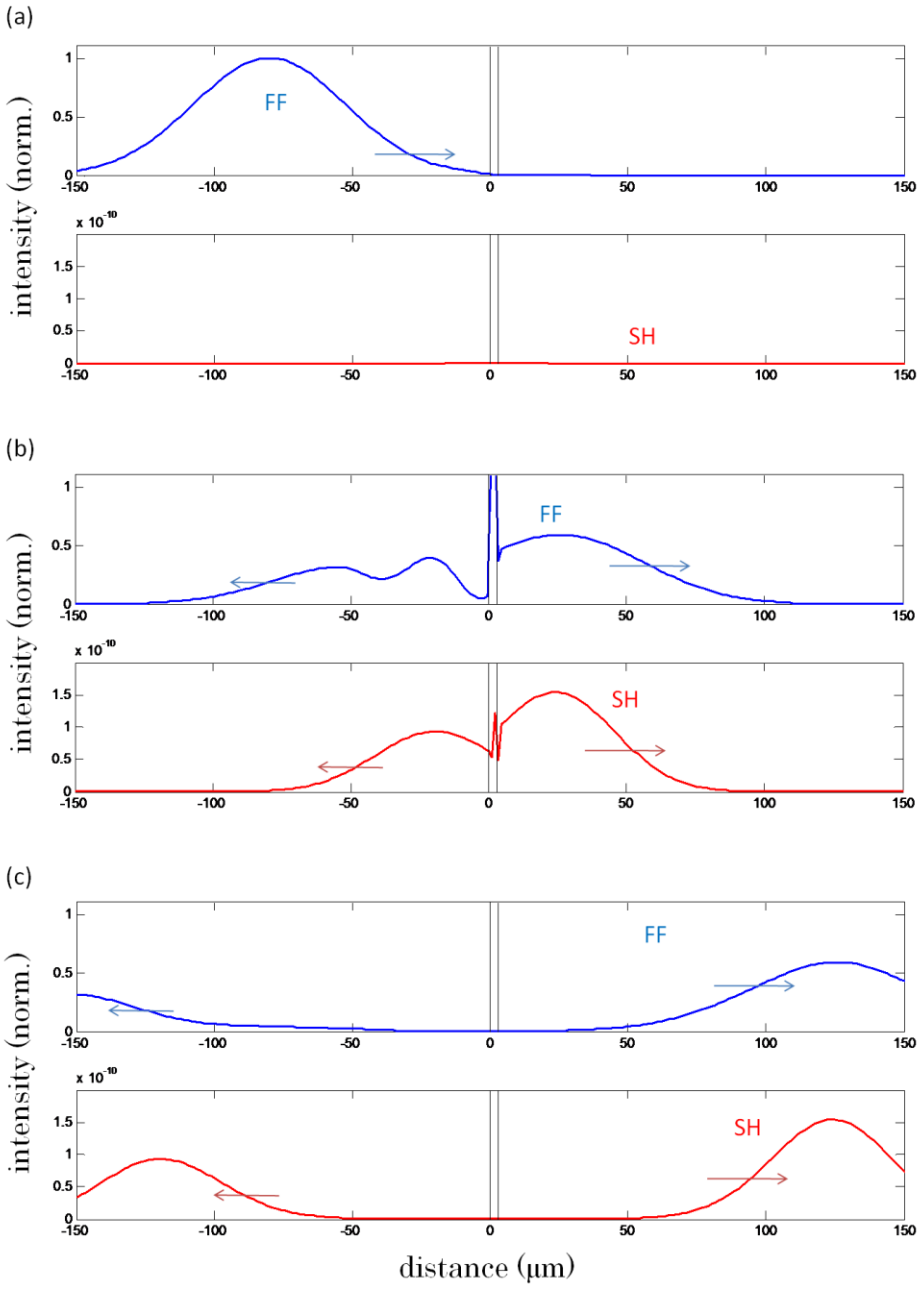

Figure 7.26. FF and generated SH propagation into the 6couple mirrors cavity sample made by GaAs-like material without absorption. From the top, the first snapshot represents the initial condition with the FF pulse propagating in the air toward the sample. In the second snapshot the FF pulse is crossing the sample and, finally, in the third snapshot has completely left it beyond.

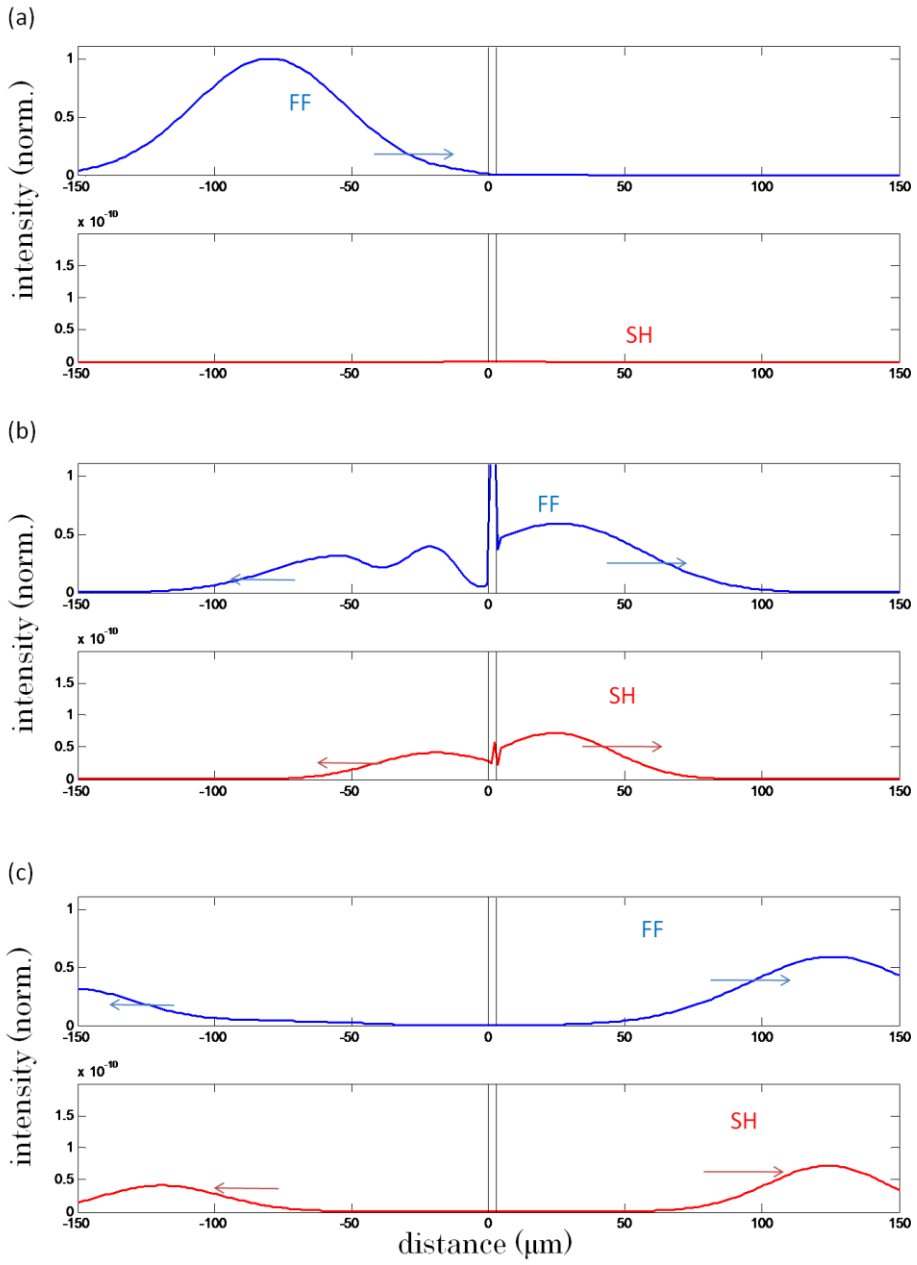

Figure 7.27. FF and generated SH propagation into the 6couple mirrors cavity sample made by GaAs (including absorption). From the top, the first snapshot represents the initial condition with the FF pulse propagating in the air toward the sample. In the second snapshot the FF pulse is crossing the sample and, finally, in the third snapshot has completely left it beyond

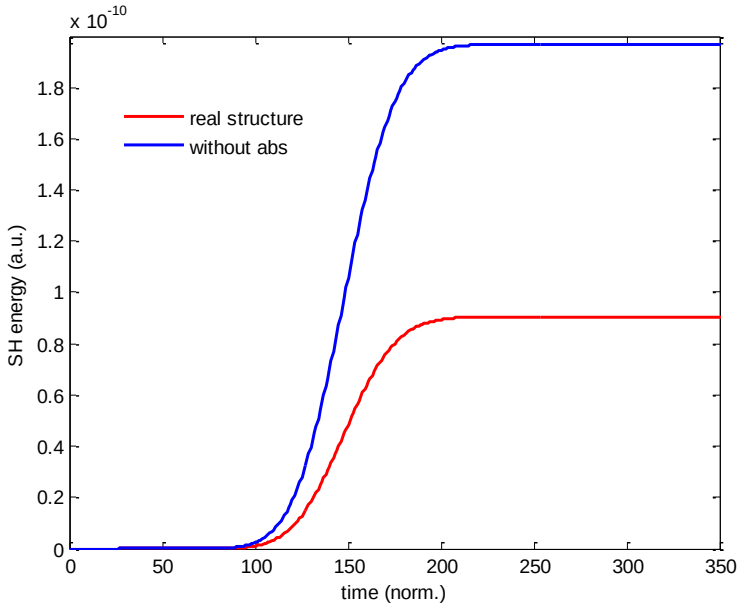

Figure 7.28. SH energy (normalized to the FF energy) versus propagation time for both the propagation cases as in Figs.7.26 and 7.27.

In addition, with the right materials it becomes possible to exploit new wavelength ranges, e.g. UV-XUV, using GaP or GaN, for example. This will be our next goal in the next Chapter.

Chapter 8

Harmonic generation in the metallic regime

8.1. SH and TH generation in GaP

Experimental results

In this last Chapter we want to turn our attention to another interesting fundamental consequence of the PL phenomenon. So far we studied the behavior of the SH when it is tuned below the absorption band edge of semiconductors, but still in the region where the index of refraction is purely positive. Our curiosity forced us to see what happen if the tuning is moved down to the region where the dielectric permittivity can assume negative values. GaP practically presents such region around UV frequencies and, at the same time, has a lower absorption band edge (around 500nm) respect to the GaAs (around 900nm). This gives us the

possibility to pump at 670nm FF and to observe the two first harmonics at the peak of higher absorption (SH) and of negative permittivity value (TH).

Following the evolution of this topic, it now comes natural to ask the following question: does this phenomenon hold for harmonic fields tuned at frequencies in the *metallic* range of material? That is to say, if the pump field is tuned in the transparency region, will a harmonic field be able to propagate if it happens to be tuned in a region where $sign(\varepsilon) \neq sign(\mu)$, where one expects no propagating solutions? The short answer to this question is *yes.* In what follows we provide experimental and numerical evidence that show how an electromagnetic field is generated and propagates in that forbidden wavelength range.

In Fig.8.1 we report the dispersion relation of the GaP as given in reference [Pal85]. The pump pulse is tuned at 670nm, in the transparency region of the material, where $\varepsilon_{670nm} = 10.7$. Consequently, the SH field falls at the UV absorption resonance located near 335nm, where $\varepsilon_{335nm} = 19.1 + i\,24.1$. In turn, the TH signal falls close the peak of the negative permittivity at 223nm, where $\varepsilon_{223nm} = -9.6 + i\,10.4$ (metallic range). With these dispersion values, an incident fields would either be completely absorbed within a few nanometers from the surface (335nm), or be completely reflected at the surface (223nm).

The experimental setup we used to measure transmitted harmonics in GaP is shown in Fig.8.2. Pump pulses centered at 670nm and 80fs in duration were generated by an optical parametric amplifier and amplified Ti:sapphire laser system operating at 1kHz repetition rate. Prior to sending the pump beam into the experimental setup, an equilateral dispersing prism and spatial filtering were used to remove background harmonics present in the beam path. A color filter (CF) was placed directly before the sample to remove any residual harmonics. At the sample position, the collimated pump beam's energy per pulse was 2.7μJ, corresponding to a peak intensity of approximately 480MW/cm^2.

After passing through the sample, the residual pump was rejected and the harmonics were highly reflected off by two set of four long wave pass (LWP) dichroic beam splitters. These mirrors each transmitted >90% of the

pump and reflected >97% of the SH (first set of mirrors) or >95% of the TH (second set of mirrors). While propagating through the sequence of LWP mirrors, a single polarization of harmonic light was selected by a polarizer with single-pass extinction ratio of ~10^{-3}. Each harmonic was reflected back through the mirrors and polarizer (RP) by a concave aluminum mirror with deep-ultraviolet coating (DUVA). Therefore, the residual pump light was suppressed by at least eight orders of magnitude and either the TM or TE component of the harmonic was selected with a contrast of at least 10^6. After passing back through the mirrors and polarizer, the harmonic was focused into an all-silica fiber coupled to a UV-sensitive spectrometer and liquid nitrogen cooled CCD.

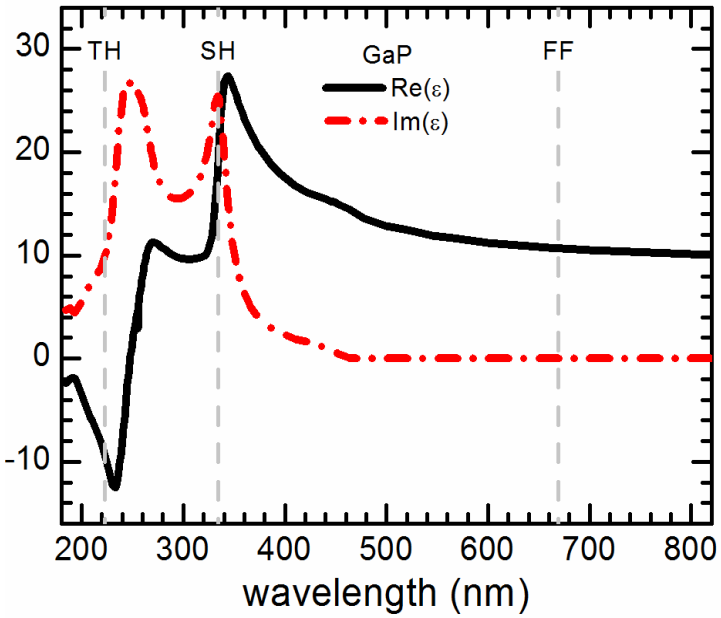

Figure 8.1. Dispersion relation of GaP from reference [Pal85]. The dashed lines indicate tuning of the fields. There are two resonances, at ~330nm and ~240nm.

In Fig.8.3 we show the measured spectra (solid curves) for the case of a TM polarized pump field. The <100> GaP 500μm thick wafer was illuminated at an angle of 40°. The basic results may be summarized as follows: the harmonic conversion efficiencies for the transmitted fields are approximately 10^{-9} for the TE-polarized SH at 335nm, and $1.8\text{x}10^{-12}$ for the TM-polarized TH at 223nm. The detection limit of the system corresponds to

a minimum detectable efficiency of ~10^{-14}. Any harmonic present with the sample removed was below this detection limit.

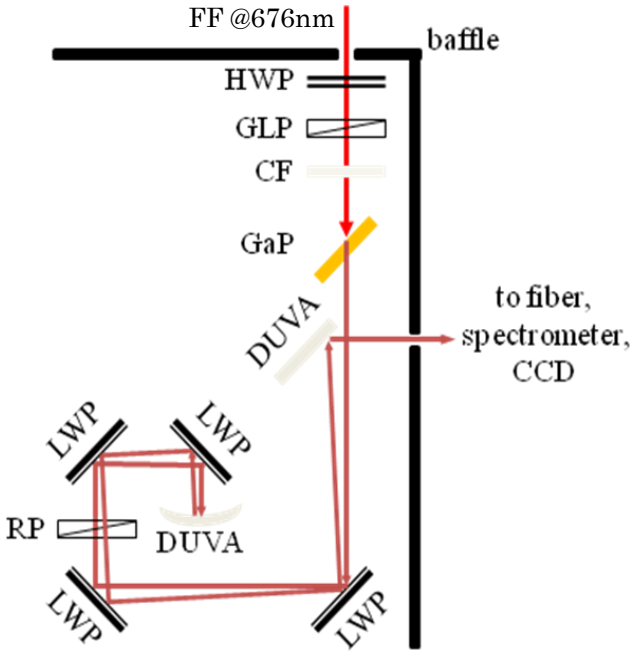

Figure 8.2. Schematic representation of the experimental Set-up. The polarization of input pump pulses at 670nm is set by a half-wave plate (HWP) and Glan-laser polarizer (GLP). A color filter (CF) removes the harmonics before the pumps strikes the GaP sample. The harmonics reflect off four LWP dichroic beam splitters. A Rochon polarizer (RP) transmits only one polarization of harmonic light. A concave aluminum mirror with deep-ultraviolet coating (DUVA) retroreflects the harmonic back through the RP/LWP system and focuses the harmonic into an all-silica fiber for detection.

Theoretical verification

Theoretical confirmation of our experimental results was obtained by numerically solving Maxwell's equations in the time domain. This time the material was modeled as a collection of doubly resonant harmonic oscillators to closer model the GaP dispersion characteristics in Fig.8.1.

The model is mainly the one described in the Chapter 1. The difference is that now we consider the extension of the theory made recently in [Sca10].

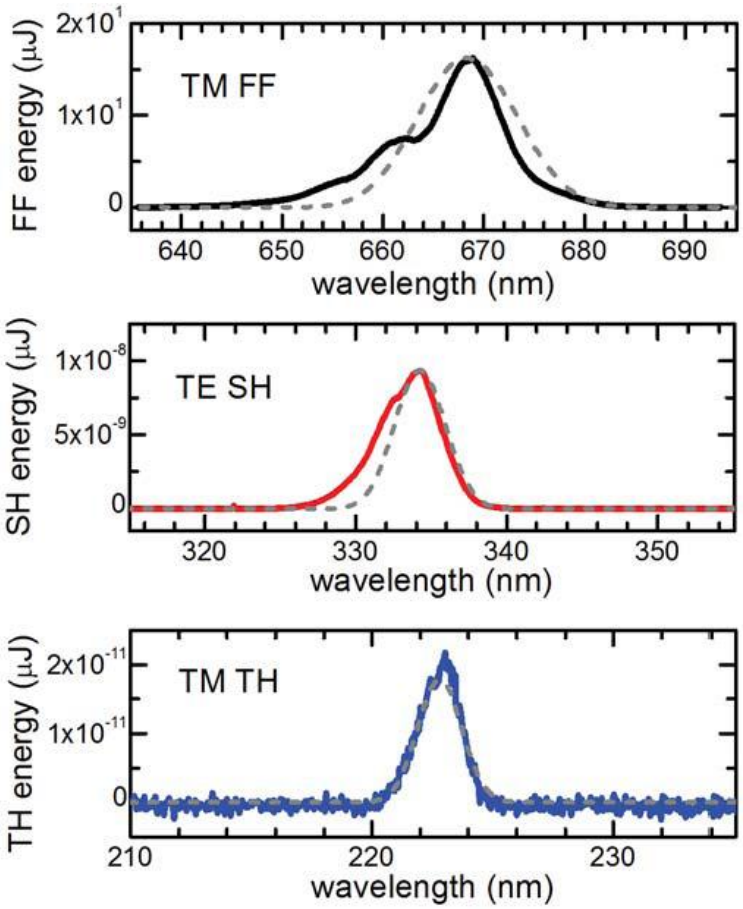

Figure 8.3. Measured spectra for the TM-polarized pump (continuous lines). Results of the numerical simulation (dashed lines).

In this work the authors provided a more explicit and detailed description of the polarization equations. Since the conversion efficiency involved are extremely low, in the experiments with opaque samples the survivor bulk inhomogeneous harmonic components can be easily confused with the harmonics signals generated at the entry and exit interfaces. In literature so far, these signals were taken into account with *phenomenological* models, which were base directly on the experimental results. The new, completely theoretical, approach used in [Sca10] allows us to practically discriminate the exact origin of any generated SH and/or TH signals.

The model is described in details in reference [Sca10]. Suffice it to say here that the oscillator model is exemplified by the following scaled

equations of motion that describe generic envelope functions that are allowed to vary rapidly in space and time [Sca10]:

$$\ddot{\mathbf{P}}_{\omega}+\tilde{\gamma}_{\omega}\dot{\mathbf{P}}_{b,\omega}+\tilde{\omega}_{0,\omega}^{2}\mathbf{P}_{b,\omega}\approx$$
$$\frac{n_0e^2\lambda_0^2}{m^*c^2}\mathbf{E}_{\omega}+\frac{e\ \lambda_0}{m^*c^2}\begin{pmatrix}-\frac{1}{2}\mathbf{E}_{\omega}^{*}\nabla\bullet\mathbf{P}_{2\omega}\\+2\mathbf{E}_{2\omega}\nabla\bullet\mathbf{P}_{\omega}^{*}\\-\frac{2}{3}\mathbf{E}_{2\omega}^{*}\nabla\bullet\mathbf{P}_{3\omega}\\-\frac{3}{2}\mathbf{E}_{3\omega}\nabla\bullet\mathbf{P}_{2\omega}^{*}\end{pmatrix}+\frac{e\ \lambda_0}{m^*c^2}\begin{pmatrix}\left(\dot{\mathbf{P}}_{\omega}^{*}+i\omega\mathbf{P}_{\omega}^{*}\right)\times\mathbf{H}_{2\omega}\\+\left(\dot{\mathbf{P}}_{2\omega}-2i\omega\mathbf{P}_{2\omega}\right)\times\mathbf{H}_{\omega}^{*}\\+\left(\dot{\mathbf{P}}_{2\omega}^{*}+2i\omega\mathbf{P}_{2\omega}^{*}\right)\times\mathbf{H}_{3\omega}\\+\left(\dot{\mathbf{P}}_{3\omega}-3i\omega\mathbf{P}_{3\omega}\right)\times\mathbf{H}_{2\omega}^{*}\end{pmatrix}$$

$$\ddot{\mathbf{P}}_{2\omega}+\tilde{\gamma}_{2\omega}\dot{\mathbf{P}}_{2\omega}+\tilde{\omega}_{0,2\omega}^{2}\mathbf{P}_{2\omega}\approx$$
$$\frac{n_0e^2\lambda_0^2}{m^*c^2}\mathbf{E}_{2\omega}+\frac{e\ \lambda_0}{m^*c^2}\begin{pmatrix}\mathbf{E}_{\omega}\nabla\bullet\mathbf{P}_{\omega}\\-\frac{1}{3}\mathbf{E}_{\omega}^{*}\nabla\bullet\mathbf{P}_{3\omega}\\-3\mathbf{E}_{3\omega}\nabla\bullet\mathbf{P}_{\omega}^{*}\end{pmatrix}+\frac{e\ \lambda_0}{m^*c^2}\begin{pmatrix}\left(\dot{\mathbf{P}}_{\omega}-i\omega\mathbf{P}_{\omega}\right)\times\mathbf{H}_{\omega}\\+\left(\dot{\mathbf{P}}_{\omega}^{*}+i\omega\mathbf{P}_{\omega}^{*}\right)\times\mathbf{H}_{3\omega}\\+\left(\dot{\mathbf{P}}_{3\omega}-3i\omega\mathbf{P}_{3\omega}\right)\times\mathbf{H}_{\omega}^{*}\end{pmatrix}$$

$$\ddot{\mathbf{P}}_{3\omega}+\tilde{\gamma}_{3\omega}\dot{\mathbf{P}}_{3\omega}+\tilde{\omega}_{0,3\omega}^{2}\mathbf{P}_{3\omega}\approx$$
$$\frac{n_0e^2\lambda_0^2}{m^*c^2}\mathbf{E}_{3\omega}+\frac{e\ \lambda_0}{m^*c^2}\begin{pmatrix}\frac{1}{2}\mathbf{E}_{\omega}\nabla\bullet\mathbf{P}_{2\omega}\\+2\mathbf{E}_{2\omega}\nabla\bullet\mathbf{P}_{\omega}\end{pmatrix}+\frac{e\ \lambda_0}{m^*c^2}\begin{pmatrix}\left(\dot{\mathbf{P}}_{2\omega}-2i\omega\mathbf{P}_{2\omega}\right)\times\mathbf{H}_{\omega}\\+\left(\dot{\mathbf{P}}_{\omega}-i\omega\mathbf{P}_{\omega}\right)\times\mathbf{H}_{2\omega}\end{pmatrix}$$

(8.1)

The Eqs.(8.1) are scaled as explained in the Chapter 1. e and m^* are the electron charge and effective mass, respectively; $\mathbf{P}_{N\omega}$, $\mathbf{E}_{N\omega}$, and $\mathbf{H}_{N\omega}$ are the polarization, the electric and the magnetic fields associated with the N^{th} harmonic. As in reference [Sca10] we also operate in a two-dimensional space, and allow the simultaneous presence of TE- and TM-polarized field that each has a two-dimensional spatial description. The scaled coefficients are

$$\tilde{\gamma}_{N\omega}=\left(\gamma-Ni\omega\right),$$

the damping coefficient, and

$$\tilde{\omega}_{0,N\omega}^{2}=(\omega_0^2-(N\omega)^2+i\gamma N\omega),$$

the resonance frequency, where N is an integer that denotes the given harmonic. This theoretical description takes into account harmonic

generation that arises from interface crossings (spatial derivatives on the polarization vector) and from the ever-present magnetic Lorentz force, which is usually neglected outside the context of metals. The total polarization that is fed back into Maxwell's equation is the vector sum of each of the solutions of Eqs.(8.1) and the nonlinear polarization that arises from $\chi^{(2)}$and $\chi^{(3)}$ bulk phenomena (see for example Eq(1.49)).

The intrinsic nature of the GaP $\chi^{(2)}$ tensor (only non-zero components are $d_{14}=d_{25}=d_{36}$) selects the TE-polarized SH signal when the pump is TM-polarized (see for example the polarization form in Section 3.3). The simulations show that in GaP the homogeneous component is completely absorbed within just a few nanometers from the entry surface, leaving only the phase locked SH. Harmonic signals generated at the surface due to symmetry breaking that inevitably take place during the interaction, on the other hand, have the same polarization as the incident pump pulse [Sca10], but have much smaller conversion efficiencies compared to $\chi^{(2)}$ contributions. Thus, cross checking the polarization of the generated signal can be used to determine its origin. Using that theoretical approach outlined in reference [Sca10] we determined that the efficiency of the transmitted, surface-generated, TM-polarized SH field is of order 10^{-11}, i.e. at least two orders of magnitude smaller than the TE-polarized component that arises from the intrinsic $\chi^{(2)}$ tensor of the medium. As a result there is little doubt that most of the TE-polarized signal originates with the bulk $\chi^{(2)}$ of GaP.

For THG, nonlinear surface sources alone that arise from Coulomb and magnetic Lorentz forces [Sca10] are inadequate to generate an observed transmitted, TM-polarized TH signal with an efficiency of 10^{-12}. An adequate prediction of THG can be made by adopting the realistic circumstances of a third order $\chi^{(3)}$ tensor being of cubic type, with $\bar{4}3m$ symmetry and four independent components [Boy03], namely

$$\chi^{(3)}_{xxxx},\ \chi^{(3)}_{yyxx},\ \chi^{(3)}_{yzyz},\ \chi^{(3)}_{yzzy},$$

with

$$\chi^{(3)}_{xxxx}=\chi^{(3)}_{yyyy}=\chi^{(3)}_{zzzz}.$$

The remaining symmetry properties of the tensor for this class of materials may be consulted in reference [Boy03]. The model thus includes surface and

volume contributions from Coulomb and magnetic Lorentz forces, as well as contributions from the realistic nonlinear second and third order tensors that give rise to SHG and THG.

Fig.8.4 summarizes the numerical results in the form of a superposition of different temporal snapshots of the incident and generated harmonic pulses. The interaction proceeds as follows. As the input pulse (Fig.8.4(a)) enters the material SHG and THG occur. In the figure we report the most intense components, namely TE-polarized SH (Fig.8.4(b)) and TM-polarized TH (Fig.8.4(c)) pulses. The homogeneous components quickly vanish due to either the high absorption (SH) or the metallic environment (TH). The inhomogeneous components are the only portions of the harmonics that survive, and can be clearly seen from the figure, they perfectly overlap the pump pulse at all times.

The amount of energy deposited by the pump pulse into each harmonic is dictated by the material index mismatch at the interface, and do not vary during the propagation.

When the pump pulse reaches the exit surface the nonlinear coupling ceases and the fields are able to propagate freely. In Fig.8.4(d) we also show is also monitor the transmitted energy as a function of time.

The calculated spectra are shown in Fig.8.3 (dashed lines) and they overlap well the experimental data provided we need to use a value of

$$\chi^{(2)} = d_{14} = d_{25} = d_{26} \approx 500\text{pm/V},$$

and

$$\chi^{(3)}_{xxxx} = \chi^{(3)}_{yyyy} = \chi^{(3)}_{zzzz} \approx 4\times10^{-19} m^2/V^2 .$$

Although the remaining third order tensor components

$$\chi^{(3)}_{yyxx},\ \chi^{(3)}_{yzyz},\ \chi^{(3)}_{yzzy}$$

are also included in the calculation and are taken to be of the same order as the diagonal terms, their contribution influences little the overall TH conversion efficiency. Our calculations thus suggest that indeed the second order coefficients tend to achieve relatively large values in the UV range, as also reported elsewhere [Ber03]. On the other hand, the magnitude of the third order coefficient is more in line with typically reported values.

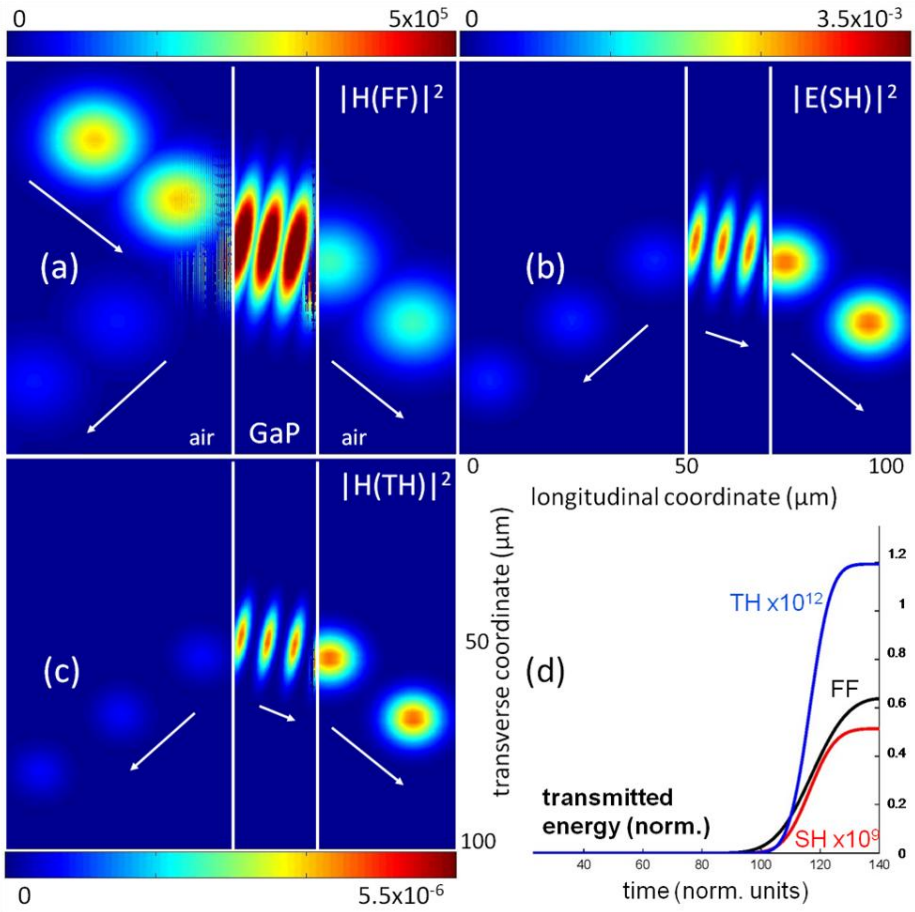

Figure 8.4. Time propagation that shows superposition of different temporal snapshots. An 80fs pump pulse impinges at 40º on a GaP 20µm-thick slab (a) and SH (b) and TH (c) signals are generated. (d) Field energies as a function of time at the right of the sample.

Beside some aspects that clearly appear to have fundamental relevance, the discovery that the PL phenomenon still applies in the UV regime for harmonics tuned in ranges where the medium displays metallic behavior may be of strong technological importance in re-thinking and re-designing semiconductor-based integrated devices at the nanoscale. Harmonic generation is only one aspect of the role that common semiconductors can play at UV wavelengths, i.e. ranges where typical semiconductors distinguish themselves only for their opacity. As another example, semiconductor based super-lenses [Vin09] and enhanced

transmission gratings [Vin10] that operate in the UV range have already been proposed.

Taken together, these results show that the functionality of semiconductors may be pushed down the wavelength scale, toward the soft-X-ray region of the spectrum. The natural next step to take beyond this work is to study the dynamics in cavity environments, as was done in the previous Chapter for GaAs sample, possibly in metal-semiconductor structures [Sca10], where the $\chi^{(3)}$ of metals can be fully exploited with the clear aim to achieve high conversion efficiencies in the deep UV range.

To summarize, we have experimentally detected the propagation of light pulses in the ultra-violet metallic frequency range of GaP. The pulse was generated near the entry surface of the sample as a TH signal using quadratic and cubic nonlinearities of the material. The propagation was possible thanks to a PL mechanism that binds inhomogeneous components to the FF, an effect that persist regardless of the dispersive characteristics of the medium at the harmonic wavelengths.

Conclusions of Part II

The solution of the Maxwell's equations in nonlinear dielectrics is composed of two parts: one resolves the homogeneous set of equations, while the other is a particular solution of the inhomogeneous equations driven by the nonlinear polarization term. For the case of harmonics generation, the homogenous component has traditionally been considered to be the only important constituent and so investigations have focused on it. Nevertheless, reports of observations of a double-peaked SH signal in the strong phase mismatched regime have been published. Worthy of note is the work of Mlejnek et al. [Mle99] where the authors showed the predictions made in 1962 that the inhomogeneous component of the SH signal travels at the group velocity of the pump pulse. At the same time, the homogeneous component of the SH refracts and travels according to the values one expects from material dispersion at that frequency.

These works did not attract much attention because for application purposes the main goal has remained the achievement of efficient harmonic generation. As we saw in Chapter 5, the inhomogeneous component is generally difficult to observe because it travels locked under the pump pulse, with conversion efficiencies that for bulk materials are still relatively low. The key observation is the fact that this SH components always travels with a k-vector double that of the pump ($2k_\omega$), even for large phase mismatches, and has a carrier frequency that oscillates at 2ω. It is then straightforward to conclude that the inhomogeneous SH signal experiences an *effective* index of refraction that is the same as the pump pulse. We also showed that the energy transfer clamps and the inhomogeneous SH component travels locked in phase with the fundamental beam.

To experimentally prove this idea, in Chapter 6 we have chosen a pump pulse centered at 1300nm and we launched it into a 500μm thick GaAs slab. Transmitted SH and TH signals were recorded at 650 and 433nm respectively, far below the material absorption band edge (~900nm). Simulations showed that the homogeneous SH and TH signals were quickly absorbed, while the inhomogeneous components continued on through the sample with an effective *complex index* of refraction identical to the index of the pump, which is tuned in a region of transparency. These results confirmed that the two components of the generated harmonics follow different destinies. This step is remarkable, because it shows that it possible to do nonlinear optics with materials opaque in the UV part of the spectrum. All the theory and the experiments (where possible) are also extended to the generation of the TH, highly broadening the validity of the discussion,

In Chapter 7, we studied, test and then provided a useful tool to enhance the inhomogeneous conversion efficiency. We theoretically investigated a free standing etalon and then we experimentally studied two GaAs-based schemes of cavity. The first scheme is a reflection single metallic mirror structure and the second one is a high-Q double dielectric mirrored cavity. The inhomogeneous generated component can now compete with the efficiency generally obtained for the homogeneous component and we can expect a number of devices that will take profit of this result. For

example, it can be designed an easy-to-build, low-cost and easy-tunable frequency conversion device that transform the typically IR lab lasers into visible or UV sources, without the needs of difficult and time consuming alignment and set-up.

From this point of view it was important the work done in Chapter 8, where we were able to go down to 223nm in wavelength and proof the stubbornness of the PL phenomenon. It was also impressive to be able to report for the first time, to our knowledge, a light propagation through a *metallic* bulk material. This event is something that fights against the common knowledge but it is the natural consequence of our theory.

This study has been performed by a non commercial numerical code that solves the Maxwell's equations in their complete form and advances the fields in time. The material response was modeled with a Lorentz set of differential equations that are solved together with the Maxwell's equation giving a high degree of management of the material dispersion for ultrashort pulse propagation. The numerical method does not rely on any of the usual approximations (such as SVEA, undepleted pump, etc…) giving us a very good confidence on the results obtained.

Even if this is not the first work to deal with the inhomogeneous component, *it is for sure the first systematic approach to its investigation*. As several times reported in the text, different characteristics have been revealed with the synergic action of theoretical analysis, numerical simulations and experimental verification. The main message we can extrapolate from this work is that the two generated harmonic components (homogeneous and inhomogeneous) have completely different behaviors and respond to completely different stimulus. We thus need to keep this clear in mind every time we want to operate either with one or the other component.

The homogeneous component faithfully obeys to the PM relation. But this relation does not seem to have any influence on the inhomogeneous component. This last one only responds to the FF, mirroring its behavior.

Obviously the work on this topic does not stop here. On the contrary it starts here, opening a new branch in the nonlinear optical field. We expect exciting new results from the application of the PL theory to *old* structures

or devices, looking at them from a new point of view. For example, at the moment, we are already working to study nonlinear grating structures in the opaque frequency range, as never was proposed before (see for example [Vin09, Vin10]).

Besides re-interpreting old devices, it is indeed interesting to sample new ideas. For example we are interested to study the case where the FF is seeded with a SH and/or TH fields. From preliminary calculations, it seems that, again, the PL phenomenon acts in a very surprising way making part of the seed trapped and forced to propagates anomalously.

Finally, it is worth of note that the introduction of almost unknown phenomena in the common knowledge is producing and exciting perturbation to the classical optical theory. As it happened for the advent of the *negative index materials* ten years ago that required the development of an extension of the electromagnetic theory to include all their effects, the better understanding of the PL phenomenon is pushing the nonlinear optical theory versus a more complete and detailed description. For example, following this wake, the work in [Sca10] starts from the needs to analyze peculiar aspects of the phase locked harmonic propagation and goes toward a detailed classical material polarization description as never assessed before.

Bibliography

[Agr07] G.P. Agrawal, *Nonlinear Fiber Optics* (Academic Press, San Diego, 2007), Chap. 3

[Ako02] N. Aközbek, A. Iwasaki, A. Becker, M. Scalora, S. L. Chin, and C. M. Bowden, Phys. Rev. Lett. **89**, 143901 (2002)

[Akt03] S. Akturk, M. Kimmel, P. O'Shea, R. Trebino, Opt. Express **11**, 491 (2003)

[Ale96] A. L. Aleksandrovskii, O. A. Gliko, I. I. Naumova, V. I. Pryalkin, Quantum Electron. **26**, 641 (1996)

[Ari10] A. Arie and Noa Voloch, Laser & Photon. Rev. **4**, 355 (2010)

[Arm62] J. A. Armstrong, N. Bloembergen, J. Ducuing, and P. S. Pershan, Phys. Rev. **127**, 1918 (1962)

[Ash66] A. Ashkin, G. Boyd, and J. Dziedzic, IEEE J. Quantum Electron. QE **2**, 109 (1966)

[Ash76] N.W. Ashcroft and N.D. Merminm, *Solid state physics* (Holt, Reinehart & Winston Inc., New York, 1976)

[Bab08] T. Baba, Nat. Photonics **2**, 465 (2008)

[Bau04] M. Baudrier-Raybaut, R. Haidar, Ph.Kupecek, Ph. Lemasson, and E. Rosencher, Nature **432**, 374 (2004)

[Bec03] K. Beckwitt, Y. Chen, F. Wise, and B. Malomed, Phys. Rev. E **68**, 057601 (2003)

[Ber03] S. Bergfeld and W. Daum, Phys. Rev. Lett. **90**, 036801 (2003)

[Ber97] V. Berger, J. Opt. Soc. Am. B **14**, 1351 (1997)

[Ber98] V. Berger, Phys. Rev. Lett. **81**. 4136 (1998)

[Ber98b] V. Bermudez, F. Caccavale, C. Sada, F. Segato, and E. Dieguez, J. Cryst. Growth 191, 589 (1998)

[Blo62] N. Bloembergen and P. S.Pershan, Phys. Rev. **128**, 606 (1962)

[Blo70] N. Bloembergen and A. Sievers, Appl. Phys. Lett. **17**, 483 (1970)

[Boy08] R. W. Boyd, Nonlinear optics (Academic Press, 2008)

[Boy66] G. D. Boyd and C. K. N. Patel, Appl. Phys. Lett. **8**, 12 (1966)

[Bri94] E. Bringuier et al., Phys. Rev. B **49**, 16971 (1994)

[Bur61] W. K. Burns and N. Bloembergen, Phys. Rev. B **4**, 3437 (1971)

[Cen01] M. Centini, G. D'Aguanno, M. Scalora, C. Sibilia, M. Bertolotti, M. J. Bloemer, and C. M. Bowden, Phys. Rev. E **64**, 046606 (2001)

[Cen06] E. Centeno and D. Felbacq, J. Opt. Soc. Am. B **23**, 2257 (2006)

[Cen06b] E. Centeno, Opt. Lett. **30**, 1054 (2005)

[Cen08] M. Centini, V. Roppo, E. Fazio, F. Pettazzi, C. Sibilia, J.W. Haus, J.V. Foreman, N. Akozbek, M.J. Bloemer, and M. Scalora, Phys. Rev. Lett. **101,** 113905 (2008)

[Cen99] M. Centini, C. Sibilia, M. Scalora, G. D'Aguanno, M. Bertolotti, M.J. Bloemer, C.M. Bowden, and I. Nefedov, Phys. Rew. E **60**, 4891 (1999)

[Cha00] F. Charra and G. Gurzadyan, *Nonlinear Dielectric Susceptibilities*, (Springer-Verlag, Berlin, 2000)

[Cha65] R. K. Chang, J. Ducuing, and N. Bloembergen, Phys. Rev. Lett. **15**, 415 (1965)

[Che95] T. J. Chen, R. N. Zitter, and R. Tao, Phys. Rev. A **51**, 706 (1995)

[Col99] J. Collier, C. Danson, C. Johnson, C. Mistry, Rev. Sci. Instrum. **70**, 1599 (1999)

[Con97] C. Conti, S. Trillo, and G. Assanto, Phys. Rev. Lett. **92**, 120404 (1997)

[Con97b] C. Conti, S. Trillo, and G. Assanto, Opt. Lett. **22**, 17 (1997)

[Con98] C. Conti, S. Trillo, and G. Assanto, Opt. Lett. **23**, 5 (1998)

[Con99] C. Conti, G. Assanto, and S. Trillo, Opt. Lett. **24**, 16 (1999)

[Dag06] G. D'Aguanno, N. Mattiucci, M. J. Bloemer, and M. Scalora, Phys. Rev. E **74**, 036605 (2006)

[Dag99] G. D'Aguanno, M.Centini, C. Sibilia, M. Betrolotti, M. Scalora, M.J. Bloemer, C.M. Bowden, Optics Lett. **24**, 1663 (1999)

[Die89] J.C. Diels, W. Rudolph, *Ultrashort Laser Pulse Phenomena* (Academic Press, San Diego, 1989)

[Dol72] G. Dolino, Phys. Rev. B **6**, 4025 (1972)

[Dor02] C. Dorrer, E.M. Kosik, I.A.Walmsley, Opt. Lett. **27**, 548 (2002)

[Dub94] A. Dubietis, R. Danielius, A. Stabinis, G. Valiulis, A. Varanavi- cius, Opt. Commun. **105**, 67 (1994)

[Dum01] Y. Dumeige, P. Vidakovic, S. Sauvage, I. Sagnes, J.A. Levenson, C. Sibilia, M. Centini, G. D'Aguanno and M. Scalora, Appl. Phys. Lett. **78**, 3021 (2001)

[Ell09] T. Ellenbogen, N. Voloch-Bloch, A. Ganany-Padowicz and A. Arie, Nature Photonics **3**, 395 (2009)

[Ewa69] P. P. Ewald, *Acta Crystallographica* Section A **25,** 103 (1969)

[Faz09] E. Fazio, F. Pettazzi, M. Centini, M. Chauvet, A. Belardini, M. Alonzo, C. Sibilia, M. Bertolotti, and M. Scalora, Opt. Express **17**, 3141 (2009)

[Fer50] E. Fermi, *Nuclear Physics* (University of Chicago Press, 1950)

[Fej92] M. M. Fejer, G. A. Magel, D. H. Jundt, R. L. Byer, IEEE J. Quantum Electron. **28**, 2631 (1992)

[Fej94] M. M. Fejer, Phys. Today **47**, 25 (1994)

[Fis06] R. Fischer, D. N. Neshev, S. M. Saltiel,W. Krolikowski, and Yu. S. Kivshar, Appl. Phys. Lett. **89**, 191105 (2006)

[Fis07] R. Fischer, D. N. Neshev, S. M. Saltiel, A. A. Sukhorukov, W. Krolikowski, and Yu. S. Kivshar, Appl. Phys. Lett. **91**, 031104 (2007)

[Fis08] R. Fisher, *Propagation of light in two-dimensional modulated nonlinear materials* (Ph.D. thesis, Australian National University, Canberra, 2008)

[Fra61] P. A. Franken, G. Weinreich, C. W. Peters, and A. E. Hill, Phys. Rev. Lett. **7**, 118 (1961)

[Fra63] P. A. Franken, and J. F.Ward, Rev. Mod. Phys. **35**, 23 (1963)

[Fuj06] N. Fujioka, S. Ashihara, H. Ono, T. Shimura, and K. Kuroda, Opt. Lett. **31**, 18 (2006)

[Fuj07] N. Fujioka, S. Ashihara, H. Ono, T. Shimura, K. Kuroda, J. Opt. Soc. Am. B **24**, 2394 (2007)

[Gai09] R.V. Gainutdinov, T. R.Volk, O. A. Lysova, I. I. Razgonov, A. L. Tolstikhina, L. I. Ivleva, Appl. Phys. B **95**, 505 (2009)

[Gal00] K. Gallo, P. Baldi, M. De Micheli, D. B. Ostrowsky, and G. Assanto, Opt. Lett. **25**, 13 (2000)

[Ger05] H. Gersen, T. Karle, R. Engelen, W. Bogaerts, J. Korterik, N. van Hulst, T. Krauss, and L. Kuipers, Phys. Rev. Lett. **94**, 073903 (2005)

[Ger09] K. Geren, S. W. Liu, H. J. Zhou, Y. Zhang, R. Tian, and M. Xiao, J. Appl. Phys. **105**, 063531 (2009)

[Gio62] J. A. Giordmaine, Phys. Rev. Lett. **8**, 19 (1962)

[Gle69] W. H. Glenn, IEEE J. Quantum Electron. **QE-5**, 6 (1969)

[Gyu79] R.N. Gyuzalian, S.B. Sogomonian, Z.Gy. Horvath, Opt. Commun. **29**, 239 (1979)

[Has95] N. Hasizume, M. Oshashi, T. Kondo and R. Ito, J. Opt. Soc. Am. B **12**, 1894 (1995)

[Hec86] Hecht and Zajac, Optica, (Addisson-Wesley, 1986)

[Hor93] M. Horowitz, A. Bekker, and B. Fischer, Appl. Phys. Lett. **62**, 2619 (1993)

[Iac98] C. Iaconis, I.A.Walmsley, Opt. Lett. **23**, 792 (1998)

[Ili08] R. Iliew, C. Etrich, T. Pertsch, and F. Lederer, Phys. Rev. B **77**, 115124 (2008)

[Ish85] Y. Ishida, T.Yajima, and A.Watanabe, Opt. Commun. **56**, 57 (1985)

[Jan77] J. Janszky, G. Corradi, and R. N. Gyuzalian, Opt. Commum. **23**, 293 (1977)

[Jer70] J. Jerphagnon, and S. K. Kurtz, J. Appl. Phys. **41**, 1667 (1970)

[Joa08] J. Joannopoulos and R. Meade and J. Winn, *Photonic crystals: molding the flow of light* (Princeton University Press, 2008)

[Kar97] H. Karlsson and F. Laurell, Appl. Phys. Lett. **71**, 3474 (1997)

[Kaw98] S. Kawai, T. Ogawa, H. S. Lee, R. C. DeMattei, and R. S. Feigelson, Appl. Phys. Lett. **73**, 768 (1998)

[Kiv95] Y. S. Kivshar, Phys. Rev. E **51**, 1613 (1995)

[Kle62] D. Kleinman, Phys. Rev. **126**, 1977 (1962)

[Kol81] C. Kolmeder,W. Zinth,W. Kaiser, Opt. Commun. **30**, 453 (1979)

[Kos98] H. Kosaka, T. Kawashima, A. Tomita, M. Notomi, T. Tamamura, T. Sato, and S. Kawakami, Phys. Rev.B **58**, 10096 (1998)

[Kos99] H. Kosaka, T. Kawashima, A. Tomita, M. Notomi, T. Tamamura, T. Sato, and S. Kawakami, Appl. Phys. Lett. **74**, 1212 (1999)

[Kri04] T. B. Kristensen and K. Pedersen, Opt. Commun. **233**, 219 (2004)

[Kry95] V. Krylov, A. Rebane, A. G. Kalintsev, H. Schwoerer, and U. P. Wild, Opt. Lett. **20**, 2 (1995)

[Lan60] L. D. Landau and E.M. Lifshitz, *Electrodynamics of Continuous Media* (Pergamon, New York, 1960), pp. 253–256.

[Leg01] Y. Le Grand, D. Rouede, C. Odiu, R. Aubry, and S. Mattauch, Opt. Commun. **200**, 249 (2001)

[Liu06] Y. Liu and J. C. Diels, IEEE J. Quantum Electron. **42**, 8 (2006)

[Llu96] Llous Torres and E. M. Wright, J. Opt. Soc. Am. B **13**, 864 (1996)

[Lom05] B. Lombardet, L. Dunbar, R. Ferrini, and R. Houdre, J. Opt. Soc. Am. B **22**, 1179 (2005)

[Lor06] H. A. Lorentz, *The Theory of Electrons* (Teubner, Leipzig, 1906)

[Mac01] H.A. Macleod, *Thin-films optical filtres*, (Philadelphia Institute of Physical Publishing, 2001)

[Mai60] T. Maiman, Nature **187**, 493 (1960)

[Mak62] P. D. Maker, R. W. Terhune, M. Nisenoff, and C. M. Savage, Phys. Rev. Lett. **8**, 21 (1962)

[Mal97] R. Maleck Rassoul, A. Ivanov, E. Freysz, A. Ducasse, and F. Hache, Opt. Lett. **22**, 268 (1997)

[Man87] J. T. Manassah and O. R. Cockings, Opt. Lett. **12**, 12 (1987)

[Mar00] M. Martinelli, L. Gomes, and R. J. Horowicz, Appl. Opt. **39**, 6193 (2000)

[Mar94] J. Martorell and R. Corbalán, Optics Comm. **108**, 319-323 (1994)

[Mar97a] J. Martorell, R. Vilaseca, R. Corbalán, Appl. Phys. Lett, **70**, 702 (1997)

[Mar97b] J. Martorell, R. Vilaseca, R. Corbalán, Phys. Rev. A, **55**, 4520 (1997)

[Mat05] N. Mattiucci, G. D'Aguanno, M. Scalora, M.J. Bloemer, Phys. Rev. E **72**, 066612 (2005)

[Mle99] M. Mlejnek, E. M. Wright, J. V. Moloney, and N. Bloembergen, Phys. Rev. Lett. **83**, 2934 (1999)

[Mol08] P. Molina, M. O. Ramirez, and L. E. Bausa, Adv. Funct. Mat. **18**, 709 (2008)

[Mor01] E. Yu. Morozov, A. A. Kaminskii, A. S. Chirkin, and D. B. Yusupov, JETP Lett. **73**, 647 (2001)

[Mor04] E. Yu. Morozov, A. S. Chirkin, Sov. J. Quantum Electron. **34**, 227 (2004)

[Mye95] L. E. Myers et al., Opt. Lett. **20**, 52 (1995)

[Nis08] C. Nistor, C. Cojocaru, Y. Loiko, J. Trull, R. Herrero, and K. Staliunas, Phys. Rev. A **78**, 053818 (2008)

[Noo90] L. D. Noordam, H. J. Bakker, M. P. de Boer, and H. B. Van Linden van den Heuvell, Opt. Lett. **15**, 24 (1990)

[Not00] M. Notomi, Phys. Rev. B **62**, 10696 (2000)

[Not01] M. Notomi, K. Yamada, A. Shinya, J. Takahashi, C. Takahashi, and I. Yokohama, Phys. Rev. Lett. **87**, 253902 (2001)

[Not02] M. Notomi, Opt. Quantum Electron. **34**, 133 (2002)

[Orl96] S. Orlov, A. Yariv, and M. Segev, Appl. Phys. Lett. **68**, 12 (1996)

[Ou93] Z. Ou and H. Kimble, Opt. Lett. **18**, 1053 (1993)

[Pal85] E. D. Palik, Handbook of Optical Constants of Solids (Academic, New York, 1985)

[Pas10] A. Pasquazi, A. Busacca, S. Stivala, R. Morandotti and G. Assanto, IEEE Photonics J. **2**, 18 (2010)

[Pen08] J. B. Pendry, Science **322**, 71 (2008)

[Pet05] E. V. Petrov and B. I. Mantsyzov, JETP **101**, 3 (2005)

[Pfi97] O. Pfister, J. S. Wells, L. Hollberg, L. Zink, D. A. VanBaak, M. D. Levenson, W. R. Bosenberg, Opt. Lett. **22**, 1211 (1997)

[Qin08] Y. Q. Qin, C. Zhang,Y.Y. Zhu, et al., Phys. Rev. Lett. **100**, 063902 (2008)

[Rag01] M. Raghuramaiah, A.K. Sharma, P.A. Naik, P.D. Gupta, R.A. Ganeev, Sadhana **26**, 603 (2001), Part 6

[Ram00] J. Rams and J.M. Cabrera, J. Mod. Opt. **47**, 1659 (2000)

[Ram04] M. O. Ramirez, D. Jaque, L. Ivleva, and L. E. Bausa, J. Appl. Phys. **95**, 6185 (2004)

[Ray04] M. Baudrier-Raybaut, R. Haidar, Ph.Kupecek, Ph. Lemasson, and E. Rosencher, Nature **432**, 374 (2004)

[Rei03] D. T. Reid, J. Opt. A, Pure Appl. Opt. **5**, S97 (2003)

[Rem88] C. Rempel,W. Rudolph, Exp. Tech. Phys. **37**, 381 (1988)

[Rom01] J. J. Romero, D. Jaque J. Garca Sol, Appl. Phys. Lett. **78**, 1961 (2001)

[Rom02] J.J. Romero, C. Aragia Sole, and A. A. Kaminskii, Appl. Phys. Lett **81**, 4106 (2002)

[Rom03] J. J. Romero, C. Arago, J. A. Gonzalo, D. Jaque, and J. Garcia Sole, J. Appl. Phys. **93**, 3111 (2003)

[Rop07] V. Roppo, M. Centini, C. Sibilia, M. Bertolotti, D. de Ceglia, M.Scalora, N. Akozbek, M. J. Bloemer, J. W. Haus, O. G. Kosareva and V. P. Kandidov, Phys. Rev. A **76**, 033829 (2007)

[Rop08] V. Roppo, D. Dumay, J. Trull, C. Cojocaru, S. M. Saltiel, K. Staliunas, R.Vilaseca, D. N. Neshev,W. Krolikowski, and Yu. S. Kivshar, Opt. Express **16**, 14192 (2008)

[Rop08b] V. Roppo, M. Centini, D. de Ceglia, M.A. Vicenti, J.W. Haus, N. Akozbek, M.J. Bloemer, and M. Scalora, Metamaterials **2**, 135 (2008)

[Rop09] V. Roppo,W. Wang, K. Kalinowski, Y. Kong, C. Cojocaru, J. Trull, R. Vilaseca, M. Scalora, W. Krolikowski and Yu. Kivshar, Opt. Express **18** 4012 (2009)

[Rop09b] V. Roppo, C. Cojocaru, F. Raineri, G. D'Aguanno, J. Trull, Y. Halioua, R. Raj, I. Sagnes, R. Vilaseca, and M. Scalora, Phys. Rev. A **80**, 043834 (2009)

[Rop10] V. Roppo, C. Cojocaru, J. Trull, R. Vilaseca and M. Scalora, Waves in Random and Complex Media **20**, 319 (2010)

[Rop11] V. Roppo, F. Raineri, C. Cojocaru, R. Raj, J. Trull, R. Vilaseca, I. Sagnes and M. Scalora, Optics Letters **?**, ?? (2011)

[Sac01] Z. Sacks, G. Mourou, R. Danielius, Opt. Lett. **26**, 462 (2001)

[Sak96] K. Sakoda and K. Ohtaka, Phys. Rev. B **54**, 5742 (1996)

[Sal05] S. M. Saltiel, A. A. Sukhorukov, Y. S. Kivshar, Prog. Opt. **47**, 1 (2005)

[Sal08] S. M. Saltiel, D. N. Neshev, R. Fischer, W. Krolikowski, and Yu. S. Kivshar, Opt. Lett. **33**, 527 (2008)

[Sal81] S. M. Saltiel, S. D. Savov, I. V. Tomov, and L. S. Telegin, Opt. Commun. **38**, 443 (1981)

[Sal82] S.M. Saltiel, S.D. Savov, I.V. Tomov, Opt. Quantum Electron. **14**, 391 (1982)

[Sal86] S. Saltiel, K. Stankov, P. Yankov, V. Telegin, Appl. Phys. B **40**, 25 (1986)

[Sal87] F. Salin, P. Georges, G. Roger, A. Burn, Appl. Opt. **26**, 4528 (1987)

[Sap05] U. Sapaev and D. Reid, Opt. Express **13**, 3264 (2005)

[Sap08] U. K. Sapaev, G. Assanto, Opt. Express **16**, 1 (2008)

[Sca05] M. Scalora, G. D'Aguanno, N. Mattiucci, N. Akozbek, M. J. Bloemer, M. Centini, C. Sibilia, M. Bertolotti, Phys. Rev. E **72** 066601 (2005)

[Sca05b] M. Scalora , M. Syrchin, N. Akozbek, E. Y. Poliakov, G. D'Aguanno, N. Mattiucci, M. J. Bloemer, A. M. Zheltikov, Phys. Rev. Lett. **95** 013902 (2005)

[Sca05c] M. Scalora, G. D'Aguanno, N. Mattiucci, M. J. Bloemer, J. W. Haus, A. M. Zheltikov, Appl. Phys B **81** 393 (2005)

[Sca06] M. Scalora, G. D'Aguanno, M. Bloemer, M. Centini, D. de Ceglia, N. Mattiucci and Y. S. Kivshar, Opt. Express **14** 4746 (2006)

[Sca06b] M. Scalora, N. Mattiucci, G. D'Aguanno, M. C. Larciprete and M. J. Bloemer, Phys. Rev. E **73** 016603 (2006)

[Sca10] M. Scalora, M. A. Vincenti, D. de Ceglia, V. Roppo, M. Centini, N. Akozbek and M. J. Bloemer, Phys. Rev. A **82**, 043828 (2010)

[Sca94] M. Scalora , M.E. Crenshaw, Opt. Comm. **108,** 191 (1994)

[Sca97] M. Scalora, M. J. Bloemer, A. Manka, J. Dowling, C. Bowden,R. Viswanathan, and J. W. Haus, Phys. Rev. A **56**, 3166 (1997)

[Sha07] V. M. Shalaev, Nat. Photonics **1**, 41 (2007)

[Sha68] S. L. Shapiro, Appl. Phys. Lett. **13**, 19 (1968)

[She07] Y. Sheng, J. Dou, B. Ma, B. Cheng, and D. Zhang, Appl. Phys. Lett. 91, 011101 (2007)

[She09] Y. Sheng, S. M. Saltiel, K.Koynov, Opt. Lett. **34**, 656 (2009)

[She10] Y. Sheng, A. Best, H. J. Butt, W. Krolikowski, A. Arie and K. Koyonv, Opt. Express **18** 16539 (2010)

[She84] Y.R. Shen, The Principles of Nonlinear Optics (Wiley, New York, 1984)

[Shu08] I. V. Shutov,I. A. Ozheredov, A. V. Shumitski, A. S. Chirkin, Opt. Spectroscopy **105**, 79 (2008)

[Shv08] V. V. Shvartsman, W. Kleemann, T. Lukasiewicz, and J. Dec, Phys. Rev. B **77**, 054105 (2008)

[Sid96] E. Sidick, A. Knoesen, and A. Dienes, Pure Appl. Opt. **5**, 709 (1996)

[Soe05] E. Soergel, Appl. Phys. B **81**, 729 (2005)

[Ste96] A. Steinbach, M. Rauner, F. C. Cruz, and J. C. Bergquist, Opt. Commun. **123**, 207 (1996)

[Sti10] S. Stivala, A. C. Busacca, A. Pasquazi, R. L. Oliveri, R. Morandotti and G. Assanto, Opt. Lett. **35**, 363 (2010)

[Su06] W. Su, L. Qian, H. Luo, X. Fu, H. Zhu, T. Wang, K. Beckwitt, Y. Chen, and F. Wise, J. Opt. Soc. Am. B **23**, 51 (2006)

[Sza83] G. Szabo, Zs. Bor, A.Mfiller, Appl. Phys. B **31**, 14 (1983)

[Ter02] K. Terabe, S. Takekawa, M. Nakamura, K. Kitamura, S. Higuchi, Y. Gotoh, A. Gruverman, Appl. Phys. Lett. **81**, 2044 (2002)

[Tre97] R. Trebino, K.W. DeLong, D.N. Fittinghoff, J.N. Sweetser, M.A. Krumbgel, B.A. Richman, Rev. Sci. Instrum. **68**, 3277 (1997)

[Tru07] J. Trull, C. Cojocaru, R. Fischer, S. Saltiel, K. Staliunas, R. Herrero, R. Vilaseca, D. N Neshev,W. Krolikowski, and Yu. S. Kivshar, Opt. Express **15**, 15868 (2007)

[Tru95] J. Trull, R. Vilaseca, J. Martorell and R. Corbalán, Opt. Lett. **20**, 1746 (1995)

[Tru98] J. Trull, R. Vilaseca and J. Martorell, J. Opt. Soc. Am. B. **15**, 2581 (1998)

[Tru99] J. Trull, R. Vilaseca and J. Martorell, J. Opt. B Quantum Semiclass. Opt. **1**, 307 (1999)

[Tun03] A. R. Tunyagi, M. Ulex, and K. Betzler, Phys. Rev. Lett. **90**, 243901 (2003)

[Tun04] A. R. Tunyagi, *Non-Collinear Second Harmonic Generation in Strontium Barium Niobate*, (PhD thesis, Fachbereich Physik, Universitat Osnabruck, Germany, 2004)

[Val20] J. Valasek, Physical Review **15,** 537 (1920)

[Ver02] G. Veres et al., Appl. Phys. Lett. **81**, 3714 (2002)

[Vid06] X. Vidal and J. Martorell, Phys. Rev. Lett. **97**, 013902 (2006)

[Vil92] P. R. Villeneuve and M. Piché, Phys. Rev. B **46**, 4969 (1992)

[Vin09] M. A. Vincenti, A. D'Orazio M. G. Cappeddu, N.Akozbek, M. J. Bloemer, and M. Scalora, J. Appl. Phys. **105**, 103103 (2009)

[Vin10] M. A. Vincenti, D. de Ceglia, M. Buncick, N. Akozbek, M. J. Bloemer, and M. Scalora, J. Appl. Phys. **107**, 053101 (2010)

[Wan01] T. Wang, L. Qian, H. Zhu, Z. Hou, and F. Li, Opt. Commun. **188**, 213 (2001)

[Wan09] W. Wang, V. Roppo, K. Kalinowski, Y. Kong, D.N. Neshev, C. Cojocaru, J. Trull, R. Vilaseca, K. Staliunas, W. Krolikowski, S. Saltiel, Yu. Kivshar, Opt. Express **17**, 20117 (2009)

[Wan10] W. Wang, K. Kalinowski, V. Roppo, Y. Sheng, K. Koynov, Y. Kong, C. Cojocaru, J. Trull, R, Vilaseca andW, Krolikowski, J. Phys. B: At. Mol. Opt. Phys. **43**, 215404 (2010)

[Web86] M. G. Weber, Phys. Rev. B **33**, 6775 (1986)

[Woi01] Th.Woike, T. Granzow, U. Dorfler, Ch. Poetsch, M.Wohlecke and R. Pankrath, Phys. Stat. Solidi A **186**, R13 (2001)

[Woo07] B. Wood, Laser & Photon. Rev. **1**, 249 (2007)

[Wya81] R.Wyatt, E. Marinero, Appl. Phys. **25**, 297 (1981)

[Xu03] F. Xu, J. L. He, J. Liao, Q. Wang, Q. Xu, N. H. Shen, H. T. Wang, and N. B. Ming, Phys. Rev. A **68**, 053803 (2003)

[Yab91b] E. Yablonovitch, T.J. Gmitter, R.D. Meade, A.M. Rappe, K.D. Brommer and J.D. Joannopoulos, Phys. Rev. Lett. **67**, 3380 (1991)

[Yar67] A. Yariv, Quantum electronics (John Wiley & Sons, 1967)

[Yar77] A. Yariv and P.Yeh, J. Opt. Soc. Am. **67**, 438 (1977)

[Yoo96] S. J. B. Yoo et al., Appl. Phys. Lett. **68**, 2609 (1996)

[Zhu97] S. Zhu, Y. Y. Zhu, N. B. Ming, Science **278**, 843 (1997)

[Zie76] J. V. D. Ziel and M. Ilegems, Appl. Phys. Lett. **28**, 437 (1976)

[Zin07] N. N. Zinovev et al., Phys. Rev. B **76**, 235114 (2007)

List of publications

In this thesis we reported completely original work. Testimony to this is the fact that summaries of this work have been published in peer-reviewed journals and presented to international conferences.

Published papers related to Part I

[1] **V. Roppo**, D.Dumay, J. Trull, C.Cojocaru, S. Saltiel, K. Staliunas, R. Vilaseca, D. Neshev, W. Krolikowski, Yu. Kivshar, *Planar secondharmonic generation with noncollinear pumps in disordered media*, **Opt. Express 16**, 14192 (2008)

[2] W.Wang, **V. Roppo**, K. Kalinowski, Y.Kong, D. N. Neshev, C. Cojocaru, J. Trull, R. Vilaseca, K. Staliunas,W. Krolikowski, S. M. Saltiel and Yu. Kivshar, *Third-harmonic generation via broadband cascading in disordered quadratic nonlinear media*, **Opt. Express 17**, 20117 (2009)

[3] J. Trull, S. Saltiel, **V. Roppo**, C. Cojocaru, D. Dumay, W. Krolikowski, D. N. Neshev, R. Vilaseca, K. Staliunas and Yu. S. Kivshar, *Characterization of femtosecond pulses via transverse second-harmonic generation in random nonlinear media*, **Appl. Phys. B 95**, 609 (2009)

[4] W. Wang, K. Kalinowski, **V. Roppo**, Y. Sheng, K. Koynov, Y. Kong, C. Cojocaru, J. Trull, R. Vilaseca and W. Krolikowski, *Second and third harmonic-parametric scattering in disordered quadratic media*, **Journ. of Phys. B 43,** 215404 (2010)

[5] **V. Roppo**, W.Wang, K. Kalinowski, Y.Kong, C. Cojocaru, J.Trull, R. Vilaseca, M. Scalora, W. Krolikowski and Yu. Kivshar, *The role of ferroelectric domain structure in second harmonic generation in random quadratic media*, **Opt. Express 18**, 4012 (2010)

Published papers related to Part II

[6] **V. Roppo**, M. Centini, C. Sibilia, M. Bertolotti, D. de Ceglia, M. Scalora, N. Akozbek, M.J. Bloemer, J. W. Haus, O. G. Kosareva and V. P. Kandidov, *The role of phase matching in pulsed second harmonic seneration: walk-off and phase-locked twin pulses in negative index media*, **Phys. Rev. A 76**, 033829 (2007)

[7] M. Centini, **V. Roppo**, E. Fazio, F. Pettazzi, C. Sibilia, J. W. Haus, J. V. Foreman, N. Akozbek, M. J. Bloemer, M. Scalora, *Inhibition of Linear Absorption in Opaque Materials Using Phase-Locked Harmonic Generation*, **Phys. Rev. Lett. 101**, 113905 (2008)

[8] **V. Roppo**, C. Cojocaru, F. Raineri, G. D'Aguanno, J. Trull, Y. Halioua, R. Raj, I. Sagnes, R. Vilaseca, and M. Scalora, *Field localization and enhancement of phase-locked second- and third-order harmonic generation in absorbing semiconductor cavities*, **Phys. Rev. A 80**, 043834 (2009)

[9] **V. Roppo**, C. Cojocaru, J. Trull, R. Vilaseca and M. Scalora, *Cavity behaviour of second and third harmonic inhomogeneous solutions of Maxwell's equations*, **Waves in Random and Complex Media 20,** 310 (2010)

[10] **V. Roppo**, C. Cojocaru, F. Raineri, G. D'Aguanno, J. Trull, Y. Halioua, R. Raj, I. Sagnes, R. Vilaseca, and M. Scalora, *Phase locked second and third harmonic localization in semiconductor cavities*, **Journ. of Opt. and Adv. Mat. 12**, 57 (2010)

[11] **V. Roppo**, J. Foreman, N. Akozbek, M.A. Vincenti and M. Scalora, *Third Harmonic Generation at 223nm in the Metallic Regime of GaP*, **App. Phys. Lett. 98**, 111105 (2011)

[12] **V. Roppo**, F. Raineri, R. Raj, I. Sagnes, J. Trull, R. Vilaseca, M. Scalora and C. Cojocaru, *Generation Efficiency of the Second Harmonic Inhomogeneous Component*, accepted for publication **Opt. Lett**. (2011)

Other published papers

[13] **V. Roppo**, M. Centini, D. de Ceglia, M.A. Vincenti, J.W. Haus, N. Akozbek, M.J. Bloemer, M. Scalora, *Anomalous Momentum States, Non-Specular Reflections and Negative Refraction of Phase-Locked, Second Harmonic Pulses*, **Metamaterials 2**, 135 (2008)

[14] M. Scalora, M. A. Vincenti, D. de Ceglia, **V. Roppo**, M. Centini, N. Akozbek and M. J. Bloemer, *Second and Third Harmonic Generation in Metal-Based Structures*, **Phys. Rev. A 82**, 043828 (2010)

[15] **V. Roppo**, C. Ciracì, C. Cojocaru and M. Scalora, *Second Harmonic Generation in a Generic Negative Index Medium*, **Journ. of Opt. Soc. Amer. B 27**, 1671 (2010)

[16] M.A. Vincenti, D. de Ceglia, **V. Roppo** and M. Scalora, *Harmonic Generation in Metallic, GaAs-Filled Nanocavities in the Enhanced Transmission Regime at Visible and UV Wavelengths*, **Opt. Express 19**, 2064 (2011)

Papers submitted and in preparation

[17] Y. Sheng, Q. Kong, **V. Roppo**, K. Kalinowski, Qi Wang, C. Cojocaru, and W. Krolikowski, *The role of the beam width on Cerenkov second harmonic generation*, submitted

[18] Y. Sheng, W. Wang, R. Shiloh, **V. Roppo**, A. Arie and W.Krolikowski, *Cerenkov third-harmonic generation in $\chi^{(2)}$ nonlinear photonic crystal,* submitted

[19] Y. Sheng, **V. Roppo**, Q. Kong, K. Kalinowski, Qi Wang, C. Cojocaru and W. Krolikowski, *Cerenkov-type second-hamonic generation in two-dimensional nonlinear photonic structure*, in preparation

[20] D. de Ceglia, M. A. Vincenti, **V. Roppo**, M. Scalora, *Nonlinear Frequency Conversion in ε-near-zero Materials*, in preparation

[21] **V. Roppo**, N. Akozbek, D. de Ceglia, M.A. Vincenti, M. Scalora, *Harmonic generation and energy transport in GaP at visible and UV wavelengths*, in preparation

[22] **V. Roppo**, C. Cojocaru, M. Scalora, J. Trull, *The role of the absorption in the inhomogeneous second harmonic generation*, in preparation

[23] N. Akozbek, **V. Roppo**, M. A. Vincenti, J. V. Foreman M. J. Bloemer, J. W. Haus and M. Scalora, *Extraordinary nonlinear optics in ordinary semiconductors*, available online at arxiv.org/abs/0904.4082

International conference contributions

- European Optical Society Annual Meeting, Paris (France) October 26-29, 2010.
  Contribution: *Generation Efficiency of the Second Harmonic Inhomogeneous Component*, V. Roppo, C. Cojocaru, J. Trull, F. Raineri, D. Chouteau, I. Sagnes, R. Raj, R. Vilaseca and M. Scalora.

- International Photonic & Electromagnetic Crystal Structures Meeting IX, Granada (Spain) September 26-30, 2010.
  C**ontribution:** Generation of Second harmonic inhomogeneous component in 1D GaAs microcavity, V. Roppo, F. Raineri, J. Trull, D. Chouteau, I. Sagnes, R. Vilaseca, M. Scalora, R. Raj, and C. Cojocaru.

- SPIE Optics+Photonics, San Diego (USA) August 1-5, 2010.
  Contribution: *Nonlinear frequency conversion in a generic Lorentz medium*, V. Roppo, C. Ciraci, C.Cojocaru and M. Scalora.
  Contribution: *Modeling the nonlinear frequency conversion in random quadratic media: second harmonic and cascaded third harmonic generation*, V. Roppo, W. Wang, K. Kalinowski, C. Cojocaru, J. Trull, R.Vilaseca, M. Scalora, W. Krolikowski and Y. Kivshar.
  Contribution: *Broadband third harmonic generation in disordered nonlinear photonic crystals*, K. Kalinowski, V. Roppo, W. Wang, Y. Kong, D. Neshev, C. Cojocaru, J. Trull, R. Vilaseca, K. Staliunas, W. Krolikowski, S. Saltiel, Y. Kivshar. **Published proceeding.**

- International Conference on Trasparent Optica Networks, Munich (Germany) June 27- July 1, 2010.
  Invited contribution: *Second and third harmonic generation in disordered quadratic nonlinear media. Application to short-pulse characterization*, V. Roppo, W.Wang, K. Kalinowski, R. Vilaseca, J. Trull, C. Cojocaru, K. Staliunas,W. Krolikowski, and Yu. Kivshar.
  Invited contribution: *The role of ferroelectric domain structure in second harmonic generation in random quadratic media*, V. Roppo, J. Trull, C. Cojocaru, R. Vilaseca, M. Scalora, W. Wang, K. Kalinowski, W. Krolikowski and Yu. Kivshar. **Published proceeding.**

- Nonlinear Photonics 2010, Karlsruhe (Germany) June 21-24, 2010.
  Contribution: *Second-Harmonic Generation in Disordered Quadratic Media: Role of a Ferroelectric Domain Structure*, V. Roppo, K. Kalinowski, W. Wang, C. Cojocaru, J. Trull, R. Vilaseca, M. Scalora, W. Krolikowski and Yu. Kivshar.
  Contribution: *Broadband Third Harmonic Generation in QuadraticNonlinear Media with Disordered Ferroelectric Domains*, K.Kalinowski, V.Roppo, W.Wang, D.N.Neshev, C.Cojocaru, J.Trull, R.Vilaseca, K.Staliunas, W.Krolikowski and Y.S.Kivshar.

- Frontiers in Optics 2009, San Jose (USA), October 11-15, 2009.
  Contribution: *The Effect of Domain Distribution on Second Harmonic Generation in Disordered Nonlinear Media*, V. Roppo, S. Saltiel, W. Wang, K. Kalinowski, J. Trull, C. Cojocaru, D.N. Neshev, W. Krolikowski, R. Vilaseca, K. Staliunas, Yu.S. Kivshar.
  Contribution: Phase-Locked second harmonic generation in Sub-wavelenght channels, D. De Ceglia, M. A. Vincenti, V. Roppo, N. Akozbek, M. J. Bloemer and M. Scalora.
  Contribution: *The Role of the Phase Locking Phenomenon in the Second and Third Harmonics Cavity Localization*, V. Roppo, C. Cojocaru, G. D'Aguanno, F. Raineri, R. Raj, J. Trull, R. Vilaseca, M. Scalora. **Published proceeding ISBN 978-1-55752-879-7**.

- Micro- to Nano-Photonics II - ROMOPTO 2009, Sibiu (Romania) Agust 31- September 3, 2009.
  Invited Contribution: *Phase Locked second and third harmonic localization in semiconductor cavities*, C. Cojocaru, V. Roppo, G.D'Aguanno, F. Raineri, J. Trull, R. Vilaseca, R. Raj, M. Scalora.

- Metamaterials 2009, London (UK) August 30 - September 4, 2009.
  Invited Contribution: *Enhanced Transmission Response from Subwavelength Slits in Semiconductors in the UV range*, M. A. Vincenti, M. Scalora, V. Roppo, D. de Ceglia, A.D'Orazio and M. J. Bloemer. **Published proceeding.**

- Nonlinear Optics, Honolulu (Hawaii) July 12-17, 2009.
  Invited Contribution: *Femtosecond pulse duration measurement by transverse second-harmonic generation in random nonlinear media*, R. Vilaseca, V. Roppo, J. Trull, C. Cojocaru, K. Staliunas, D. Dumay, W. Krolikowski, S. Saltiel, D. N. Neshev and Y. Kivshar. **Published proceeding NWA6.**

- International Laser Physics Workshop, Barcelona (Spain) July 13-17, 2009.
  Invited Contribution: *Second harmonic generation in disordered media: fundamentals and applications*, V. Roppo, W. Wang, K. Kalinowski, S. Saltiel, J. Trull, C. Cojocaru, D.N. Neshev, W. Krolikowski, R. Vilaseca, K. Staliunas and Y.S. Kivshar.

- International Conference on Trasparent Optica Networks, Ponta Delgada (Portugal) June 27- July 2, 2009.
  Invited Contribution: *Phase locked Second Harmonic etalon localization in opaque materials,* C. Cojocaru, V. Roppo,G. D'Aguanno, F. Raineri, J. Trull, R. Raj, R. Vilaseca, M. Scalora. **Published proceeding.**

- The European Conference on Lasers and Electro-Optics, Munich (Germany) June 14-19, 2009.
  Contribution: *Phase locked Second Harmonic etalon localization*, V. Roppo, G. D'Aguanno, C. Cojocaru, F. Raineri, J. Trull, R. Vilaseca, R. Raj and M. Scalora. **Published proceeding CD2_2.**

- International Photonic & Electromagnetic Crystal Structures Meeting, Sydney (Australia) April 5-9, 2009.
  Contribution: *Localization of the Phase Locked Second Harmonic field*, V. Roppo , C. M. Cojocaru, J. Trull, M. Scalora.
  Contribution: *Transverse Second-Harmonic Generation in Disordered Media – New Tool for Reconstruction of Short Pulses*, D. N. Neshev, A. A. Sukhorukov, D. Dumay, S. Ha, V. Roppo, J. Trull, C. Cojocaru, S. Saltiel, K. Staliunas, R. Vilaseca, W. Krolikowski and Yuri Kivshar. **Published proceeding ISBN 978-0-646-50323-3**.

- IEEE LEOS Conference, Innsbruck (Austria) January 12-14, 2009.
  Invited contribution: *New Propagation Effects in Semiconductors in the UV Range:Inhibition of Absorption, Negative Refraction, Anomalous*

Momentum States, Sub-Wavelength Imaging and Non-Plamonic Nanometer-size Guided Waves, M. Scalora, M.A. Vincenti, V. Roppo, John V. Foreman, J. W. Haus, N. Akozbek, M.J. Bloemer. **Published proceeding ISBN 978-1-4244-2611-9.**

- Frontiers in Optics 2008, Rochester (USA) October 20-24, 2008.
  Contribution: *Reconstruction of short pulses via transverse second-harmonic generation in disordered media*, D. N. Neshev, A. A. Sukhorukov, D. Dumay, S. Ha, V. Roppo, J. Trull, C. Cojocaru, S. Saltiel, K. Staliunas, R. Vilaseca, W. Krolikowski and Y. Kivshar.
  Contribution: *New Propagation Effects in Semiconductors in the UV Range: Inhibition of Absorption, Negative Refraction, Anomalous Momentum States, and Sub-Wavelength Imaging*, M. Scalora, V. Roppo, John V. Foreman, M. Centini, M.A. Vincenti, Neset Akozbek, M.J. Bloemer. **Published proceeding.**

- European Optical Society Annual Meeting, Paris (France) September 29 - October 2, 2008.
  Contribution: *Femtosecond pulse duration measurements by transverse second harmonic generation in random nonlinear media*, V.Roppo, J. Trull, C.Cojocaru, R. Vilaseca, K. Staliunas,S. Saltiel, D. Neshev, W. Krolikowski, Yu. Kivshar.

- Metamaterials 2008, Pamplona (Spain) September 21-26, 2008.
  Contribution: *On the Inhibition of Linear Absorption in Opaque Materials*, M. Centini, V. Roppo, E. Fazio, F. Pettazzi, C. Sibilia, J. W. Haus, M.A. Vincenti, J. V. Foreman, N. Akozbek, M. J. Bloemer, M. Scalora.
  Contribution: *Negative refraction and sub-wavelength resolution below the dif-fraction limit using a semiconductor-based superlens*, A. Vincenti, V. Roppo, A. D'Orazio, N. Akozbek, M. Scalora, M.J. Bloemer.
  Contribution: *New propagation effects in semiconductors in the UV range: inhibition of absorption, negative refraction, anomalous momentum states, and sub-wavelength imaging*, M. Scalora, V. Roppo, J. V. Foreman, M. Centini, M. A. Vincenti, N.Akozbek, M.J. Bloemer. **Published proceeding**.

- International School on Nanophotonics and Molecular Photonics, Santander (Spain), June 16-20, 2008.
  Contribution: *On the Inhibition of Linear Absorption in Opaque Materials*, M. Centini, V. Roppo, E. Fazio, F. Pettazzi, C. Sibilia, J. W.Haus, J. V. Foreman, N. Akozbek, M. J. Bloemer, M. Scalora.

- Discrete Optic and Beyond, Bad-Honnef (Germany) May 19 -22, 2008.
  Contribution: *On the Inhibition of Linear Absorption in Opaque Materials*, M. Centini, V. Roppo, E. Fazio, F. Pettazzi, C. Sibilia, J. W. Haus, J. V. Foreman, N. Akozbek, M. J. Bloemer, M. Scalora.

Acknowledgments

The most important lesson I learned in these last years is that it is not enough to get what it takes in order to succeed, both in the professional and in the private life. The people we run into during our life are crucial to determine the direction we will follow in our journey.

It is almost impossible for me to properly thank all the people that contributed at any level to make my doctorate experience so extraordinary, but I will try anyway.

I want first thanks Crina, Jose and Ramon V. who has followed me every day with the patience that only those who love their work can do. They taught me much more than they will never admit.

Thanks to Wieslaw Krolikowski who kept giving me priceless possibilities to grow up scientifically and personally, watching the world up-side down.

Thanks to all the members of DONLL for the time spent together and for the improbable conversations we were always about to have (especially about the Catalan identity!).

Grazie alla mia famiglia, che è sempre stata orgogliosa e felice per me anche se faccio questo strano lavoro. E` il supporto piu importante che abbia potuto avere.

Grazie ad Alessia, che ha deciso di scommetere tutto e per la sua straodinaria capacitá di reinvenarsi una vita pur di affrontare con me questo percorso.

Grazie a Cristian per essere stato un punto fisso e un cofronto continuo in questo cambiamento senza fine. E' la prova che le amicizie prescindono anche dalla geografia.

Thanks to Elisa, Domenico, Antonella, Fiorenza, Santanu, Yuni, Daniele, Ana and to all the other people I met in Huntsville. They were extraordinary to made me feel home.

Finally, thanks to Mike, for so many reasons that would be limiting even try to list here.